

2015-01-01

Design of a High Intensity Turbulent Combustion System

Mohammad Arif Hossain
University of Texas at El Paso, mhossain3@miners.utep.edu

Follow this and additional works at: https://digitalcommons.utep.edu/open_etd



Part of the [Aerospace Engineering Commons](#), [Art and Design Commons](#), and the [Mechanical Engineering Commons](#)

Recommended Citation

Hossain, Mohammad Arif, "Design of a High Intensity Turbulent Combustion System" (2015). *Open Access Theses & Dissertations*. 1068.
https://digitalcommons.utep.edu/open_etd/1068

This is brought to you for free and open access by ScholarWorks@UTEP. It has been accepted for inclusion in Open Access Theses & Dissertations by an authorized administrator of ScholarWorks@UTEP. For more information, please contact lweber@utep.edu.

DESIGN OF A HIGH INTENSITY TURBULENT COMBUSTION SYSTEM

MOHAMMAD ARIF HOSSAIN

Department of Mechanical Engineering

APPROVED:

Ahsan R. Choudhuri, Ph.D., Chair

Norman D. Love, Ph.D., Co-Chair

Tzu-Liang (Bill) Tseng, Ph.D.

Charles Ambler, Ph.D.
Dean of the Graduate School

Copyright ©

by

Mohammad Arif Hossain

2015

Dedication

This work is dedicated to my parents. Without their support, it was impossible for me to come this far in my life.

*-Mohammad Arif Hossain
May 13, 2015*

DESIGN OF A HIGH INTENSITY TURBULENT COMBUSTION SYSTEM

by

MOHAMMAD ARIF HOSSAIN, B.SC.Engg. (Mech)

THESIS

Presented to the Faculty of the Graduate School of

The University of Texas at El Paso

in Partial Fulfillment

of the Requirements

for the Degree of

MASTER OF SCIENCE

Department of Mechanical Engineering

THE UNIVERSITY OF TEXAS AT EL PASO

May 2015

Acknowledgements

I would like to acknowledge the great contributions and amazing mentorship of my supervisor Dr. Ahsan Choudhuri. It is an honor and privilege to express my appreciation to my committee members Dr. Norman Love and Dr. Tzu-Liang (Bill) Tseng who have given their valuable time and support. I would like to thank my group members, Arturo Acosta and Marco Quiroz, who have spent their last two years working with me to make this project successful. It was impossible for me to come this far with this project without their help and cooperation. I would also like to thank Gloria Salas, Laura Orozco and Alejandra Garcia for their extraordinary support during my graduate study. Furthermore, a special thanks to all the members of cSETR for supporting me all the time. Finally, I would like to acknowledge the financial support provided by NASA under award No(s) NNX09AV09A and W911NF-13-1-0156 via the Army Research Office (ARO).

Abstract

In order to design next generation gas turbine combustor and rocket engines, a systemic study of flame structure at high intensity turbulent flow is necessary. The fundamental study of turbulent premixed combustion has been a major research concern for decades. The work is focused on the design and development of a high intensity turbulent combustion system which can be operated at compressible ($0.3 < M < 0.5$), preheated ($T_0=500\text{K}$) and premixed conditions in order to investigate the '*Thickened Flame*' regime. An air-methane mixture has been used as the fuel for this study. An optically accessible backward-facing step stabilized combustor has been designed for a maximum operating pressure of 6 bar. A grid has been introduced with different blockage ratios ($BR = 54\%, 61\% \text{ \& } 67\%$) in order to generate turbulence inside the combustor for the experiment. Optical access is provided via quartz windows on three sides of the combustion chamber. Finite Element Analysis (FEA) is done in order to verify the structural integrity of the combustor at rated conditions. In order to increase the inlet temperature of the air, a heating section was designed to use commercially available in-line heaters. Separate cooling subsystems have been designed for chamber cooling and exhaust cooling. The LabVIEW software interface has been selected as the control mechanism for the experimental setup. A 10 kHz Time Resolved Particle Image Velocimetry (TR-PIV) system and a 3 kHz Planer Laser Induced Fluorescence (PLIF) system have been integrated with the system in order to diagnose the flow field and the flame respectively. The primary understanding of the flow field inside the combustor was achieved through the use of Detached Eddy Simulation (DES) by using commercially available software package ANSYS FLUENT. Preliminary validation is done by 10 kHz TR-PIV technique. Both qualitative and quantitative analysis have been done for CFD and experiment. Major flow parameters such as average velocity, fluctuation of velocity, kinetic energy, and turbulent intensity have been calculated for two distinct Reynolds number ($Re = 815 \text{ \& } 3500$). PIV results are compared with CFD results which show significant agreement with each other.

Table of Content

Acknowledgements	v
Abstract.....	vi
Table of Content.....	vii
List of Tables	ix
List of Figures	x
Chapter 1: Introduction.....	1
1.1 Objective	3
1.2 Thesis Outline	4
Chapter 2: Theory and Literature Review	6
2.1 Turbulent Flow	6
2.1.1 Statistical Description of Turbulent Flow	8
2.1.2 Properties of Turbulent Flow	11
2.1.3 Turbulent Length Scale and Eddy Cascade	14
2.1.4 Grid Induced Turbulence	19
2.1.5 Flow Over a Backward Facing Step	21
2.2 Combustion.....	23
2.2.1 Laminar Premixed Flame.....	25
2.2.2 Laminar Flame Speed (S_L)	26
2.2.3 Turbulent Premixed Combustion	29
2.2.4 Flame Regime	32
Chapter 3: Experimental Setup Design.....	37
3.1 Experimental Criteria	37
3.2 Combustor Design.....	39
3.2.1 Von Mises Stress Calculation	43
3.3 Entrance and Exhaust Section Design.....	51
3.4 Grid Design.....	58
3.5 Window Design	61
3.6 Heating and Exhaust System Design.....	65
3.7 Combustion Chamber Cooling	67

3.8	Test Setup	69
Chapter 4: Instrumentation and Measurement		74
4.1	Particle Image Velocimetry (PIV)	74
4.2	Planer Laser Induced Fluorescence (PLIF)	80
4.3	Flow rate Measurement	86
4.4	Temperature and Pressure Measurement	88
4.5	Control System	90
Chapter 5: Result and Discussion.....		92
5.1	Particle Image Velocimetry (PIV) Data	92
5.1.1	Measurement of Average Velocity.....	94
5.1.2	Measurement of Kinetic Energy.....	102
5.1.3	Measurement of Turbulent Intensity	106
5.2	CFD Modeling.....	111
5.2.1	Computational Domain and Meshing.....	112
5.2.2	Case Setup and Solution	113
5.2.3	CFD Measurement of Average Velocity	114
5.2.5	CFD Measurement of Turbulent Intensity.....	122
Chapter 6: Conclusion		127
6.1	Summary	127
6.2	Future Work.....	128
Reference		129
Appendix I		136
Appendix II		143
Appendix III.....		144
Appendix IV		148
Glossary.....		151
Vita		152

List of Tables

Table 2. 1: Calculation of stoichiometric coefficient	25
Table 2. 2: Laminar flame speed of the Stoichiometric Methane-Air at various range of ϕ , T_u and P_u	27
Table 2. 3: Experimental study of turbulent flame speed.	31
Table 3. 1: Combustor design criteria.....	37
Table 3. 2: UNS 316 Stainless Steel properties.....	40
Table 3. 3: Fused Quartz properties.....	40
Table 3. 4 Calculation of deformation for thermal and pressure loading.	50
Table 3. 5: Calculation of hole diameter for the grid.	58
Table 3. 6: Heater specification.....	65
Table 4. 1: Detection wavelength of different species.....	82

List of Figures

Figure 1.1: Conceptual CAD model of the combustor system.....	2
Figure 2. 1: Planer image of concentration in a turbulent jet: (a) $Re = 20,000$ and (b) $Re = 5000$ [4].....	7
Figure 2. 2: Velocity measurement on the n th repetition of a turbulent-flow experiment. [1]	8
Figure 2. 3: Velocity measurement on the n th repetition of a turbulent-flow experiment.....	9
Figure 2. 4: (a) CDF of a random variable U representing the probability event of the event $C = \{V_a \leq U \leq V_b\}$; (b) the corresponding PDF.	10
Figure 2. 5: Statistically homogeneous isotropic turbulence.	14
Figure 2. 6: Energy cascade of turbulent flow.	15
Figure 2. 7: Tow point velocity correlation.	16
Figure 2. 8: Relation between two point correlation coefficient and integral length scale.....	16
Figure 2. 9: Energy spectrum of turbulence length scale.....	18
Figure 2. 10: Grid turbulence and its different stages [21]	20
Figure 2. 11: (a) Sketch of grid, $M =$ grid spacing, (b) Decay of Reynolds stress	20
Figure 2. 12: Schematic of different separation zone in a backward facing step flow.	21
Figure 2. 13: CFD result validation with experimental data.[35].....	22
Figure 2. 14: Concentration & temperature profile. (a) premixed, (b) diffusion flame.	23
Figure 2. 15: Simplest representation of stoichiometric combustion of hydrocarbon fuel	24
Figure 2. 16: Laminar flame structure. Temperature and species concentration profile [46]	26
Figure 2. 17: Laminar flame speed of methane-air at 298K and 1 atm pressure [61]	28
Figure 2. 18: Laminar flame speed of methane-air at 0.25 to 20 atm [61]	29
Figure 2. 19: Laminar flame speed of methane-air at elevated temperature [69].....	29
Figure 2. 20: Turbulent flame speed measured by Filatyev et al [72].....	31
Figure 2. 21: Flame regime diagram by Borghi modified by Peter.....	32
Figure 2. 22: Different flame regime and its characteristic	33
Figure 2. 23: Wrinkled flame. (a) schematic presentation, (b) CH-LIF image of actual flame	34
Figure 2. 24: Corrugated flame (a) Flame regime, (b) corrugated flame structure [84].....	34
Figure 2. 25: Thickened flame (a) Flame regime, (b) DNS of flame structure.....	35
Figure 2. 26: Distributed flame (a) Flame regime, (b) DNS of flame structure.....	36
Figure 3. 1: Exploded view of the combustor assembly	38
Figure 3. 2: Sectional view of the combustor assembly	39
Figure 3. 3: Relationship between flow velocity and effective diameter.....	41
Figure 3. 4: Combustor schematic.....	42
Figure 3. 5: Detail drawing of the combustor	43
Figure 3. 6: Contour of Von Mises stress at 25 bar pressure loading.....	45
Figure 3. 7: Von Mises stress along the thickness of the side window slot.	46
Figure 3. 8: Von Mises stress along the thickness of the top window slot.	47
Figure 3. 9: Von Mises stress along the thickness of the side wall at three different locations.	47
Figure 3. 10: Von Mises stress along the thickness of the top wall at three different locations	48
Figure 3. 11: Von Mises stress along the thickness of the bottom wall at three different locations.	48
Figure 3. 12: Contour of maximum shear stress (left) and maximum principle stress (right).	49

Figure 3. 13: Contour of deformation due to thermal and pressure loading.	50
Figure 3. 14: Entrance section profile.....	52
Figure 3. 15: Exhaust section profile.....	52
Figure 3. 16: Tangential stress distribution.....	53
Figure 3. 17: Stress distribution along the length.....	53
Figure 3. 18: Contour of principle normal stress, shear stress, von mises stress and deformation.	54
Figure 3. 19: Stress distribution along the length.....	55
Figure 3. 20: Stress distribution along the wall thickness.....	55
Figure 3. 21: Contour of stress components for first exhaust part.	56
Figure 3. 22: Contour of stress components for second exhaust part.....	56
Figure 3. 23: Stress distribution along the length for second exhaust part.	57
Figure 3. 24: Stress distribution along the length for the second exhaust part.....	57
Figure 3. 25: Relation between number of hole with blockage ratio.....	59
Figure 3. 26: Stress distribution along the thickness of the grid.	59
Figure 3. 27: Stress distribution along the length for the grid.....	60
Figure 3. 28: Contour of stress components and deformation for the grid.	60
Figure 3. 29: Detail drawing of the side window.	61
Figure 3. 30: Factor of safety and pressure relation at different window thickness.	62
Figure 3. 31: Stress distribution along the thickness of the top window.	62
Figure 3. 32: Contour of von mises stress and deformation of top and side window.....	63
Figure 3. 33: Stress distribution along the thickness of the side window.....	64
Figure 3. 34: Stress distribution along the thickness of the side window.....	64
Figure 3. 35: Heater schematic. (a) CAD model, (b) detail dimensions.....	65
Figure 3. 36: Steady state and transient thermal analysis of the heater.	66
Figure 3. 37: Exhaust gas cooling chamber assembly.....	66
Figure 3. 38: Heat exchanger for combustion chamber cooling.	67
Figure 3. 39: Transient temperature profile at different thickness of the chamber.	68
Figure 3. 40: CAD model of the system assembly.....	68
Figure 3. 41: Flow schematic of the main system and the pilot flame.	70
Figure 3. 42: Combustion chamber assembly.....	71
Figure 3. 43: Air line with different instrumentation.	72
Figure 3. 44: Mixing chamber with air line and methane line.	72
 Figure 4. 1: Schematic of experimental arrangement for PIV [101].	 75
Figure 4. 2: Schematic representation of light plane and image plane.	76
Figure 4. 3: Experimental image plane and location of step, walls and grid.	77
Figure 4. 4: Nd-YLF laser unit, seeder assembly and laser beam direction.	78
Figure 4. 5: Flow schematic of the PIV subsystem.	79
Figure 4. 6: Electric connection of the PIV system with the CPU, camera and BNC timer box.	79
Figure 4. 7: (a) Demonstration of the fluorescence technique. (b) Energy distribution.	80
Figure 4. 8: Typical OH and CH PLIF signal of a turbulent jet flame [111].	83
Figure 4. 9: PLIF assembly along with the pump laser and the dye laser.....	84
Figure 4. 10: Beam diagram of the Dye laser.	84
Figure 4. 11: The electric line diagram for the PLIF system.	85

Figure 4. 12: Assembly of simultaneous PIV-PLIF measurement.	86
Figure 4. 13: (a) 120V solenoid valve. (b) DC proportional control valve.	87
Figure 4. 14: (a) 12V DC valve for methane line. (b) 12V DC valve for pilot flame.	87
Figure 4. 15: (a) Thermocouple in the main airline (b) Thermocouple in the methane line.	88
Figure 4. 16: Pressure transducer (a) Main airline, (b) Pilot flame line, (c) Combustor step	89
Figure 4. 17: Transient temperature profile at different thickness of the chamber.	90
Figure 4. 18: LabVIEW front panel of the control system.	91
Figure 4. 19: LabVIEW block diagram of the control system.	91
Figure 5. 1: Raw PIV image at $Re = 815$	93
Figure 5. 2: Average PIV image at $Re = 815$	93
Figure 5. 3: Interrogation image field and six different locations for quantitative calculation.	94
Figure 5. 4: Instantaneous velocity vector colored by U-velocity at $Re = 815$	95
Figure 5. 5: Instantaneous velocity vector colored by U-velocity at $Re = 3500$	95
Figure 5. 6: Instantaneous U-velocity at a single point at $Re = 3500$	96
Figure 5. 7: Instantaneous V-velocity at a single point at $Re = 3500$	97
Figure 5. 8: U_{mean} velocity from PIV calculation at $Re = 815$ and $x/L = 0.06$	97
Figure 5. 9: U_{mean} velocity from PIV measurement before the step at $Re = 815$	98
Figure 5. 10: V_{mean} velocity from PIV measurement before the step at $Re = 815$	98
Figure 5. 11: U_{mean} velocity from PIV measurement after the step at $Re = 815$	99
Figure 5. 12: V_{mean} velocity from PIV measurement after the step at $Re = 815$	99
Figure 5. 13: U_{mean} velocity from PIV measurement before the step at $Re = 3500$	100
Figure 5. 14: V_{mean} velocity from PIV measurement before the step at $Re = 3500$	101
Figure 5. 15: U_{mean} velocity from PIV measurement after the step at $Re = 3500$	101
Figure 5. 16: V_{mean} velocity from PIV measurement after the step at $Re = 3500$	102
Figure 5. 17: Kinetic energy without the grid at $Re = 815$	103
Figure 5. 18: Kinetic energy at $Re = 815$	103
Figure 5. 19: Kinetic energy at $Re = 3500$	104
Figure 5. 20: Normalized kinetic energy before the step at $Re = 815$	104
Figure 5. 21: Normalized kinetic energy after the step at $Re = 815$	105
Figure 5. 22: Normalized kinetic energy before the step at $Re = 3500$	105
Figure 5. 23: Normalized kinetic energy after the step at $Re = 3500$	106
Figure 5. 24: PIV measurements of Vorticity contour at $Re = 815$	107
Figure 5. 25: PIV measurements of Vorticity contour at $Re = 3500$	107
Figure 5. 26: Turbulent intensity before the step at $Re = 815$	108
Figure 5. 27: Turbulent intensity after the step at $Re = 815$	108
Figure 5. 28: Turbulent Intensity before the step at $Re = 3500$	109
Figure 5. 29: Turbulent Intensity after the step at $Re = 3500$	109
Figure 5. 30: Turbulent Intensity at $x/L = 0.33$ at different Reynolds number.	110
Figure 5. 31: Turbulent Intensity at $x/L = 0.73$ at different Reynolds number.	110
Figure 5. 32: CFD domain of a backward facing step channel.	112
Figure 5. 33: CFD result validation with experimental data. The line 'CFD Project' represents the computational result [35].	114
Figure 5. 34: Average U-velocity from PIV and CFD calculation at $Re = 815$ and $x/L = 0.06$	115

Figure 5. 35: CFD result of instantaneous U-velocity contour at $Re = 815$	116
Figure 5. 36: CFD result of instantaneous V-velocity contour at $Re = 815$	116
Figure 5. 37: CFD result of average U-velocity distribution before the step at $Re = 815$	117
Figure 5. 38: CFD result of average V-velocity distribution before the step at $Re = 815$	117
Figure 5. 39: CFD result of instantaneous U-velocity contour at $Re = 3500$	118
Figure 5. 40: CFD result of instantaneous U-velocity contour at $Re = 3500$	118
Figure 5. 41: Normalized kinetic energy distribution before the step at $Re = 815$	119
Figure 5. 42: CFD result of instantaneous pressure contour at $Re = 815$	120
Figure 5. 43: CFD result of instantaneous pressure contour at $Re = 3500$	120
Figure 5. 44: CFD calculation of static pressure coefficient before the step at $Re = 815$	121
Figure 5. 45: CFD calculation of static pressure coefficient after the step at $Re = 815$	121
Figure 5. 46: Comparison of Turbulent Intensity at $x/L = 0.06$ for PIV and CFD.....	122
Figure 5. 47: CFD result of instantaneous vorticity contour at $Re = 815$	123
Figure 5. 48: CFD result of instantaneous vorticity contour at $Re = 3500$	123
Figure 5. 49: CFD result of turbulent intensity distribution before the step at $Re = 815$	124
Figure 5. 50: CFD result of Turbulent intensity for different blockage ratio at $x/L = 0.33$	125
Figure 5. 51: CFD result of strain rate contour at $Re = 815$	125
Figure 5. 52: CFD result of strain rate contour at $Re = 3500$	126
Figure 5. 53: CFD result of path line at $Re = 815$ colored by stream function.	126

Chapter 1: Introduction

The fundamental understanding of turbulent premixed combustion is one of the major research areas in recent time both in aviation and the industry. It has become one of the prior research interests of the Air Force Office of Scientific Research (AFSOR). In order to design and optimize next generation gas turbine combustor and rocket engines, a systemic study of flame structure at high intensity turbulent flow is necessary. Numerous researches have been studying to understand the fundamentals of flame structure and its interaction with the flow. But the behavior of turbulent combustion is still not very clear to the scientific community. Designers still rely on the design-test-modify method which is not only time consuming but also expensive. Therefore, the industrial community is eagerly waiting for a reliable and effective numerical model in order to design next generation combustor which needs a detailed experimental analysis of the fundamentals of turbulent flame structure and a wide range of experimental data.

The development of high repetition rate laser diagnostic technique such as Particle Image Velocimetry (PIV) and Laser Induced Fluorescence (LIF) enable us to study the turbulent flow and turbulent combustion in a whole new dimension. These non-intrusive techniques help us to study the actual high speed flow without affecting the flow field which provides the answer of the following questions-

- What are the characteristics of premixed flame structure at compressible and high intensity turbulent combustion?
- What are the limit of regime boundaries of this conditions?
- What are the scales affecting the characteristics of different flame zone?

In order to answer the aforementioned questions with the advanced flow diagnostics technique, a safe and reliable high intensity combustion system needs to be developed. The main goal of this study is to design and develop a robust high intensity turbulent combustion system which can be operated at high pressure (approximately 6 bar) and high velocity ($\text{Mach} > 0.3$).

In order to achieve different operating conditions, the combustion system has to be designed for a wide range of variables such as flow rate, pressure, preheated temperature and different level of turbulent intensity. Moreover, the combustor has to be optically accessible for the high speed laser diagnostic. As the primary purpose of this experiment is to study the flame structure of a preheated premixed turbulent flame, the combustor has to be safe enough to operate for a longer period of time. All of these conditions have to be fulfilled in order to design and develop the combustion system. Figure 1.1 shows the conceptual CAD model of the combustor and its different features.

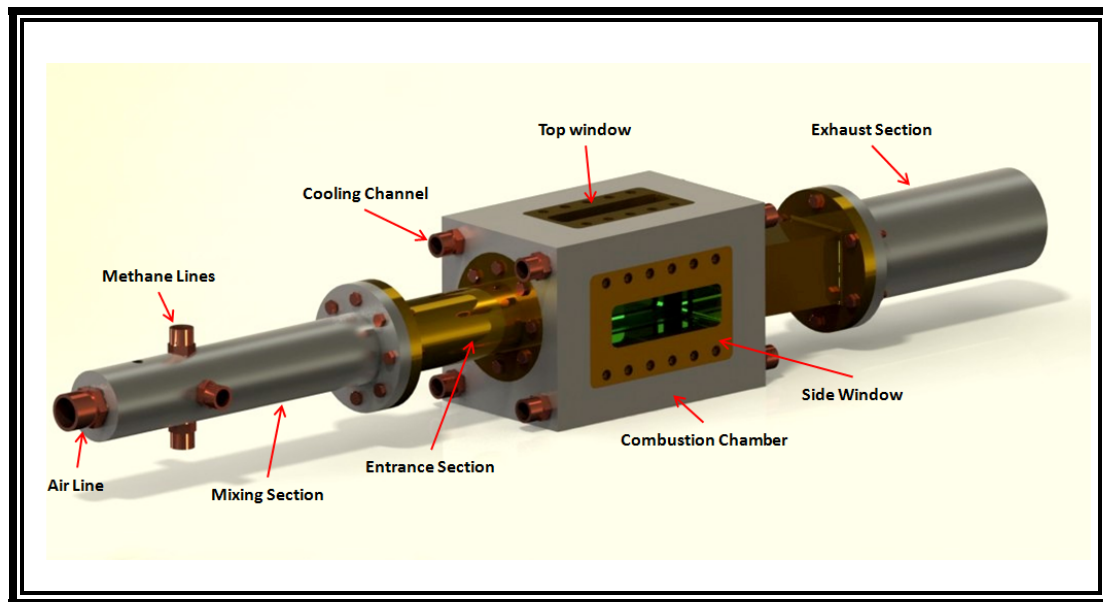


Figure 1.1: Conceptual CAD model of the combustor system.

1.1 Objective

The Center for Space Exploration Technology Research (cSETR) at the University of Texas at El Paso has a unique facility for combustion research. It has state of the art kHz level laser diagnostic system consisting of a 10kHz Particle Image Velocimetry (PIV) and a 3 kHz Planer Laser Induced Fluorescence (PLIF) system. The facility also has 3 kHz high speed imaging system and a 190 cfm compressor system which can be operated at a maximum pressure of 140 psi. This specific experiment is supported by the Army Research Office (ARO) and a collaboration with Princeton University. The main objectives of this project are as follow-

- To study the global characteristics of a backward facing step stabilizing flame in compressible and high intensity turbulent flow using high speed flow visualization technology.
- To study flow and flame characteristics using Time Resolved Particle Image Velocimetry (TR-PIV) and OH/CH Planer Laser Induced Fluorescence (PLIF) imaging.
- To generate components of turbulent intensity and turbulent kinetic energy.
- To delineated the effects of bulk velocity parameters, turbulence parameters and recirculation zone characteristics on location, shape, fluctuation, reaction zone and local displacement speed.

There are some specific tasks to compete for each objective. The first task is to develop an optically accessible backward facing step stabilized combustor with a fully functional control system. The next task is to integrate the sub systems and validate the functionality of the system. There are some other tasks such as experimental measurements to evaluate global flow and flame regime, simultaneous PIV and OH/CH-PLIF imaging of the flame which can be done after a successful system development of a reliable and safe high intensity combustion system. At this

stage, the author's primary goal is to design and develop a fully functional optically accessible high intensity turbulent combustion system in order to diagnose the flow and flame by PIV and PLIF technique respectively.

1.2 Thesis Outline

The author tried to focus on the design and development of the combustion system which includes a detailed review of previous work on combustor design, the theory of mechanical design and system design, fundamental working principle of flow and flame diagnostic techniques (PIV & PLIF), system integration, data acquisition and CFD analysis of flow inside the combustor.

Chapter one of this thesis describes the objectives of this work and its importance. Chapter two includes the detail theory and literature review of turbulent flow, statistical analysis of turbulent flow, properties of turbulent flow, characteristic length scale and time scale definition, grid induced turbulence, flow through a backward facing step channel. In this chapter the author also describes the theory and literature review of combustion, laminar flame speed, turbulent premixed combustion and different flame regime.

Chapter three includes the detail design of the combustor and the system integration. First the author described the previous combustor design done by different researcher. Then a detail design approach has been described based on experimental criteria and requirements. The design of each individual component has been described in this chapter which includes the main chamber, the entrance and exhaust section, the window, the grid and the step. The Von Mises stress has been calculated and showed in this section for each components. Moreover the heating and exhaust system have been described with chamber cooling and exhaust cooling analysis. Finally the system assembly has been showed with flow schematic and detailed description.

Chapter four consists of the description of different instrumentation and measurement devices. It includes the working principal of Particle Image Velocimetry (PIV) and its setup criteria for this specific experiment. Then the similar description for Planer Laser Induced Fluorescence (PLIF) has been added. A detailed description of pressure, temperature and flow rate measurement have been described. Finally the control system and the data acquisition system have been described.

Chapter five shows the PIV results and the CFD results of the combustor flow field. A preliminary flow analysis of the combustor with different grid and different Re have been showed. Vector field of velocity, contour of vorticity, kinetic energy from PIV analysis have been included. The CFD result includes the contour of velocity field, vorticity, and pressure distribution inside the combustor for different Re. Finally the average velocity calculated from both CFD and PIV are compared. The plot of mean velocity, fluctuation of velocity, turbulent intensity and turbulent kinetic energy at different location of the combustor are shown for both CFD and PIV analysis.

Chapter 2: Theory and Literature Review

2.1 Turbulent Flow

Turbulent flow is the most common phenomena in engineering application. In general, turbulent flow is unsteady, irregular, chaotic and seemingly random [1]. Almost all of the internal and external flow applications experience turbulent flow. For example, flows around airplanes, automobiles, ships are mostly turbulent flow. Similarly, flow through lines, pumps and compressors are also highly turbulent. Moreover, the mixing of the reactants in chemical reactors, boilers, furnaces and mixing of fuel and air in engines take place in turbulent flow.

One of the most important characteristics of turbulent flow is its ability to transport. This transport results in mixing of fluid more efficiently than laminar flow which is well demonstrated by Osborne Reynolds [2] where dye is injected on the centerline of a long water flowing pipe. Later he established single non-dimensional flow characteristic parameter known as Reynolds number, Re [3]. In general, Reynolds number is defined as-

$$Re = \frac{UL}{\nu}$$

where U and L are the characteristic velocity and length scales of the flow, and ν is the kinematic viscosity of the fluid. For different case and geometry, the Reynolds number dictates whether the flow should be laminar or turbulent. Careful observations show that for different Reynolds number the scale motion and flow behavior changes significantly. Figure 2.1 shows a typical planar images of a turbulent jet at two different Reynolds number which shows the irregularity and large range of length scale. The effectiveness of turbulence for mixing and transporting is one of the main applicable features in industry. It is expected that, when two fluids are brought together, mixing would be as rapidly as possible which is important for pollutant dissolving to the atmosphere that comes from different chemical reactor and other combustion devices. Moreover the efficiency of heat and mass transfer, combustion and

chemical reaction depends on the mixing process where turbulence plays significant role. Turbulence also results in mixing of momentum of fluid for which air craft wing and ship hull experience wall shear stress [1]. In addition, rate of heat and mass transfer at different interface are enhanced by turbulent flow.

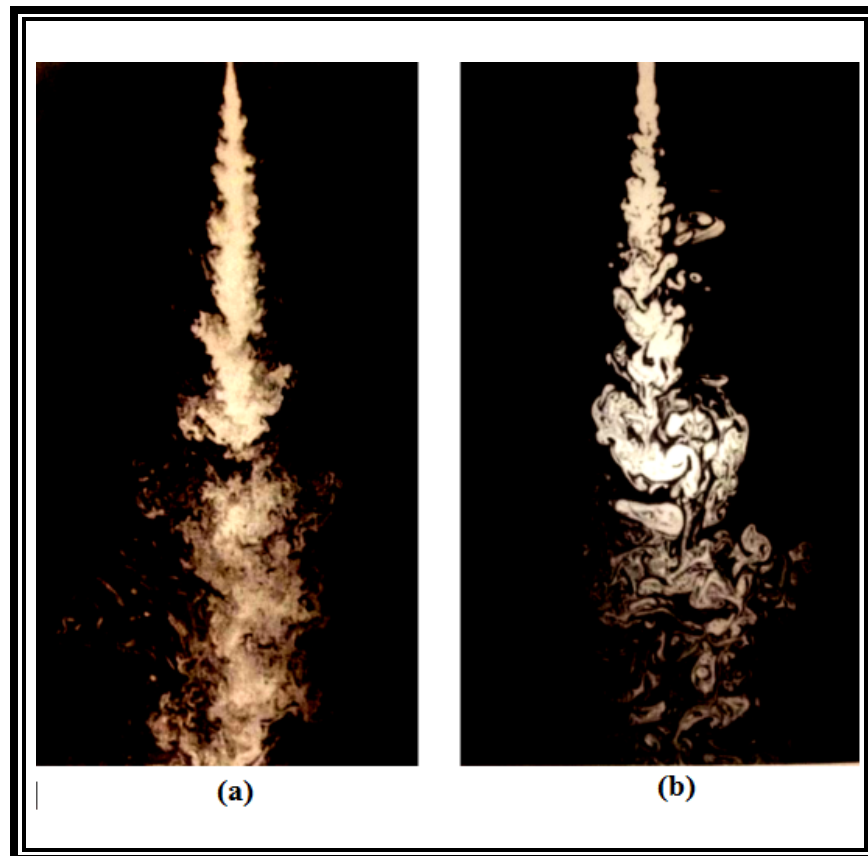


Figure 2. 1: Planer image of concentration in a turbulent jet: (a) $Re = 20,000$ and (b) $Re = 5000$ [4]

As numerous practical applications are involved in turbulent flow for transport and mixing of matter ; and as the rate of transport and mixing largely enhanced by turbulence, ample amount of studies have been done on turbulent flow. Many people tried to find the answer of some basic questions on turbulent flow and its behavior. Every fluid motion consists of different scale motion. Among them large scale motion entirely depends on the geometry of the flow and they plays the main role to control transport and mixing [1]. On the other hand the behavior of small scale motion depends on the rate of energy transferred from large scale and the viscosity

which is independent of flow geometry. Batchelor [5], Monin and Yaglom [6], Panchev [7], Lesieur [8] and McComb [9] tried to address the mathematic of these small scale motion.

2.1.1 STATISTICAL DESCRIPTION OF TURBULENT FLOW

Turbulent flow phenomena shows non linear behavior. The velocity field $U(x,t)$ is random. In a turbulent flow field, the velocity, temperature and pressure change with time. When this change is independent of direction, it is known as isotropic turbulence. Figure 2.2 shows a typical velocity measurement of an experiment which shows the randomness of velocity due to turbulence.

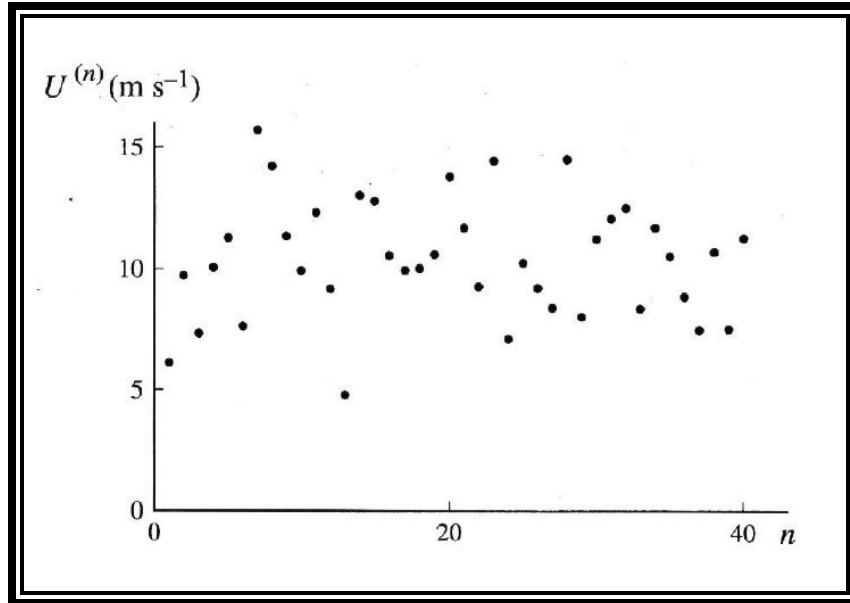


Figure 2. 2: Velocity measurement on the nth repetition of a turbulent-flow experiment. [1]

Due to this random behavior, the local flow parameters are characterized into a mean and a fluctuating component. Figure 2.3 demonstrates the mean and fluctuation of velocity in a turbulent flow field which is also shown in equation 2.1. Here, $u(t)$ is the instantaneous velocity which is divided into a mean U and a fluctuating $[u'(t)]$ term. The mean velocity is the time average velocity of the flow field where the fluctuation of velocity is a function of time and the time average of the fluctuation of velocity is zero.

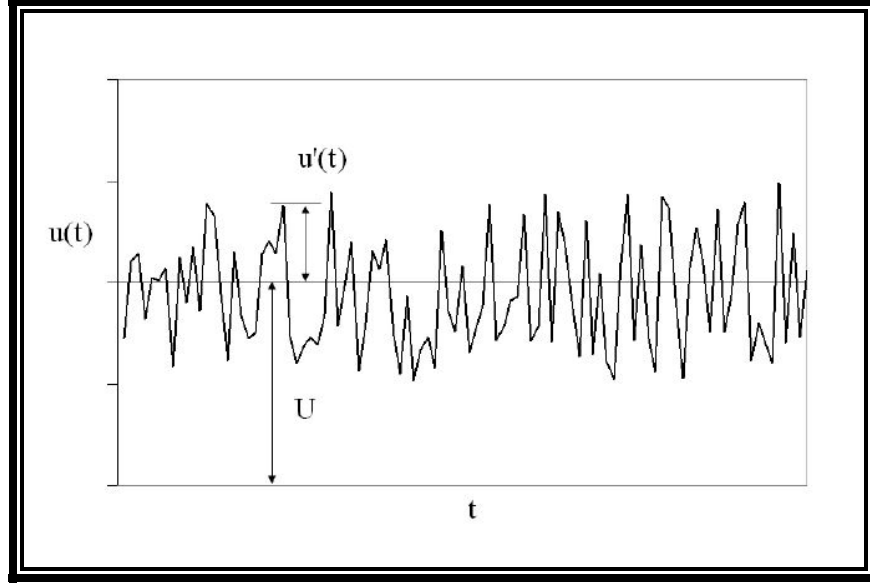


Figure 2. 3: Velocity measurement on the n th repetition of a turbulent-flow experiment.

$$u(t) = U + u'(t) \quad (2.1)$$

As the velocity variable U in a turbulent flow field is a random variable, the Navier-Stokes equation cannot predict the velocity variable accurately. Therefore, researchers have developed ample of theory to determine the probability of an event such as $P \approx [U < N \text{ ms}^{-1}]$. The random variable U can be characterized by its probability density function (PDF). The probability of an event can be defined by the cumulative distribution function (CDF). For example, if the probability of two events A and B is $P(A)$ and $P(B)$ such that -

$$P(A) = P\{U < V_a\}$$

$$P(B) = P\{U < V_b\}$$

Then from definition, the cumulative probability distribution function of both event would be-

$$F(V_a) = P\{U < V_a\}$$

$$F(V_b) = P\{U < V_b\}$$

Therefore, the probability of an event C can be defined as-

$$P(C) = P\{V_a \leq U \leq V_b\} = P\{U < V_b\} - P\{U < V_a\}$$

$$P(C) = F(V_b) - F(V_a) \quad (2.2)$$

The probability density function (PDF) is defined as the derivative of the CDF and it is non-negative and it satisfies the normalization condition [1]. Equation 2.3 - 2.5 defines the mathematical relation and properties of PDF. Moreover, figure 2.4 demonstrates the graphical relation between CDF and PDF [1].

$$f(V) \equiv \frac{dF(V)}{dV} \quad (2.3)$$

$$f(V) \geq 0 \quad (2.4)$$

$$\int_{-\infty}^{+\infty} f(V) dV = 1 \quad (2.5)$$

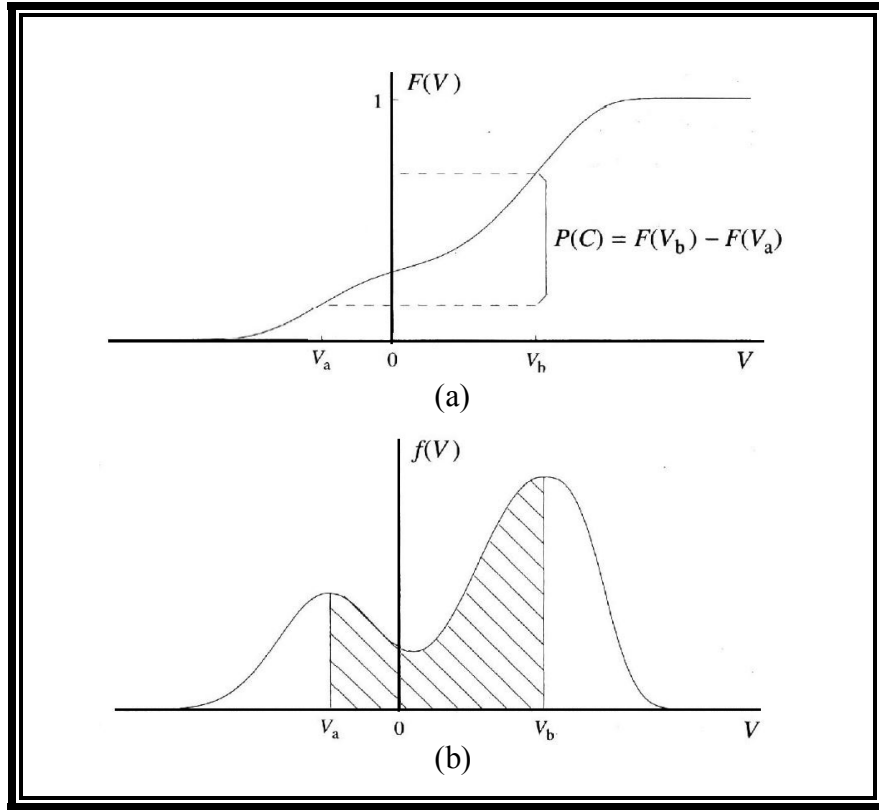


Figure 2. 4: (a) CDF of a random variable U representing the probability event of the event $C = \{V_a \leq U \leq V_b\}$; (b) the corresponding PDF.

Now, the definition of mean and fluctuation of the random variable U can be written as-

$$\langle U \rangle \equiv \int_{-\infty}^{+\infty} V f(V) dV \quad (2.6)$$

$$u \equiv U - \langle U \rangle \quad (2.7)$$

But the most important parameter for turbulence study is the variance of the random variable which is also known as the mean-square fluctuation. The square-root of the variance is the standard deviation which is also known as root mean square (r.m.s) of U . Equation 2.8 and 2.9 defines the variance and r.m.s respectively.

$$var(U) \equiv \langle u^2 \rangle = \int_{-\infty}^{+\infty} (V - \langle U \rangle)^2 f(V) dV \quad (2.8)$$

$$u_{rms} = u' = sdav(U) = \sqrt{var(U)} = \langle u^2 \rangle^{\frac{1}{2}} \quad (2.9)$$

2.1.2 PROPERTIES OF TURBULENT FLOW

Turbulence is considered one of the greatest unsolved problem in classical physics. Due to its non-linear behavior, turbulence is very difficult to define mathematically. Numerous researchers have done significant amount of work in order to characterize the turbulent flow. To measure different turbulent properties in the laboratory, researcher have developed couple of method to generate laboratory scale turbulence. One of the most common methods among them is the grid induced turbulence where the a wire mesh or grid are placed in the flow field in order to generate a homogenous and isotropic turbulence [10]. Another method is the von Karman swirling flow [11,12] where two coaxial counter-rotating discs are used in the middle of the flow field which also generates homogenous and isotropic turbulence. Classical experiments have measured the velocity $\mathbf{u}(\mathbf{x}, t)$ by using hot-wire anemometers. But this experiment fails to predict the velocity components at different direction. Moreover the spatial and temporal resolution cannot be measured by this method [13,14].

The invention of flow visualization technique such as Laser-Doppler Velocimetry [13], Particle Image velocimetry [14], Particle Tracking Velocimetry and Topographic PIV [15] have enabled the opportunity to find the velocity field without affecting the flow field directly. These measurement techniques are able to predict the following properties of turbulence-

Turbulence Kinetic Energy, k

The turbulence kinetic energy (TKE), k , is defined as the energy per unit mass of the turbulent fluctuation, u'_i , in a turbulent flow field. It is characterized by root-mean-square velocity fluctuation. The S.I unit of TKE is J/Kg or m^2/s^2 . For a 3-dimensional flow field, if the r.m.s of the velocity fluctuation of x, y and z direction are $\overline{u'^2_x}$, $\overline{u'^2_y}$ and $\overline{u'^2_z}$ respectively, then the TKE can be calculated by eqn. 2.10.

$$k = \frac{1}{2} \overline{u'_i u'_i} = \frac{1}{2} (\overline{u'^2_x} + \overline{u'^2_y} + \overline{u'^2_z}) = \frac{3}{2} \overline{u'^2} \quad (2.10)$$

Turbulence dissipation, ε

The turbulence dissipation, ε , is defined as the rate at which the turbulence kinetic energy is converted into thermal energy. Most of these energy is internal thermal energy. The quality and efficiency of many industrial process are dictated by turbulence dissipation rate. The S.I unit of ε is J/kgs or m^2/s^3 . There are three main approaches by which ε can be measured [16]. Such approaches are : time series analysis [17], spatial correlation technique [18] and direct calculation from spatial velocity derivatives [19]. Turbulence dissipation rate for incompressible and compressible flow can be defined by eqn. 2.11 & 2.12 respectively-

$$\varepsilon \equiv \nu \overline{\frac{\partial u'_i}{\partial x_k} \frac{\partial u'_i}{\partial x_k}} \quad (2.11)$$

$$\varepsilon \equiv \frac{1}{\rho} \overline{\tau_{ij} \frac{\partial u'_i}{\partial x_j}} \quad (2.12)$$

where τ_{ij} is defined as viscous stress which is given by the eqn. 2.13-

$$\tau_{ij} \equiv 2\mu S_{ij}^* \equiv 2\mu \left[\frac{1}{2} \left(\frac{\partial u_i}{\partial x_j} + \frac{\partial u_j}{\partial x_i} \right) - \frac{1}{3} \frac{\partial u_k}{\partial x_k} \delta_{ij} \right] \quad (2.13)$$

Turbulence intensity, I

The turbulence intensity is a scalar parameter that refers the turbulence level of a flow field. In general, it is expressed as a percent. An ideal flow which has no velocity fluctuation, has the turbulence intensity of 0%. The definition of turbulence intensity is-

$$I \equiv \frac{u'}{U} \quad (2.14)$$

Here u' is the r.m.s of the turbulent velocity fluctuation at a particular location over a specific period of time and U is the mean velocity at the same location over same time period. Typically the turbulence intensity of high speed flow inside rotation machineries and inside complex geometry is around 5% to 20%. The level of turbulence plays very significant role in the design of aircraft, automotive body and chemical mixing process.

Isotropic Turbulence

Isotropy is the property which is independent of orientation and homogeneity implies the independence of position in space. Therefore, isotropic homogenous turbulence implies that, the average properties are independent of direction which is shown in figure 2.5. More precisely, the flow is assumed to be isotropic if rotation and buoyancy are not important and there is no mean flow. On the other hand, if there are no spatial gradients in any averaged flow quantity, then the flow is considered as homogenous. In isotropic turbulence, all statistics are invariant under translation, rotation and reflection of the coordinate system such that-

$$\begin{aligned} \overline{u_1'^2} &= \overline{u_2'^2} = \overline{u_3'^2} \\ \overline{u_i' u_j'} &= 0 \end{aligned}$$

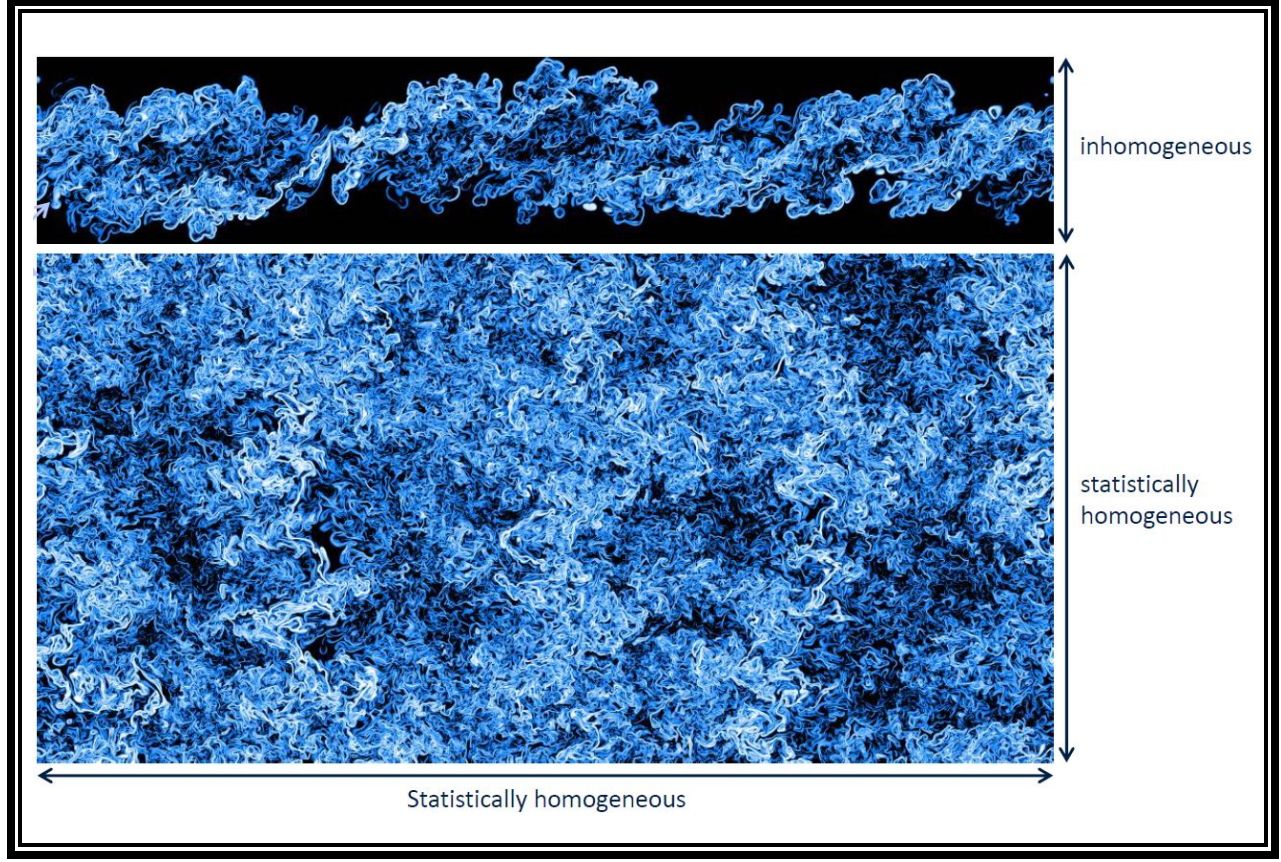


Figure 2. 5: Statistically homogeneous isotropic turbulence.

2.1.3 TURBULENT LENGTH SCALE AND EDDY CASCADE

Turbulent flow carries different size of eddies. These size varies with the energy associated with each eddy. The turbulent length scale, l , is defined as the size of the large energy containing eddies in a turbulent flow field. It is used to estimate the turbulent properties in a turbulent model. The largest eddies in the flow contains the most of the transport energy and momentum and the size of these eddies are dictated by the physical boundaries of the flow. This large scale is also referred as integral length scale, L_n . The size of the smallest eddies, η , are determined by the viscosity which depends on the Reynolds's number. As the eddies approach smaller and smaller, the effect of viscosity become more dominant and eventually the kinetic energy of the flow is dissipated into heat.

The interactions between these large scale and small scale structures can be described by the Kolmogorov's hypothesis [20] and energy cascade principle. According to the Kolmogorov hypothesis, larger eddies contain the maximum energy and the energy transfers from the larger eddies to smaller eddies as an energy cascade manner. Eventually the energy dissipates due to viscosity and converted into heat. A pictorial representation of energy cascade is shown in figure 2.6.

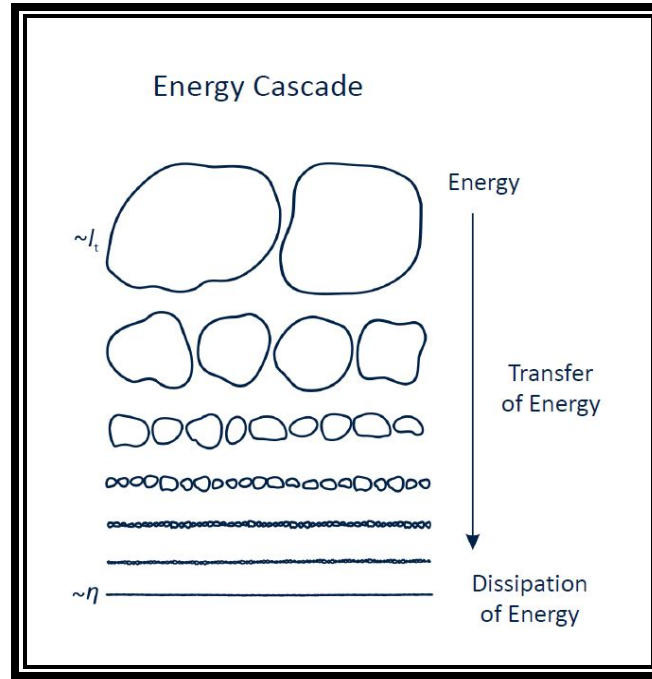


Figure 2. 6: Energy cascade of turbulent flow.

Turbulent length scale can be determined by a two-point correlation. Suppose, two points (point 1 and 2) are considered (figure 2.7) in a two-dimensional flow field which is separated by the distance, X_i and spatial velocity components are measured. If any vortex passes through the points then the velocities at those points can be correlated. The correlation coefficient of the velocity, u , can be expressed as-

$$R_{12} = \frac{\overline{\Delta u_1 \cdot \Delta u_2}}{u'_1 \cdot \Delta u'_2} \quad (2.15)$$

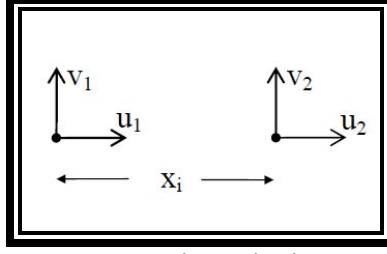


Figure 2. 7: Two point velocity correlation.

The value of R_{12} varies from 0 to 1. 0 corresponds no correlation between the velocity components of the two points and 1 indicates the velocity components are perfectly correlated. The value of the coefficient, R_{12} increases as the distance between point 1 and 2 decreases. The size of the large length scale can be calculated by integrating R_{12} along the coordinate X_i which can be presented by equ. 2.16. Here, l is called the integral length scale and the relation between the distance, X_i and l is shown in figure 2.8.

$$L_n = \int_0^{\infty} R_{12}(X_i) dX_i \quad (2.16)$$

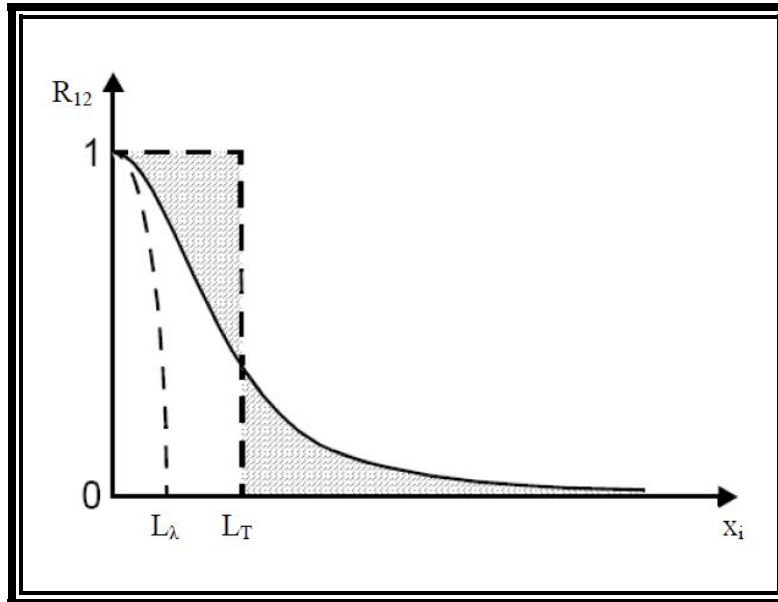


Figure 2. 8: Relation between two point correlation coefficient and integral length scale.

According to Kolmogorov's hypothesis, at high Reynolds number, the small scale turbulent motions are statistically isotropic [20]. The dominating factors influencing the behavior of small scale motion are the overall kinetic energy dissipation rate (ε) and the viscosity (ν). The length scale formed from these two quantities is-

$$\eta = \left(\frac{\nu^3}{\varepsilon}\right)^{\frac{1}{4}} \quad (2.17)$$

This length scale is called the Kolmogorov length scale, η , in turbulent flows. Kolmogorov's hypothesis also stated that, the rate at which the energy is transferred to successively smaller eddies is universal and does not depend on the eddy size. Therefore the energy distribution in a turbulent flow measured by eqn 2.18 which is known as length scale cascade.

$$\varepsilon = -\frac{\partial k}{\partial t} \sim \frac{E_n}{\tau_n} \sim \frac{u'^3}{L_n} \rightarrow E_n \sim (\varepsilon \cdot L_n)^{\frac{2}{3}} \quad (2.18)$$

Here, k is the turbulent kinetic energy, L_n is the integral length scale and E_n is energy content of length scale cascade. If L_n is replaced by $1/\kappa$ where κ is a wave number then eqn 2.18 can be written as-

$$E_n(\kappa) = \frac{\partial E_n}{\partial \kappa} \propto \varepsilon^{\frac{2}{3}} \kappa^{-\frac{5}{3}} \quad (2.19)$$

The above relation is true for the inertial sub-range (figure 2.9) where the amount of energy in the small scale (high wave number) decreases as the structure become smaller and the dissipation of large scale (low wave number) decreases as the structures become larger. Figure 2.9 shows the energy cascade in logarithmic scale. From the figure, it is obvious that the large eddies contain most of the energy and small eddies are much weaker as they contains less energy.

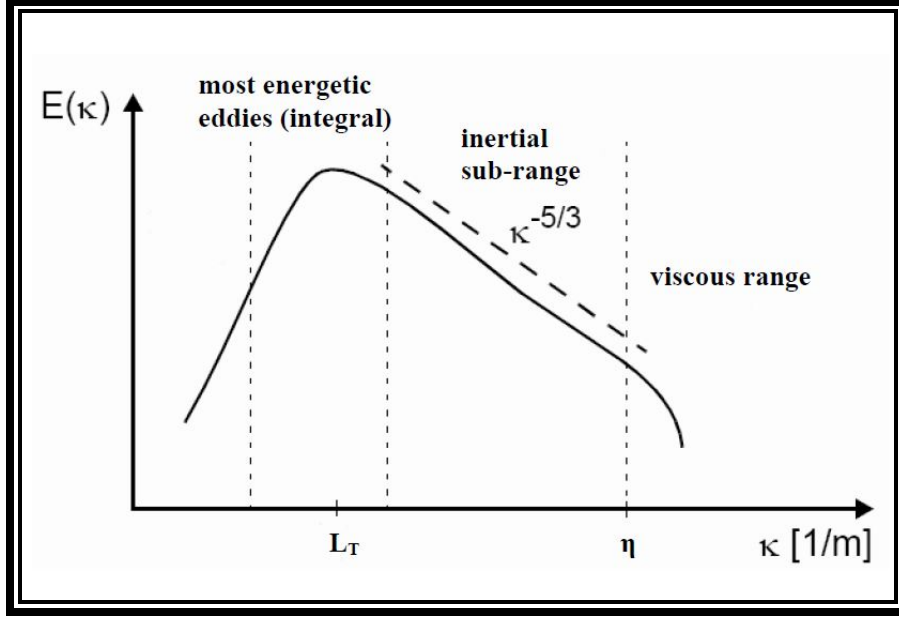


Figure 2. 9: Energy spectrum of turbulence length scale

In order to relate the Kolmogorov scale to the largest scale, an estimation of dissipation rate in terms of large scale flow is necessary. Since the dissipation rate is proportional to kinetic energy product rate, it can be assumed that the kinetic energy transfer rate to the small scale is proportional to U^2 . On the other hand the time scale of the large eddies can be estimated as L/U . From the definition of kinetic energy dissipation rate, it is known that the kinetic energy supply rate will be related to the inverse of the time scale. Hence, the dissipation rate is approximated as $\varepsilon \sim \frac{UU}{L/D} \sim \frac{U^3}{L}$ which shows that dissipation does not depends on the viscosity. Using this relation in eqn 2.17, the definition of small length scale becomes $\eta = \left(\frac{v^3 L}{U^3}\right)^{1/4}$. This relation gives an estimation for the ratio of the largest scales in the flow-

$$\frac{L}{\eta} \sim \left(\frac{UL}{v}\right)^{3/4} = Re^{3/4} \quad (2.20)$$

where Re is the Reynolds number based on the large scale flow feature. Another Reynolds number often used in turbulence study which is known as turbulent Reynolds number Re_λ . Here λ is the Taylor microscale which is defined as $\left(\frac{\partial u'}{\partial x}\right)^2 = \frac{u'^2}{\lambda^2}$. Therefore the turbulent Reynolds number is defined as-

$$Re_\lambda = \frac{u'\lambda}{\nu}$$

Another important parameter of turbulence study is the time scale. Just like the integral length scale, the large eddy turnover is defined as $t_L = \frac{L}{U}$. Similarly the time scale for the small eddies are related to viscosity and the dissipation such as $t_\eta = \left(\frac{\nu}{\varepsilon}\right)^{1/2}$. Therefore the relation between the time scale of large eddies and small eddies is-

$$\frac{t_L}{t_\eta} \sim \left(\frac{UL}{\nu}\right)^{1/2} = Re_L^{1/2} \quad (2.21)$$

2.1.4 GRID INDUCED TURBULENCE

In order to create homogenous turbulence, wire mesh or wire grid are used. It has been a common laboratory practice to generate turbulence by grid. One of the key characteristics of grid induced turbulence is that it can generate decaying homogenous turbulence where the flow statistics changes only in x-direction [1]. The turbulence can be characterized by the grid size d , and grid spacing M . It is assumed that with a uniform stream velocity U_0 , the grid can generate homogenous turbulence with evolve with time such as $t = x/U_0$ [1]. The behavior of grid induced turbulence is virtually identical as the large fluid tank which has been vigorously stirred and then left to itself. This type of turbulence is called *freely evolving* turbulence [21]. There are some distinctive features in grid induced turbulence. Figure 2.10 shows the difference stages of grid turbulence. The first stage is the transition stage for the flow to become turbulence by the grid. The second stage is the fully developed turbulence where the turbulence is fully homogenous and finally the decay of the turbulence through small-scale which is shown in stage III. Comte-Bellot and Corrsin [22] studied different features of grid induced turbulence. Figure 2.11 shows the grid of a turbulence generator and the decay of Reynolds stress. Figure 2.11(b) shows the measurement of $\langle u^2 \rangle$ and $\langle v^2 \rangle$ from the grid-turbulence experiment [22]. As an ideal case the experiment shows that $\langle v^2 \rangle$ and $\langle w^2 \rangle$ are equal. From the figure, it is also seen that the r.m.s

axial velocity $\langle u^2 \rangle^{1/2}$ is 10% greater than the lateral r.m.s $\langle v^2 \rangle^{1/2}$ [22] which provides a good approximation to the ideal homogenous isotropic turbulence.

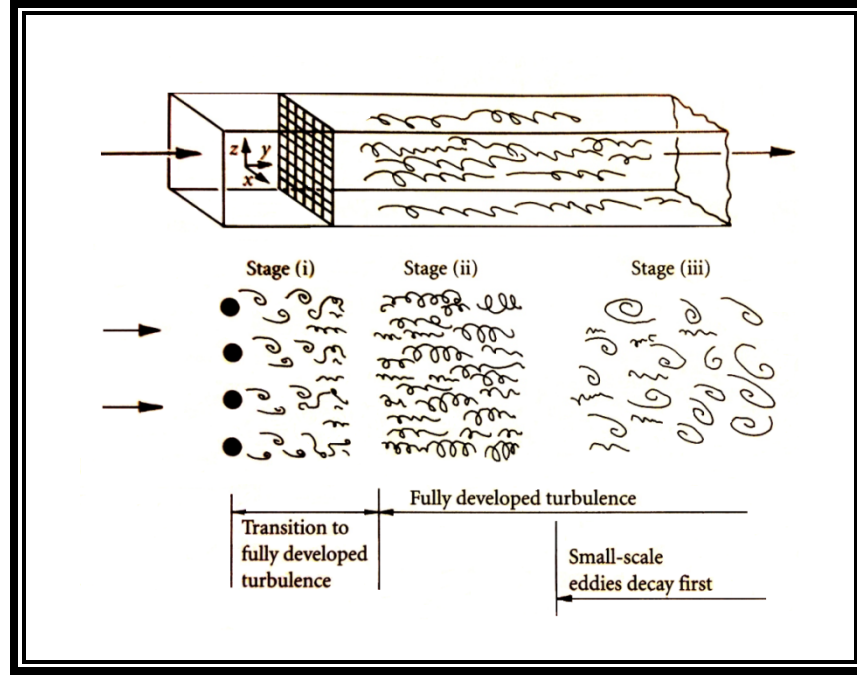


Figure 2. 10: Grid turbulence and its different stages [21]

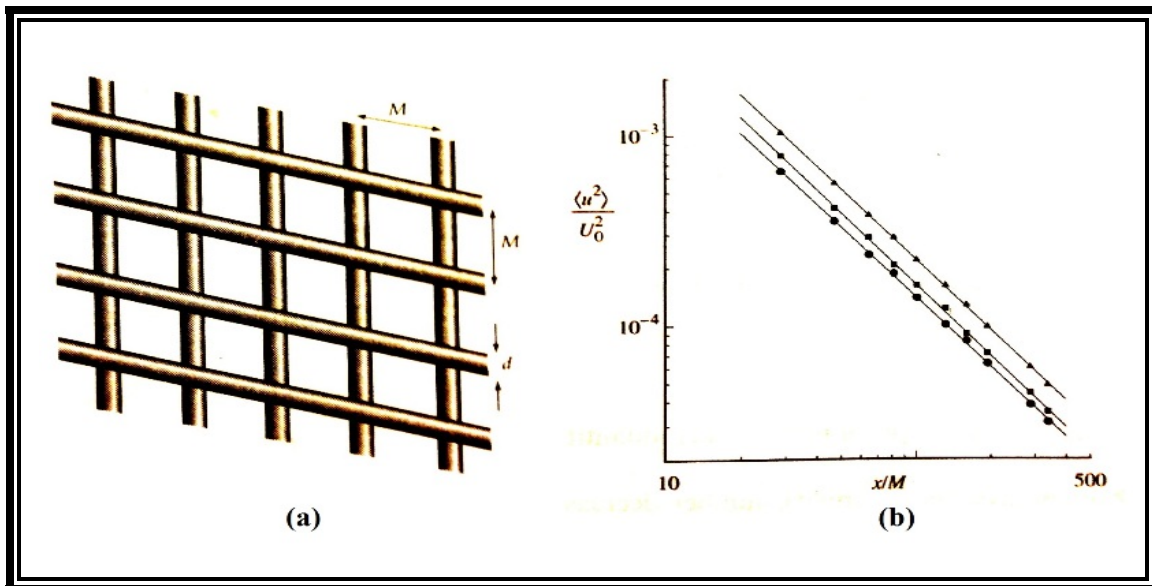


Figure 2. 11: (a) Sketch of grid, M = grid spacing, (b) Decay of Reynolds stress

2.1.5 FLOW OVER A BACKWARD FACING STEP

Flow over a backward facing step is one of the classical fluid mechanics problem. Extensive experimental and numerical works have been done on this problem. Due to its geometric simplicity and flow diagnostic technique, this phenomena has become a practice for numeric validation for computational fluid dynamics (CFD). A significant amount of work on flow through backward facing step has been done by Armaly et al [23]. They did a detailed analysis of flow behavior inside a backward facing step channel experimentally and numerically. Ample amount of work have been done by numerous people. Lee and smith [24] used the potential flow theory to address the problem. The potential flow theory did not able to predict the flow separation or reattachment region behind the step.

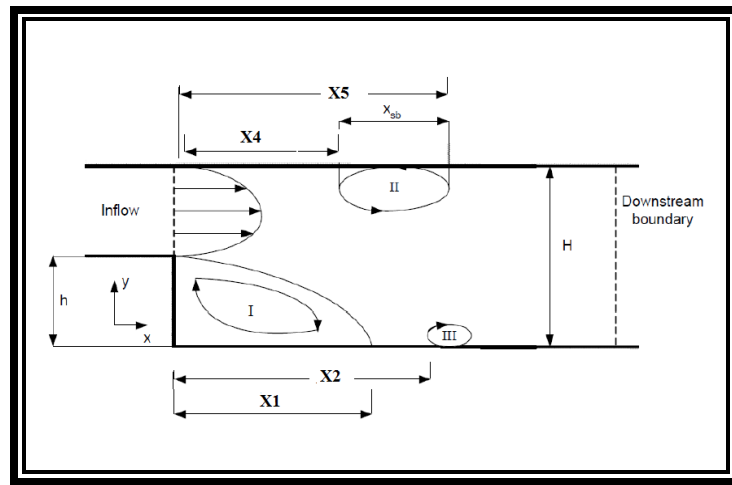


Figure 2. 12: Schematic of different separation zone in a backward facing step flow.

Early numeric predictions of backward facing step flows were done by Roache [25], Taylor and Ndefo [26] and Durst and Pereira [27]. A separation region at the lower corner of the step was predicted by Alleborn et al [28] after a careful study of a sudden expansion of such channel. Brandt et al [29] and Hack bush [30] used multigrid method and Lange et al [31] used local block refinement technique in order to predict more precise result. Armaly et al [23] detailed experimental work with a step geometry having $H/h = 1.94$. Kim and Moin [32] computed using a second order space-time technique. The found a good agreement with

experimental data for Re up to 500. The computed data started to deviate from the experiment from Re = 600. Durst et al [33] observed a second flow separation zone in two dimensional numerical simulation of a symmetric sudden expansion flow. Kaiktsis et al [34] observed that the unsteadiness was created by convective instability. Hossain et al [35] also studied flow separation and matched with existing data.

Figure 2.12 shows a schematic of different separation zone in a backward facing channel. In the present study, primary CFD analysis has been done. Figure 2.13 shows the validation of the data in a 2D backward facing step channel with an expansion ratio of 2:1. The detail of the CFD analysis are described in the later part of this chapter. Figure 2.13 demonstrates the separation length with respect to Reynolds number. As the Reynolds number increases the separation length also increases. It is important to note that this result is used only for the validation of the CFD model. The 'CFD project' represents the results No grid is used to generate the turbulence. The author used the experimental geometry and boundary conditions [23].

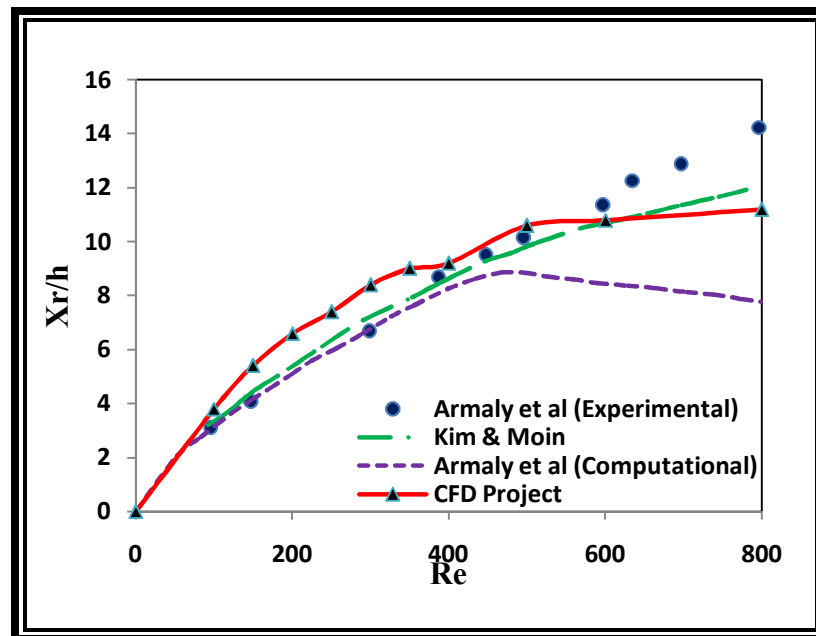


Figure 2. 13: CFD result validation with experimental data.[35].

2.2 Combustion

Combustion is a rapid oxidation process generating heat or both light and heat [36]. The flame is thin reaction zone where intense chemical reaction propagates through the unburned air-fuel mixture. This thin reaction zone or flame releases the heat of reaction which causes the rise of the temperature and pressure of the surrounding gas. Combustion can happen both in flame or non-flame mode. In the flame mode concept, combustion can be categorized into two main types such as-

- Premixed combustion or premixed flame
- Non-premixed combustion or diffusion flame

Behind the thin reaction zone (flame) are the hot combustion product. The released energy of fuel increases the temperature and pressure of the unburned gas which accelerates the reaction process and therefore continue the combustion. The premixed and non-premixed are related to their state of mixedness of the reactants. In the premixed flame, the fuel and oxidizer are mixed at the molecular level prior to the chemical reaction. On the other hand, in a diffusion flame, the reactants are initially sprayed, and reaction occurs at the interface of the fuel and oxidizer. One of the key features of a diffusion flame is, both mixing and reaction occurs at the same time.

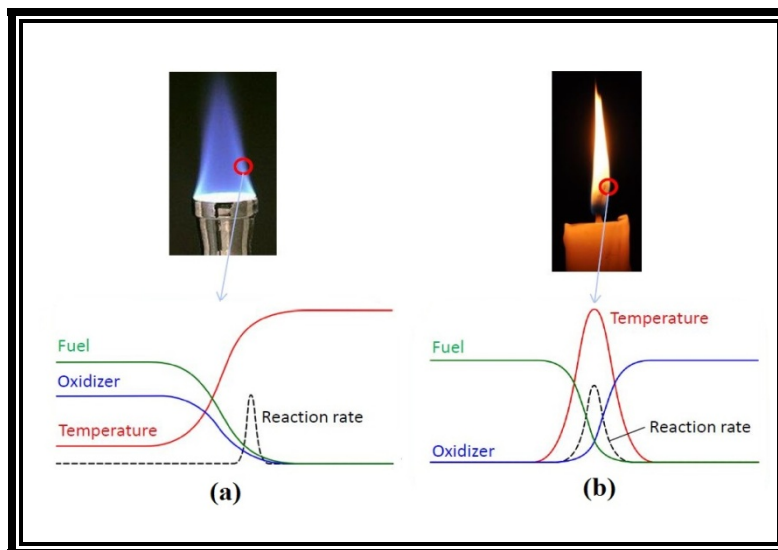


Figure 2. 14: Concentration & temperature profile. (a) premixed, (b) diffusion flame.

In this current experiment, a premixed methane-air flame has been studied. In order to initiate the combustion, methane-air has been mixed within their flammability limit and ignited by a spark plug. The detail of the experiments are described in the later chapters. Although most of the hydrocarbon combustion produces carbon dioxide (CO_2) and water (H_2O), the mechanism of this combustion process is not straight forward. In recent years researchers have been trying to describe combustion process at the level of elementary chemical steps with their detail chemical kinetic mechanisms [37- 44]. Some mechanism contains thousands of elementary reaction steps among hundreds of chemical species. For example, hydrogen combustion is included with 21 steps among 8 chemical species, combustion of carbon monoxide with 30 steps among 11 species, methane, methanol, ethane, ethylene, and acetylene combustion with 134 steps among 30 species and propane, propene, allene, and propyne combustion with 177 steps among 37 species [45]. In order to avoid complexity, a simplified path of CH_4 combustion can be written as-

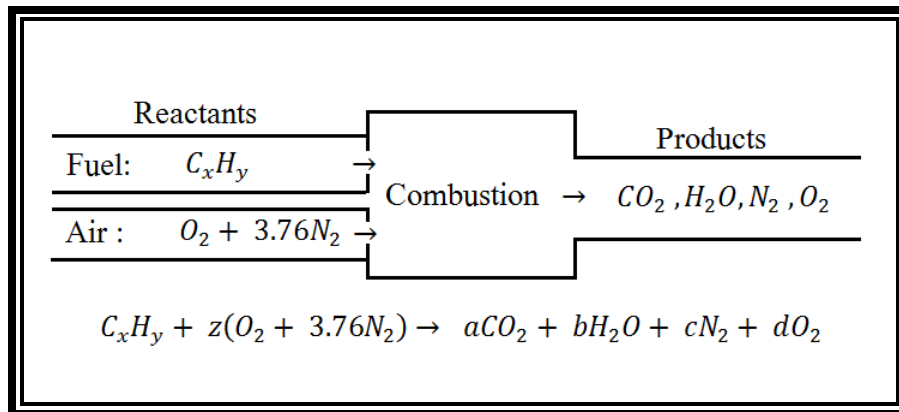
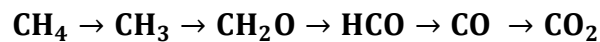


Figure 2. 15: Simplest representation of stoichiometric combustion of hydrocarbon fuel .

The basic combustion process can be described by the fuel and the oxidizer known as reactants which undergo a chemical process while releasing heat to form the product. When all the carbons in the fuel convert into carbon dioxide (CO_2) and all the hydrogen forms water (H_2O) then the combustion process is known as Stoichiometric Combustion. Figure 2.15 shows

the simplest representation of stoichiometric combustion where z is the stoichiometric coefficient of the oxidizer. The reaction yields five unknown: z, a, b, c, d . For stoichiometric combustion, as there is no excess oxygen, thus $d = 0$. Balancing the number of atoms of the reaction shown in figure 2.15, the other variables (a, b, c, z) can be found which is shown in table 2.1. Therefore, for methane combustion, the stoichiometric equation is be written as-

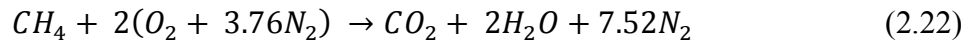


Table 2. 1: Calculation of stoichiometric coefficient

Elements	Amount in reactants	=	Amount in Products	Reduced Equation
Carbon (C)	x		a	$a = x$
Hydrogen (H)	y		$2b$	$b = y/2$
Oxygen (O)	$2z$		$2a+b$	$z = a + b/2$
Nitrogen (N)	$2(3.76)z$		$2c$	$c = 3.76z$

2.2.1 LAMINAR PREMIXED FLAME

Laminar premixed flame is the one of the simplest flames to study the fundamentals of combustion. Understanding laminar premixed flame is the first step towards understanding turbulent flames. The physical process of laminar and turbulent flow phenomena are similar. Therefore, a handful number of turbulent flame theories are developed based on laminar flame structure. It is also used to determine important design parameters such as flame-stability characteristic, flashback and blowoff limit, flammability limit, ignition and extinction phenomena. In order to study the flame, it is very important to understand different zones of combustion. Friedman and Burke [46] indentified two distinct zones (preheat zone & reaction zone) in a laminar flame structure. Figure 2.16 shows the two different zones of a laminar flame structure. In the preheat zone the heat is little released and the temperature gradient is small but in the reaction zone, the bulk of chemical energy released and the temperature gradient is high.

Moreover, the reaction zone can be divided into two sub-zones. The primary reaction zone is the fast-chemistry zone which is a very thin zone having a very large gradient temperature and species concentration. These large gradients provide the driving force that causes the flame to be self-sustaining [47]. The secondary reaction zone is the slow-reaction zone where the chemistry is dominated by three-body radical reactions. This zone can be extended several millimeters in atmospheric pressure.

Another popular technique of characterizing the flame is visual radiation. The fast reaction zone appears blue results from the excited CH radicals in high temperature zone. OH radicals also contribute visual radiation. These radiations such as fluorescence and chemiluminescence are used for flame front characterization [48-50].

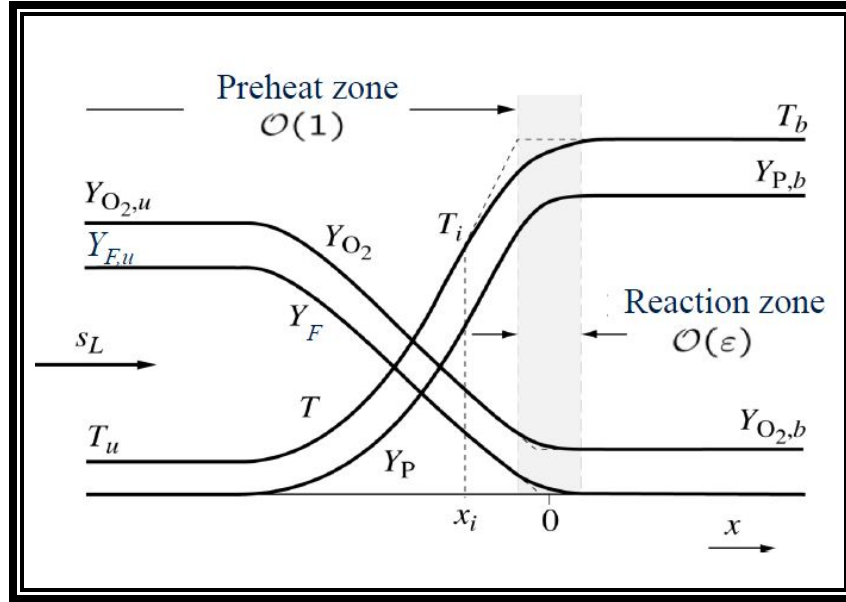


Figure 2. 16: Laminar flame structure. Temperature and species concentration profile [46] .

2.2.2 LAMINAR FLAME SPEED (S_L)

Characterizing a flame front is basically measuring the flame speed (S_L) and flame thickness (δ). Flame speed is defined as the rate of expansion of the flame front in a combustion reaction. Laminar flame is defined as the speed at which an un-stretched laminar flame front will

propagate through a quiescent mixture of unburned reactants. Laminar flame speed depends on the temperature of the reaction zone, the rate of reaction and the thermal diffusivity of the mixture. There are different measurement technique for determining flame speed. When a tube containing combustible mixture, the flame speed is the propagation speed of the flame front towards the unburned mixture. On the other hand, in a flat flame burner the flame front is stationary and the approaches the flame front at a speed equivalent to the flame speed thus establishing the flame. The laminar flame speed of reactive mixture depends on its equivalence ratio (ϕ), initial pressure (P_0) and initial temperature (T_0) of the air-fuel mixture. A simple relation of determining flame speed is given by equ. 2.23.

$$S_L = S_{L,0} \left(\frac{T_u}{T_{u,0}} \right)^\alpha \quad (2.23)$$

Table 2. 2: Laminar flame speed of the Stoichiometric Methane-Air at various range of ϕ , T_u and P_u

Researcher	ϕ	T_u (K)	P_u (atm)	S_u (ϕ_{\max})	$S_{u,0}$ at $\phi = 1.0$
Yan et al. [54]	0.6-1.4	283-373	1.0	38.0(1.05)	36.9(1.72)
Takizawa et al. [55]	0.7-1.3	280-330	0.8-1.1	36.5(1.07)	35.5(1.88)
Liao et al. [56]	0.6-1.4	300-400	0.5-1.5	39.1(1.05)	39.4(1.58)
Gu et al. [57]	0.8-1.2	300-400	1-10	36.0(1.00)	36.0(1.61)
Stone et al. [58]	0.6-1.4	293-454	0.5-10.4	37.6(1.00)	37.6(1.42)
Iijima & Takeno [59]	0.8-1.3	291-500	0.5-30	36.9(1.12)	34.5(1.60)
Sharma et al. [60]	0.8-1.2	300-600	1-8	34.1(1.10)	33.0(1.68)

where α is the temperature exponent which is a function of pressure and mixture equivalence ration and $S_{L,0}$ is the laminar flame speed at ambient condition. In this current study, the primary fuel is methane and the total concentration of this study is focused on methane-air combustion. Therefore it is important to learn the methane-air combustion phenomena. Ample amount of research have been done by many researcher. The flame speed for methane-air

combustion is well documented. Figure 2.17 shows the flame speed of methane-air combustion at atmospheric pressure [51-53]. Various power law correlations have been proposed in the literature for methane-air mixtures. Table 2 shows the laminar flame speed deduced from different correlation available in the literature.

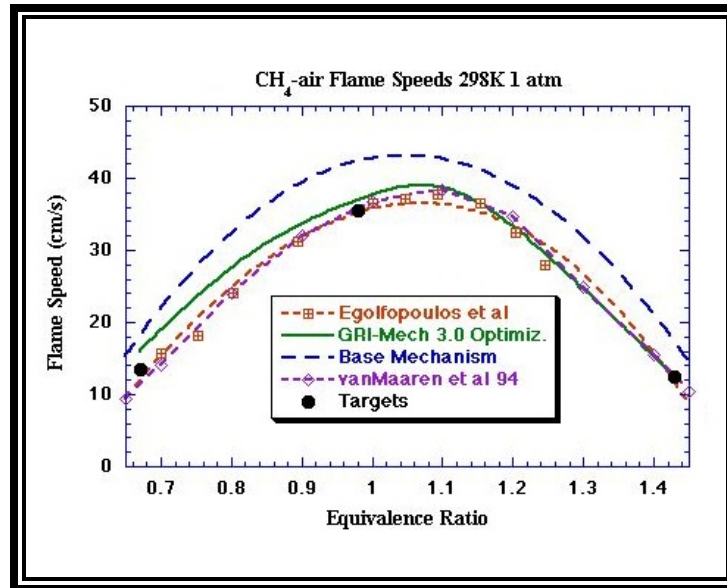


Figure 2. 17: Laminar flame speed of methane-air at 298K and 1 atm pressure [61]

The effect of pressure and temperature are also studied by number of researchers. Among them the most significant works have been done by Law [62], Garforth [63], Babkin et al [64-66] Andrews [67] and Lijima [68]. They measured the laminar flame speed at pressure range of 0.25 to 20 atm. Figure 2.18 shows their results. Moreover, the effect of preheat temperature has been studied by Kumar et al [69]. They performed experiment for a wide range of mixture temperature (370 to 650 K) and equivalence ratio (figure 2.19). In this study, the combustion chamber has been designed for 5 bar pressure and a maximum preheated temperature of 500K. Therefore, important data have been considered from figure 2.19 and 2.20 during the design of the chamber.

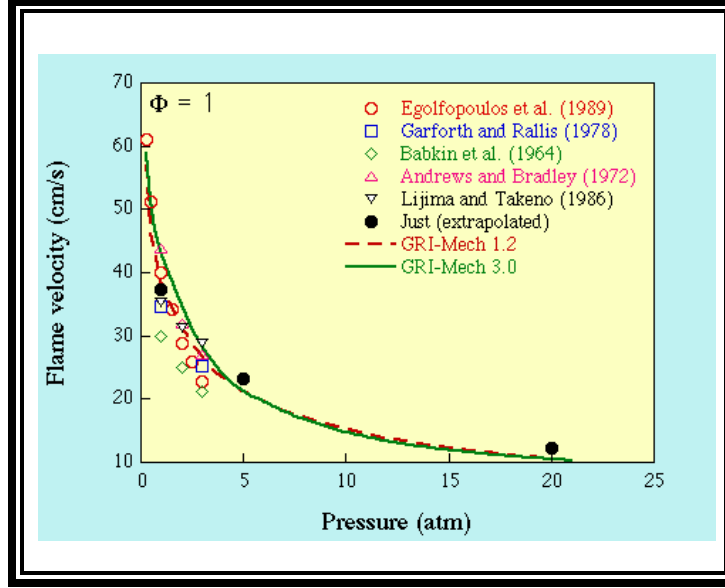


Figure 2. 18: Laminar flame speed of methane-air at 0.25 to 20 atm [61]

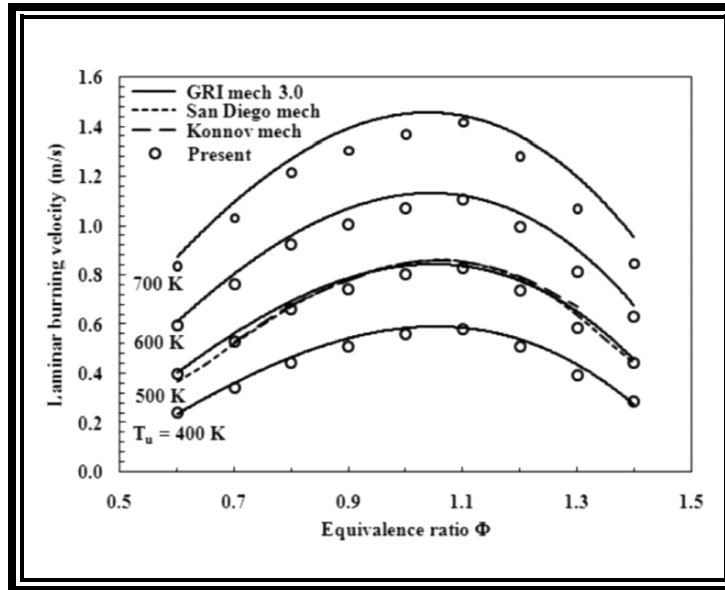


Figure 2. 19: Laminar flame speed of methane-air at elevated temperature [69]

2.2.3 TURBULENT PREMIXED COMBUSTION

Just like laminar flame, turbulent flame is also dictated by the flow Reynolds number. In order to fully understand turbulent combustion, the turbulent flamelet structure and turbulent flame speed need to be described. Turbulent flamelet structure consists of reaction layer surface

area per unit volume (Σ), the brush thickness (δ_T) and the stretch factor (I_o). The relation between these parameters with the turbulent flame speed can be defined by equ. 2.24.

$$\frac{S_T}{S_{Lo}} = I_o \int_{-\infty}^{+\infty} \Sigma d\eta = I_o \Sigma_{max} \delta_T \quad (2.24)$$

Turbulent premixed flame have different structure at different conditions. These structures depends on the turbulent length scale and the chemical time scale. The interaction between the turbulent flow field and flame front are characterized by some dimensionless number. Most common dimensionless number in turbulent combustion are Turbulent Reynolds number (Re_T), Damkohler number (Da) and Karlovitz number (Ka). The turbulent Reynolds number is a function of integral length scale (L_T), velocity fluctuation (u'), laminar flame speed (S_L) and laminar flame thickness (δ_L) which is shown in equ 2.25. The Damkohler number is the ratio of turbulent scale (L_T/u') and the chemical reaction time scale (δ_T/S_L). Equation 2.26 shows the definition of Damkohler number. Large Damkohler number ($Da \gg 1$) refers the turbulent time is larger than the chemical time scale. For high intensity turbulent combustion, the Damkohler number is much higher. The Karlovitz number (eqn 2.27) defines the relation between the laminar flame thickness (δ_L) and the smallest turbulent length scale (η) commonly known as Kolmogorov length scale.

$$Re_T = \frac{u' L_T}{S_L \delta_L} \quad (2.25)$$

$$Da = \frac{\tau_m}{\tau_c} = \frac{L_T}{u'} \frac{S_L}{\delta_L} \quad (2.26)$$

$$Ka = \left(\frac{L_T}{\delta_L} \right)^{-\frac{1}{2}} \left(\frac{u'}{S_L} \right)^{\frac{3}{2}} \quad (2.27)$$

Ample amount of research have been done to measure turbulent flame speed, flamelet structure and integral scale. Table 2.3 shows the list of authors who made the significant contributions on finding turbulent flame speed. Figure 2.20 represents the turbulent flame speed for methane-air stoichiometric mixture.

Table 2. 3: Experimental study of turbulent flame speed.

Authors	Type	Fuel
Cheng and Shepherd [70]	Bunsen	CH ₄ , C ₂ H ₄
Chen and Bilger [71]	Bunsen	CH ₄ , C ₃ H ₈
Filatyev [72]	Bunsen	CH ₄
Lee et al [73]	Bunsen	CH ₄ , C ₂ H ₄
Shepherd and Cheng [74]	Flat low swirl	CH ₄
Bedat et al [75]	Flat low swirl	CH ₄
Cheng [76]	Flat low swirl	CH ₄ , C ₂ H ₄
Cho et al [77]	Flat counterflow	CH ₄

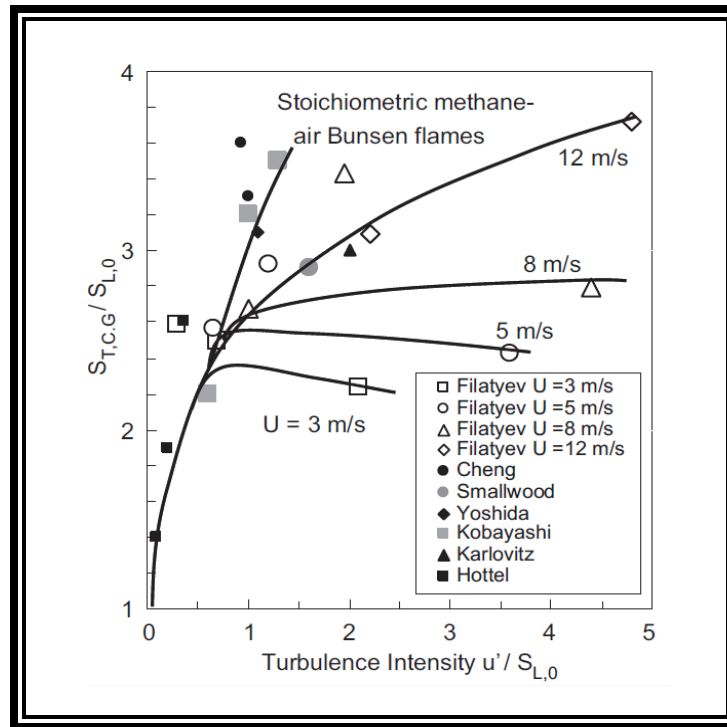


Figure 2. 20: Turbulent flame speed measured by Filatyev et al [72]

2.2.4 FLAME REGIME

Cheng and Shepherd [74] have suggested four different categories of turbulent premixed flames:

- Envelope flame: axisymmetric [78].
- Oblique flame: V-flame [79].
- Flat flames : low swirl, counter flow [80].
- Spherical flames [81].

But the most popular classifications of turbulent flames are proposed by Borghi [82] which is known as flame regime diagram. This diagram (figure 2.21) was modified by Peter [83]. The diagram is characterized by dimensionless parameters (Re_T , Da , Ka), turbulent parameters (u' , L_T) and flame parameters (S_L , δ_L). This diagram also assumed that the mass diffusivity and the thermal diffusivity is equal. Therefore, the Schmidt number is unity. Figure 2.22 shows a pictorial representation of different flame regimes.

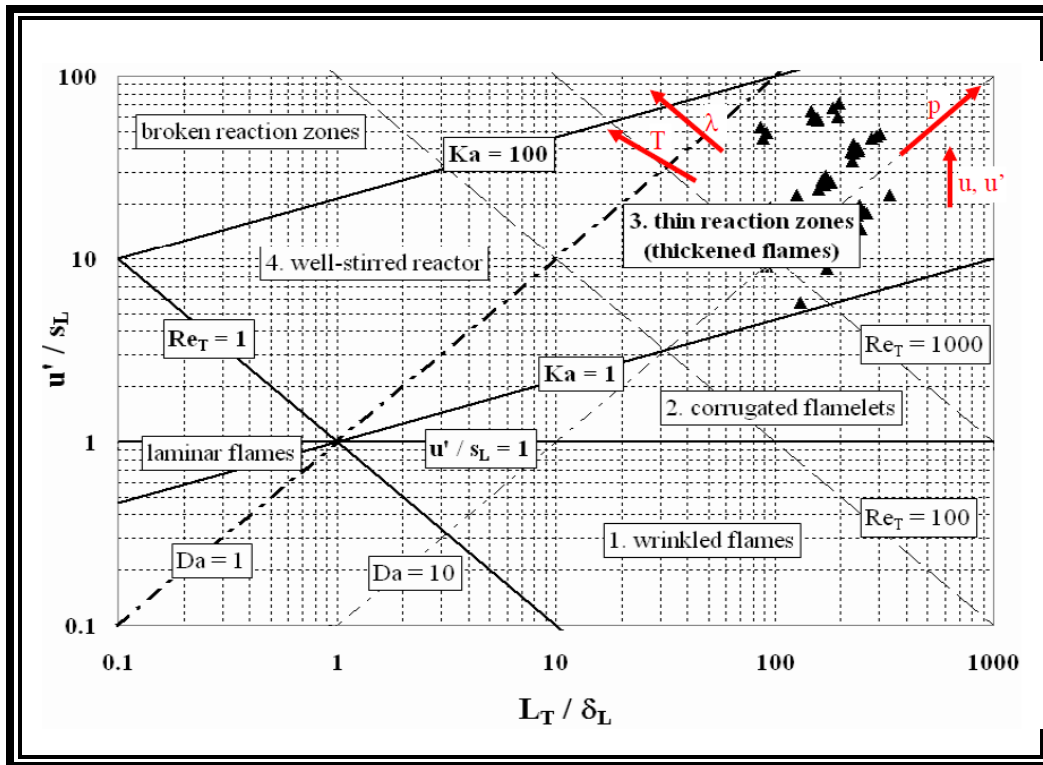


Figure 2. 21: Flame regime diagram by Borghi modified by Peter.




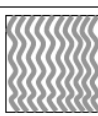
flame regime	Re_T	Da	Ka	u'/s_L	δ_L/η	graphical illustration of the flame front
wrinkled flame	> 1	> 1	< 1	< 1	< 1	
corrugated flame	> 1	> 1	< 1	> 1	< 1	
thickened flame (thin reaction zones)	$\gg 1$	≥ 1	> 1	$\gg 1$	> 1	
distributed flame (well-stirred reactor)	> 1	< 1	> 1	> 1	> 1	

Figure 2. 22: Different flame regime and its characteristic

Wrinkled Flame Regime

The line $Re_T > 1$ separates all the turbulent flame regime. The first category of these flame is wrinkled flame regime where both $\frac{u'}{s_L}$ & $\frac{L_T}{\delta_L}$ terms are less than one which refers that the turbulent flame speed is much faster than the turbulent time scale. On the other hand the integral length scale is much larger than the flame thickness. Large eddies interact with the reactions zone results in wrinkling in the flame front. Figure 2.23 shows the typical wrinkled flame under CH-Laser Induced Fluorescence (LIF) image.

Corrugated Flame Regime

Corrugated flame regime is characterized by $u' > S_L$, $Re_T > 1$ and $Ka < 1$. This small Karlovitz number implies that the flame thickness is much smaller than the Kolmogorov length scale. The Kolmogorov eddies are not able to penetrate the reaction zone as they are still very big. The physical structure of corrugated flame is quite similar to the wrinkled flame but the number of wrinkles are higher and more intense. These intense turbulence results in small flame

pockets in a corrugated flame which can be detected from a continuous flame sheet (figure 2.24). This flame is also known as quasi-laminar flame.

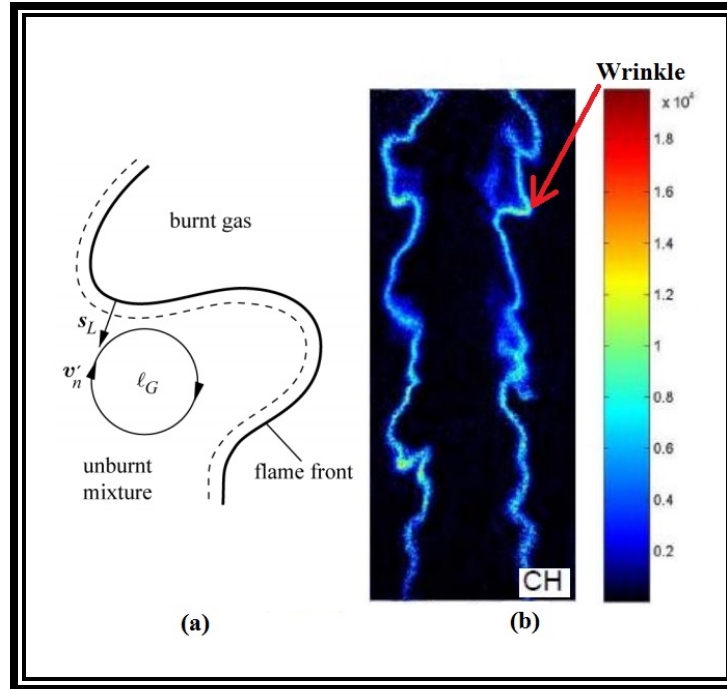


Figure 2. 23: Wrinkled flame. (a) schematic presentation, (b) CH-LIF image of actual flame

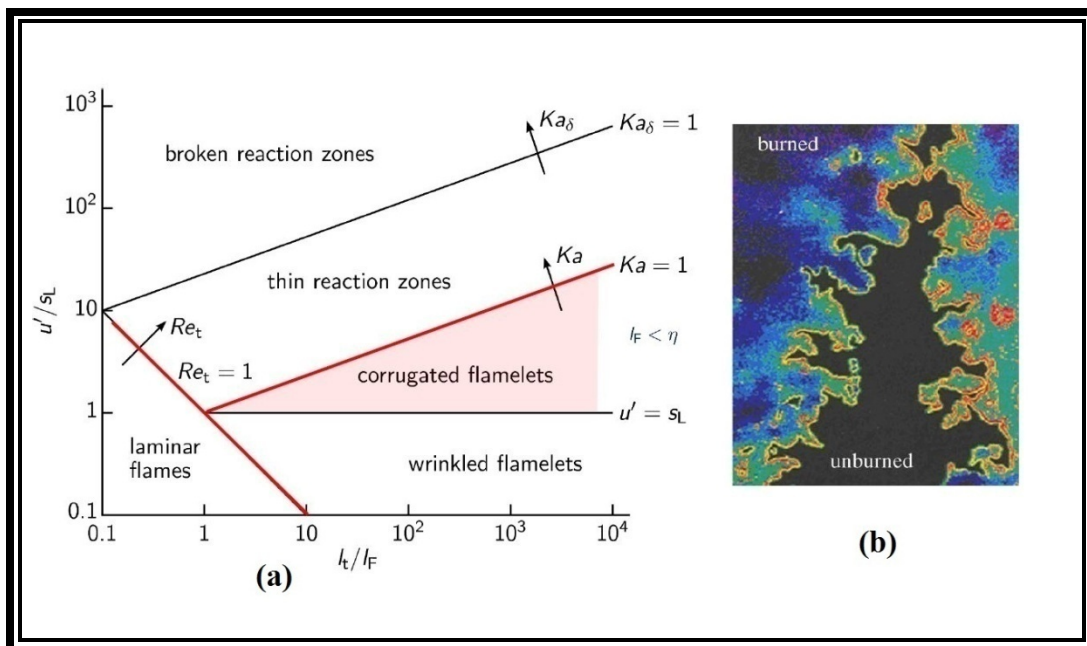


Figure 2. 24: Corrugated flame (a) Flame regime, (b) corrugated flame structure [84]

Thickened Flame Regime

The thickened flame regime or the thin reaction zone regime is characterized by $\frac{u'}{s_L} \gg 1$, $Re_T \gg 1$ and $Ka > 1$. The large Karlovitzs number refers that the smallest length scale or the kolmogorove scale (η) are very small ($\eta < \delta_T$) that they can enter the reaction zone. This flame is postulated by Zimont [85]. In this zone the flamelets are not laminar anymore. They are thickened by the turbulence as the small turbulent scales enter into the flame structure and thus thickened the flame. Another concept about this regime was proposed by Peter [83]. This concept described this zone as highly stretched which is divided into an inner sub-layer of thickness (δ) and a pre-heated zone. Peter described that the pre-heating zone is chemically inert and a majority of the reactions take place in the inner layer. The stretching of the flame results in higher flame speed and higher thermal diffusion thereby thickened the flame. The main purpose of this study is to investigate this thickened flame regime and to determine the interaction between the turbulent length scale and the flame front. Although some Direct Numerical Simulation (DNS) have been done to explain the concept of thickened flame regime which is shown in figure 2.25, more important characteristics are yet to be explained.

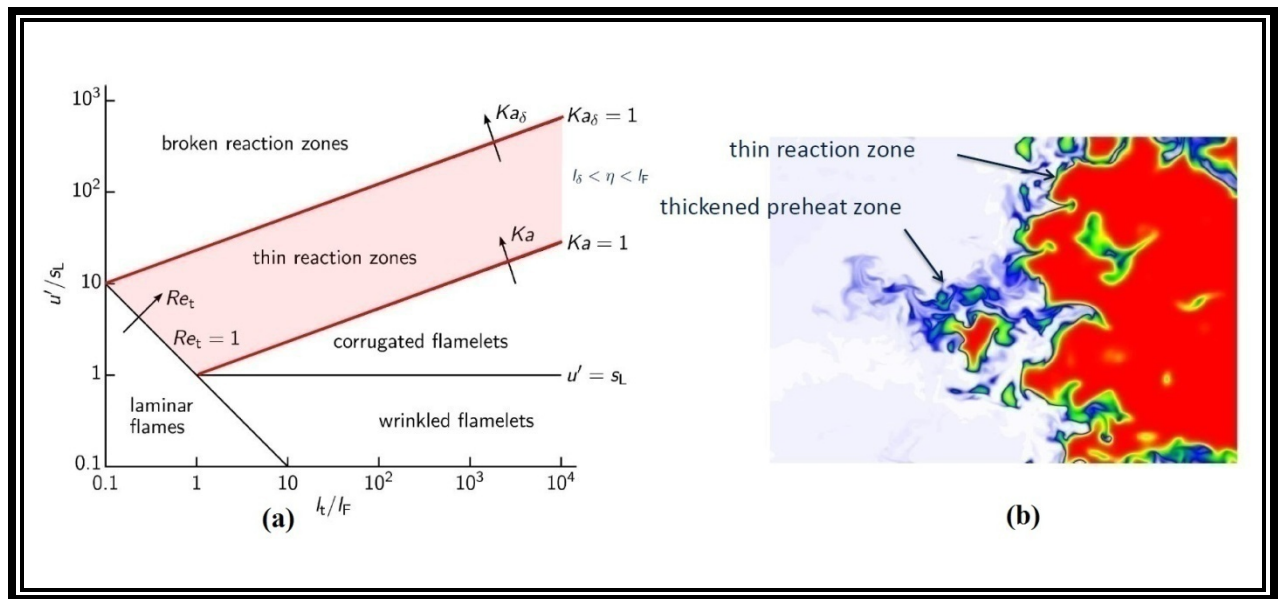


Figure 2. 25: Thickened flame (a) Flame regime, (b) DNS of flame structure.

Distributed Flame Regime

The distributed flame regime or the well-stirred reactor flame regime is characterized by $Da \gg 1$, $\frac{u'}{s_L} > 1$, $Re_T > 1$ and $Ka > 1$. Due to the high value of Damkholer number, the mixing time scale is smaller than the chemical time scale. Thus the combustion process is controlled by the chemical kinetics. This regime refers the perfectly premixed combustion. Therefore the classical flame front does not exist. This type of combustions are often used to investigate the effects of turbulence from the effects of chemical kinetics. Figure 2.26 shows the DNS of well-stirred reaction.

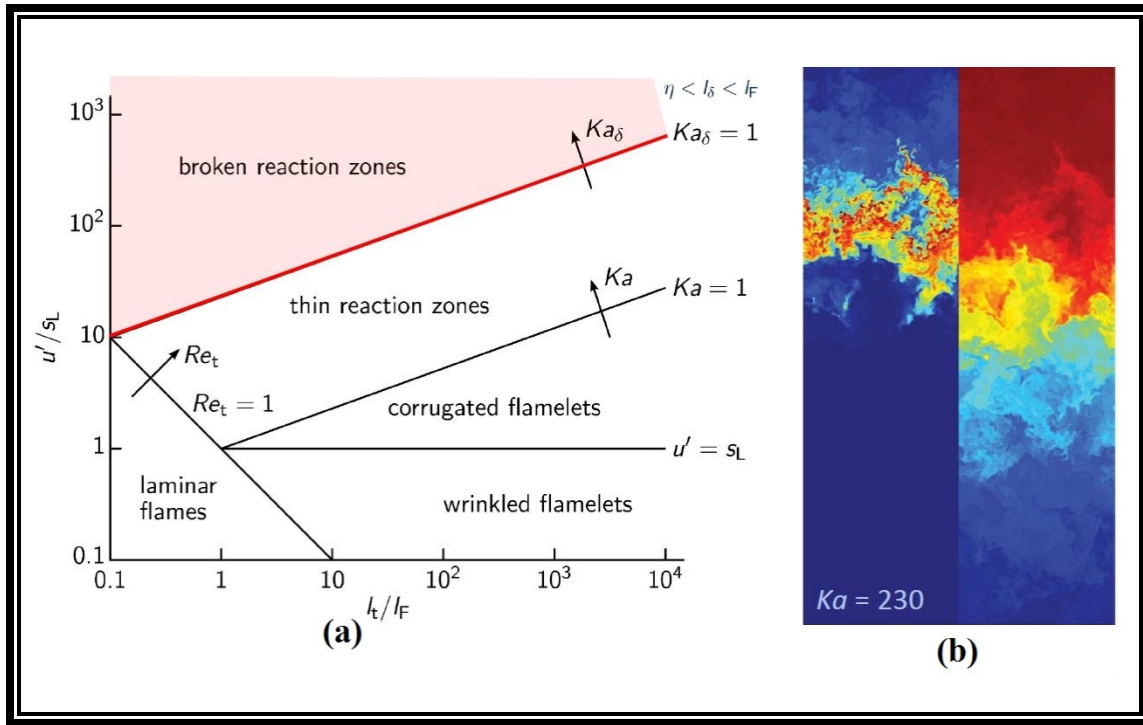


Figure 2. 26: Distributed flame (a) Flame regime, (b) DNS of flame structure.

Chapter 3: Experimental Setup Design

3.1 Experimental Criteria

The main goal of this study is to design an optically accessible combustion system in order to study high intensity turbulent combustion process. The key feature that limits the design process is the optical access. To the author's knowledge, many optically accessible combustors have been developed for research purpose. Cambridge university developed high-pressure test facility in order to test aero engine gas turbine fuel injector [86]. This combustor is rated for a maximum pressure of 1.003 MPa with maximum air flow rate of 0.9 kg/s. The National Energy Technology Laboratory (NETL) has designed their gas turbine test rig which is compatible for natural gas and liquid fuel [87]. This test rig can be operated up to 3.039 MPa pressure and a wide variety of fuel. Frank et al [88] described their combustor which can be operated at a pressure of 5MPa with a flow rate of 0.4kg/s. Moreover some other optically accessible combustor design are described by Tse et al [89], Tomezal et al [90] and Liewen [91].

Table 3. 1: Combustor design criteria.

System	Requirement
Combustion chamber	Optically accessible
	Grid turbulence generator
	Changeable step size (variable dimesion)
	Max Pressure: 6 bar (87 psi)
Reactants	Air / CH ₄
Air	Pre-heated at 400-600 K (260 – 620 F)
	Velocity Mach > 0.3
	Flow rate: Max at 0.47 kg/s
CH ₄	Flow rate: Variable (max 0.07 kg/s)
Inlet pressures	100 - 600 kPa (14 - 87 psi)
u'/S_L	5-10
L_T/δ	50-200

Most recently a high pressure combustor has been designed and developed by the center for Space Exploration Technology Research (cSETR) at the mechanical engineering department of the University of Texas at El Paso. This optically accessible combustor is rated for 1.5MPa pressure and 500 kW thermal power [92]. A detail design process is described in this chapter for a new optically accessible combustor. Table 3.1 shows the design criteria for the combustor. The combustor has a three sided optical access and a backward facing step at the bottom. The purpose of the step is to hold the flame by creating a recirculation zone in order to supply continuous air-fuel mixture. An exploded view of the combustor is shown in figure 3.1 with its different components. The major components of the combustor are - the mixing section, the entrance section, windows and window covers, a backward facing step, a grid and the exhaust sections. There are cooling channels inside the combustor wall. The sectional view (figure 3.2) also clearly shows the step and the grid which acts as a turbulence generator.

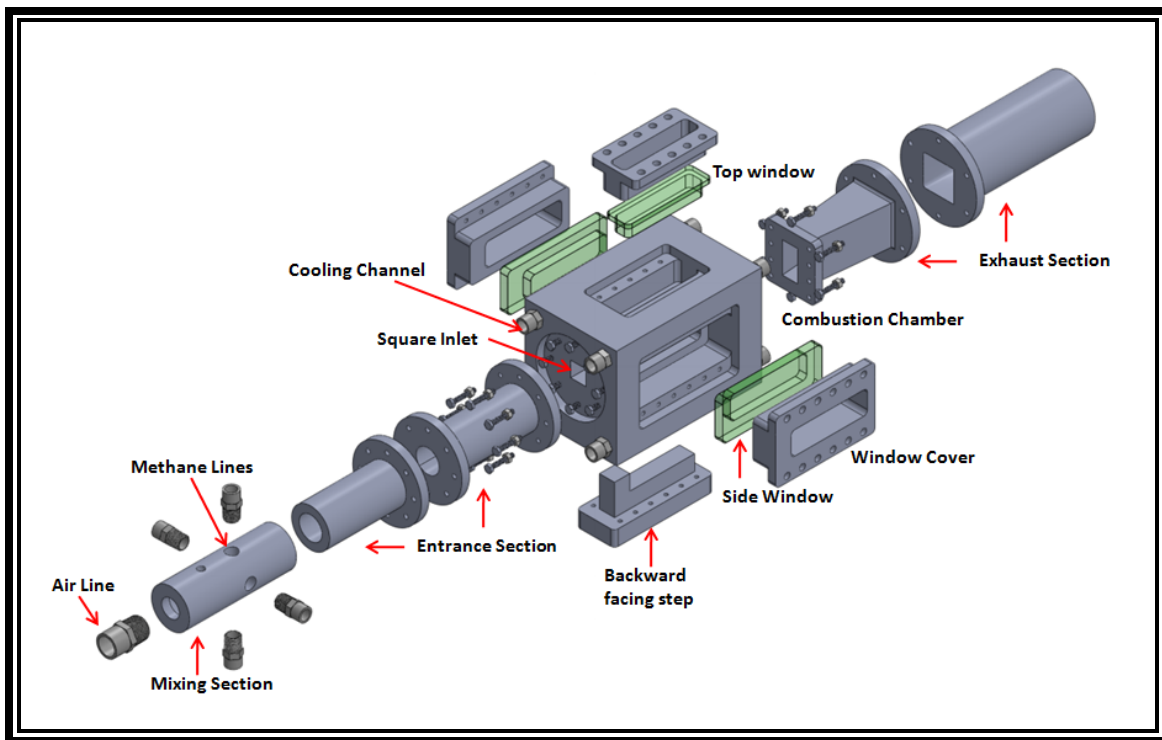


Figure 3. 1: Exploded view of the combustor assembly.

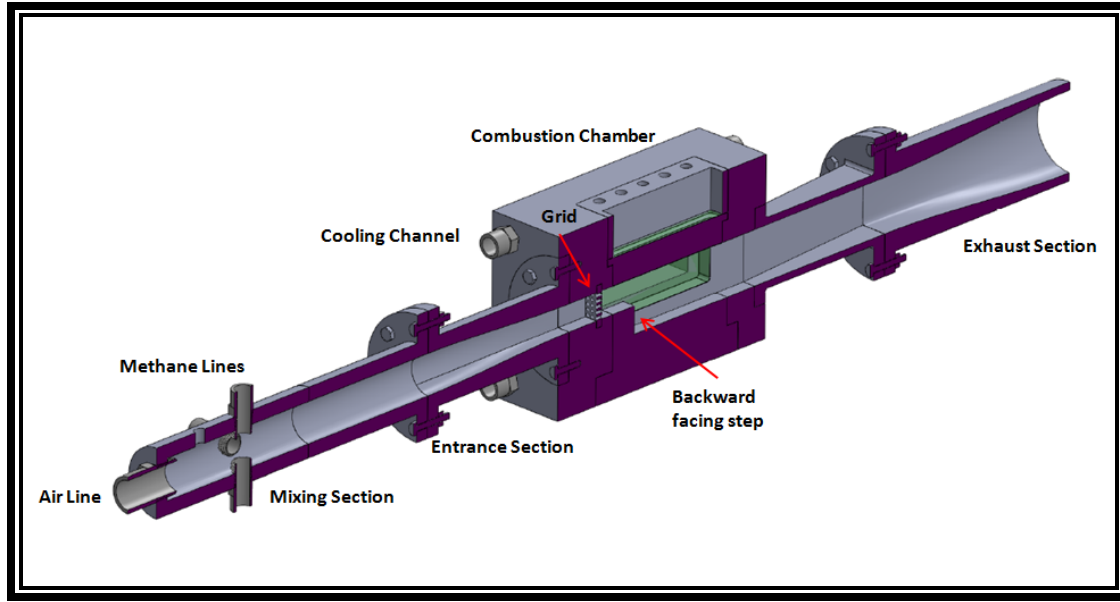


Figure 3. 2: Sectional view of the combustor assembly.

3.2 Combustor Design

Combustor design is one of the critical parts of this project. The combustor has optically accessible windows for laser diagnostic. It also has a backward facing step for flame stabilization. All of these components are designed with UNS S316 Stainless steel. The glass window is designed with fused quartz glass. Table 3.2 shows the AISI 316 material properties. The combustor is designed for a maximum pressure of 25 bar. But the window design limits the total design criteria. Table 3.3 shows the material properties of quartz glass. All of the designs are based on analytical and numerical calculation. FEA analysis is done using commercially available FEA software ANSYS. The Von Mises stress (Equivalent stress) is calculated for the design. As combustors have similar loading as pressure vessel, the analytical calculations are done based on pressure vessel calculation. On the other hand, the window calculation are done based on beam stress analysis available in the literature. The detail design of each components are described in the later parts of this chapter.

Table 3. 2: UNS 316 Stainless Steel properties.

Properties	Unit of Measure
Density	8000 kg/m ³
Tensile Strength	485 MPa
Yield Strength (0.2%)	205 MPa
Elongation (% in 50mm)	40
Modulus of Elasticity	193 GPa
Coefficient of Thermal Expansion (0-538 ⁰ C)	17.5 $\mu\text{m}/\text{m}^{\circ}\text{C}$
Rockwell Hardness	95

Table 3. 3: Fused Quartz properties.

Properties	Unit of Measure
Density	2200 kg/m ³
Tensile Strength	48.3 MPa
Poisson's Ratio	0.17
Thermal Conductivity	1.3 W/m-K
Bulk Modulus of Elasticity	37 GPa
Coefficient of Thermal Expansion	5.5 $\mu\text{m}/\text{m}^{\circ}\text{C}$
Hardness	8.8 GPa
Specific Heat Capacity	45.3 J/mol-K

The cSETR lab facility consists of two compressed air supply lines. One of them can supply 100 cfm of air at 120 psi. Another line can supply 190 cfm of air at 140 psi. The flow area is calculated based on these two flow rates and a square section has been considered for the combustor inlet in order to achieve a flow velocity of Mach 0.3 to 0.5. Figure 3.3 shows the

relationship for effective diameter and flow velocity. The effective diameters are calculated for both air supply line for a wide range of velocity. Finally a 1.128 inch effective diameter has been considered which is equivalent to the area of a (1.0in x 1.0in) square section.

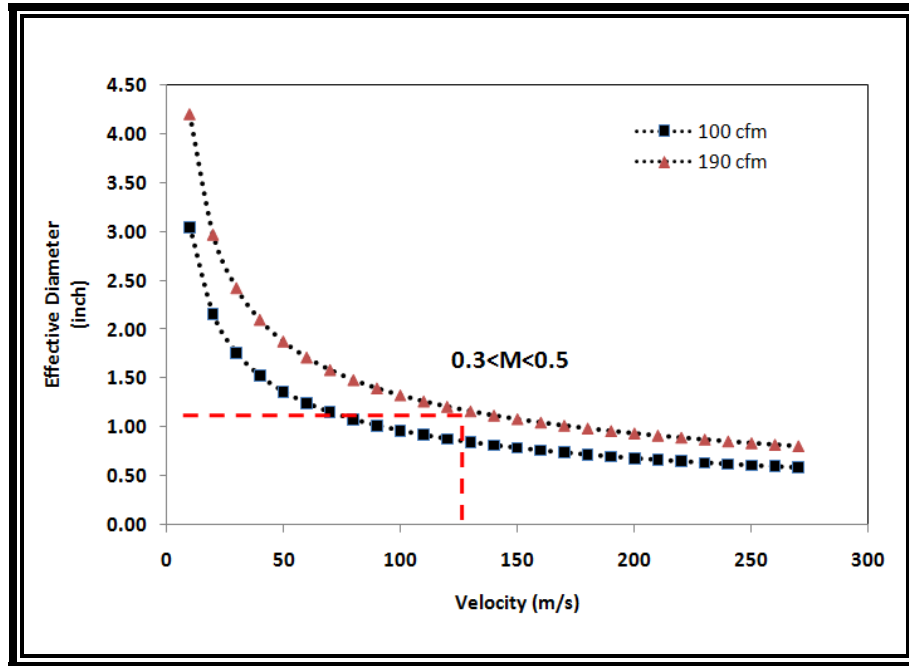


Figure 3. 3: Relationship between flow velocity and effective diameter.

The combustor is a 9.5 inch long and 6 inch wide rectangular shape structure. The height is 6.5 inch. It has a 1 inch square hole for combustion. It also has optical access from the top and from the two sides. Therefore it has window slots in three sides and a slot for a step in the bottom. Figure 3.4 shows the isometric view of the combustor. The front section of the combustor is designed to accommodate the entrance section. A 4.5 inch flange can be placed here. The entrance section can be attached here with eight 1/4-20 bolts. There is a rectangular slot inside the square hole for grid insertion. This slot is 0.25 inch by 1.5 inch in dimension. The side window slots are 5 inch long and 1.5inch wide. The thickness of this slot is 0.5 inch. Quartz windows are placed here. The top window slot is 5inch long and 1inch wide. The thickness is 0.75 inch here. Schematics are shown in figure 3.5.

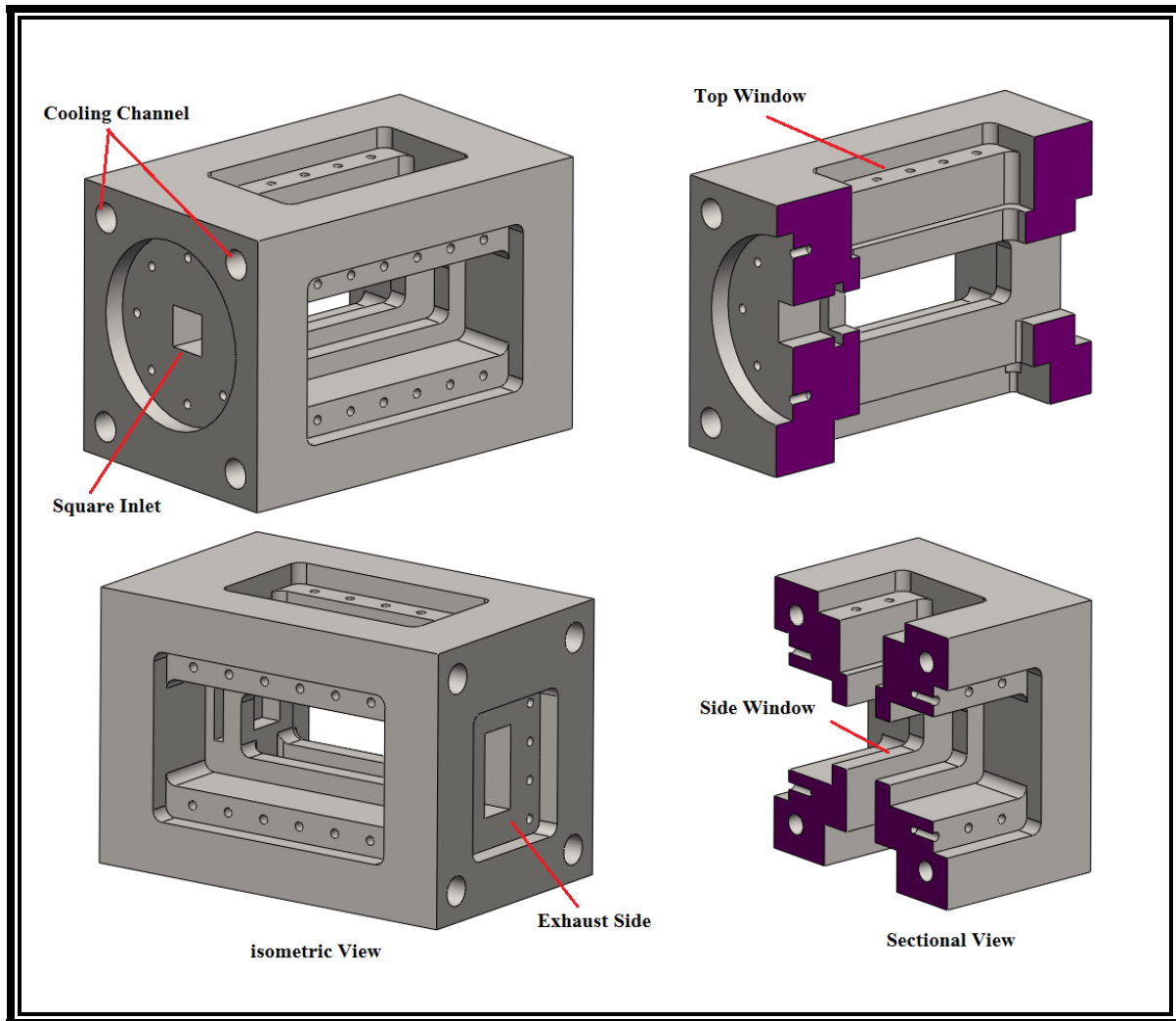


Figure 3. 4: Combustor schematic

There are cooling channels inside the combustor wall. The channel diameter is 0.5 inch. An 1/2"MNPT connection is used for the cooling channels and Dynalene HC is used for the coolant. The combustion chamber has a backward facing step with a 1:2 expansion ratio. Therefore the effective area become a (1inch x 2inch) rectangular section after the step. The step can be attached from the bottom of the combustor. Both the side window covers and the bottom step is attached with twelve 1/4-20 annealed stainless steel bolts. The top window cover is attached by ten 1/4-20 bolts. A rectangular cavity has been made in the exhaust section of the combustor in order to attach the exhaust section. The exhaust section can be attached with eight 1/4-20 stainless steel bolts. The exhaust section consists of two individual section. The first

section is a transition section from a (1inch x 2inch) rectangular to a (2inch x 2inch) square section and the next section is a transition from (2inch x 2inch) square section to a 3 inch diameter circular section. Detail drawing of each components are presented in APENDIX I.

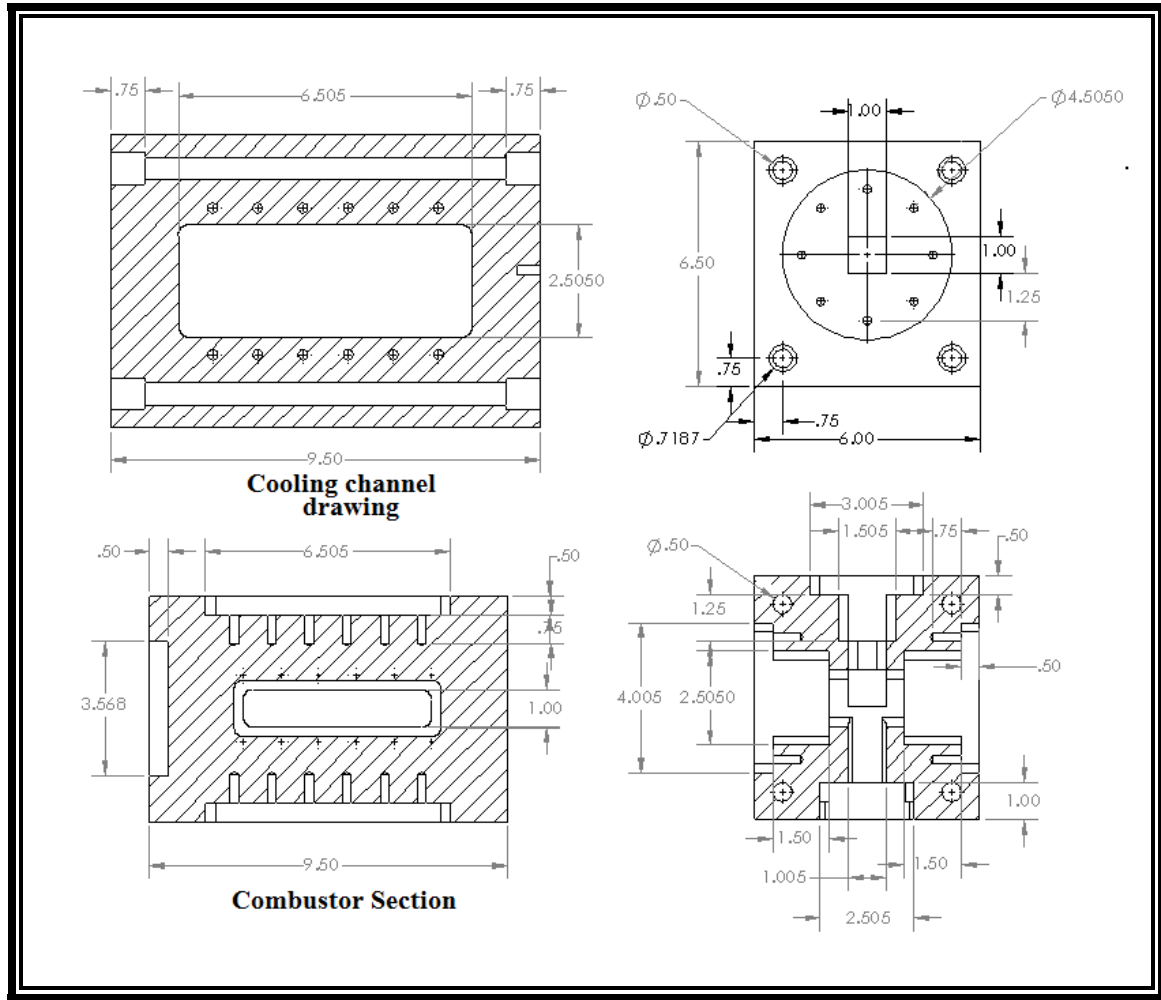


Figure 3. 5: Detail drawing of the combustor

3.2.1 VON MISES STRESS CALCULATION

Von Mises stress is often used in design calculation. It is widely used when the body is subjected to a complex loading condition. Engineers calculate the Von Mises (VM) stress for complex part design and compare with the material's yield strength. Von Mises stress criteria is effective when the material is ductile in nature. This stress theory is developed from the

'distortion energy failure theory' [93] which refers that failure occurs when the distortion energy in actual case is more than the distortion energy in a simple tension case at the time of failure. The von mises stress consists of two stress tension known as - Hydrostatic stress and Deviatoric stress. Hydrostatic stress is the three normal stress components of the stress tensor and deviatoric stress is the remaining components of the stress tensor. Equation 3.1 shows the stress tensor in 3-dimensional form. The hydrostatic and deviatoric stress are shown in equ 3.2 where σ_{ij} is the stress tensor and $\delta_{ij}\sigma_{kk}$ is the hydrostatic component and σ'_{ij} is the deviatoric components. Here, $\sigma_{11}, \sigma_{22}, \sigma_{33}$ are the normal stress components in 3-dimensional space. The Von Mises stress is directly related to the deviatoric strain energy. When this strain energy combines with Hooke's law, the Von Mises stress equation can be derived which is shown in eqn 3.3 and 3.4.

$$\sigma_{ij} = \frac{1}{3}\delta_{ij}\sigma_{kk} + \sigma'_{ij} \quad (3.1)$$

$$\sigma_{hyd} = \frac{1}{3}\delta_{ij}\sigma_{kk} = \frac{1}{3}(\sigma_{11} + \sigma_{22} + \sigma_{33}) \quad (3.2)$$

$$\sigma_{VM} = \left[\sigma_{11}^2 + \sigma_{22}^2 + \sigma_{33}^2 - \sigma_{11}\sigma_{22} - \sigma_{22}\sigma_{33} - \sigma_{33}\sigma_{11} + 3(\tau_{12}^2 + \tau_{23}^2 + \tau_{31}^2) \right]^{1/2} \quad (3.3)$$

$$\sigma_{VM} = \left[\frac{3}{2}\delta_{ij}\sigma_{kk} - \frac{1}{2}(\sigma_{kk})^2 \right]^{1/2} \quad (3.4)$$

According to the distortion energy theory, the failure occurs when the von mises stress exceeds the material yield strength (σ_y). Therefore the failure condition can be simplified as-

$$\sigma_{VM} \geq \sigma_y \quad (3.5)$$

In order to calculate the σ_{VM} , ANSYS APDL is used. The solid geometry has been developed by commercial CAD software SOLIDWORKS. Then the solid part is exported in to ANSYS Workbench platform. Approximately 2.8 million tetrahedral mesh elements are used

during FEA analysis. The boundary condition has been given in terms of pressure loading. The pressure is considered to be 25 bar only for the combustor wall. The thermal condition is also considered during the analysis. Although there are no such wall that has direct contact with the flame as the combustor is surrounded with quartz window, a constant wall temperature of 80°C has been considered. Figure 3.6 shows the contour of Von Mises stress. The contour clearly shows that the stresses are developed in the side wall of the window slot and top and the bottom wall of the main chamber.

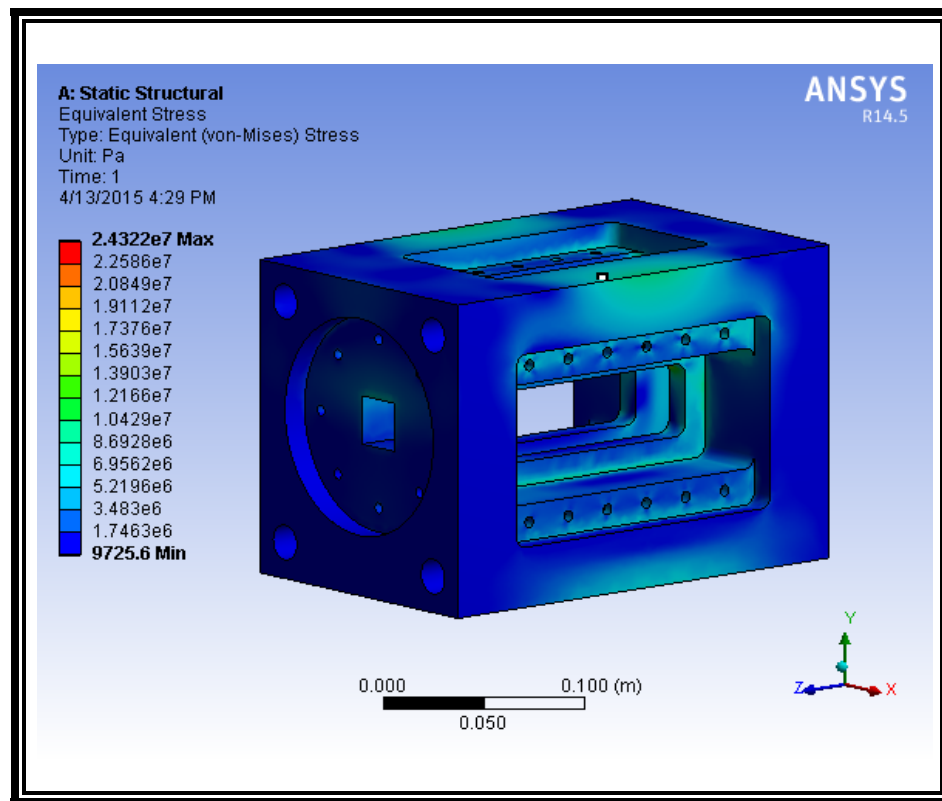


Figure 3. 6: Contour of Von Mises stress at 25 bar pressure loading.

A detail stress distribution has been shown in figure 3.7 for the side window slot of the combustor. The stress is distributed along the thickness of the slot wall which is located at 0.5 inch from the square hole. The wall is 0.5 inch thick and the x-axis of this plot represents the thickness. The zero point is consider at the inner wall of the window slot. The stress distribution clearly indicates that the developed stress is higher at the outer wall of the window slot. The

maximum developed stress is around 16.8MPa which is well below the yield stress of the UNS316 steel. Figure 3.8 shows the Von Mises stress distribution for the top window slot. The distribution is shown at the middle of the slot along the thickness of the slot. The zero location of the x-axis of this plot is close to the combustion hole and the maximum developed at the outside of the wall as the same pattern has been seen for the side window slot. The maximum developed stress in this case is 12.6 MPa which is also well below the material yield stress limit. Figure 3.6 shows the coordinate system for the combustor and z-direction is along the length of the combustor.

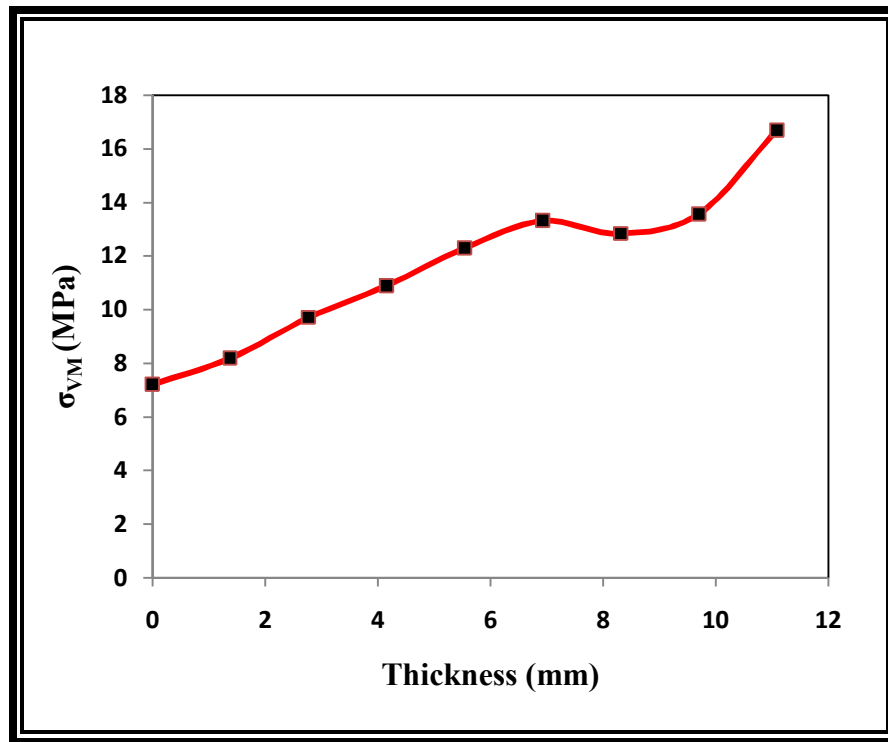


Figure 3. 7: Von Mises stress along the thickness of the side window slot.

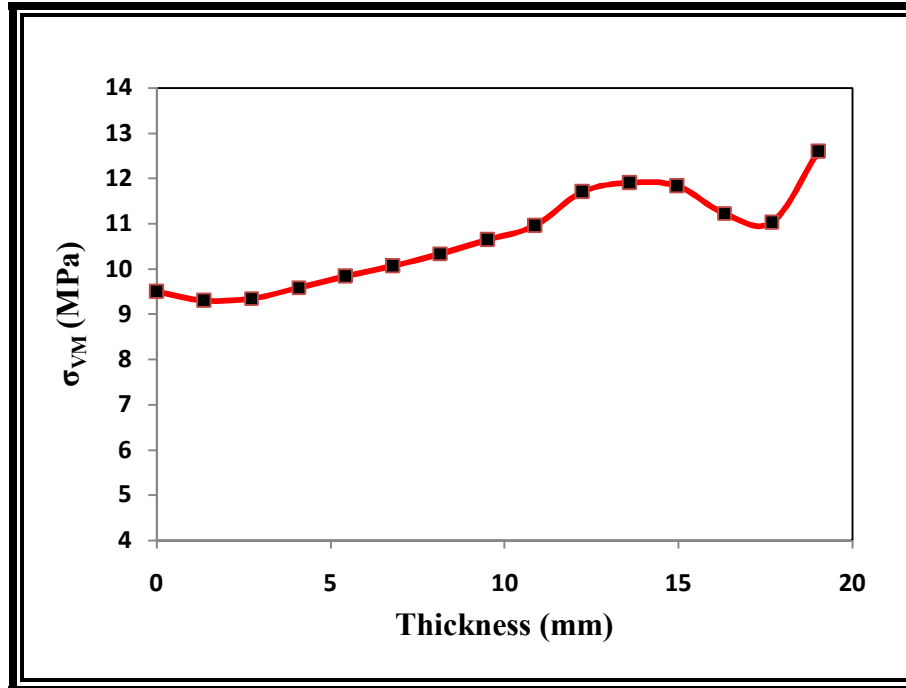


Figure 3. 8: Von Mises stress along the thickness of the top window slot.

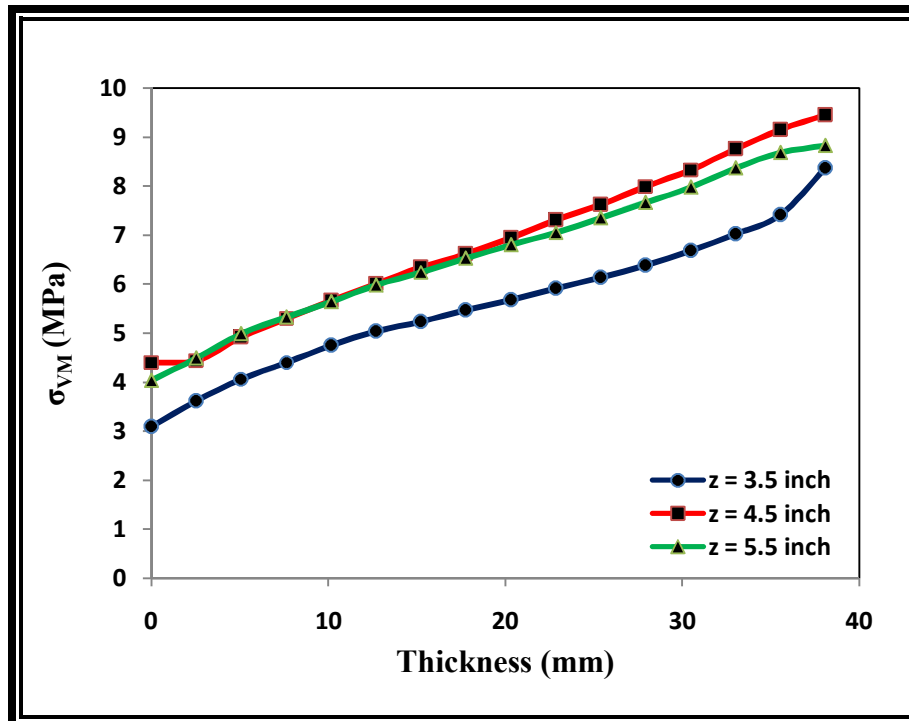


Figure 3. 9: Von Mises stress along the thickness of the side wall at three different locations.

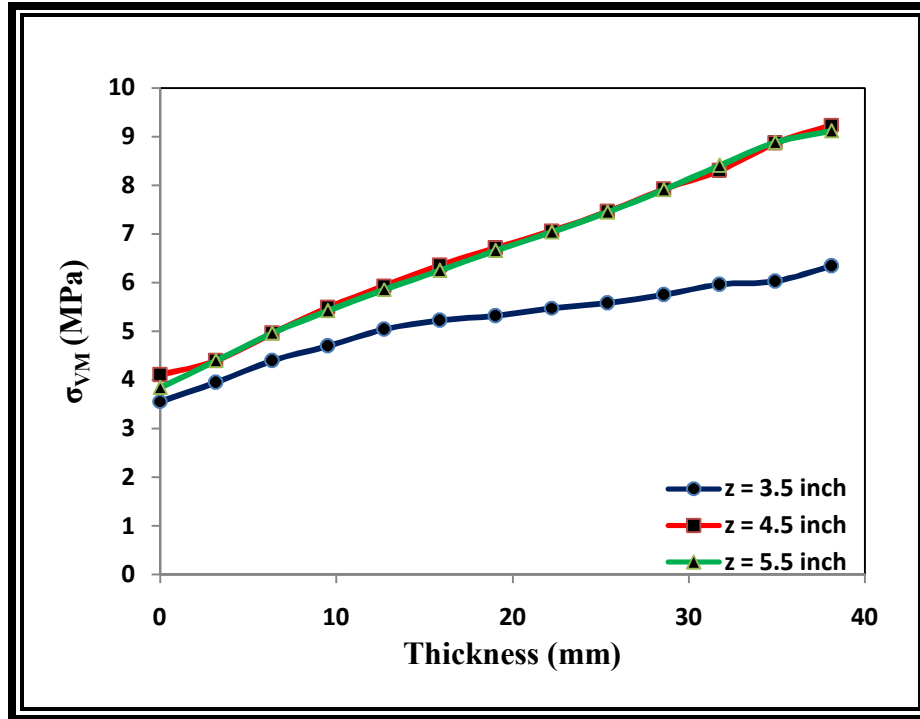


Figure 3. 10: Von Mises stress along the thickness of the top wall at three different locations.

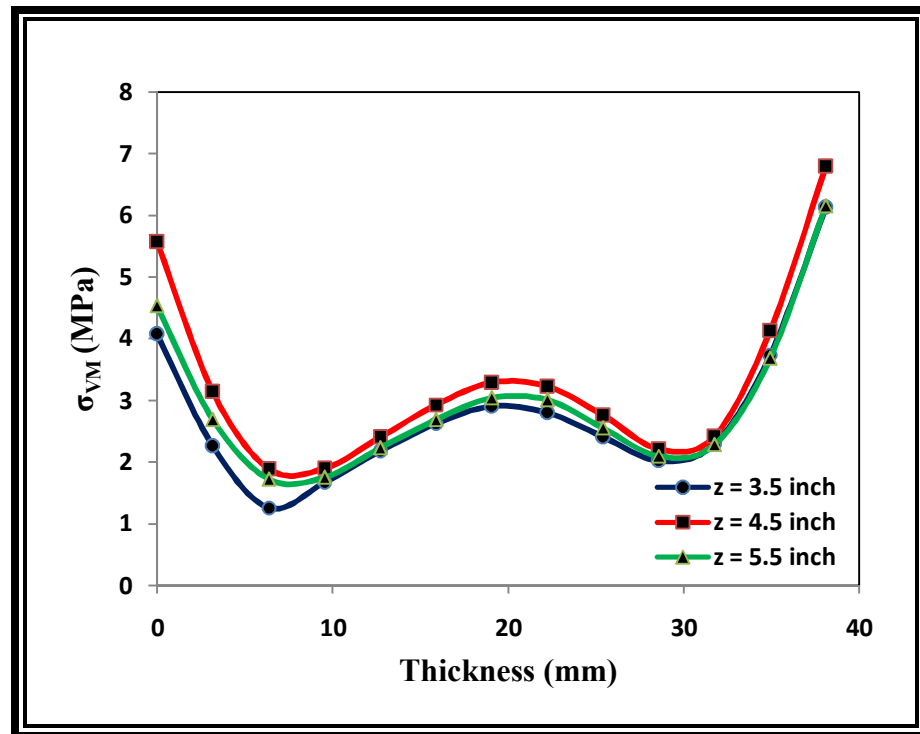


Figure 3. 11: Von Mises stress along the thickness of the bottom wall at three different locations.

Figure 3.9 shows the von mises stress of the side wall of the combustor at three different locations. The first location is 3.5 inch from the front corner of the combustor along the z-direction. The other two lines are one inch apart from the previous line. From the figure, it is found that the stress distribution is maximum at the middle of the combustor. The red line ($z=4.5$ inch line) represents the stress distribution at the middle portion of the combustor. The maximum von mises stress calculated here is 9.45 MPa. Similar stress distributions have been found at the top wall for the corresponding location and the maximum stress calculated here is 9.24 MPa which is shown in figure 3.10. However, the bottom wall for the same corresponding locations show different stress distribution. The stresses are larger at the edges of the combustor and the maximum stress here is 6.78 MPa which is shown in figure 3.11. The FEA analysis was also able to predict the maximum principle stress and maximum shear stress which is shown in figure 3.12. The maximum principle stress developed here is around 16.15 MPa. On the other hand the maximum shear stress developed here is around 12.88 MPa. Moreover, Thermal deformation has been calculated for both thermal and pressure loading condition. Figure 3.13 shows the thermal deformation of the combustor. The maximum deformation is around $6.8\mu\text{m}$ which is used for tolerance calculation of the combustor parts.

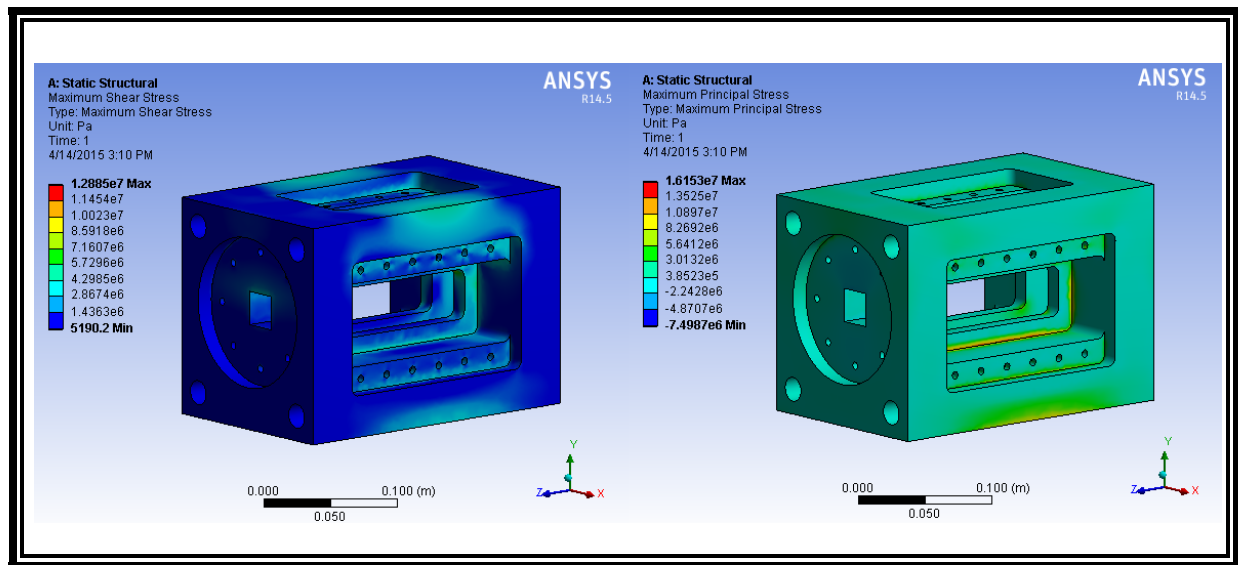


Figure 3. 12: Contour of maximum shear stress (left) and maximum principle stress (right).

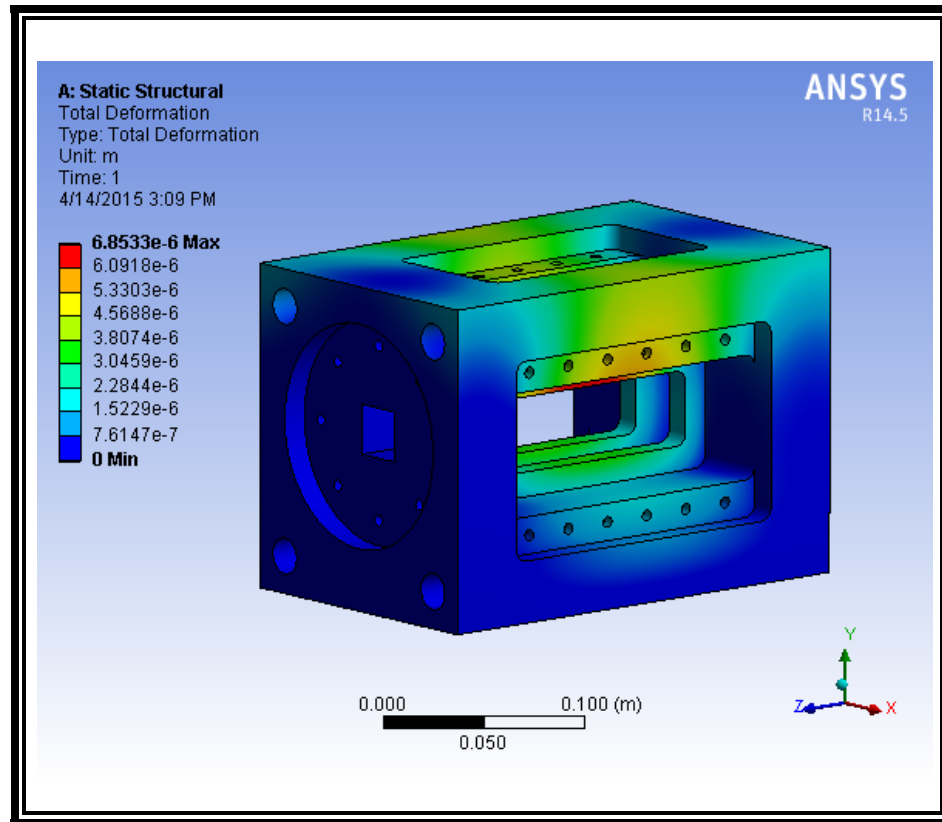


Figure 3. 13: Contour of deformation due to thermal and pressure loading.

The clearance for different part assembly has been calculated based on thermal deformation and deformation due to pressure loading. These deformations have been calculated by both analytic and numeric method. The results show close match between both deformation. Table 3.4 shows the result for a maximum normal force of 3kN and a maximum wall temperature of 300⁰C. A nominal clearance of 0.127mm (0.005inch) has been considered for window and window cover.

Table 3. 4 Calculation of deformation for thermal and pressure loading.

Deformation	Analytical	Simulation
Strain	1.243 μm	1.397 μm
Thermal deformation	0.517 mm	0.468 mm

3.3 Entrance and Exhaust Section Design

The entrance section is specially designed for a particular inlet condition. The main air line has 1 inch tubing and the mixing section has a 1.5 inch diameter circular section. But the combustor inlet is 1 inch square section. So a transition section has been designed from a circular cross section to a square cross section. This transition section is the entrance section. The curvature of this section is calculated based on eqn 3.6 in order to achieve a '*top hat*' velocity profile at the combustor inlet. Similar approach is used for the exhaust section for the transition from a square to a circular section. Equation 3.7 and 3.8 show the curvature relation for the entrance and the exhaust section respectively. Detail calculations are shown in APPENDIX II. The curvature of the entrance section and exhaust section are shown in figure 3.14 and 3.15 respectively. These curvatures are derived from eqn 3.7 and 3.8 respectively.

$$r = ax^5 + bx^4 + cx^3 + dx^2 + ex + f \quad (3.6)$$

$$r = -0.000589x^5 + 0.00736x^4 - 0.02456x^3 + 0.75 \quad (3.7)$$

$$r = 0.0000307x^5 - 0.000786x^4 + 0.005122x^3 + 0.787 \quad (3.8)$$

A simple analytical stress calculation has been done assuming a thick wall cylinder. Equation 3.9 represents the simplified tangential stress formula for thick wall cylinder with inside pressure of 6 bar. Here, r_i is the inner radius and r_o is the outer radius of the section. A maximum shear stress of 1.28 MPa has been found by analytic calculation using eqn 3.9. On the other hand, the FEA analysis gives a maximum shear stress of 1.43 MPa. Moreover, the shear stress distribution along the thickness of the wall at different axial locations are shown in figure 3.16. Other important stress distributions along the length have been shown in figure 3.17. Detail FEA analysis has also been done for these sections and maximum shear stress, maximum principle stress, von mises stress and deformation have been shown in figure 3.18.

$$\sigma_t = \frac{r_i^2 P_i}{r_o^2 - r_i^2} \left[1 + \frac{r_o^2}{r_i^2} \right] \quad (3.9)$$

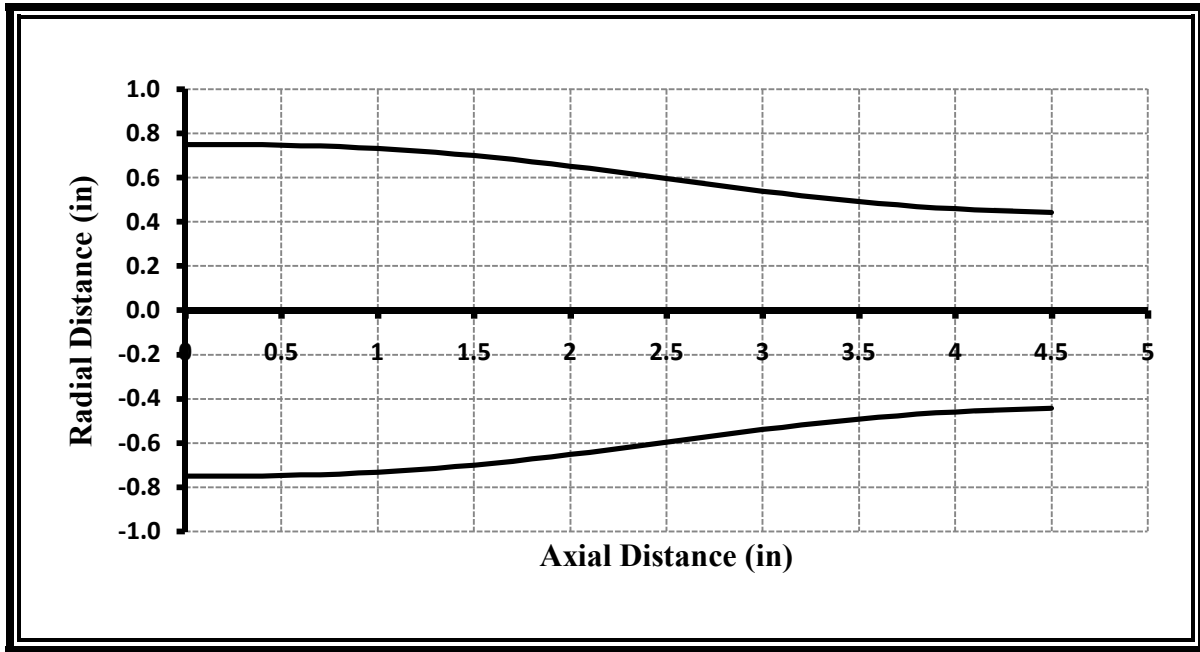


Figure 3. 14: Entrance section profile.

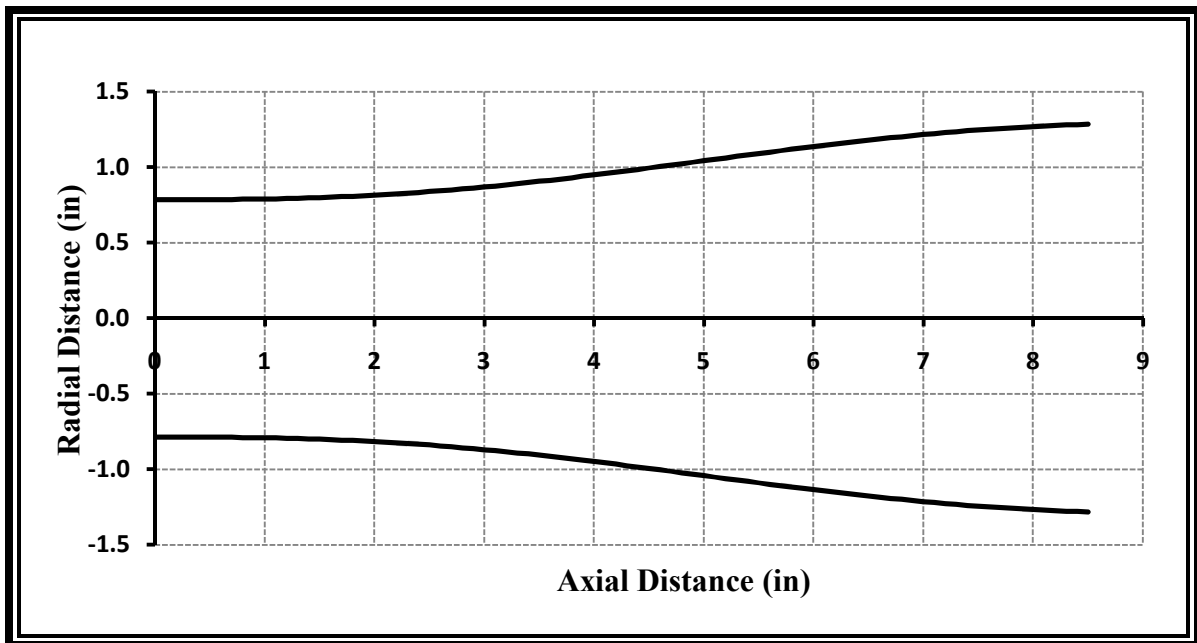


Figure 3. 15: Exhaust section profile.

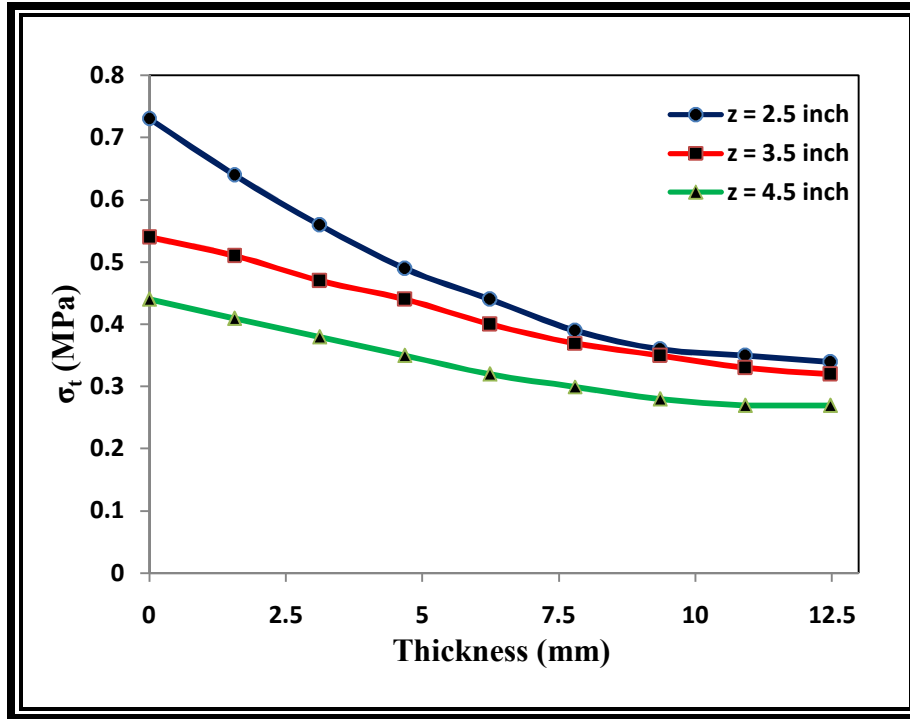


Figure 3. 16: Tangential stress distribution.

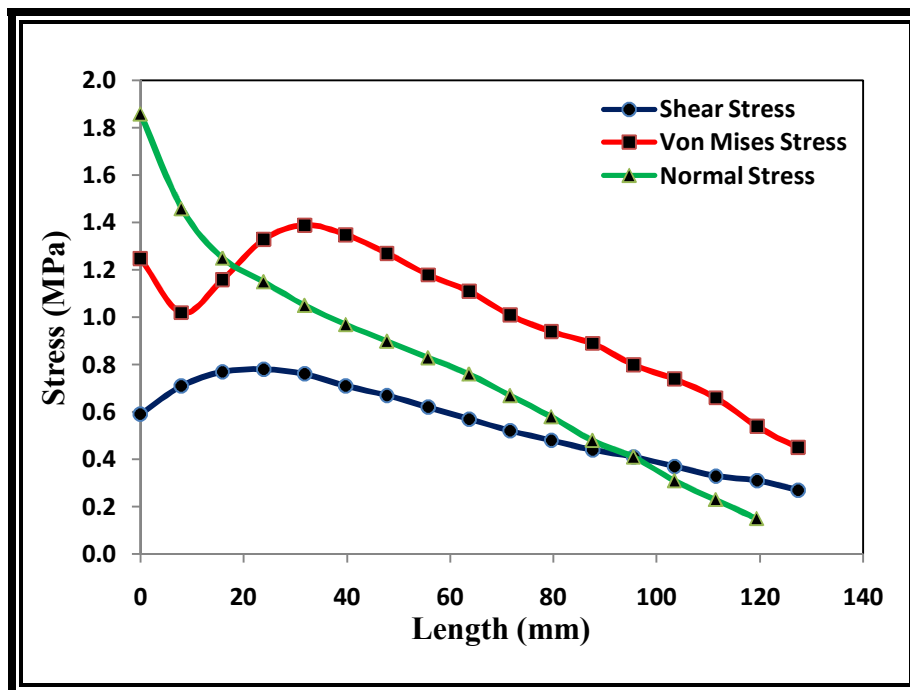


Figure 3. 17: Stress distribution along the length.

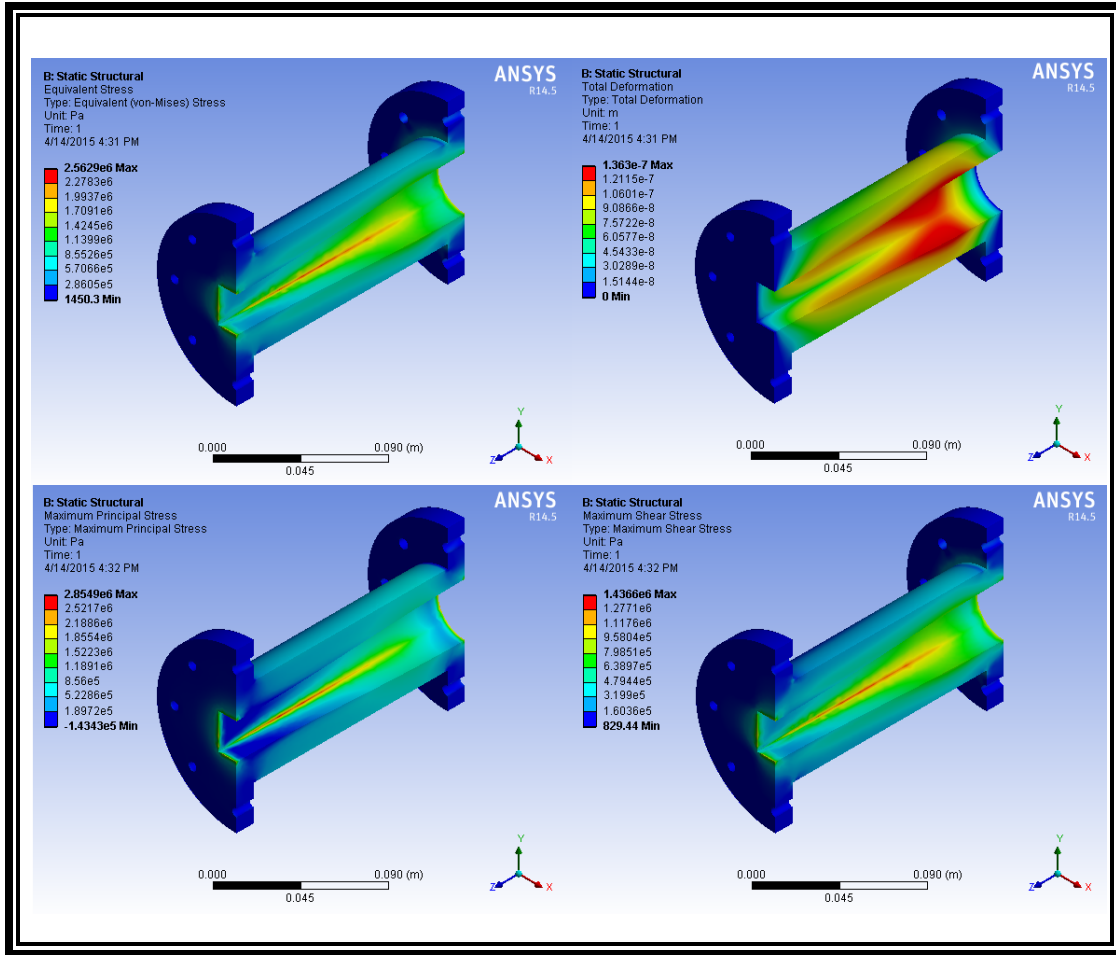


Figure 3. 18: Contour of principle normal stress, shear stress, von mises stress and deformation.

Similar analysis has been done for two exhaust parts. The first exhaust section is a transitional section from a rectangular cross section (1in x 2in) to a square cross section (2in x 2in). The second part is the transition from the square section to a circular cross section (3.5 in dia). Figure 3.19 shows the von mises stress, the principal stress and the shear stress distribution along the thickness for the first exhaust part. Figure 3.20 shows the similar stress distribution along the wall thickness for the corresponding component. Moreover, figure 3.21 and 3.22 show the contours of different components and deformation. The stress distribution along the length and thickness of the second exhaust part are shown in figure 3.22 and 3.23 respectively.

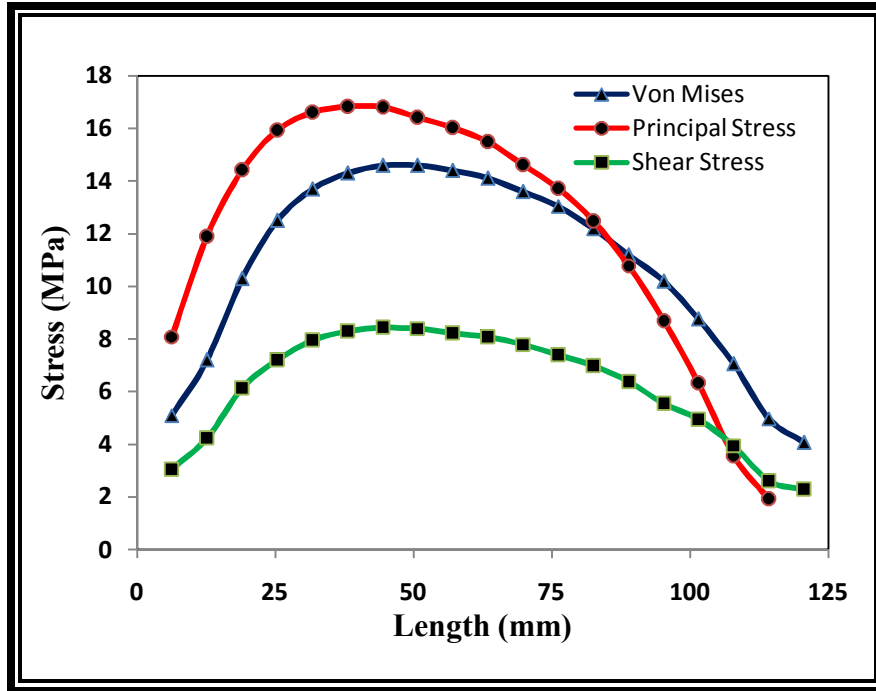


Figure 3. 19: Stress distribution along the length.

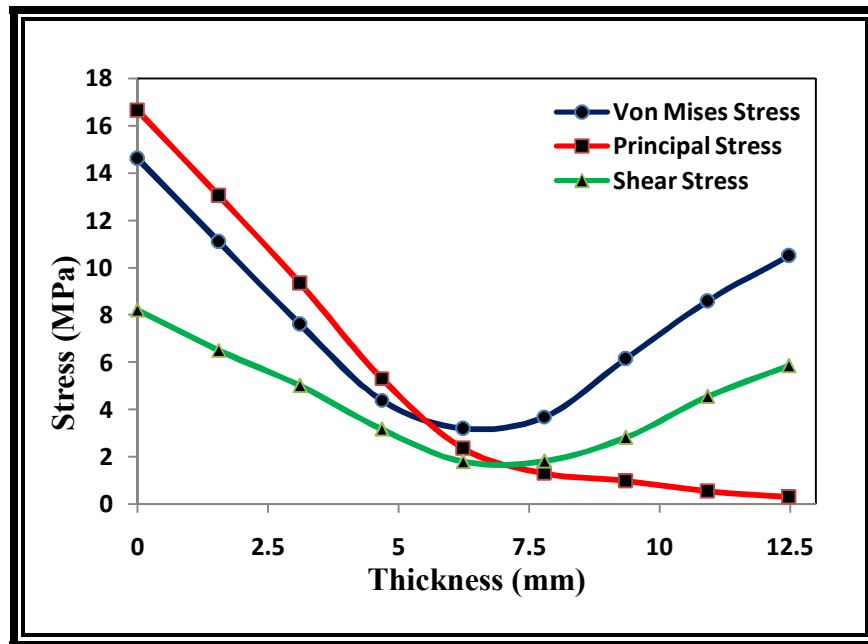


Figure 3. 20: Stress distribution along the wall thickness.

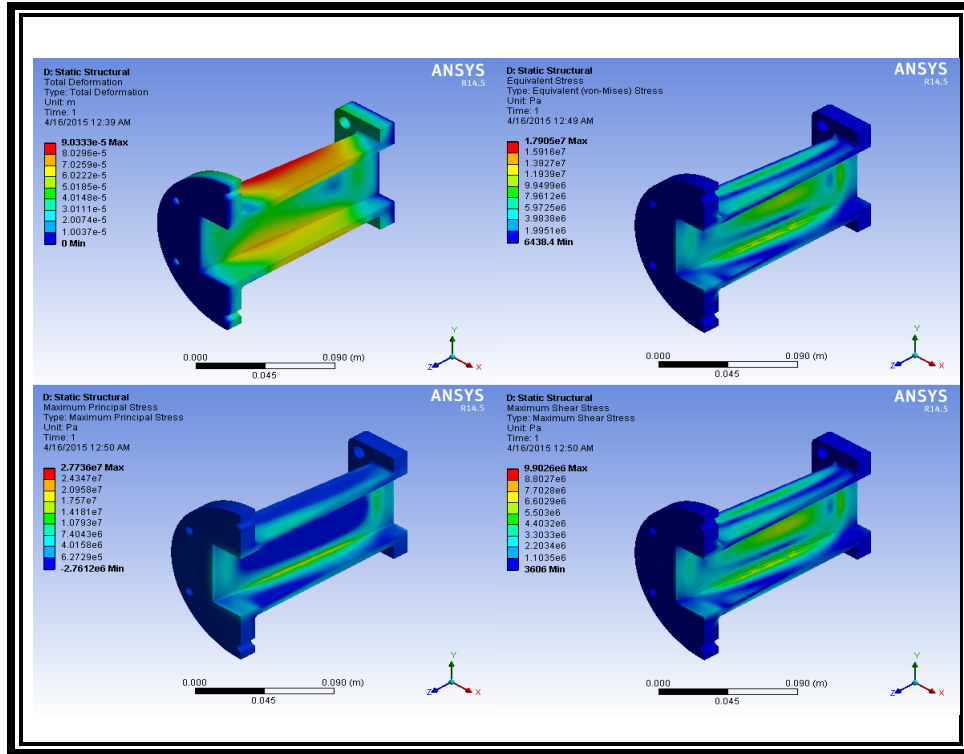


Figure 3. 21: Contour of stress components for first exhaust part.

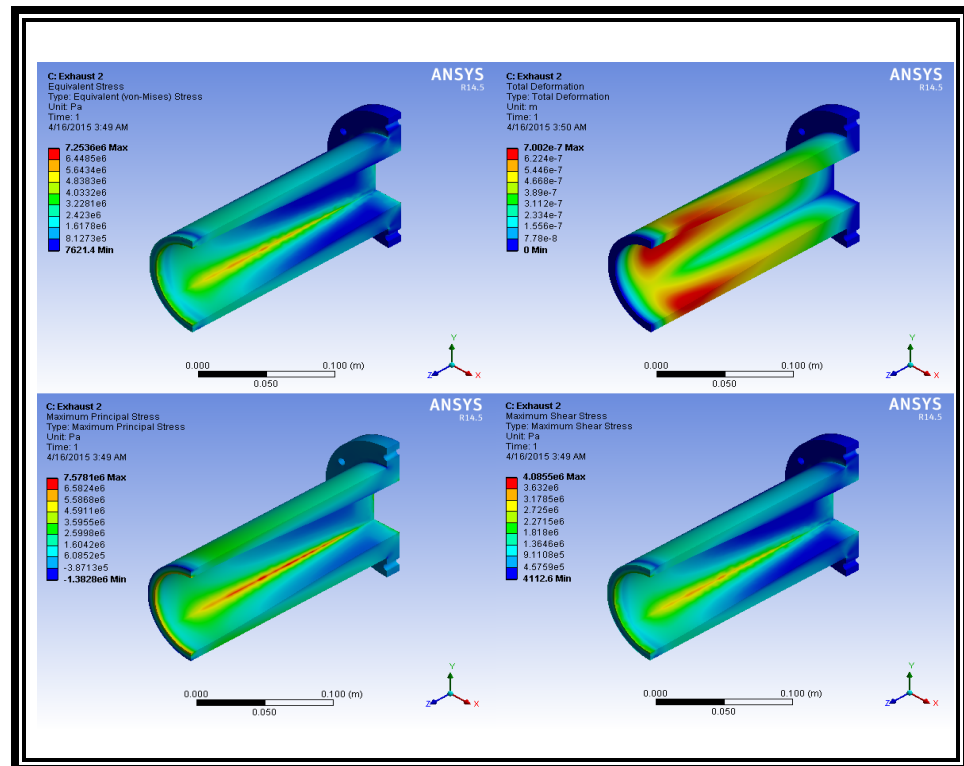


Figure 3. 22: Contour of stress components for second exhaust part.

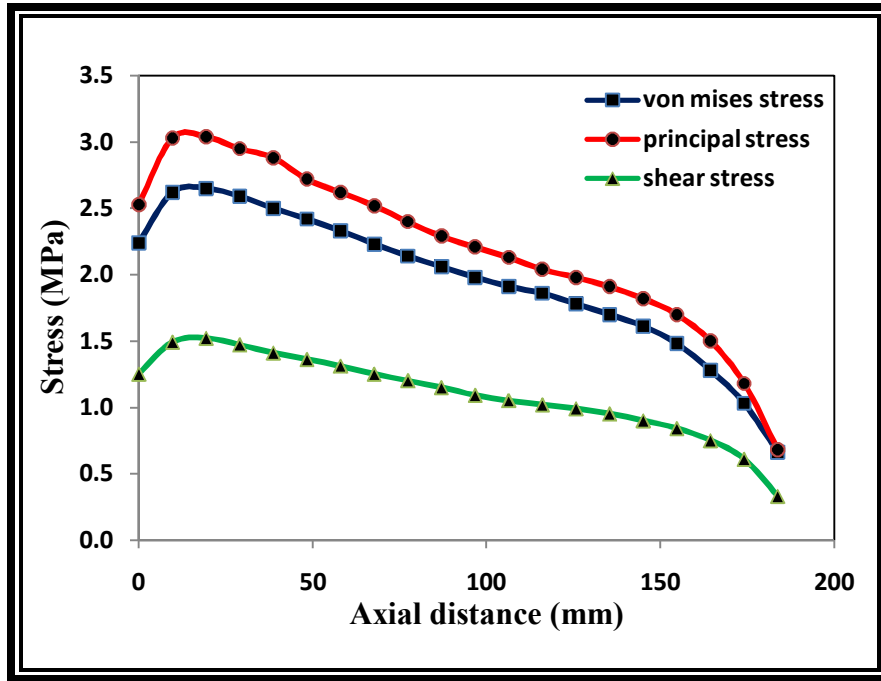


Figure 3. 23: Stress distribution along the length for second exhaust part.

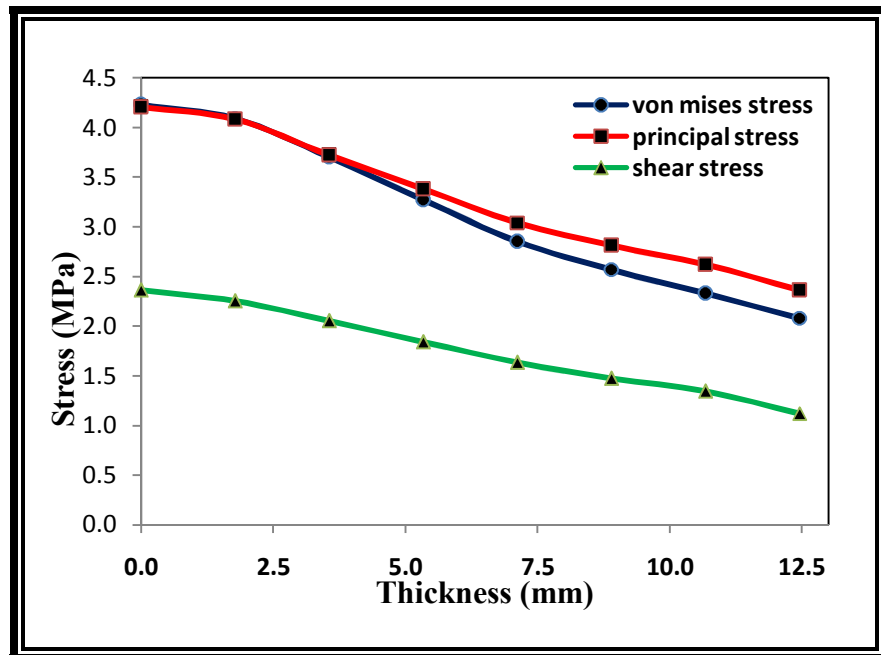


Figure 3. 24: Stress distribution along the length for the second exhaust part.

3.4 Grid Design

The grid is designed as a turbulence generator. The key parameter for a grid is the blockage ratio (BR). In this experiment, three different grids have been used. The blockage ratio has been calculated according to the effective flow area. Then the effective flow area is subtracted from the combustor inlet flow area which is 1 inch square. This gives the blockage area which eventually gives the blockage ratio. Table 3.5 shows diameter calculation of the three different grids. The initial flow area is a 1 inch by 1 inch square section and 25 holes have been chosen in a 5x5 array for the grid. Figure 3.25 shows the relationship between number of grids with the blockage ratio. From this figure, an optimum hole number has been chosen which is 25. The only parameter that varies in different grids is the hole diameter.

A detailed FEA analysis has been done for the grid. Figure 3.26 shows different stress distribution along the thickness of the grid. The maximum developed stress here is around 9 MPa which is well below the material yield strength. Figure 3.27 also shown similar stress distribution along the length of the grid. It shows that the maximum stress developed at the middle of the grid as it has less material due to the grid hole. Also there are stress concentration at the edges of the grid due to its shape corner. Figure 3.28 shows the contour of von mises stress, principal stress, maximum shear stress and deformation. All the stress components are well below the material yield strength and the deformation is well below the clearance limit.

Table 3. 5: Calculation of hole diameter for the grid.

Blockage ratio (BR)	54%	61%	67%
Effective area (A_{eff})	0.46	0.39	0.33
Hole area ($A_{hole} = \frac{A_{eff}}{25}$)	0.0184	0.0156	0.0132
Hole diameter ($D_h = \left[\frac{A_{hole} * 4}{\pi} \right]^{1/2}$)	0.153	0.140	0.129
Hole diameter (D_h) in mm	3.8	3.5	3.2

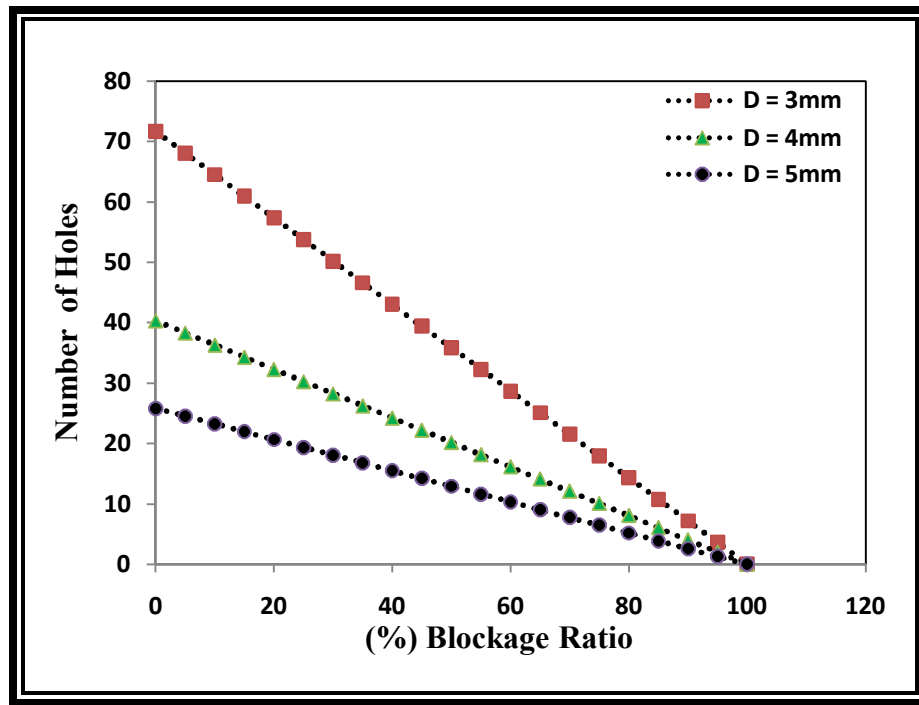


Figure 3. 25: Relation between number of hole with blockage ratio.

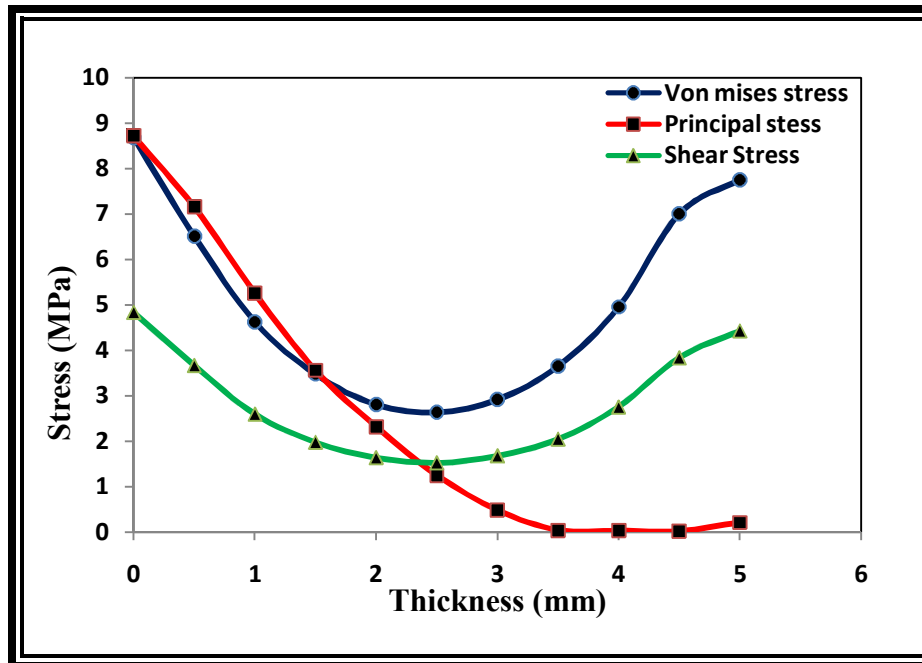


Figure 3. 26: Stress distribution along the thickness of the grid.

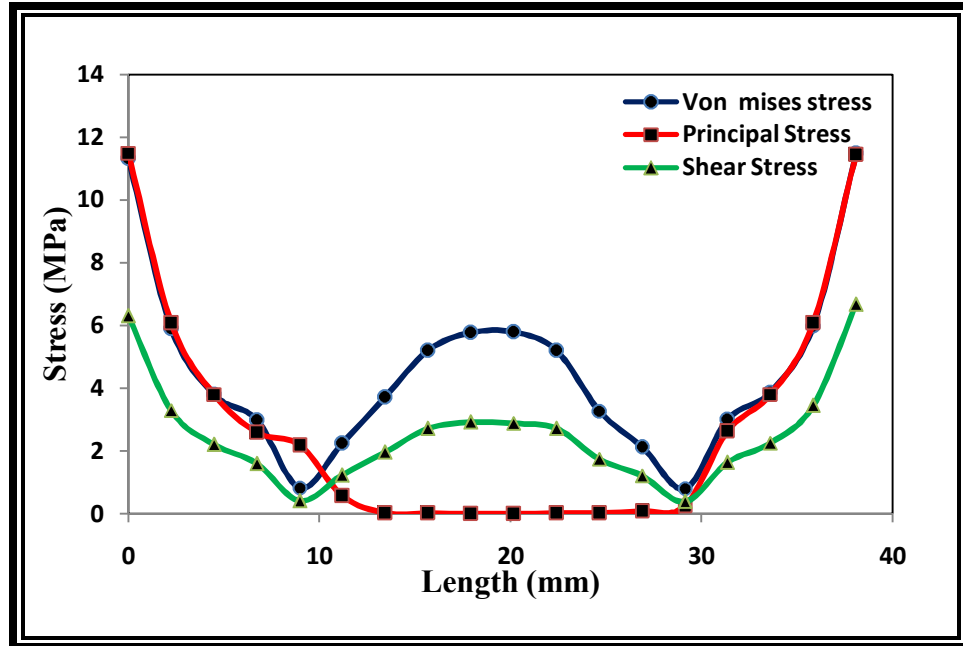


Figure 3. 27: Stress distribution along the length for the grid.

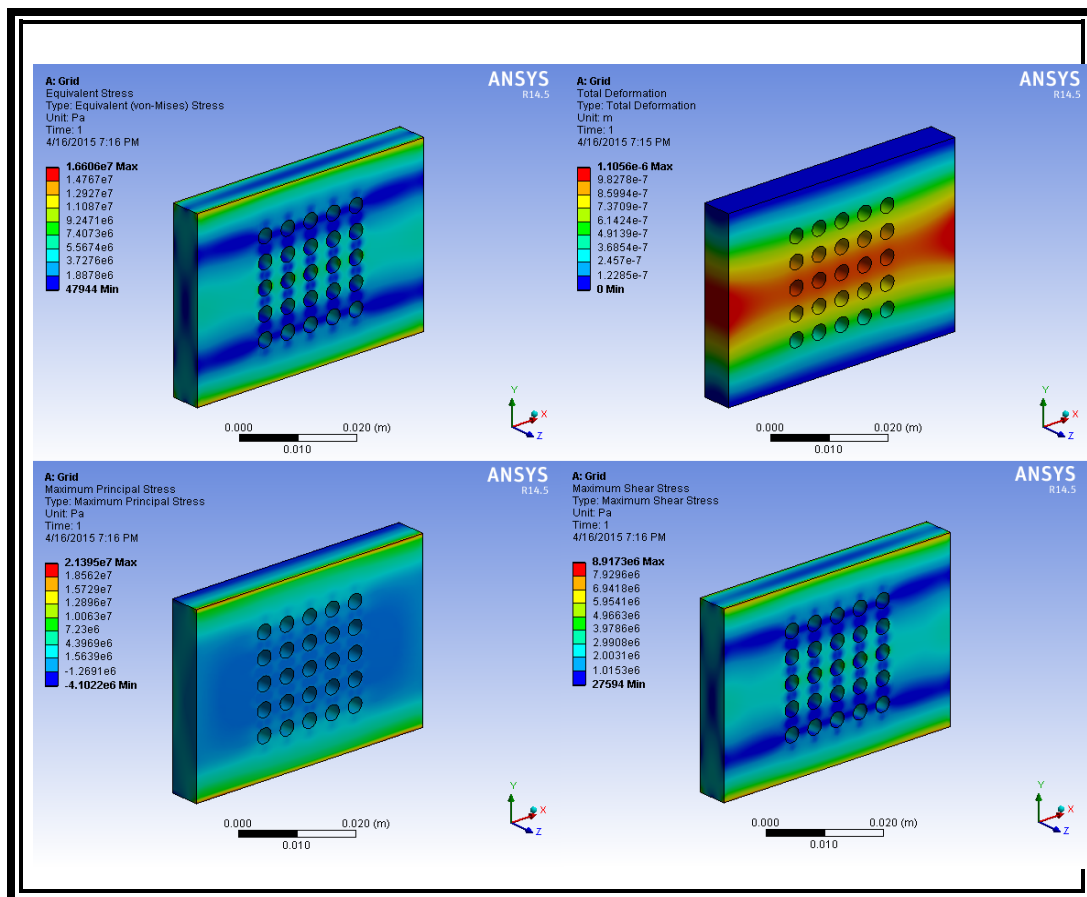


Figure 3. 28: Contour of stress components and deformation for the grid.

3.5 Window Design

The windows are the most critical parts of the combustor. All of the design parameters are dictated by the window. Fused quartz glass has been considered for the window material. Table 3.2 shows the material properties for quartz window. There are three windows in the combustor. The side windows are 6.5x2.5 square inch in cross section and 1 inch thick. The top window is 5.5x1.5 square inch in cross section and 1 inch thick. The top window is designed for laser light transmission and the side windows are designed for the particle image velocimetry (PIV) and laser induced fluorescence (LIF) imaging. The glass window is modified from the conventional design as the combustion chamber has to be perfectly square cavity. Therefore the window is designed as a 'T' shape window which is shown in figure 3.29. Here all the dimensions are shown in inch. The window thickness is considered to be 1 inch. The thickness has been calculated by the formula available in the literature [95]. Figure 3.30 shows the factor of safety and operating pressure at different thickness of quartz window. The chamber is designed for 6 bar (85 psi) pressure and for the minimum thickness (0.25 inch), the factor of safety is around 3.5.

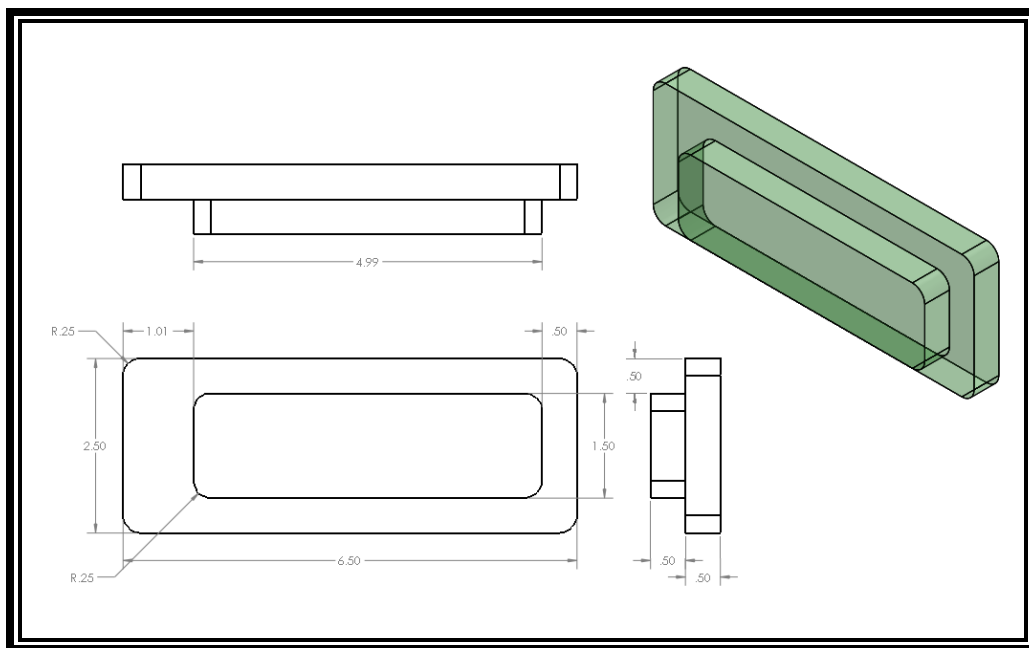


Figure 3. 29: Detail drawing of the side window.

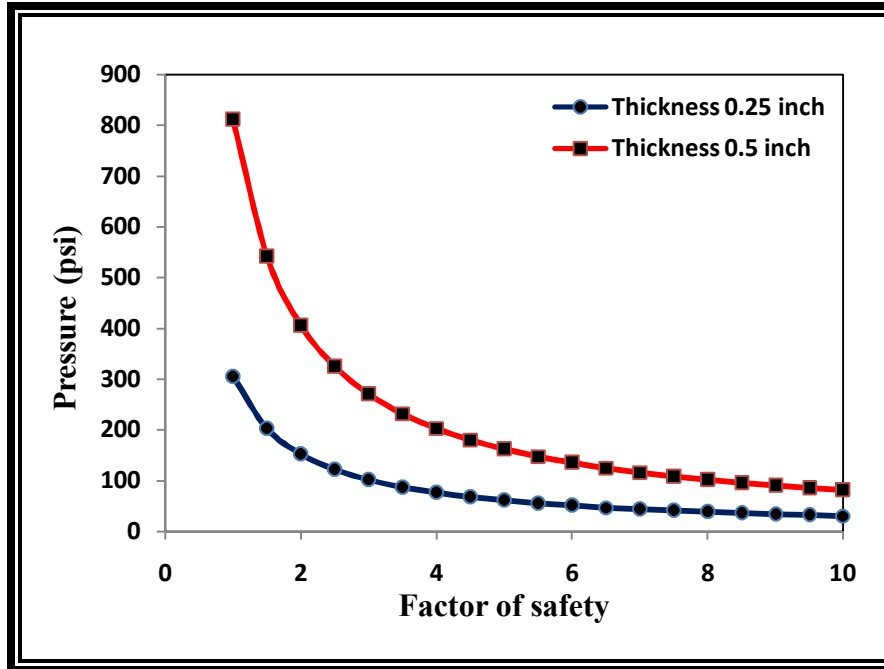


Figure 3. 30: Factor of safety and pressure relation at different window thickness.

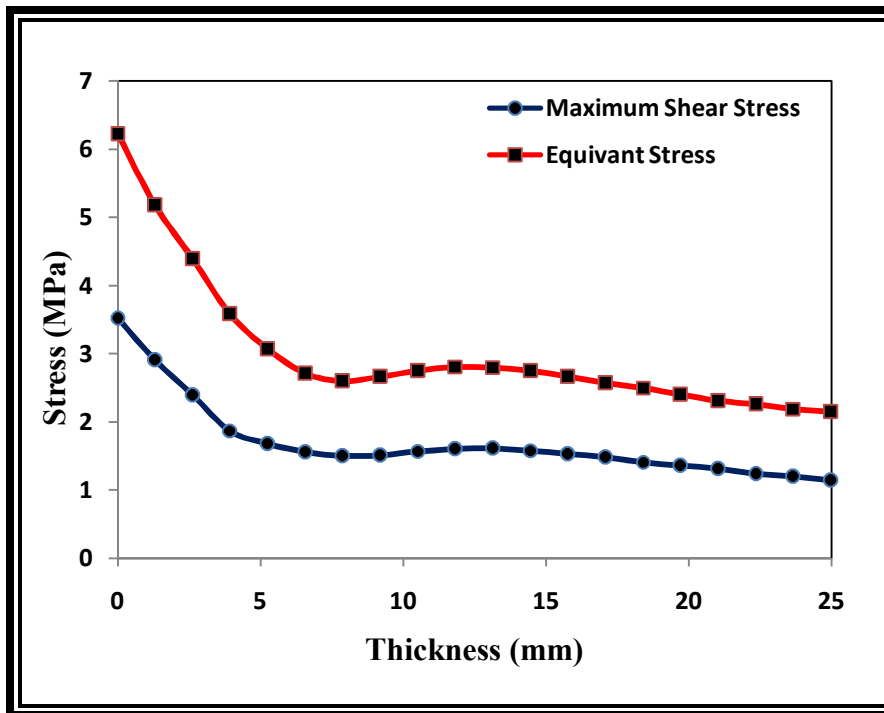


Figure 3. 31: Stress distribution along the thickness of the top window.

Detailed FEA analysis gives the different stress distribution of the window. Figure 3.31 shows the von mises stress and shear stress distribution along the thickness of the top window. The maximum developed von mises stress is around 6.2 MPa. A simplified shear stress calculation has been done for the window with the help of shear force bending moment diagram. Moreover, figure 3.32 represents the contour of von mises stress and deformation for both top and side window. Similar stress analysis has been done for the side window as well. Figure 3.33 shows the different stress distribution along the width of the window. Figure 3.34 also shows the von mises stress and the shear stress distribution along the thickness of the side window.

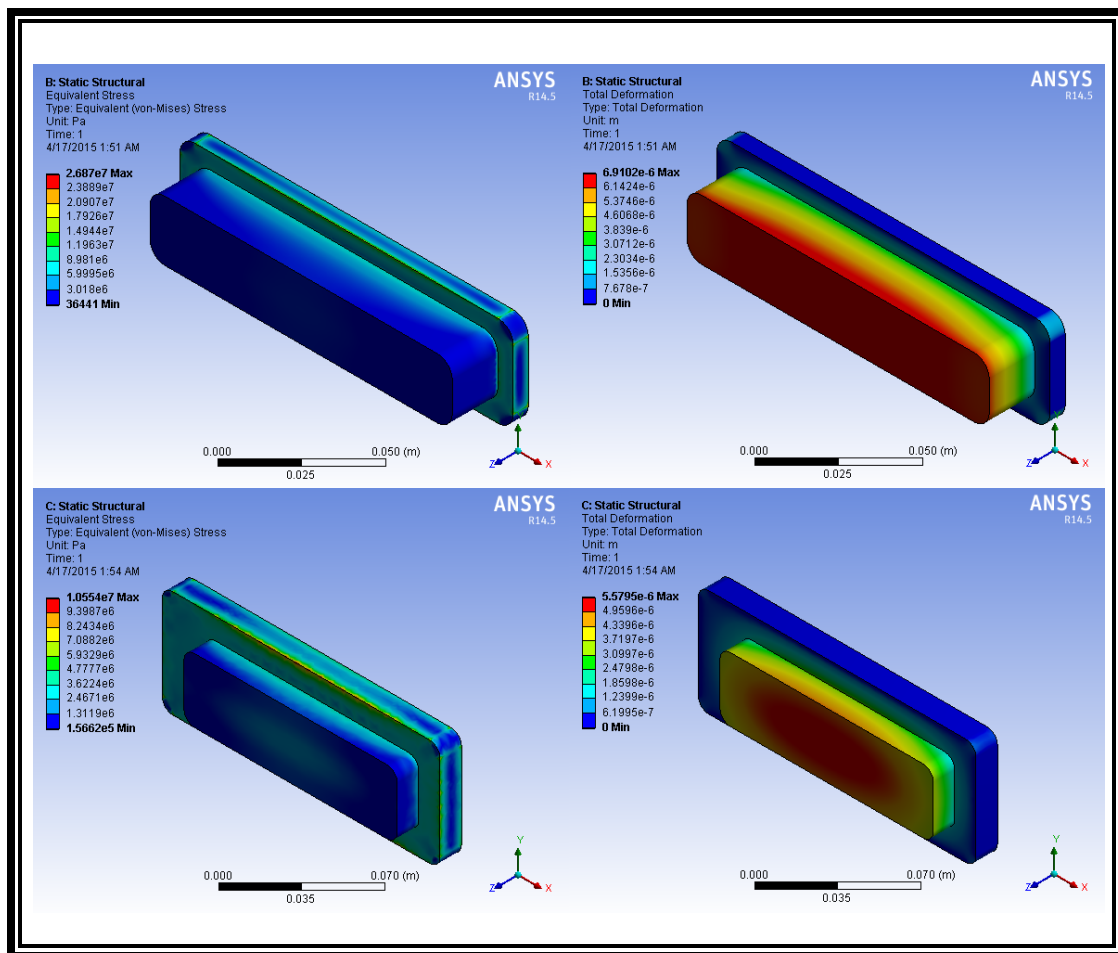


Figure 3. 32: Contour of von mises stress and deformation of top and side window.

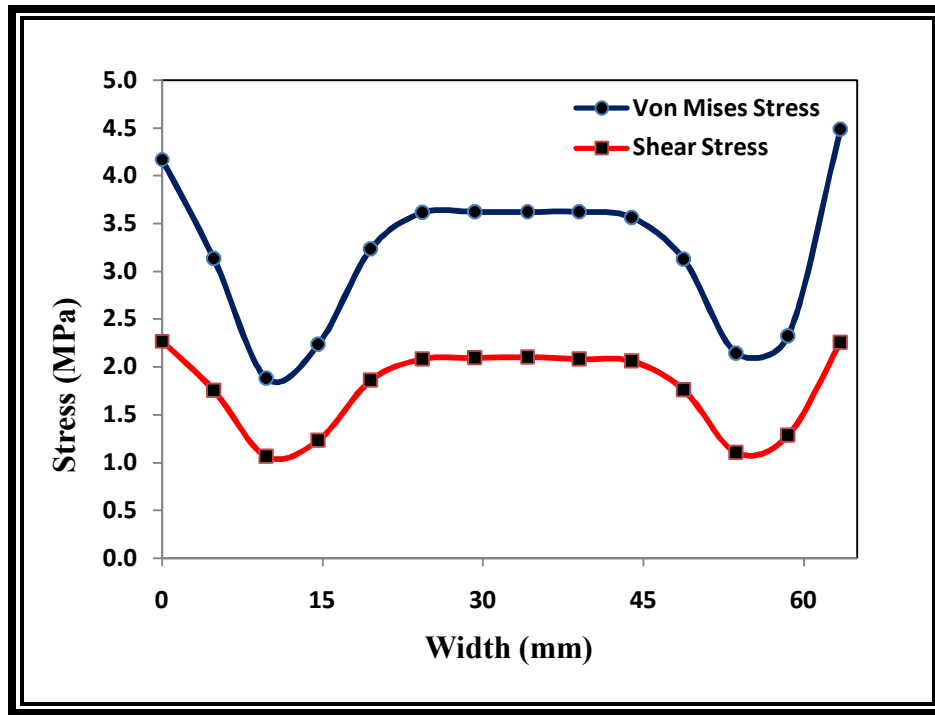


Figure 3. 33: Stress distribution along the thickness of the side window.

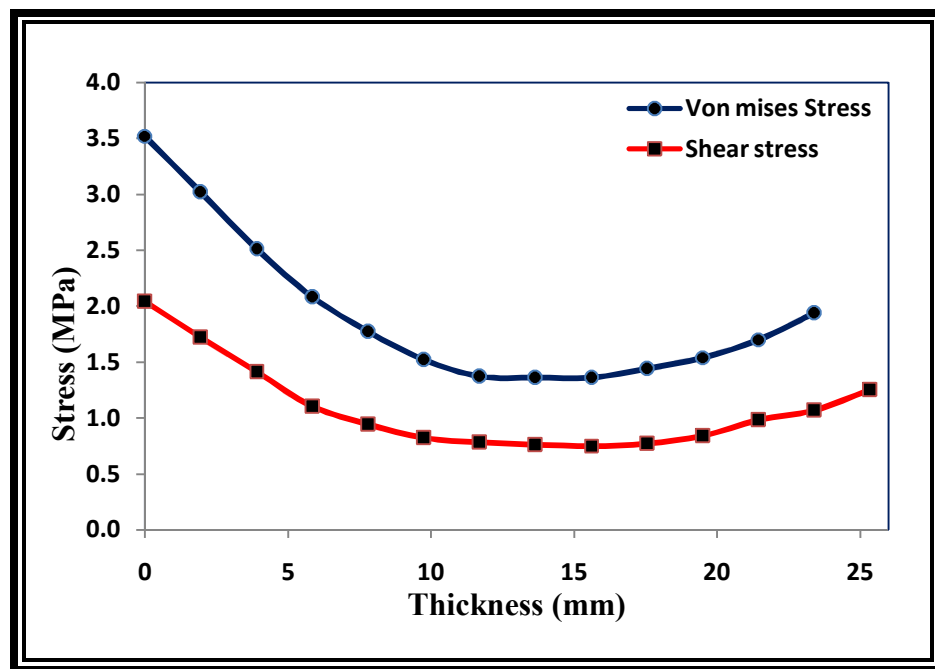


Figure 3. 34: Stress distribution along the thickness of the side window.

3.6 Heating and Exhaust System Design

One of the major criteria of this experiment is to preheat the air before combustion. In order to preheat the air-fuel mixture, an electric inline heater of 100 KW has been selected. The air is expected to heat up to 500K before entering the combustion chamber. The heater specification is shown in table 3.6. Figure 3.35 shows the schematic of the heater. Steady state and transient thermal analysis has been done in order to predict the temperature of the air using this heater. Figure 3.36 shows the temperature distribution along the heater length. Both steady state and transient thermal analysis has been shown in this figure. The transient analysis is done in a range of 300 second. The average temperature of the air coming out from the heater is 519K.

Table 3. 6: Heater specification.

Description	Voltage (volt)	Power (KW)	Phase	Length (inch)	Diameter (inch)
23 W/in ² steel tank 36 alloy-800 elements	480	100	3	84.375	14.875

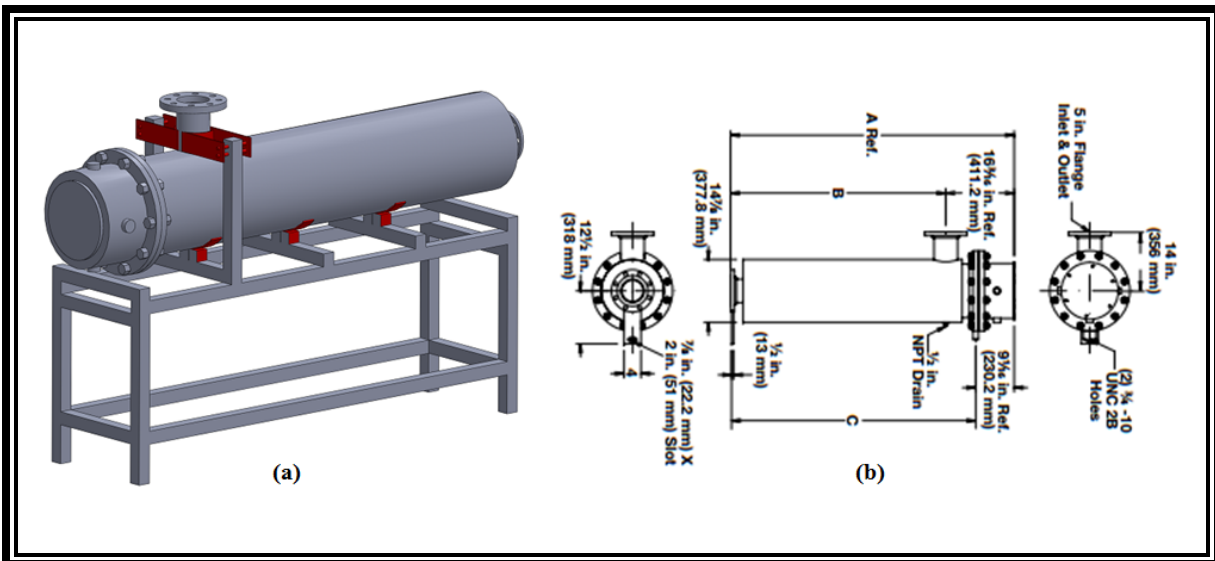


Figure 3. 35: Heater schematic. (a) CAD model, (b) detailed dimensions

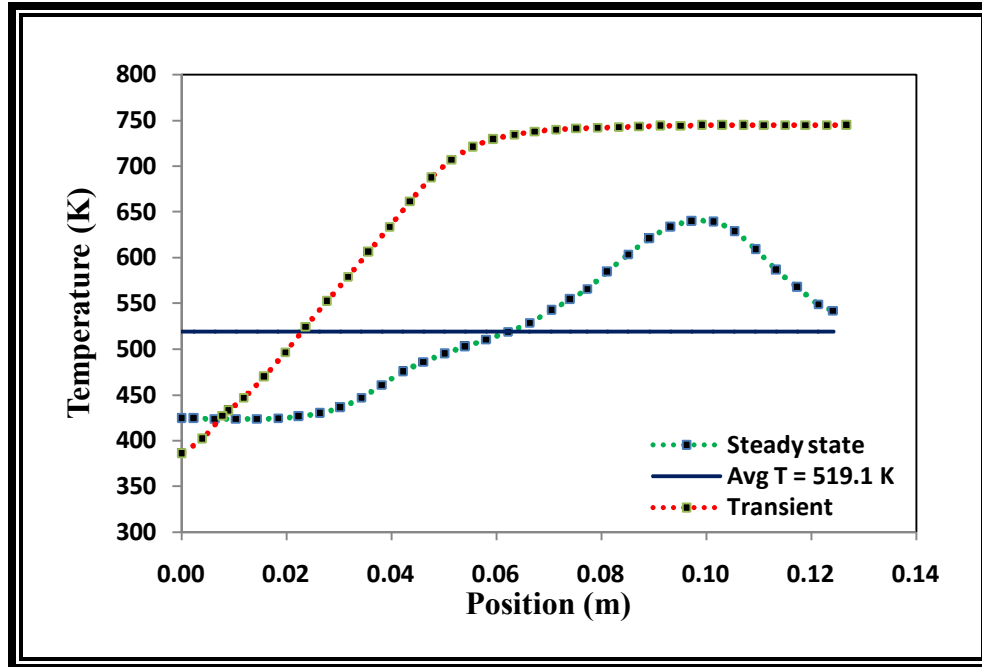


Figure 3. 36: Steady state and transient thermal analysis of the heater.

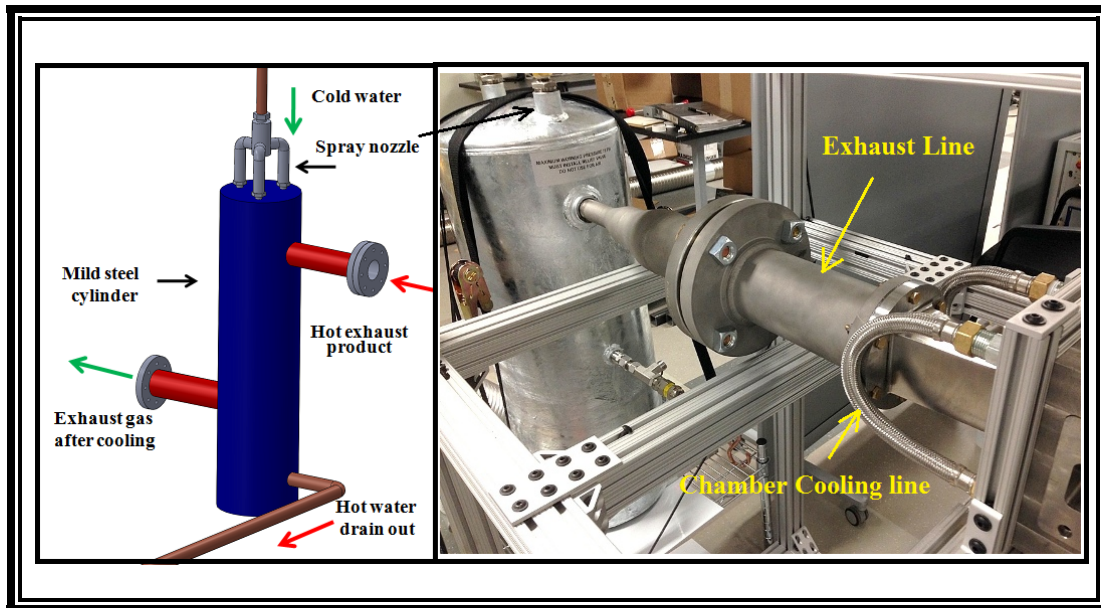


Figure 3. 37: Exhaust gas cooling chamber assembly.

The hot exhaust gas has been cooled by direct spray of water inside a cylindrical chamber. The cooling chamber is designed to cool down the exhaust gas up to 60⁰C. Moreover, orifice plates has been used to drop the exhaust gas pressure. The class 150 ANSI flanges are used for the connection with the combustor exhaust section. Figure 3.37 shows the assembly of

the exhaust gas cooling chamber. Spray nozzles are attached at the top of the chamber for direct spray water cooling. Approximately 13 gpm of water flows through the nozzle. There is a drain pipe in order to drain out excess water.

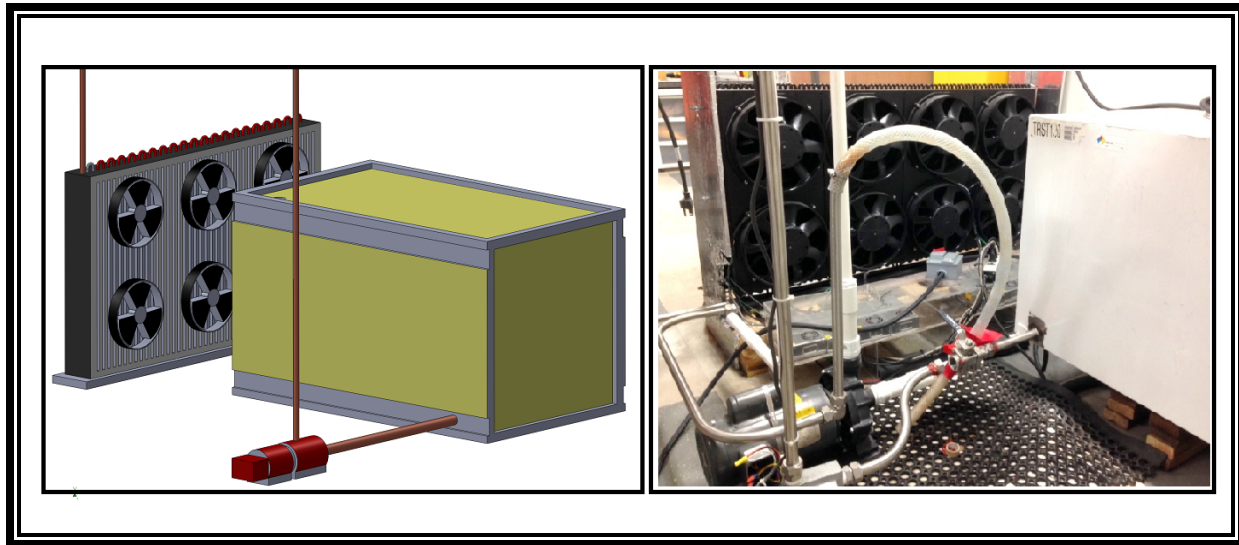


Figure 3. 38: Heat exchanger for combustion chamber cooling.

3.7 Combustion Chamber Cooling

The combustion chamber is cooled by an external heat exchanger. There is a 200kW capacity heat exchanger available in the cSETR lab. The heat exchanger contains 'Dynalene HC-10' coolant. The flow rate of the cooling system can be varied from 3.6 to 10 gpm. Copper tubing is used to carry the coolant from the heat exchanger to the combustor. There are cooling holes inside the combustion chamber. The diameter of those holes are 0.5 inch. Figure 3.38 shows the schematic of the heat exchanger. Transient heat transfer analysis has been done for the combustion chamber. Figure 3.39 represents the temperature of the combustor with respect to time. The result shows that the cooling system prevents the chamber temperature to exceed 100°C for 5 minute of operation. The figure also shows the results at maximum and minimum thickness for the combustor.

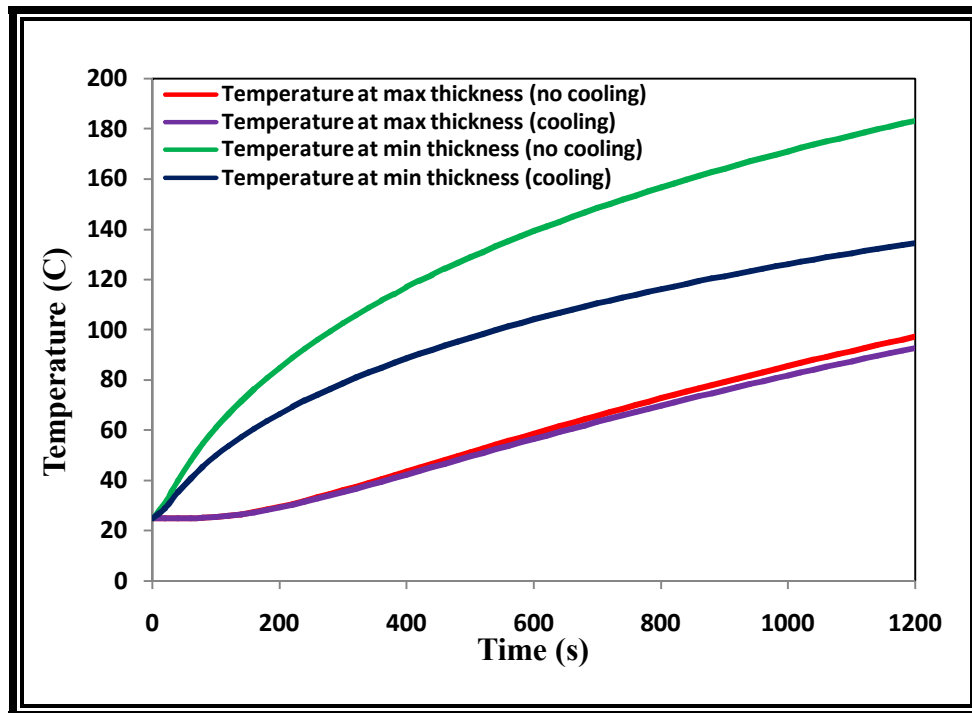


Figure 3. 39: Transient temperature profile at different thickness of the chamber.

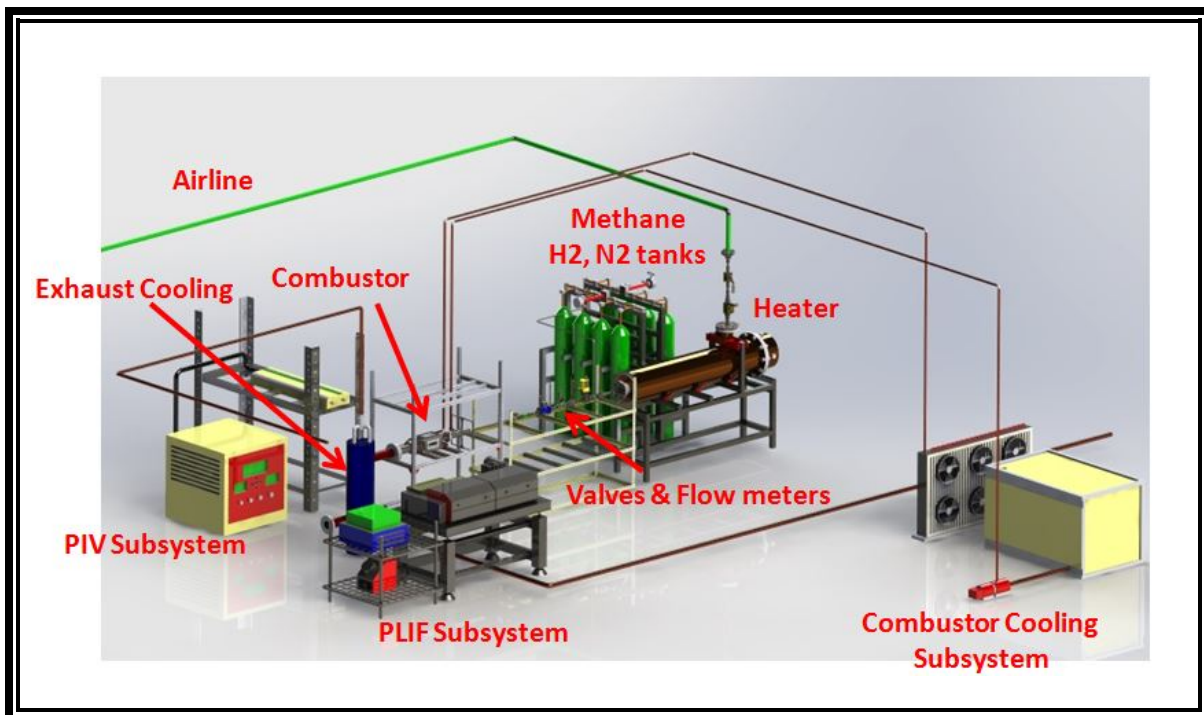


Figure 3. 40: CAD model of the system assembly.

3.8 Test Setup

The whole system consists of numerous subsystem. Each system has its own unique function. The subsystems can be categorized as follow-

- Main air line
- Methane line
- Heater section
- Mixing section
- Main combustion chamber assembly
- Pilot flame assembly
- Main control system
- Exhaust cooling system
- Chamber cooling system
- PIV system
- PLIF system

All the subsystems are assembled and tested prior to the main experiment. Figure 3.40 shows the complete assembly of the system. The CAD model has been developed from the actual dimensions and locations of the different subsystems. The PIV subsystem and the PLIF subsystem are described in the later chapter.

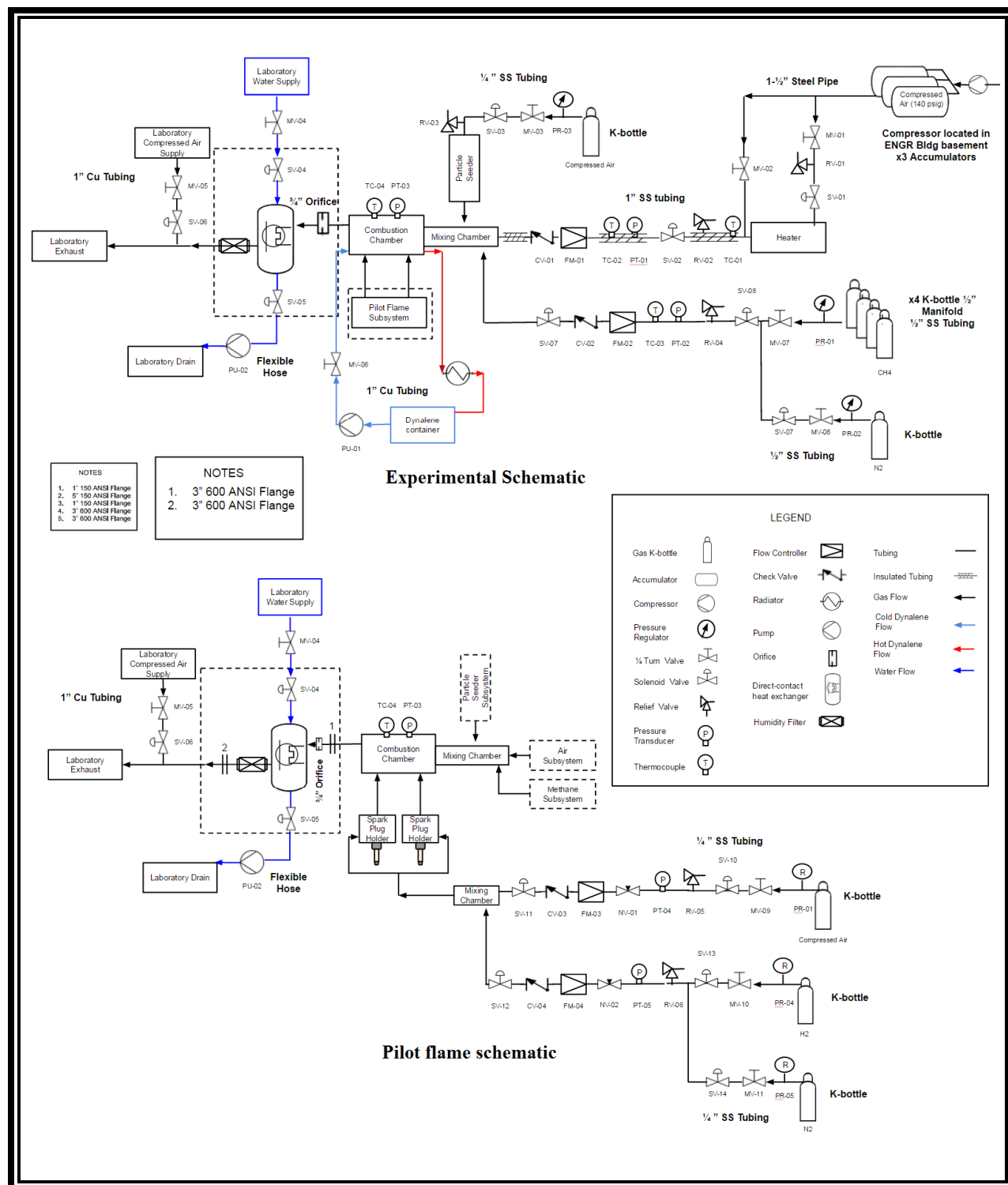


Figure 3. 41: Flow schematic of the main system and the pilot flame.

Figure 3.41 shows the flow schematic of both the main system and the pilot flame. Different flanges are shown here. Each schematic shows different connections of valves, transducers, thermocouples and flow meters. It also refers the location of different subsystems and its connections. Regular k-bottles are used for methane supply. Hydrogen-air mixture is used for the pilot flame. Nitrogen tanks are used for purging of the system before and after the experiment. External compressed air has been used for the PIV seeder line. Moreover external water supply lines have been used in order to cool the exhaust gas. The flow has been controlled by proportional control valves. Moreover some solenoid valves have been used at different location for different purpose. Figure 3.42 shows the assembly of the combustor and the air line with other components. Combustor parts are shown in APPENDIX I.

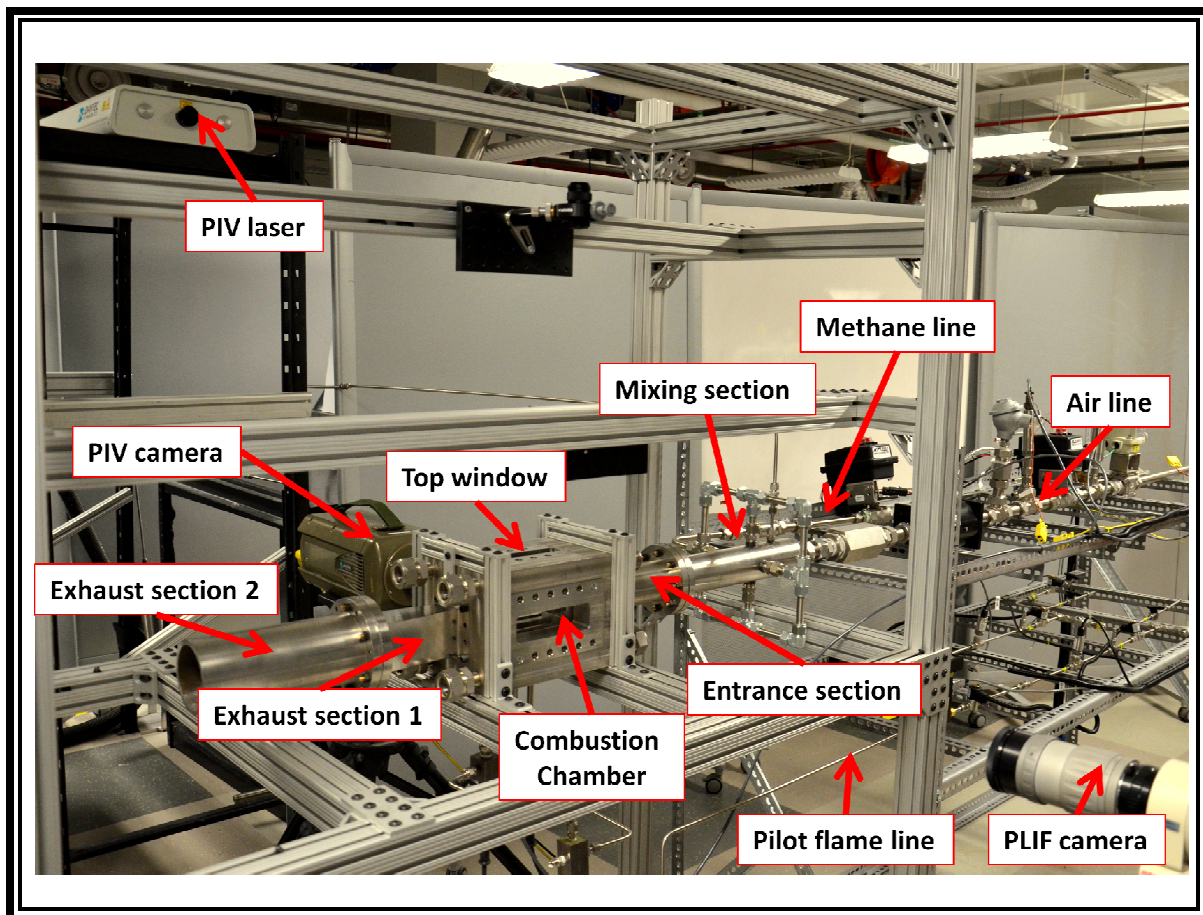


Figure 3. 42: Combustion chamber assembly.

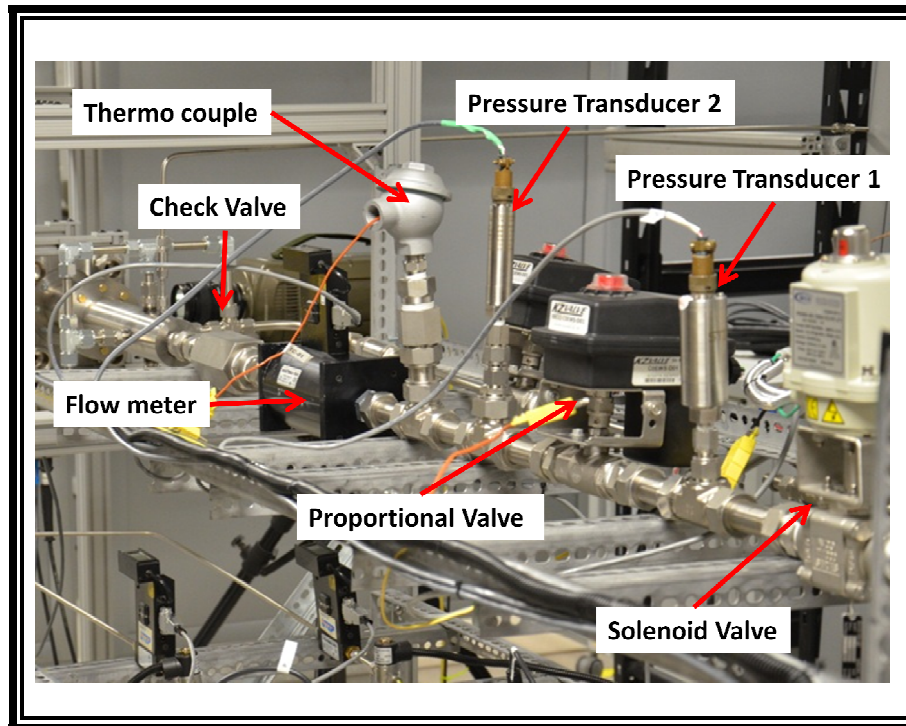


Figure 3. 43: Air line with different instrumentation.

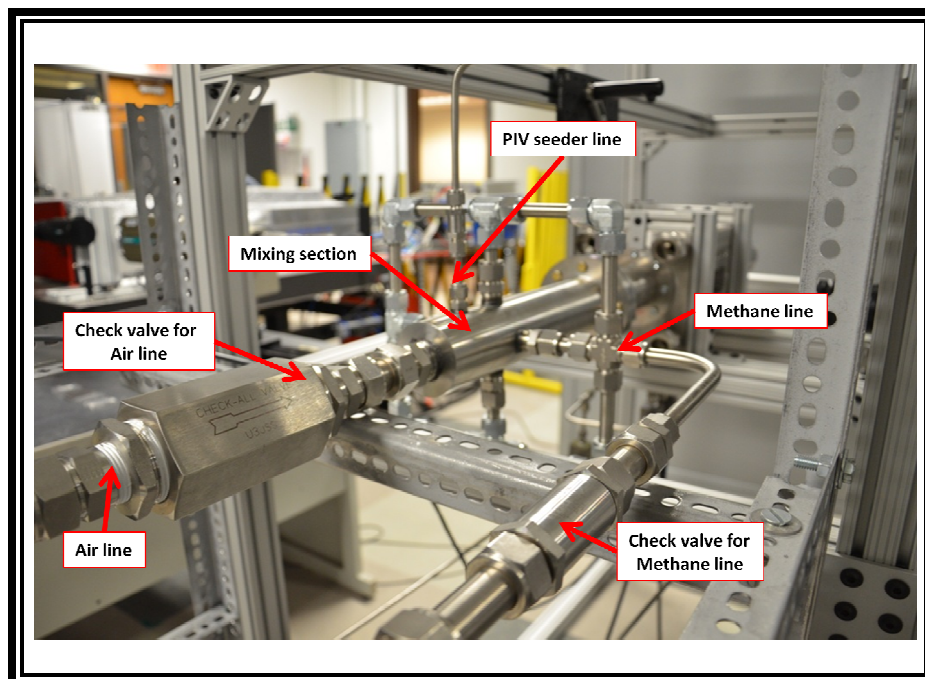


Figure 3. 44: Mixing chamber with air line and methane line.

Figure 3.43 and 3.44 shows the air line and the methane line assembly. They also illustrate the mixing chamber assembly. The airline is connected through a solenoid valve to the main air supply line of the lab facility. This 120V AC valve allows to pass air from the facility to the system. A pressure transducer is installed after the solenoid valve which measures the upstream air pressure of the feed line. The transducer is also used to measure the flow rate of the air. The detail specification of the pressure transducer used in this system are shown in APPENDIX III.

A proportional control valve has been used to control the air flow which is installed after the pressure transducer 1 (figure 3.43). This valve is being controlled by the central control unit with varying the output voltage of the valve. Pressure transducer 2 has been installed just after the proportional control valve. This transducer is used to measure the flow rate of the air along with the pressure transducer 1. A thermocouple is connected in the main airline to measure the inlet air temperature of the system. This thermocouple is installed just after the pressure transducer 2. In order to calibrate the system, a mass flow meter has been used which is installed next to the thermocouple. The capacity of this flow meter is 500 l/min. Finally a check valve has been used before the air enters into the mixing chamber. The methane line consists of similar instrumentations. The methane line is connected with the methane manifold with specially designed regulator. In order to provide large amount of methane supply, this regulator is used. Then a manual control valve along with a solenoid valve is installed in the methane line. In order to purge the methane line, a separate Nitrogen line has been connected with the methane line after the solenoid valve. A pressure relief valve has been attached in the line in order to avoid the high pressure in the fuel line. Pressure transducer and thermocouple is installed to measure the pressure and temperature of the fuel feed line before it enters into the mixing chamber. A mass flow meter has been used (figure 3.41) in order to measure the flow rate of the methane gas. Finally a check valve has been installed in the methane line for safety. More detail instrumentations are described in the next chapter.

Chapter 4: Instrumentation and Measurement

4.1 Particle Image Velocimetry (PIV)

Particle Image Velocimetry (PIV) is non-intrusive experimental technique that gives instantaneous velocity vector field with detail spatial resolution. It also gives instantaneous coherent flow structure, vorticity, strain and divergence of the flow. In general, a PIV system consists of the following three important components-

- Flow tracer or seeding particle
- Illumination source or Laser light sheet
- Imaging system or CCD camera system

These components give a significant experimental flexibility and allow the PIV system to use at a wide range of flow configurations. Significant development has been done in the technique by Lourenco[96], Adrian[97] and Grant[98]. To provide a velocity field, PIV uses particle displacement over a specified small finite separation time, Δt . Correlation analysis is used to extract the particle displacement, Δx and first-order velocity estimate-

$$u = \frac{\Delta x}{\Delta t} \quad (4.1)$$

where Δx is the average displacement of the particle in the fluid over the time interval $\Delta t = t_2 - t_1$ [97]. The t_1 and t_2 can be recorded in to same frame or in a separate frames. The success of the PIV imaging depends on the accurate coupling between the fluid and the particles. The number of particles per unit volume should be sufficiently low in order to preserve the original flow characteristics [99-100]. Such dilute condition is expressed in inequality 4.2 where d_p and ρ_p are the particle diameter and density, respectively and μ , v_r , δ_p are the fluid viscosity, average particle velocity and average distance between particles respectively.

$$\frac{\rho_p \pi d_p^4 v_r}{18 \pi \delta_p^3} < 1 \quad (4.2)$$

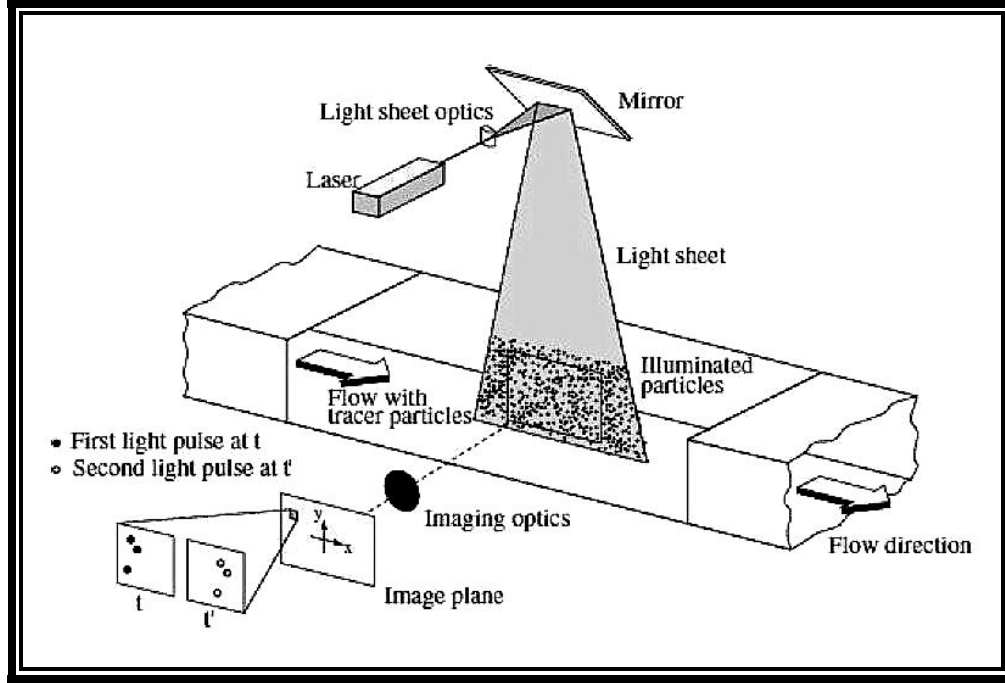


Figure 4. 1: Schematic of experimental arrangement for PIV [101].

Figure 4.1 shows a simplified PIV experimental arrangement. It is very important to select the accurate particle size for a specific experimental setup. The size can be determined by the help of Stokes number, St_{PIV} which is defined as τ_s/τ_{PIV} where τ_s is the particle relaxation time and τ_{PIV} is the small finite separation time between two observation or pulse separation time. In order to achieve negligible particle-fluid velocity difference over the pulse separation, St_{PIV} must be less than 1. Equation 4.3 represents the particle relaxation time. Moreover the relative velocity error due to Brownian motion is shown in equation 4.4 where D is the diffusion coefficient, k is the Boltzman's constant, T is the absolute fluid temperature and u is the mean velocity of fluid [102]. In this experiment the velocity magnitude and particle size are in the order to 20 m/s and $1\mu\text{m}$ respectively.

$$\tau_s = d_p^2 \frac{\rho_p}{18\mu} \quad (4.3)$$

$$\varepsilon_B = \frac{1}{u} \sqrt{\left[\frac{2D}{\Delta t} \right]}, \text{ where } D = \frac{kT}{3\pi\mu d_p} \quad (4.4)$$

In order to explain the PIV technique, it is sometime very confusing to understand some common terminology. Some of the common terms are described in the later paragraph which will be used frequently throughout this article. The '*light plane*' is the volume of the fluid illuminated by the light sheet. The '*image plane*' is the image from the light plane taken on the charged coupled diode (CCD) sensor. It is very important to note that the light plane is a 3D space or volume while the image plane is a 2D space or surface. Figure 4.2 shows the difference between a light plane and an image plane. On the other hand, the sub volume selected from the light plane is the '*interrogation volume*' and the corresponding location of this interrogation volume in the image plane is known as the '*interrogation area*'.

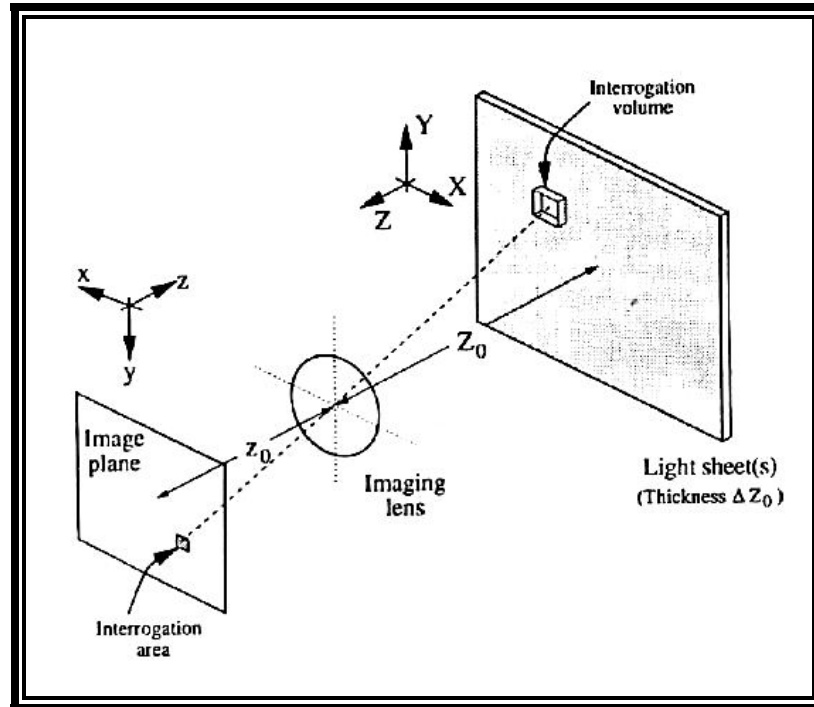


Figure 4. 2: Schematic representation of light plane and image plane.

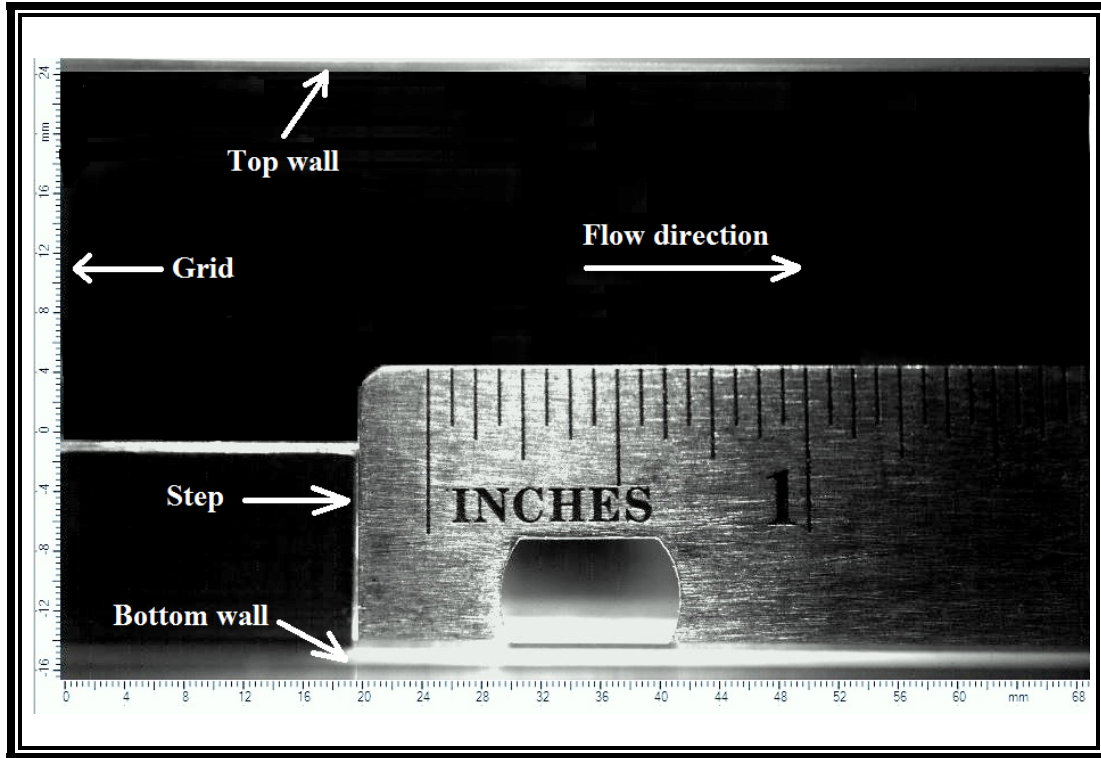


Figure 4. 3: Experimental image plane and location of step, walls and grid.

In this experiment, the light plane is generated by a '*15-1000 Dual power*' 527nm Neodymium-doped Yttrium Lithium Fluoride (Nd-YLF) laser with a pulse energy of 15mJ/pulse. The maximum power output of this laser is 100W and the pulse duration is 150ns/CW which is shown in figure 4.4. This laser generated a 75mm wide 0.1mm thick light sheet which is guided by a 45⁰ angle of attack (AOA) line mirror and a telescope lens. The image plane is captured by a '*Speed sense 9070*' CCD camera with a frame rate of 3.1 kHz. The image plane is 72mm x 40mm in dimension or 1280 x 800 pixel. Figure 4.3 shows the typical image plane taken just before the actual experiment. This image is also used for image calibration for PIV post processing. The laser system was supplied by 'Dantec Dynamics Inc'. Figure 4.4 shows the actual laser system along with the chiller and the seeder system. The figure also shows the beam diagram for the PIV measurement. A 45⁰ degree mirror is used to deflect the laser beam and guide it from the top window of the combustor. A telescope lens is used to make the beam into light sheet. The spreading angle of the lens is 10 degree.

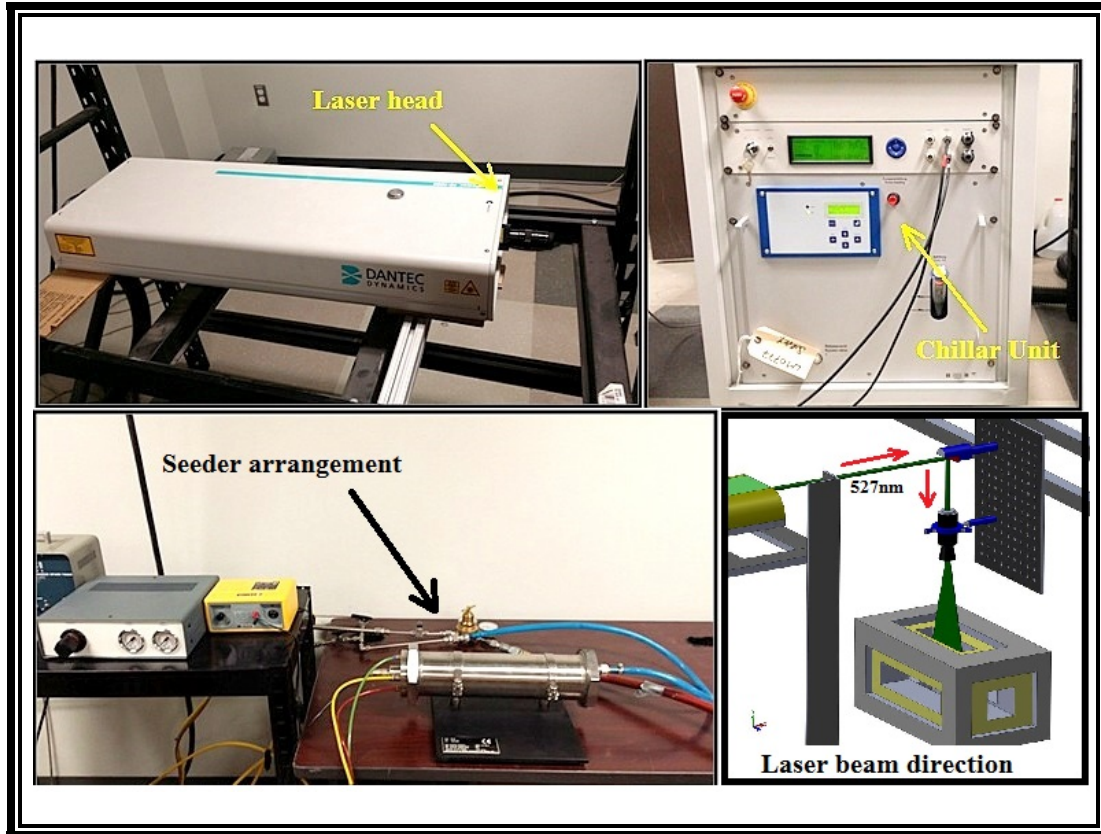


Figure 4. 4: Nd-YLF laser unit, seeder assembly and laser beam direction.

The laser system has a 115V three phase power requirement with 15 amp current supply. The seeder line has been introduced at the mixing chamber before the particle enters inside the combustor. The seeder bomb has been pressurized by an external air supply. The particle flow has been controlled by varying the pressure of the seeder regulator. The seeder line is controlled by a solenoid valve at the upstream of the line. The seeder line is a 0.25 inch steel tube. The total air flows through this line is significantly low that it can be assumed that this air does not change the total amount of air flow at the combustor. Figure 4.5 shows the flow schematic of the PIV subsystem. The electric connection of the PIV system is also shown in figure 4.6. The BNC cables are connected with the camera and the laser controller via a timer box. The BNC cable carries the trigger signals for the laser which is controlled by the BNC 575-8 time box. The timer box controls the laser pulse and the camera frame rate and synchronizes them according to the '*dynamic studio*' software commend.

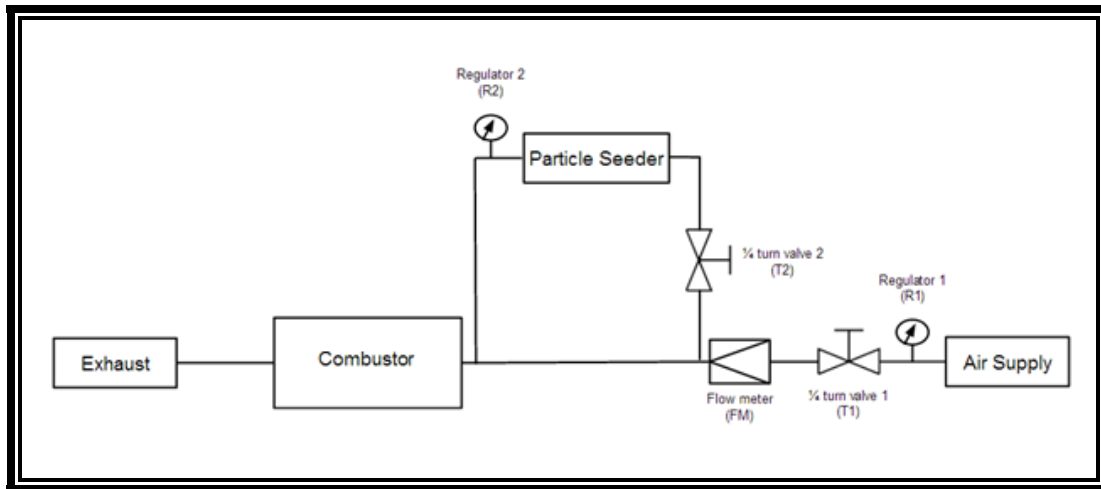


Figure 4. 5: Flow schematic of the PIV subsystem.

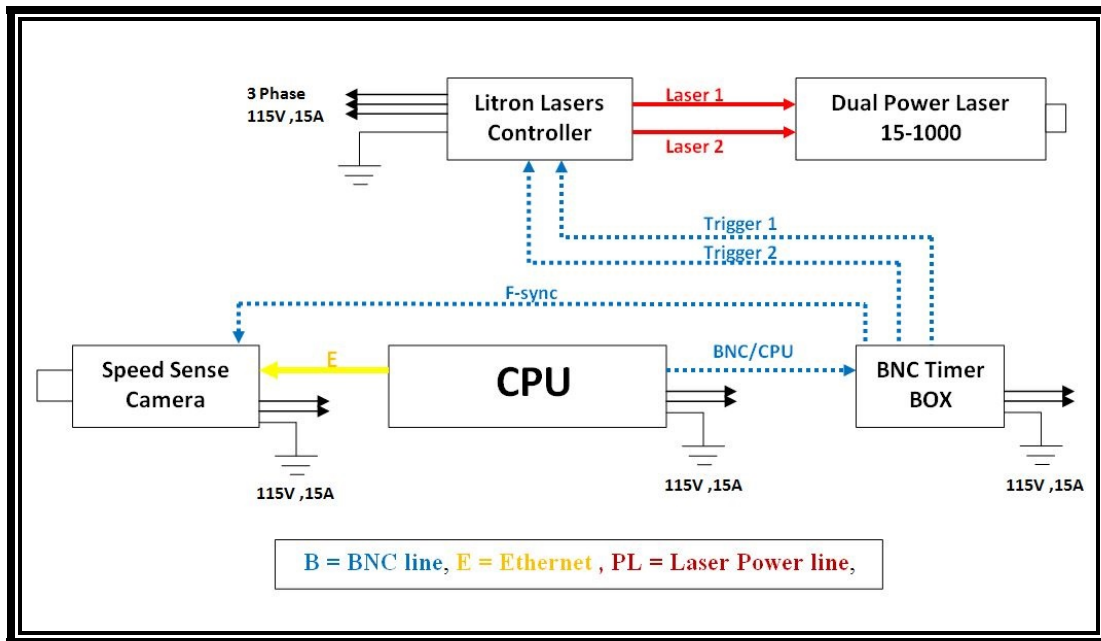


Figure 4. 6: Electric connection of the PIV system with the CPU, camera and BNC timer box.

4.2 Planer Laser Induced Fluorescence (PLIF)

Spectroscopy is widely used in combustion diagnostics which can measure the interaction between matter and light. The strength of spectroscopy can be measured as a function of wave length and optical frequency. Laser spectroscopy is very promising because of the following reasons-

- Good temporal and spatial resolution.
- Narrow line width
- Wave length tunability
- Wide range of optical power
- Ultra short pulse generation

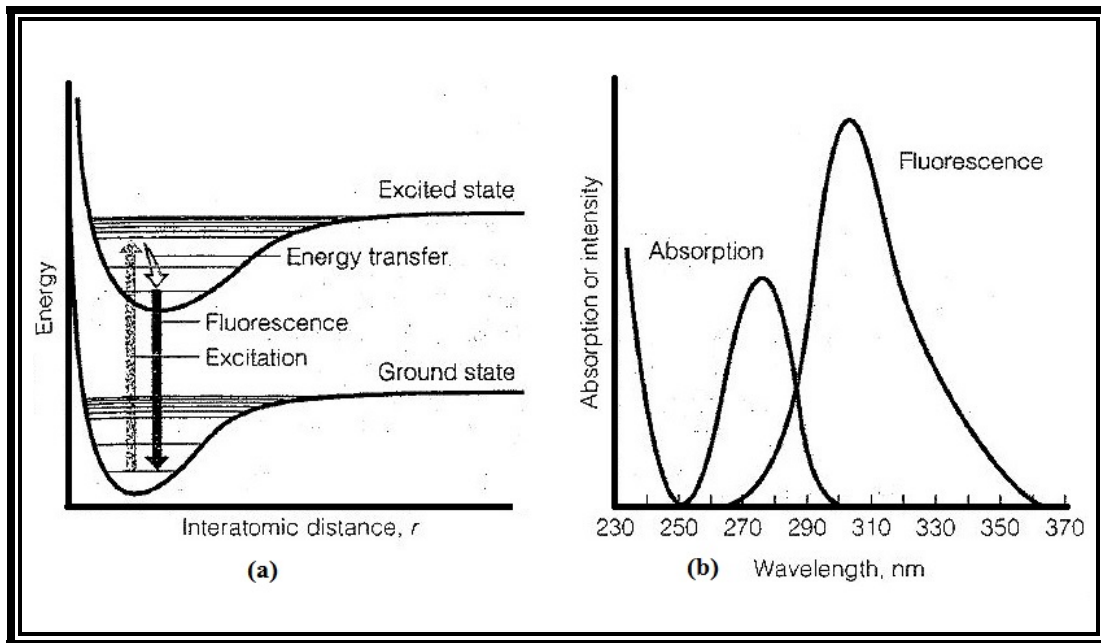


Figure 4. 7: (a) Demonstration of the fluorescence technique. (b) Energy distribution.

There are different types of lasers for different spectroscopy application. High energy fixed wave length solid state lasers are used for Raman Spectroscopy. On the other hand, Dye Lasers can be used for its accessibility of broad range of wavelength, particularly in the visible spectral range, but also in the near ultraviolet and near infrared region. Fluorescence denotes the

radiation emitted by an atom or a molecule when it relaxes by spontaneous emission of photon from a higher to lower energy level. Similarly, Laser Induced Fluorescence (LIF) is a spectroscopy technique where the upper energy level is populated using laser excitation with a wavelength tuned to a resonance between excited state and a discrete lower state. Figure 4.7 demonstrates the simplified fluorescence technique. This non-intrusive optical technique resolves important information about the structure of the flow and the combustion process for the next generation combustor design. Moreover, a detailed study of large and small scale structures within the image plane is possible in both reacting and non-reacting flow as well as fundamental studies for the validation of turbulent modeling. PLIF is useful due to its sensitivity to species composition, temperature, number density and velocity. After its introduction in early 80's [103-104], PLIF has been providing instantaneous information over the whole flow field. This technique has successfully demonstrated the quantitative time-averaged imaging of concentration, temperature, pressure and velocity [105].

In order to perform quantitative measurements on a given species, it is a requirement to know the absorption and emission spectrum of that specific molecule. Then the rate of radiative decay of the excited state which directly influences the fluorescence signal must be known. Finally, all the excited state losses, specially from collisions, photo-ionization and pre-dissociation must be taken into account. In a typical single line PLIF measurement technique, the UV laser beam is tuned to excite a molecular transition. A system of cylindrical and spherical lenses is used to focus the laser beam into thin sheet. The fluorescence signal from the light sheet is collected by an imaging lens at the right angle, and imaged on a gated intensified CCD camera. A spectral band pass filter is placed in front of the intensifier lens to reject the scattered light such as chemiluminescence emission. The spatial resolution depends on the following parameters.

- Pixel size of detector array.
- Image magnification factor.
- Size of the beam.

- Depth of field.
- Energy of the beam.

A trigger system is needed to drive the pulsed laser and synchronous amplification of the CCD camera over a suitable gate duration. The LIF signal is used to trace the flame front in combustion research. As the flame front release the maximum amount of energy, it is important to indentify tracer radical at the flame from. OH, CH, CH₂O, CHO are such radicals that helps to identify the flame front during LIF measurement. The OH radical is widely used for the flame front tracer as it gives significant amount of fluorescence signal. The OH PLIF imaging is performed by a high energy, pumped laser to pump a dye laser to generate 532nm visible radiation that may be subsequently converted to the desired 283nm UV output via frequency-doubling. Table 4.1 shows detection wavelength of a list of species used for PLIF.

Table 4. 1: Detection wavelength of different species.

Molecule	Absolute wavelength (nm)
OH	306
C ₂	516
CH	431
CN	388
NH	336
NO	226
CH ₂ O	320-360
NO ₂	450-470

Although OH radical has diffusion prosperity which actually implies the post flame zone during LIF measurement due to its long lifetime. OH concentrations are large in the lean regions of the flame front where the chemical reactions involved in the combustion process are complete. In a premixed flame OH produced in the flame front is slowly consumed in burnt gas. After numerous experimentations, researcher concluded that, OH is not a reliable indicator of the heat release and flame front location [106]. But it leaves a trace of the flame front in the flow field. In

order to identify the actual location of the flame front, CH radical is used as CH is produced during the initial reaction of hydrocarbons [107-110]. CH PLIF imaging is performed by a high energy, pumped laser to pump a dye laser to generate 390nm visible radiation that may be subsequently converted to the desired UV output via frequency-doubling or sum frequency mixing. Figure 4.8 shows a typical PLIF imaging of turbulent flame.

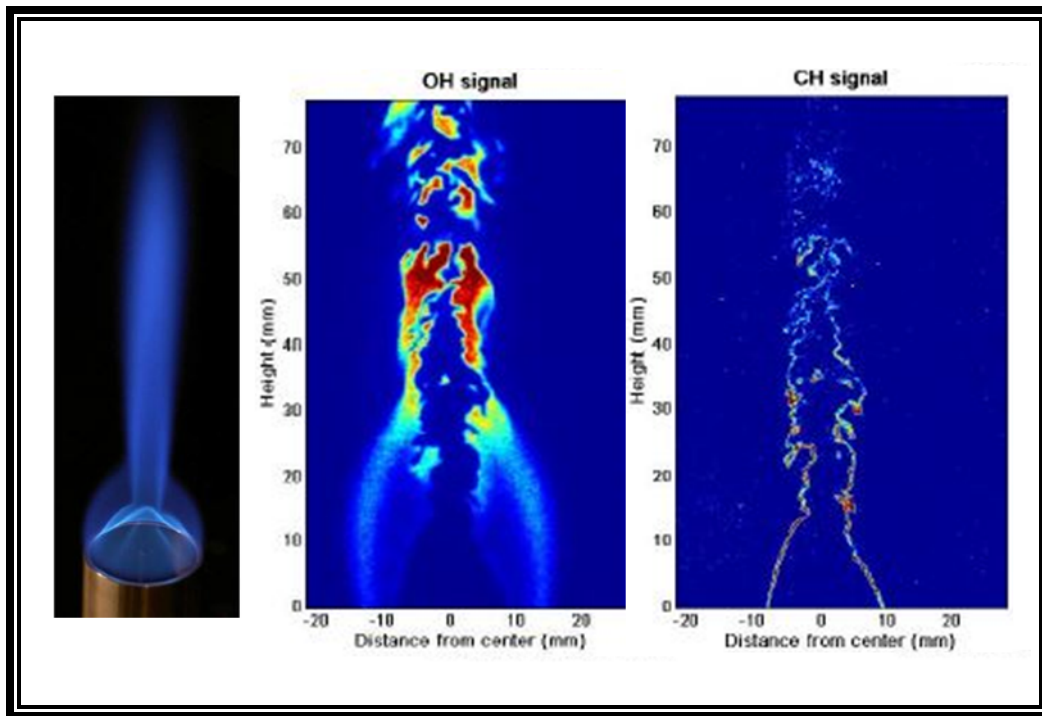


Figure 4. 8: Typical OH and CH PLIF signal of a turbulent jet flame [111].

In this experiment, the OH-PLIF system consists of a frequency doubled dye laser (*Radiant Dyes NarrowScan HighRep Dye Laser*) pumped by a Q-switched DPSS laser (Nd-YAG *Edgewave IS series*) and an intensified high frame rate CCD camera (*'Speed sense 9070'* with *Hamamatsu C10880-01C*). The dye laser used Rhodamine-6G in ethanol and produce approximately 0.30 mJ/pluse at 3 kHz. Figure 4.9 shows the laser system assembly. The laser is tuned to 283.28nm to excite the isolated Q1 line of the A-X (1-0) transition of OH. The beam diagram for the dye laser are shown in figure 4.10.

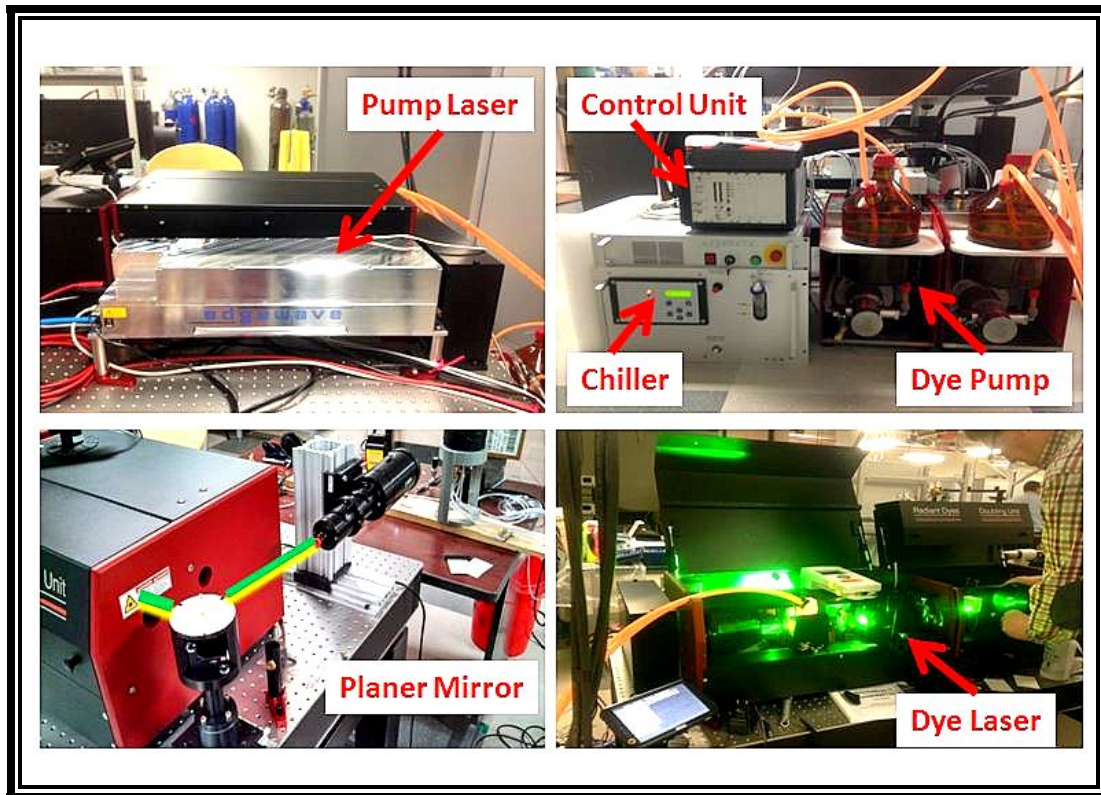


Figure 4. 9: PLIF assembly along with the pump laser and the dye laser.

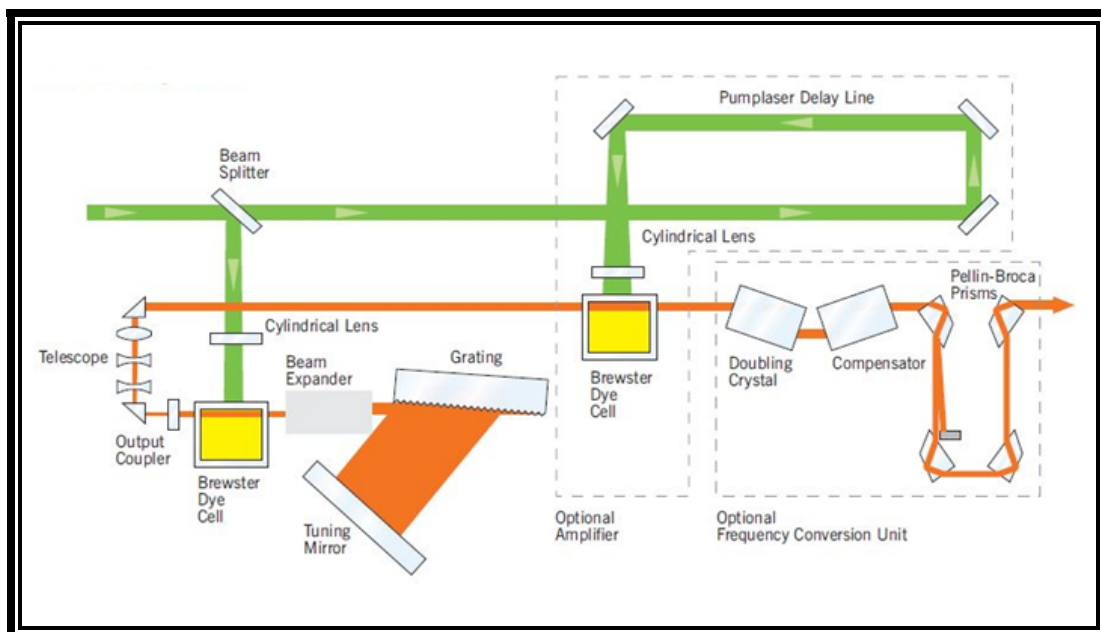


Figure 4. 10: Beam diagram of the Dye laser.

The electric line diagram for the PLIF system are shown in figure 4.11. These line diagram also shows the water line for the chiller, the BNC line for the times box and the Ethernet connection for the camera and the computer. The laser pulses were formed into an approximately 50mm tall sheet using a cylindrical telescope lens. The UV laser sheet has been overlapped with that of the PIV system using a 25 mm dichroic mirror as shown in figure 4.12. Fluorescence signals were collected at 310nm bandpass intensifier filter. Background flame luminosity was minimized by a short 1 μ s intensifier gate. 750 PIV images were acquired per run at 1280 x 800 pixel image size corresponding to a field of view of 72 x 40 mm. On the other hand, the PLIF images were acquired per run at 1280 x 800 pixel image size corresponding to a field of view of 50 x 25 mm.

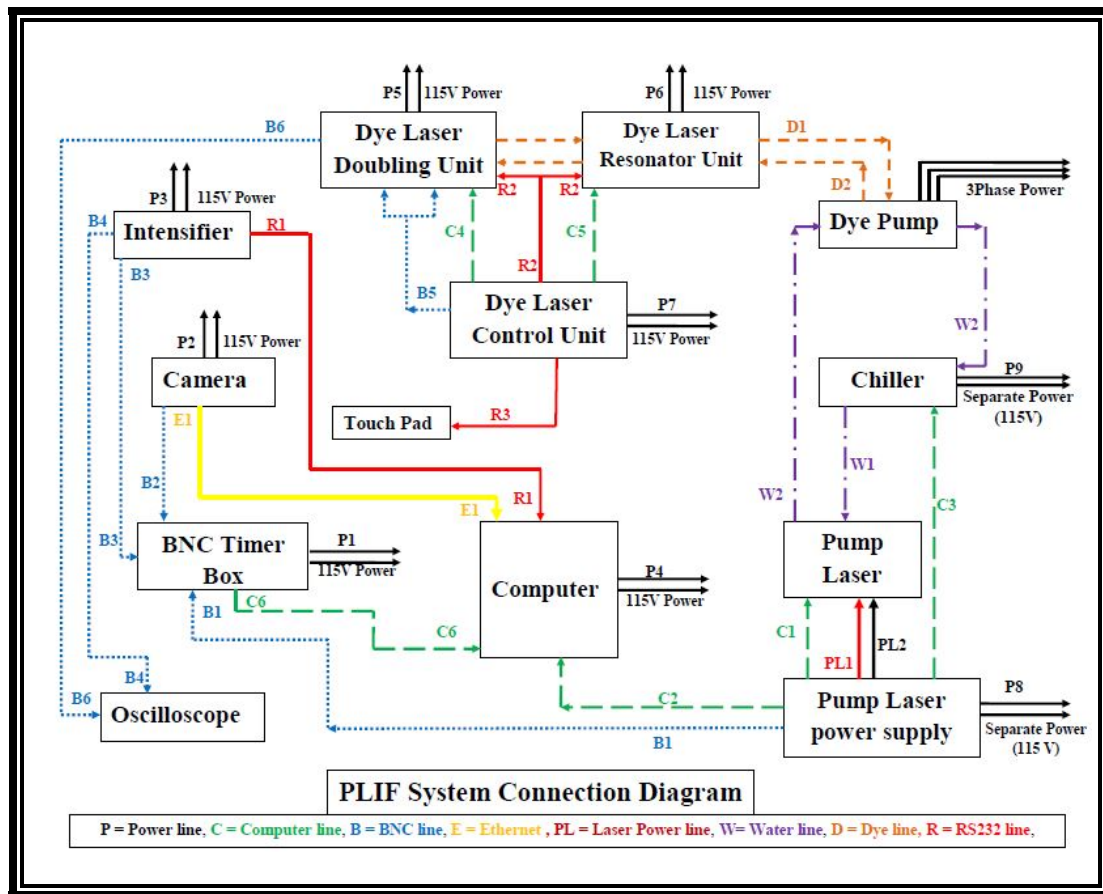


Figure 4. 11: The electric line diagram for the PLIF system.

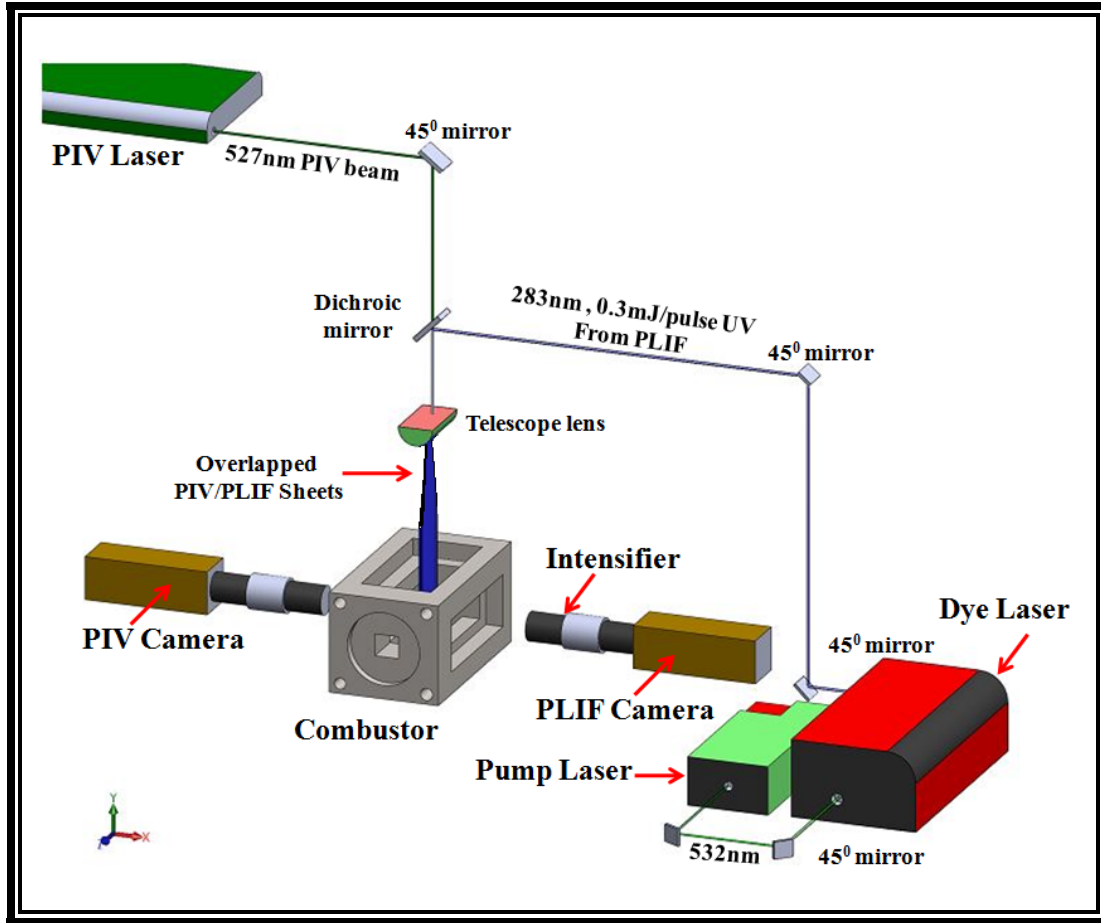


Figure 4. 12: Assembly of simultaneous PIV-PLIF measurement.

4.3 Flow rate Measurement

The flow of main air line is controlled by different types of valves. There is a manual control valve that allows air to enter the main air line from the laboratory compressed air facility line. Then the air passes through a 120 V (*AVCO E03/05 8P14*) solenoid valve. The valve has a maximum torque 35 Nm at 0.5 amp. The valve takes 12 second to open fully for the maximum flow. Figure 4.13 shows the location of the valves in the main air line. After that the flow passes through a DC (*EZ 88E22-C0EWS-D01*) proportional control valve. When air passes through that proportional control valve, it enters into a 1000L/min mass flow meter (*FMA1700A/1800A Series*) . The main airline has space for the installation of chock venture flow meter.

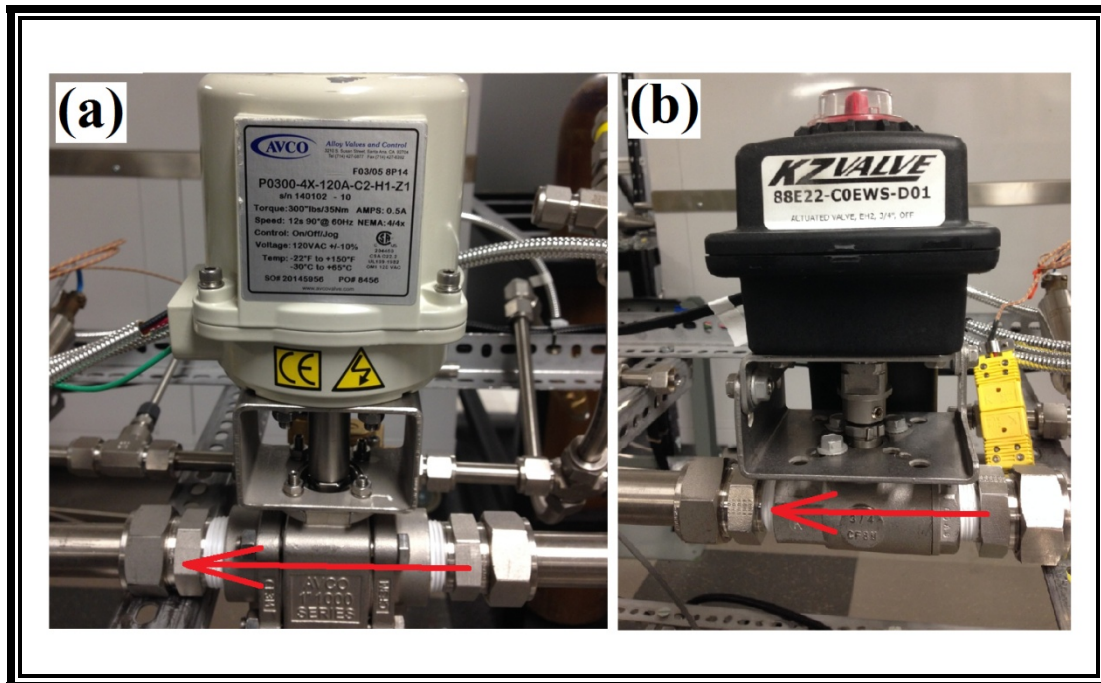


Figure 4. 13: (a) 120V solenoid valve. (b) DC proportional control valve.

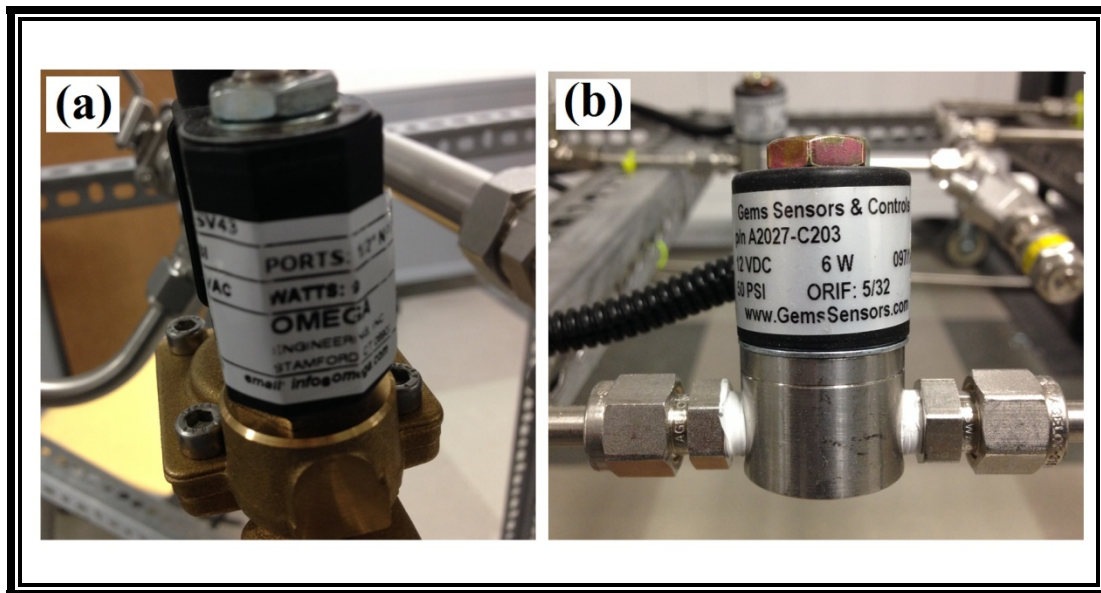


Figure 4. 14: (a) 12V DC valve for methane line. (b) 12V DC valve for pilot flame.

The DC solenoid valves are also used in the pilot flame lines, the nitrogen line and the airline for the PIV seeder sub system, the exhaust water discharge line and the airline for the exhaust cooling section. Figure 4.14(a) shows the valve (*Omega F-SV43*) used for the nitrogen line, PIV seeder and the exhaust cooling line. Figure 4.14(b) shows the valve (*PLN A2017-C203*)

used in the pilot flame line. All the valves and transducers are controlled by LabVIEW program which is synchronized by three *CCA-PCI-652* high voltage relay board.

4.4 Temperature and Pressure Measurement

The temperature are measured at some specific location throughout the whole system. Figure 3.41 shows the locations of the thermocouple in the feed line. All the temperature are measured by K-type thermocouple which is mounted in the combustor and the main airline. The thermocouple installed in the main airline gives the preheated air temperature reading before it enters into the combustor. The thermocouple installed inside the combustor gives the temperature reading of the combustion chamber during the combustion process. Figure 4.15 shows the thermocouple mounted in the main airline and the methane line.

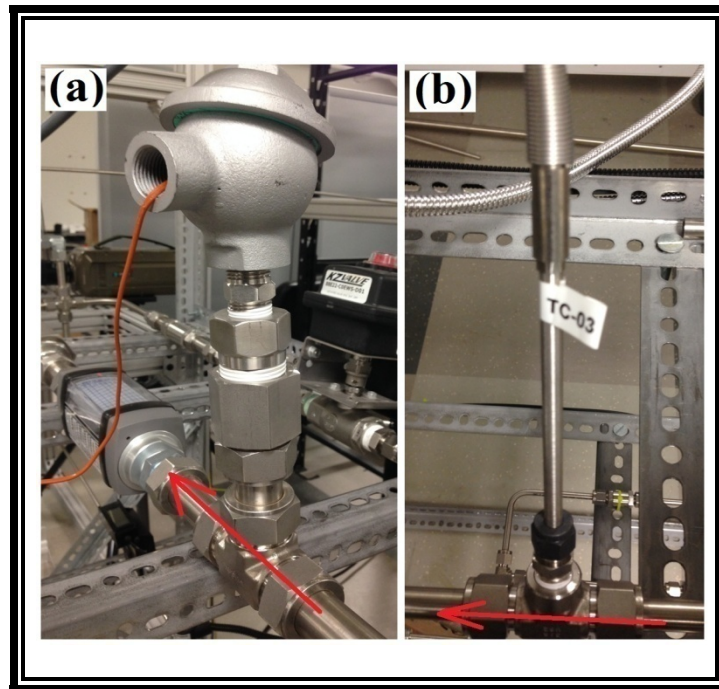


Figure 4. 15: (a) Thermocouple in the main airline (b) Thermocouple in the methane line.

The pressure has been measured at different location of the airline, methane line, pilot flame line and inside the combustor. Just like the thermocouple location, figure 3.41 also shows

the location of the pressure transducer for the whole system. Six different pressure transducers have been used in this experiment. Two of them (*LORD STI PT1700-150G-171*) are used in the main airline, One is used in the methane line and the combustor. Other two (*OMEGA PX309-100G 5V*) are used in the pilot flame line. Figure 4.16 shows the pressure transducer mounted in the airline and the pilot flame line. The calibration curve for the pressure transducer are shown in APPENDIX III which is used for the LabVIEW for determining coefficient of the voltage signal which is then turned into pressure reading. There is another pressure transducer which can measure the pressure and the temperature simultaneously, is installed inside the combustion from the bottom of the step which is also shown in figure 4.16(c).

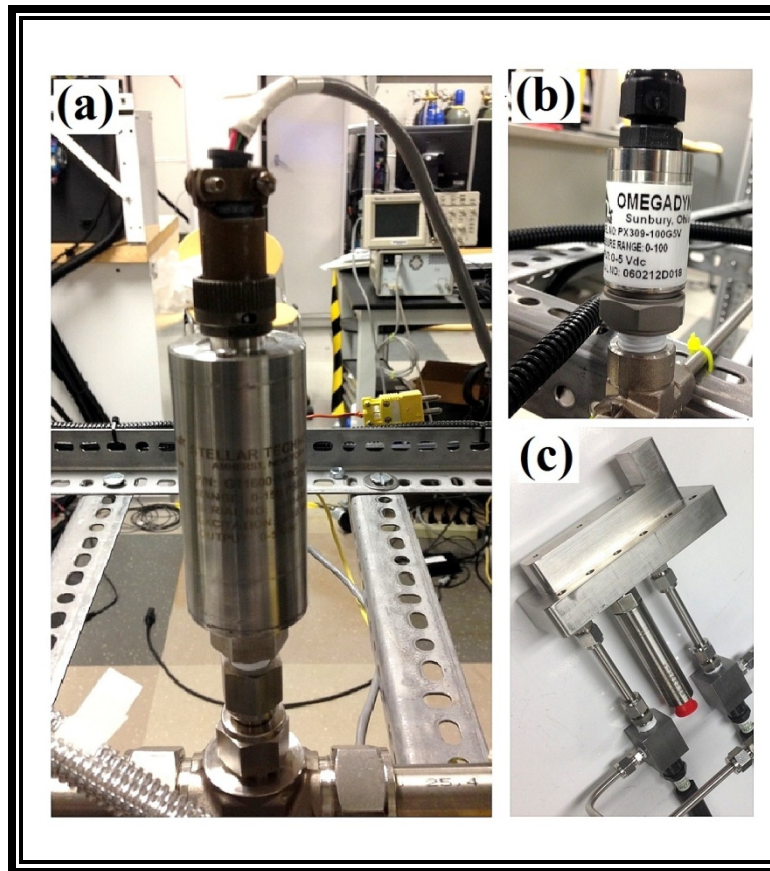


Figure 4. 16: Pressure transducer (a) Main airline, (b) Pilot flame line, (c) Combustor step

4.5 Control System

The control system has been developed with the help of LabVIEW software. 'National Instrument' PCI data acquisition connector blocks are used to control the valves and acquire the temperature and pressure reading of the system. Figure 4.17 shows the control unit and the DAC system. The system is designed to control the valves both automatically and manually. There is a master switch (red switch in figure 4.17a) which is a double pole double throw switch. This switch is used for the total system to change from automatic control to manual control. There are two emergency shut off switch for safety which is designed to operate the system safely. Separate power supplies are used to operate the AC and DC valves. Figure 4.18 shows the LabVIEW front panel which shows the temperature of the air of the main line, temperature of methane and the temperature inside the chamber. The front panel also shows pressure reading of the airline, methane line and the chamber pressure reading during the experiment. Figure 4.19 shows the block diagram of the LabVIEW program. Four DAC assistance functions have been used. One of them is used to acquire the temperature, pressure and flow reading. another one is used to control the main air and methane line. Other two are used for pilot flame line and proportional control valve operation.

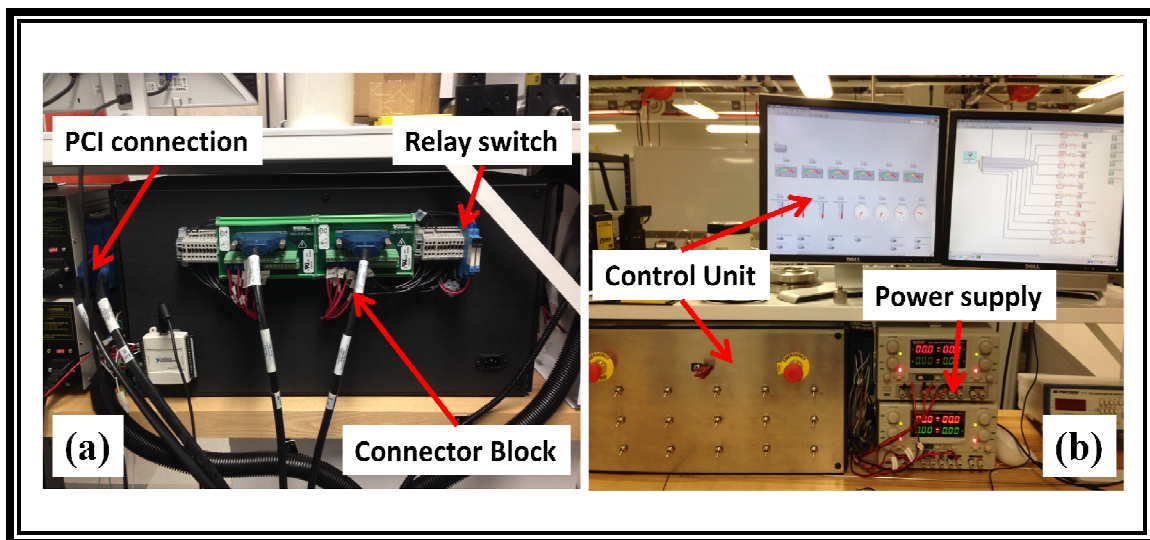


Figure 4. 17: Transient temperature profile at different thickness of the chamber.

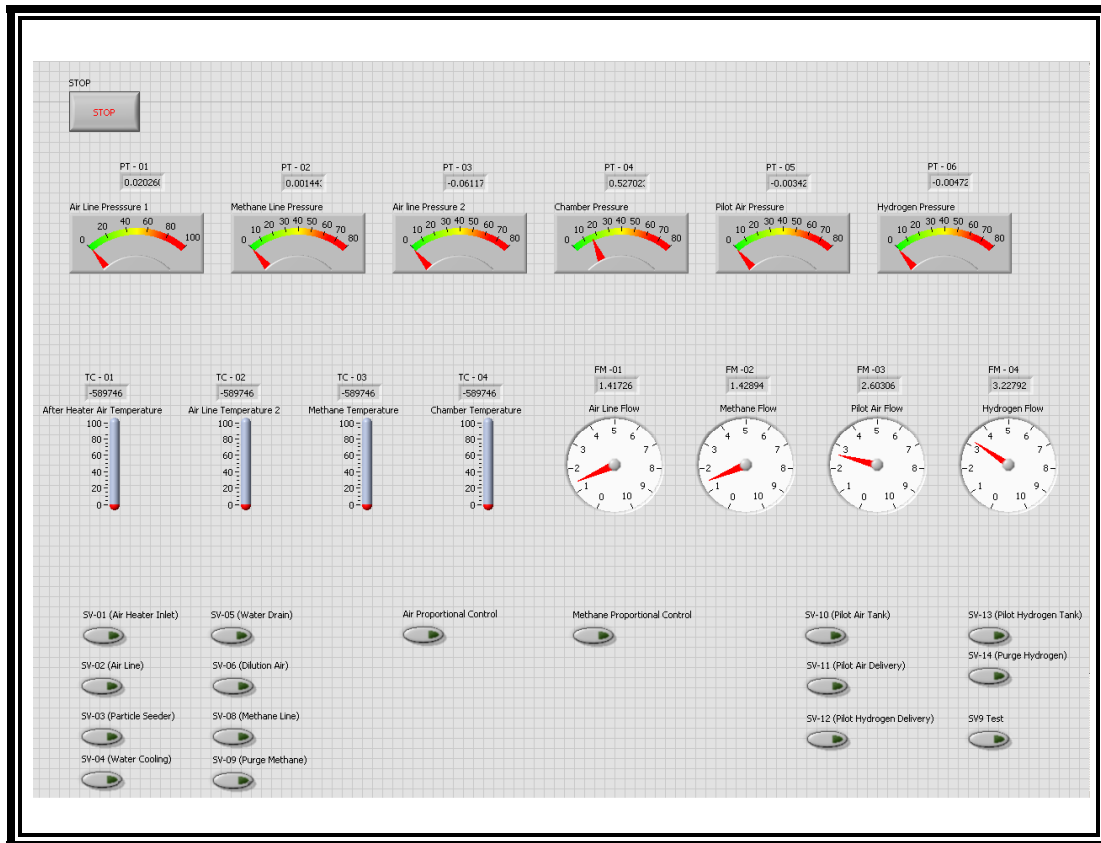


Figure 4. 18: LabVIEW front panel of the control system.

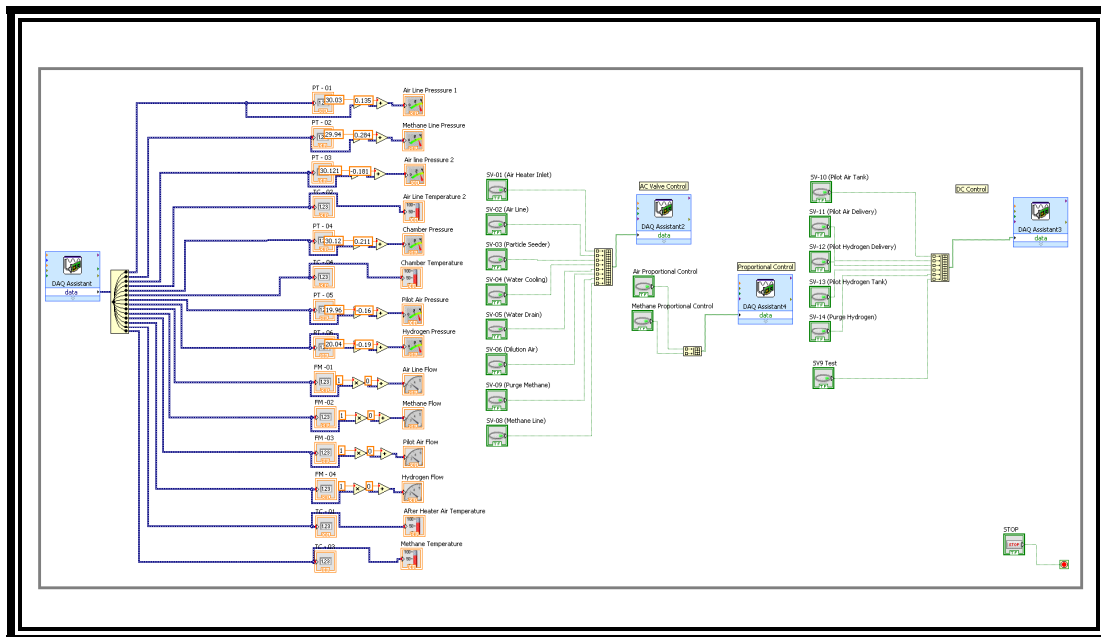


Figure 4. 19: LabVIEW block diagram of the control system.

Chapter 5: Result and Discussion

5.1 Particle Image Velocimetry (PIV) Data

The flow field inside the combustor is measured by Particle Image Velocimetry (PIV) technique. During the experiment, the light plane was generated by a '*15-1000 Dual power*' 527nm Neodymium-doped Yttrium Lithium Fluoride (Nd-YLF) laser with a pulse energy of 15mJ/pulse. This laser generates a 75mm wide 0.1mm thick light sheet which is guided by a 45° angle of attack (AOA) line mirror and a telescope lens. The image plane is captured by a '*Speed sense 9070*' CCD camera with a frame rate of 3.1 kHz. The image plane is 72mm x 40mm in dimension or 1280 x 800 pixel. The flow field was seeded with 1µm aluminum particle. The particles were seeded far away from the inlet of the combustor so that It did not have any effect on the actual flow field. The camera and the laser pulse were controlled by a BNC 575-8 timer box. The BNC cable carries the trigger signals for the laser which controls the laser pulse and the camera frame rate and synchronizes them according to the '*dynamic studio*' software commend. The raw PIV images were taken at a rate of 3kHz. Approximately 750 images have been taken in a time span of 0.25 second.

Figure 5.1 shows the raw PIV image and the instantaneous flow field. The instantaneous PIV image gives an idea of the flow field inside the combustor. The shear layers due to the step are clearly visible. Moreover the vortex breakdown due to the grid are also observed. When fifteen consecutive raw PIV images were taken and an average image was created by the image averaging technique, a clear recirculation zone was observed. Figure 5.2 shows the average image of fifteen consecutive raw PIV images. The step was designed to create this recirculation zone and the average PIV image shows the predicted recirculation zone. The PIV measurements were done at 4.81 and 20.60 m/s velocity which corresponds to $Re = 815$ and 3500 respectively. Quantitative data were calculated at six different locations from $x/L = 0.06$ to 0.93 where L is the length of interrogation area. Figure 5.3 shows the locations of the flow field where quantitative measurements were calculated.

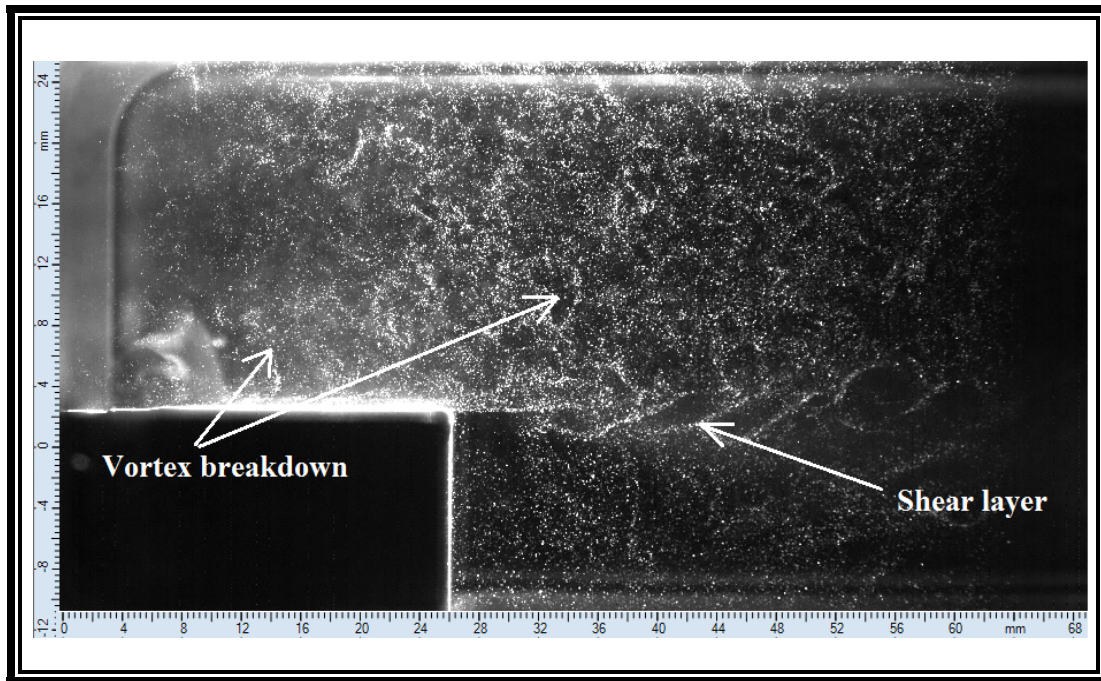


Figure 5. 1: Raw PIV image at $Re = 815$

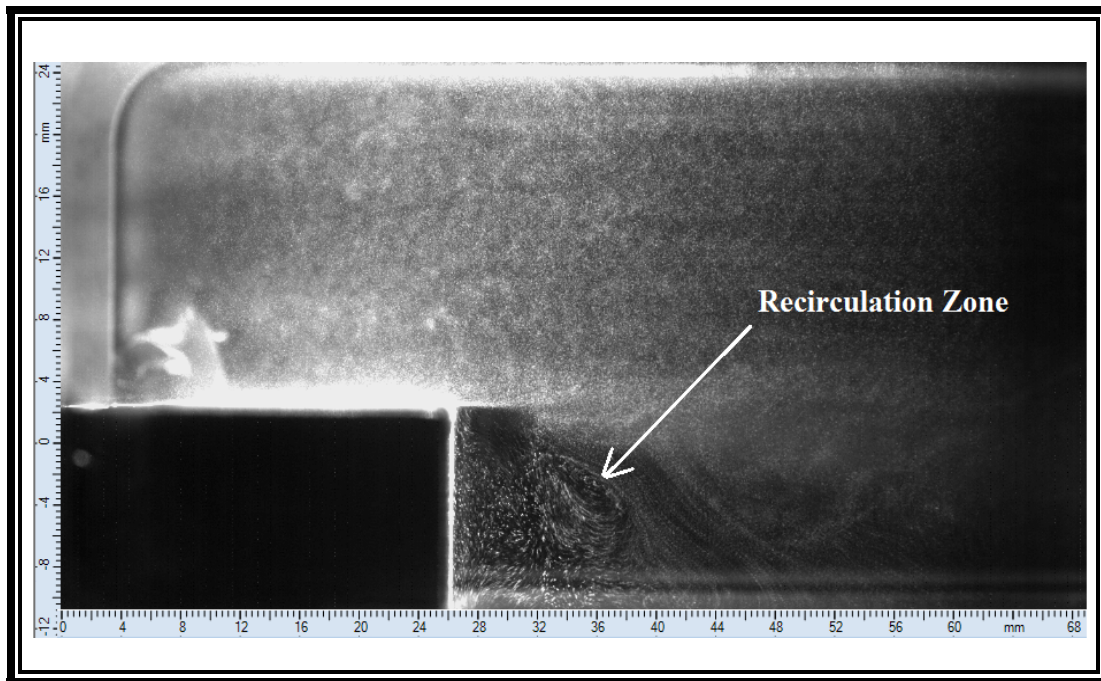


Figure 5. 2: Average PIV image at $Re = 815$

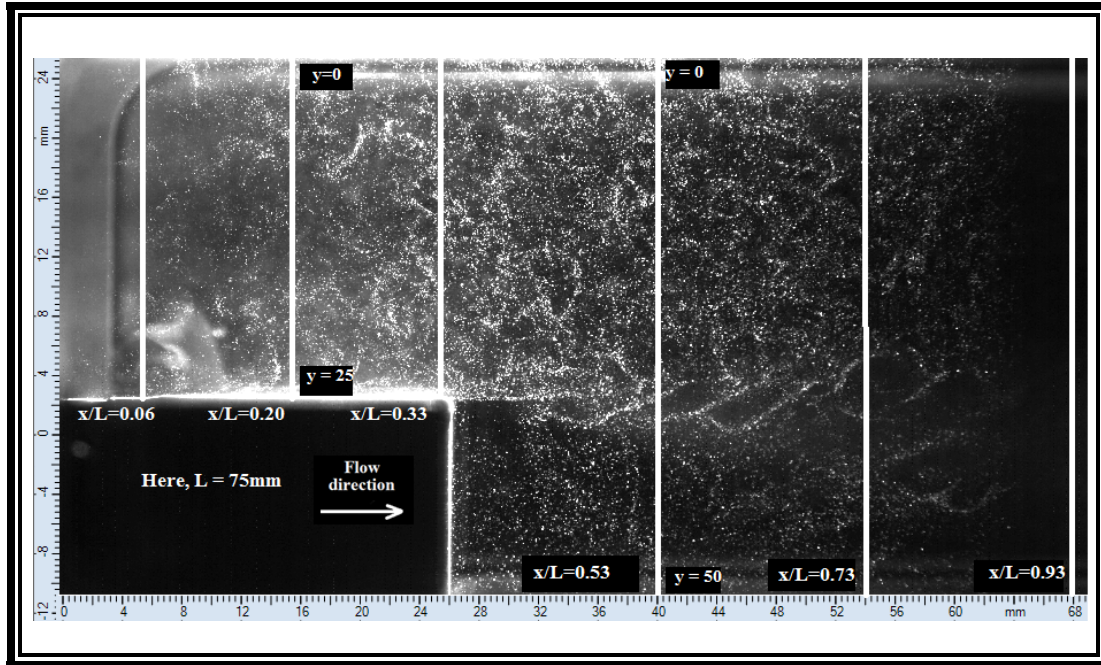


Figure 5. 3: Interrogation image field and six different locations for quantitative calculation.

5.1.1 MEASUREMENT OF AVERAGE VELOCITY

The horizontal velocity component or the U-velocity and the vertical velocity component or the V-velocity were measured at $Re = 815$ and 3500 . During the PIV post processing, the interrogation area was considered in a 32×32 pixel area. Vector fields were determined by adaptive correlation in 'Dynamic Studio' software. Approximately 750 images were processed for determining the vector field. Figure 5.4 shows the instantaneous vector field at $Re = 815$ colored by U-velocity. The vector field shows different recirculation zones and velocity fluctuations. Figure 5.5 also shows the instantaneous velocity vector at $Re = 3500$ colored by U-velocity. Similar recirculation zones and velocity fluctuations were observed here. The most important observation here is the low velocity zone just after the step. This low velocity zone was observed in both case which create a recirculation zone (vortex) observed in the raw PIV image.

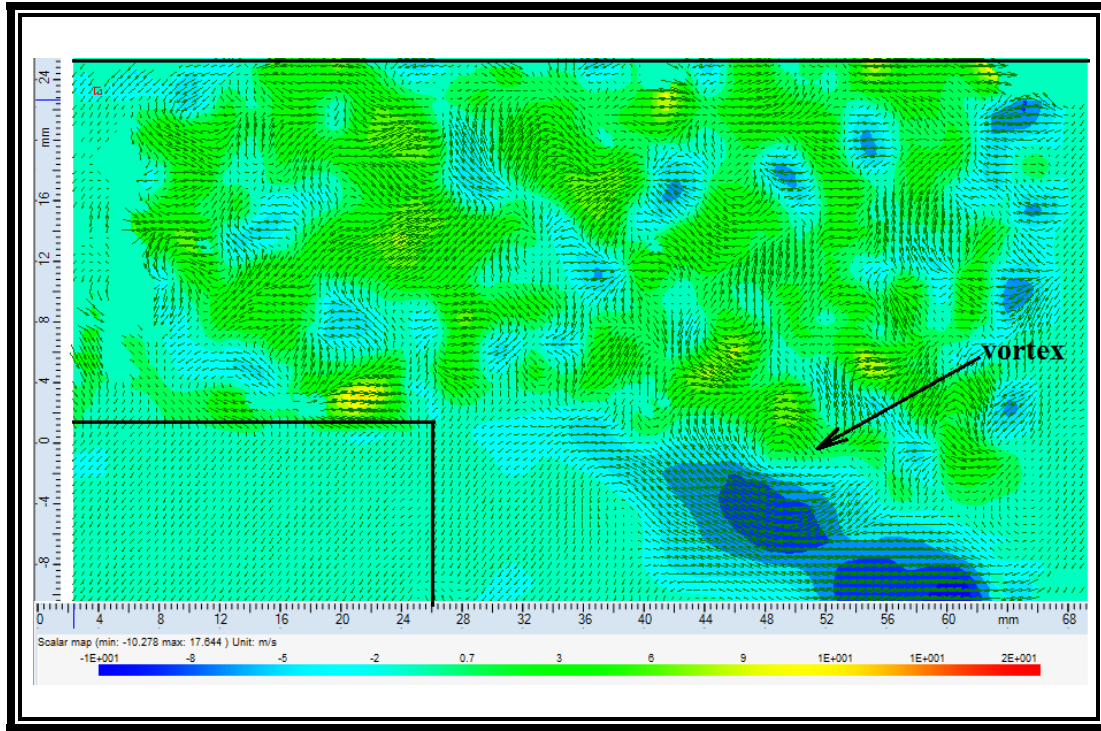


Figure 5. 4: Instantaneous velocity vector colored by U-velocity at $Re = 815$.

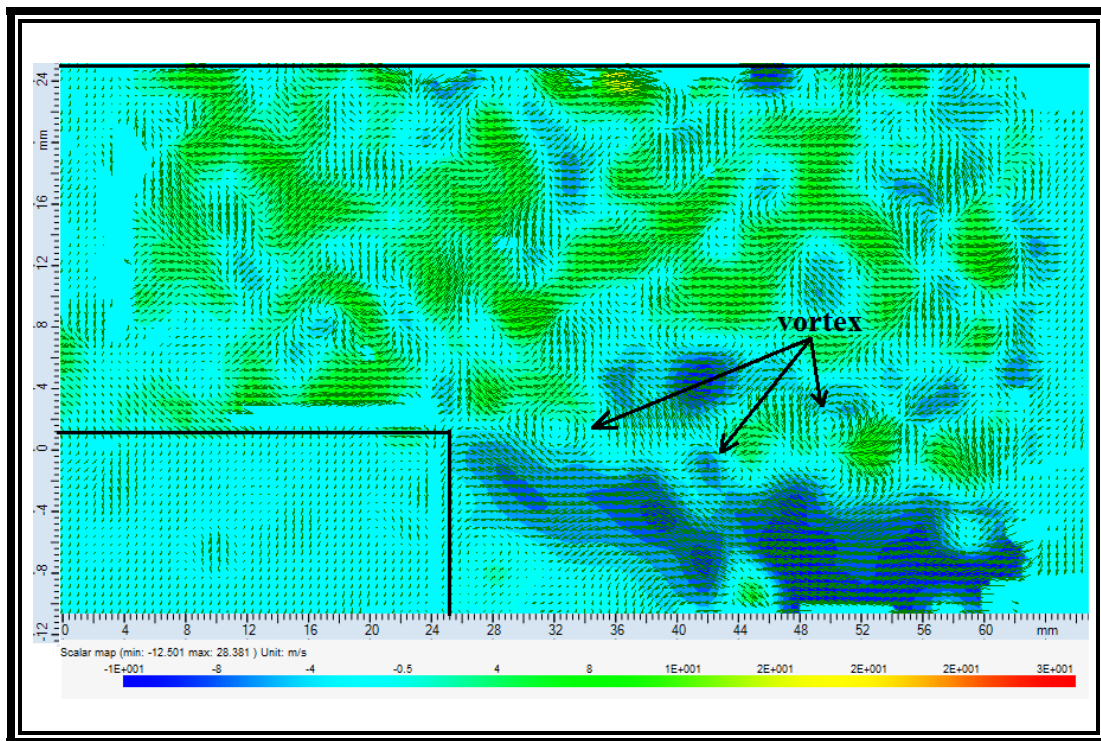


Figure 5. 5: Instantaneous velocity vector colored by U-velocity at $Re = 3500$.

Quantitative measurements were done for instantaneous U-velocity and V-velocity. Figure 5.6 shows the U-velocity fluctuation with respect to time. This figure clearly shows that the flow field is highly turbulent due to the grid. Similar fluctuations were observed for V-velocity which is shown in figure 5.7. Both measurements were done at $Re = 3500$. Figure 5.8 shows the average U-velocity distribution at $x/L=0.06$ for $Re = 815$. The overall error for PIV measurement was assumed as 10%. Five distinctive velocity peak were observed due to the five grid holes. This velocity distribution implies that the velocity become higher at the grid hole and the velocity fluctuation become dominant after that. Figure 5.9 shows the average U-velocity distribution at first three locations before the step at $Re = 815$. The average velocity varies along the y-direction due to turbulence. Similar fluctuations were also observed in the V-velocity distribution for the first three location before the step which is shown in figure 5.10. Figure 5.11 and 5.12 shows the average U-velocity and V-velocity distribution at three different locations after the step.

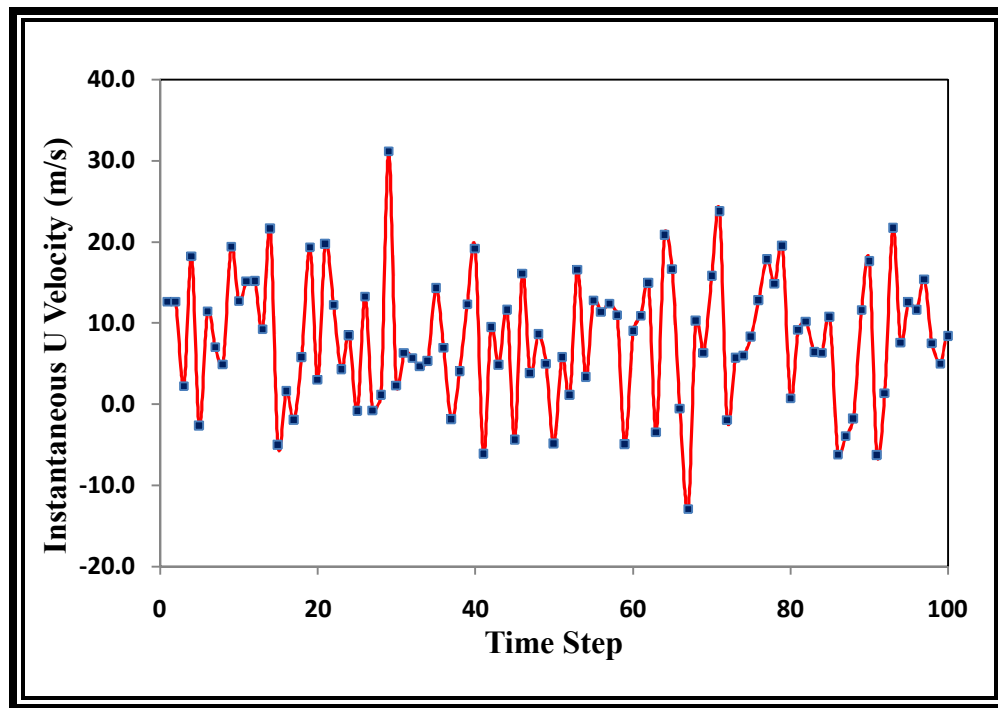


Figure 5. 6: Instantaneous U-velocity at a single point at $Re = 3500$.

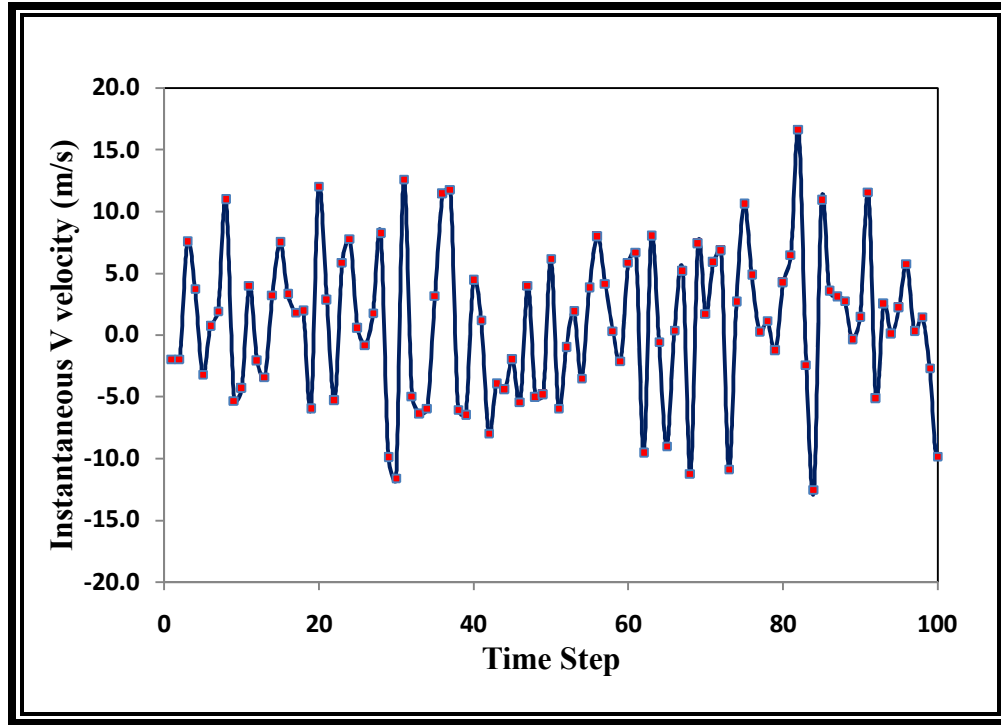


Figure 5. 7: Instantaneous V-velocity at a single point at $Re = 3500$.

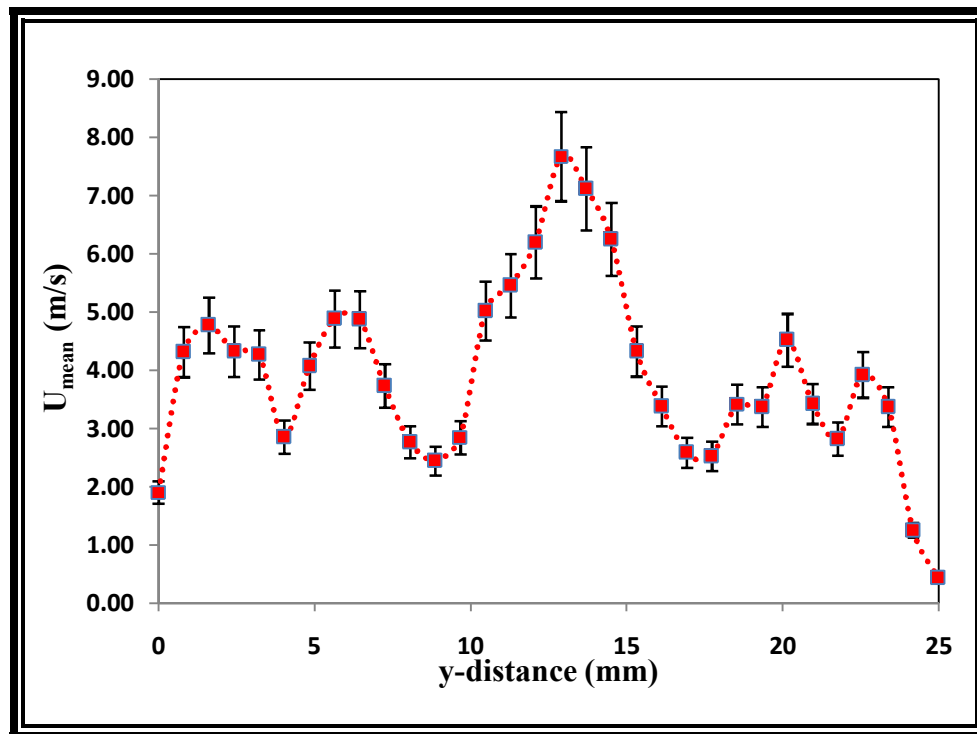


Figure 5. 8: U_{mean} velocity from PIV calculation at $Re = 815$ and $x/L = 0.06$

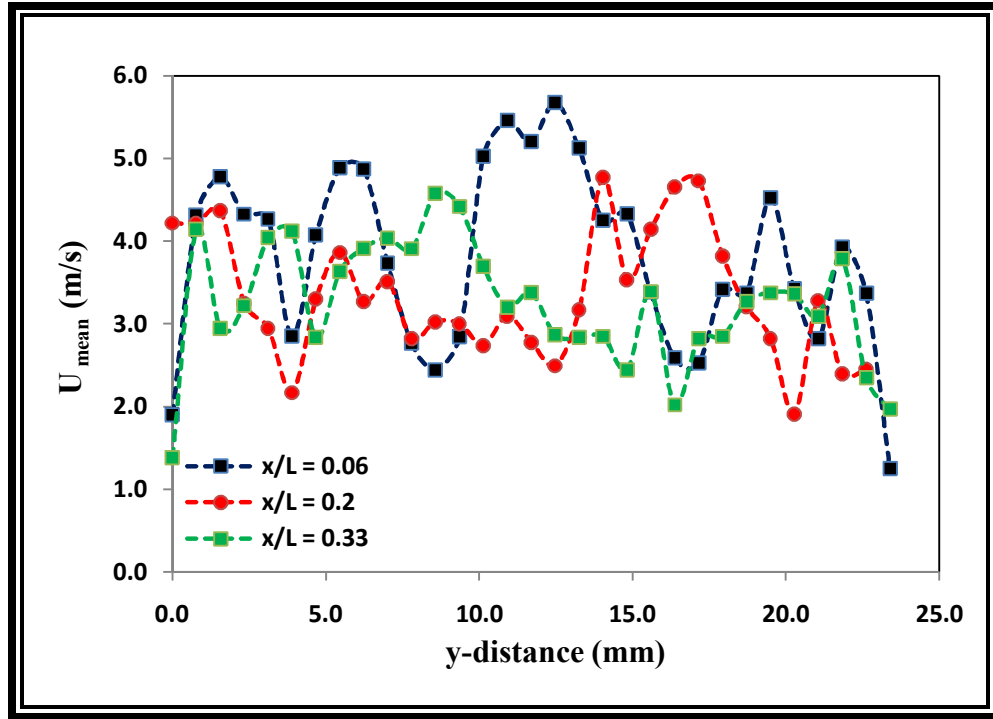


Figure 5. 9: U_{mean} velocity from PIV measurement before the step at $Re = 815$.

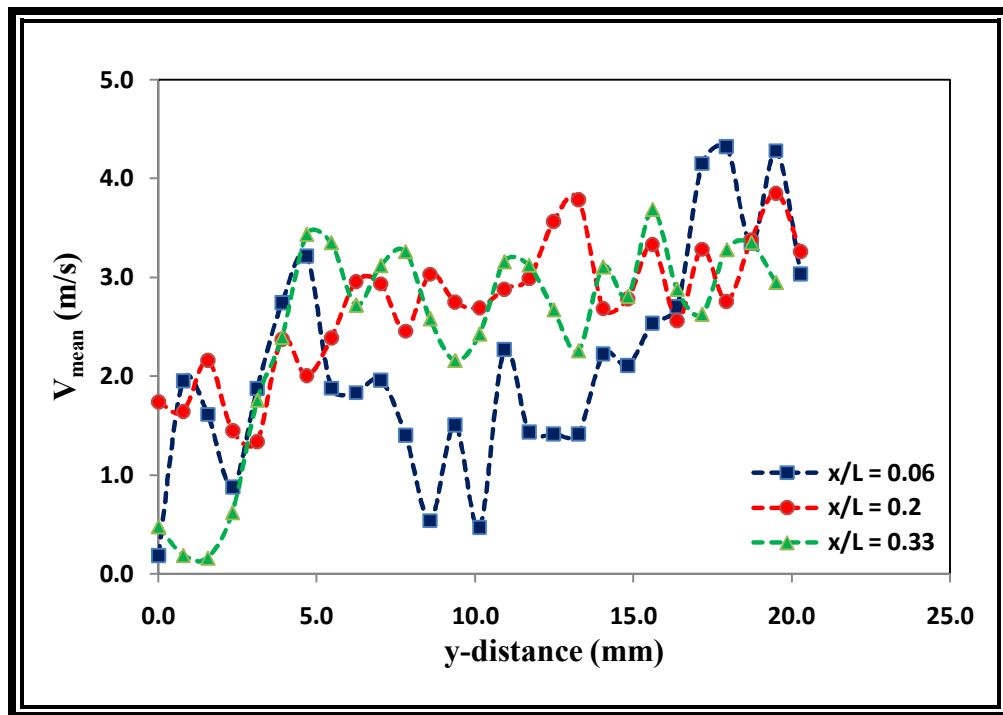


Figure 5. 10: V_{mean} velocity from PIV measurement before the step at $Re = 815$.

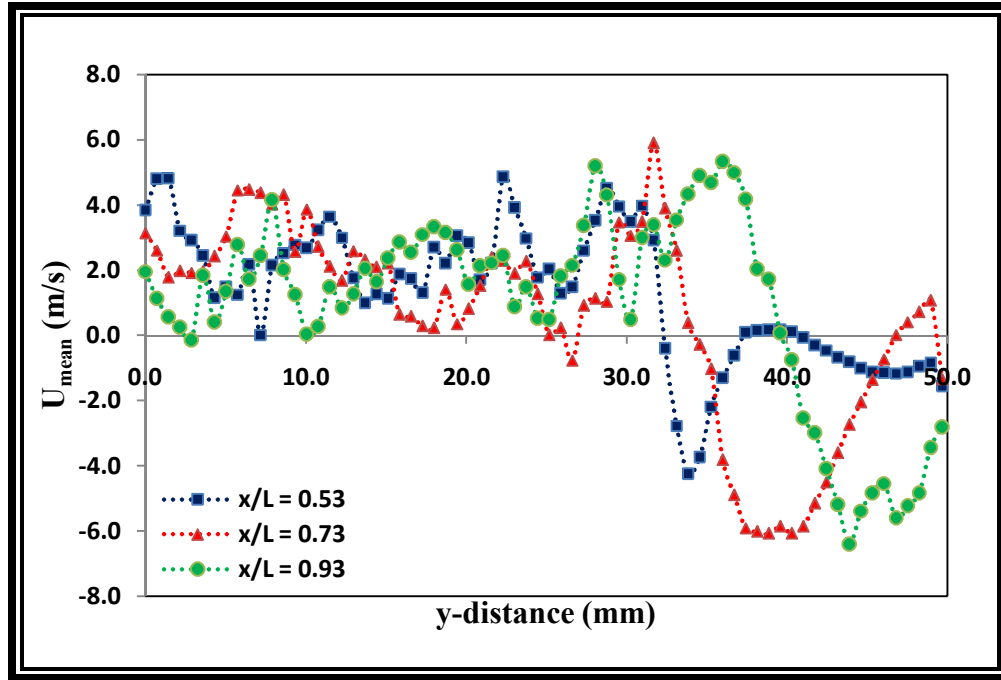


Figure 5. 11: U_{mean} velocity from PIV measurement after the step at $Re = 815$.

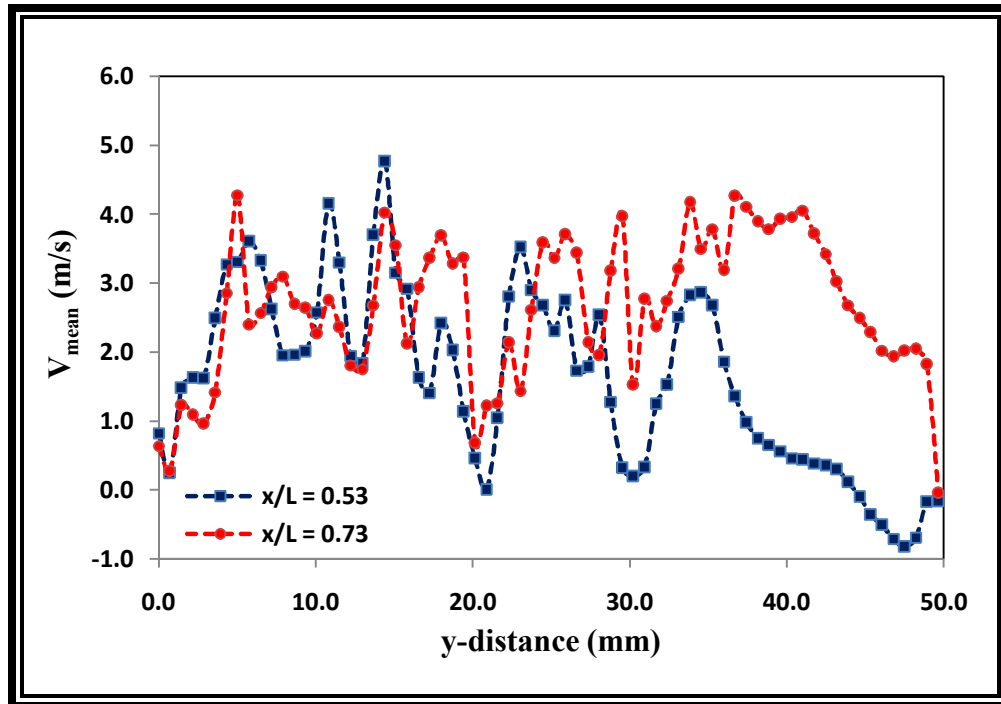


Figure 5. 12: V_{mean} velocity from PIV measurement after the step at $Re = 815$.

The velocity distributions were calculated along the y-direction of the chamber. The zero location in the plot was considered at the top wall and the measurements were shown from the top wall to the bottom wall. Figure 5.11 shows the negative velocity zone which corresponds to the low velocity zone (recirculation zone) after the step. Similar distributions were found for the V-velocity distribution for the corresponding locations as shown in figure 5.12. Figure 5.13 and 5.14 shows the average U-velocity and V-velocity distributions along the first three locations before the step at $Re = 3500$. Although the distinctive velocity peaks were not observed in this case as they were observed at $Re = 815$, the velocity fluctuations were visible and they varies along the y-direction. Moreover, figure 5.15 and 5.16 shows the average velocity distribution along three locations after the step at $Re = 3500$. Similar low velocity zones were observed which happen due to the recirculation zone created by the step.

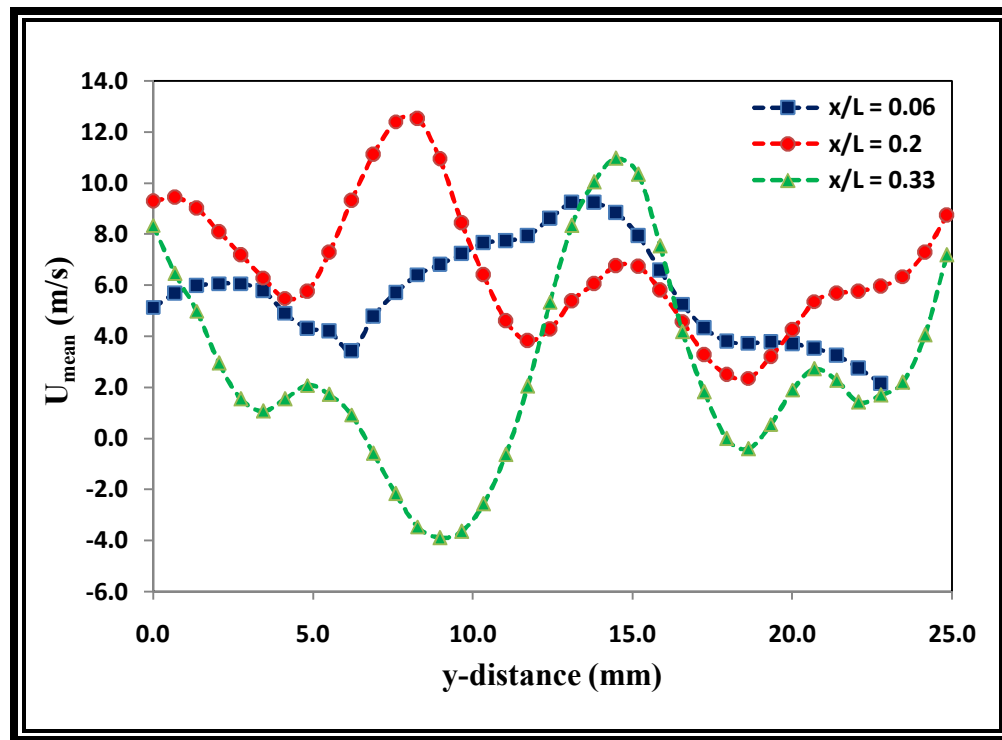


Figure 5. 13: U_{mean} velocity from PIV measurement before the step at $Re = 3500$.

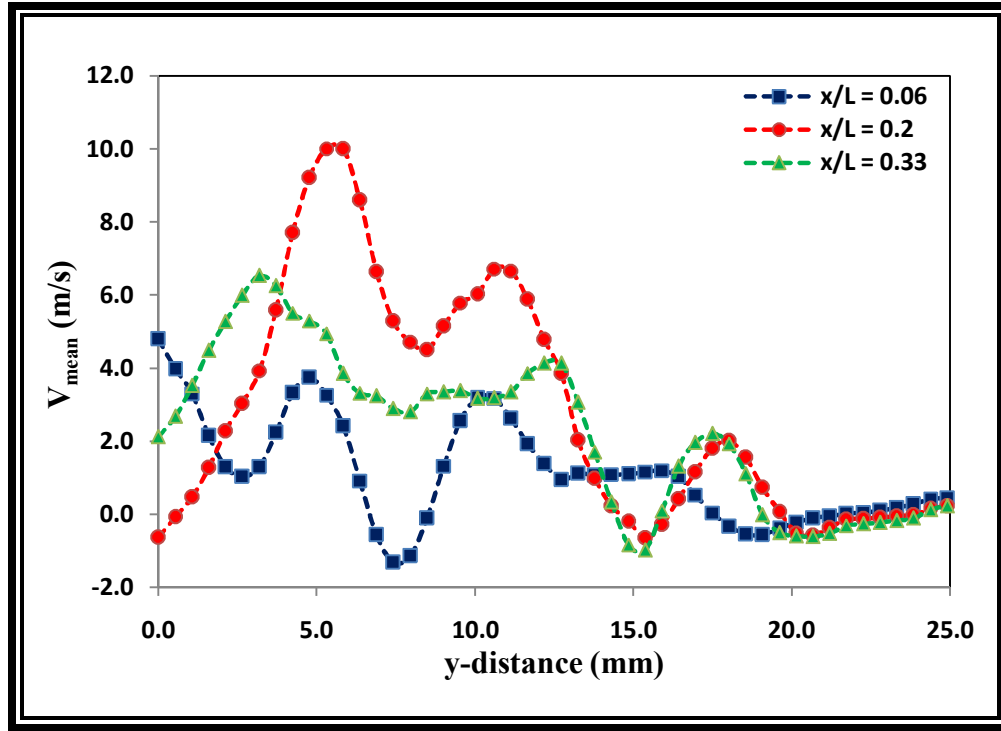


Figure 5. 14: V_{mean} velocity from PIV measurement before the step at $Re = 3500$.

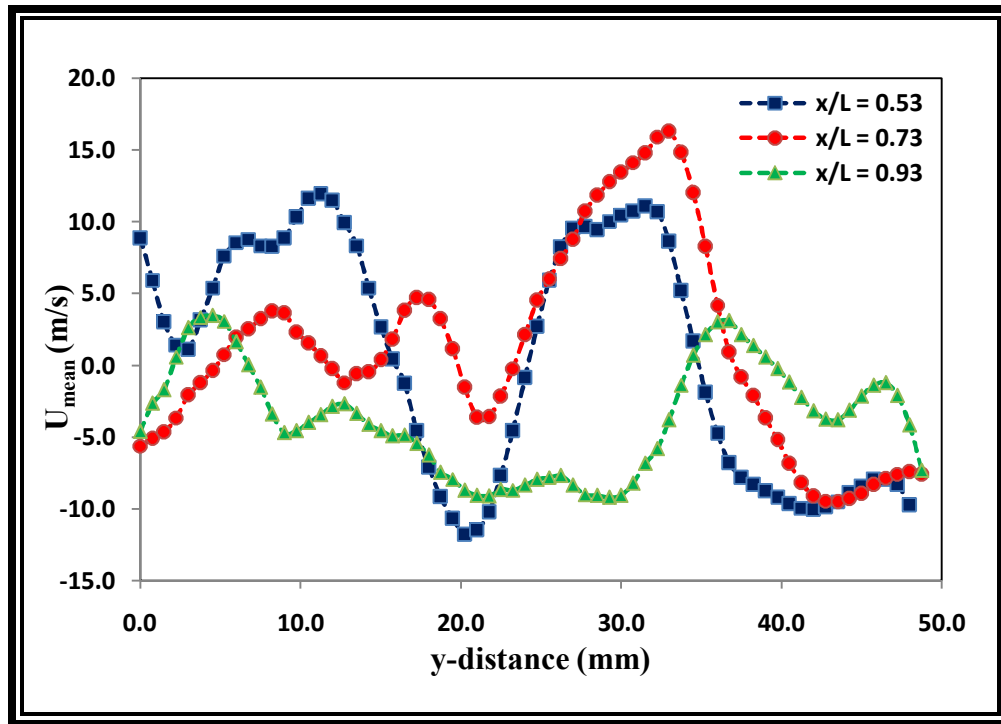


Figure 5. 15: U_{mean} velocity from PIV measurement after the step at $Re = 3500$.

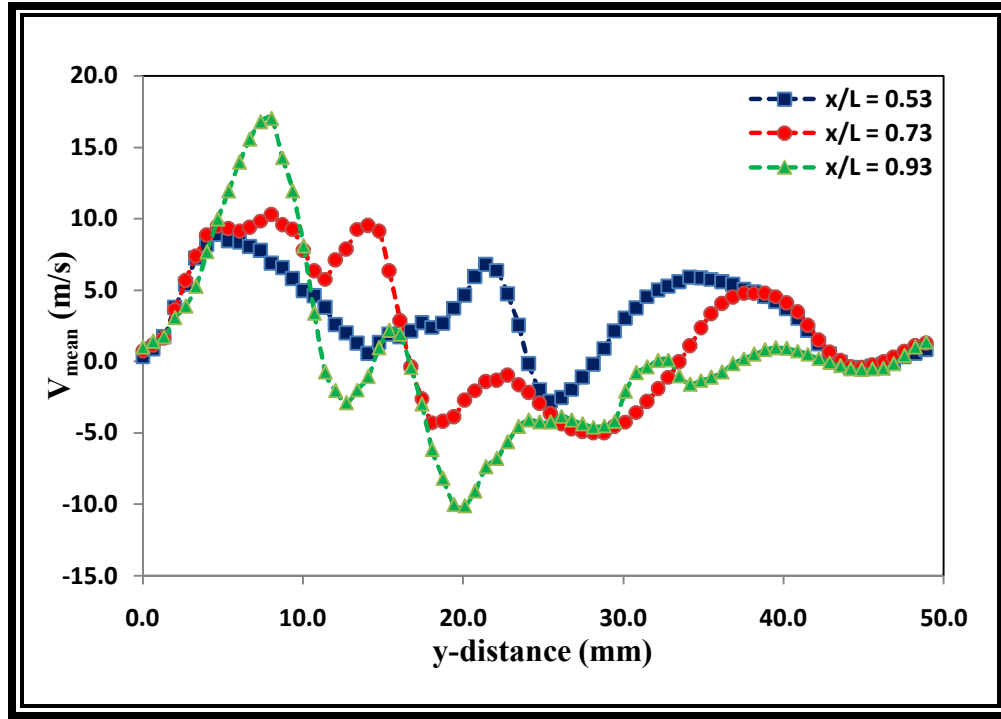


Figure 5. 16: V_{mean} velocity from PIV measurement after the step at $Re = 3500$.

5.1.2 MEASUREMENT OF KINETIC ENERGY

The kinetic energy represents the momentum effect of the flow field. It gives an idea of the velocity field as well. The kinetic energy has been calculated by equ 2.10 described in chapter 2. The kinetic energy was determined for two different Reynolds number ($Re = 815$ & 3500). Initially the kinetic energy was determined without the grid at $Re = 815$ which is shown in figure 5.17. A uniform energy distribution has been observed in this case. But when the grid was introduced, the kinetic energy distribution changes dramatically due to vortex breakdown. Figure 5.18 shows the kinetic energy contour at $Re = 815$. Similar contours were observed at $Re = 3500$ which is shown in figure 5.19. The quantitative measurements are shown in figure 5.20 and 5.21. Here the kinetic energy distributions are shown for different locations before and after the step respectively at $Re = 815$. Both figures refer the high intensity of turbulence in the flow field. Similar distributions are shown in figure 5.22 and 5.23 at $Re = 3500$.

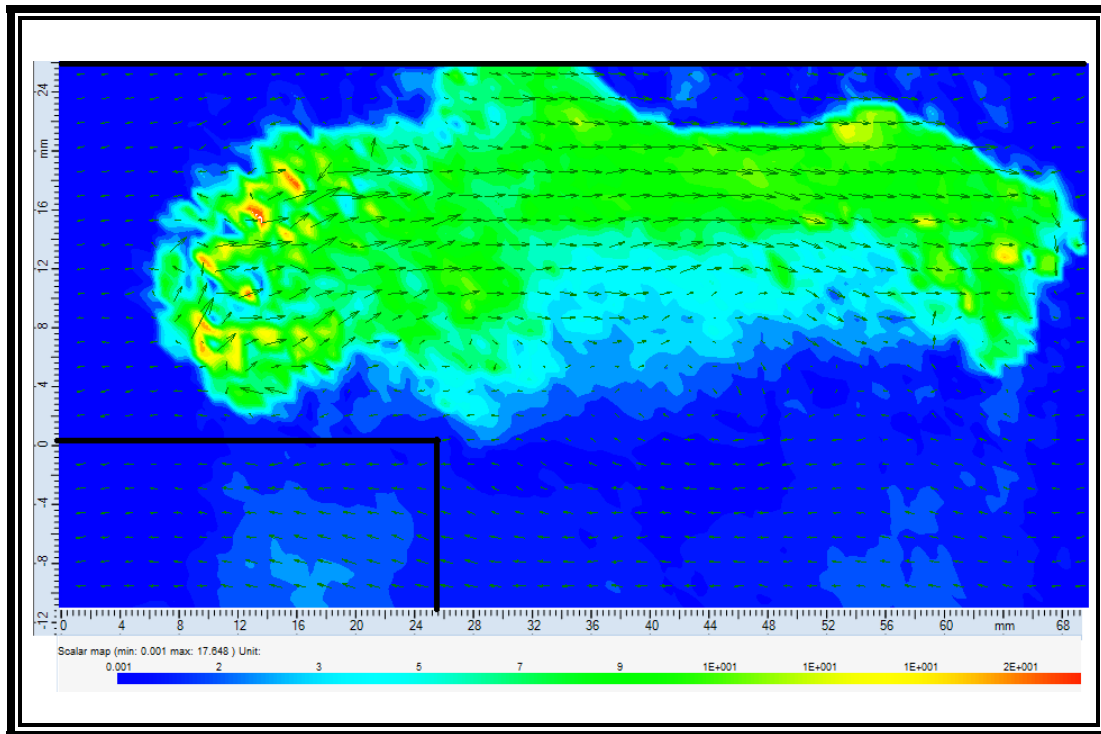


Figure 5. 17: Kinetic energy without the grid at $Re = 815$

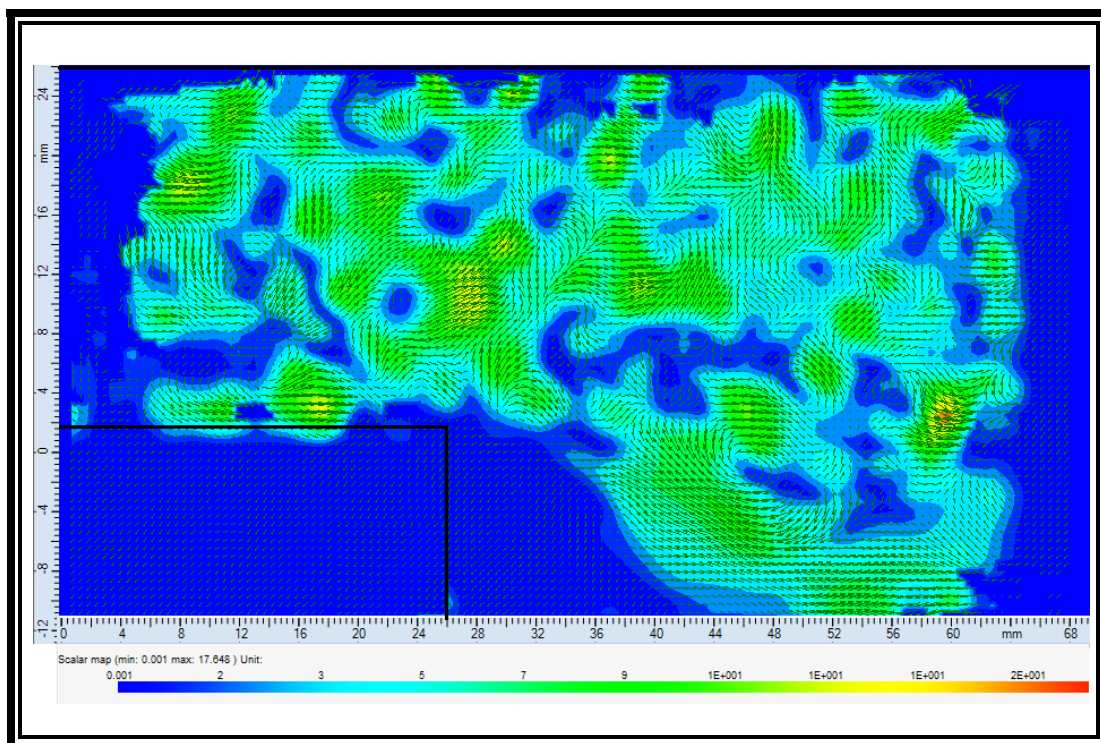


Figure 5. 18: Kinetic energy at $Re = 815$

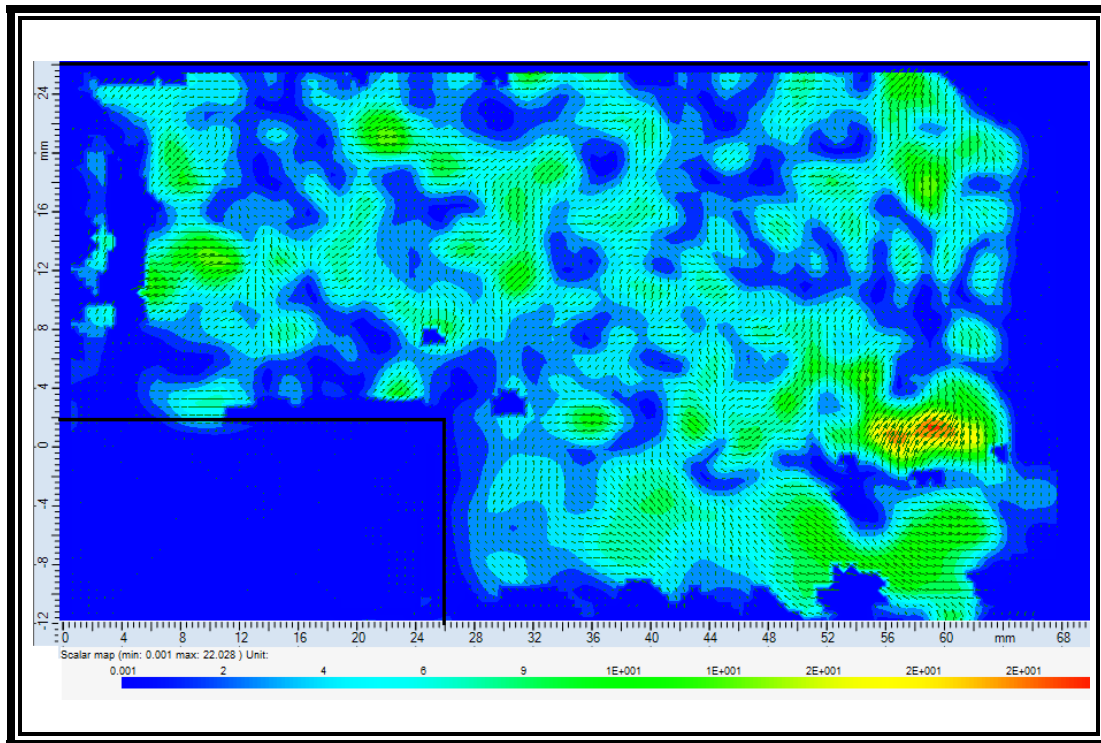


Figure 5. 19: Kinetic energy at $Re = 3500$.

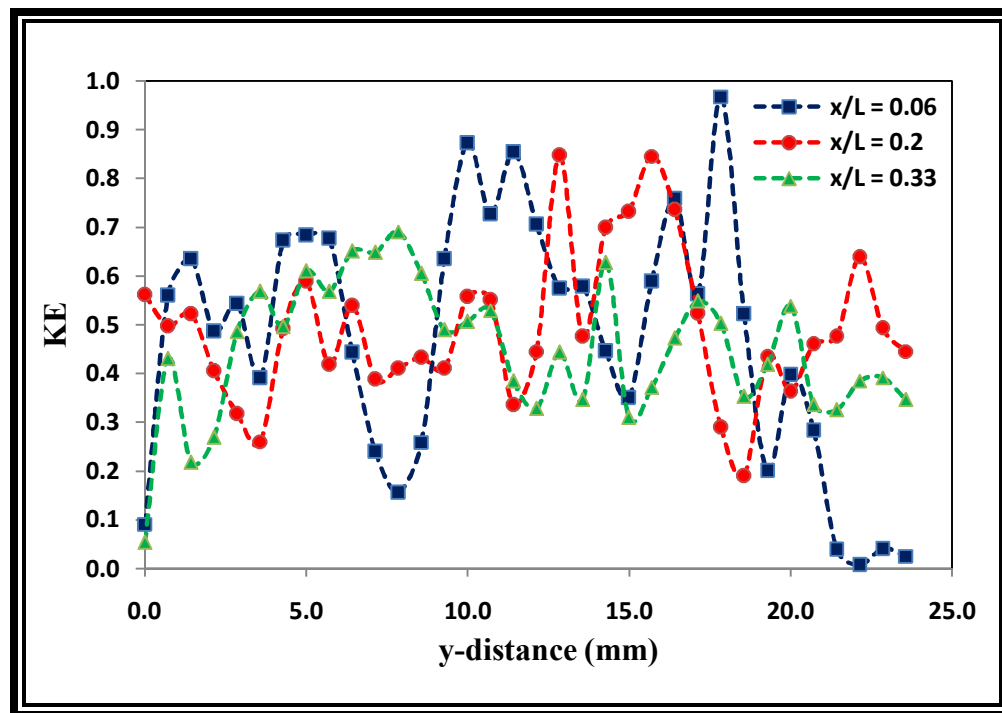


Figure 5. 20: Normalized kinetic energy before the step at $Re = 815$.

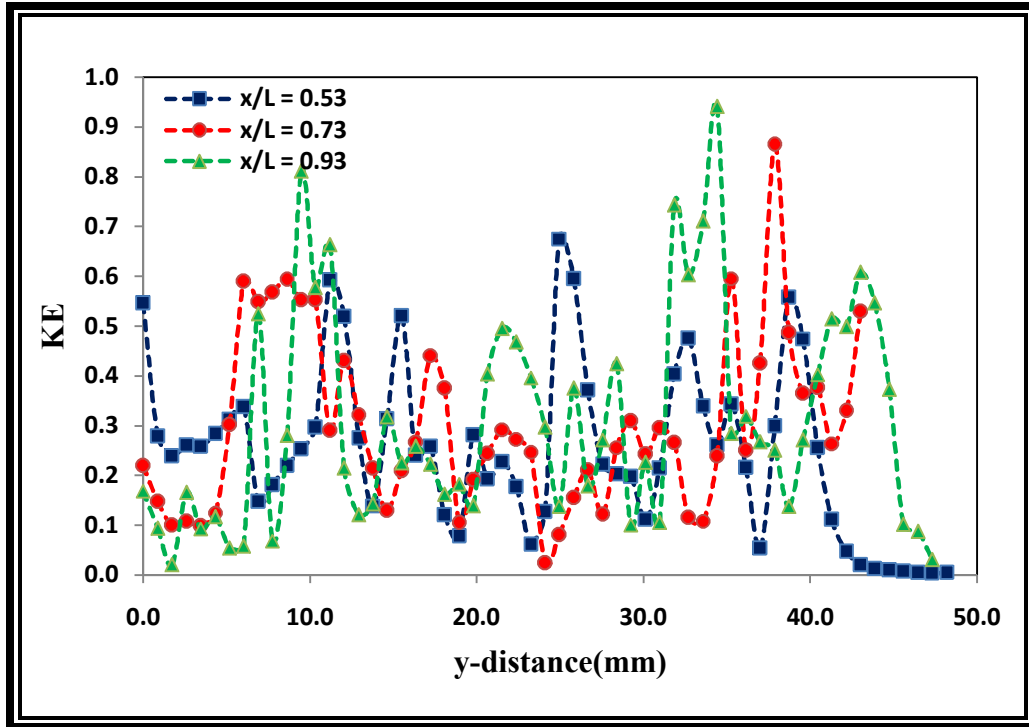


Figure 5. 21: Normalized kinetic energy after the step at $Re = 815$.

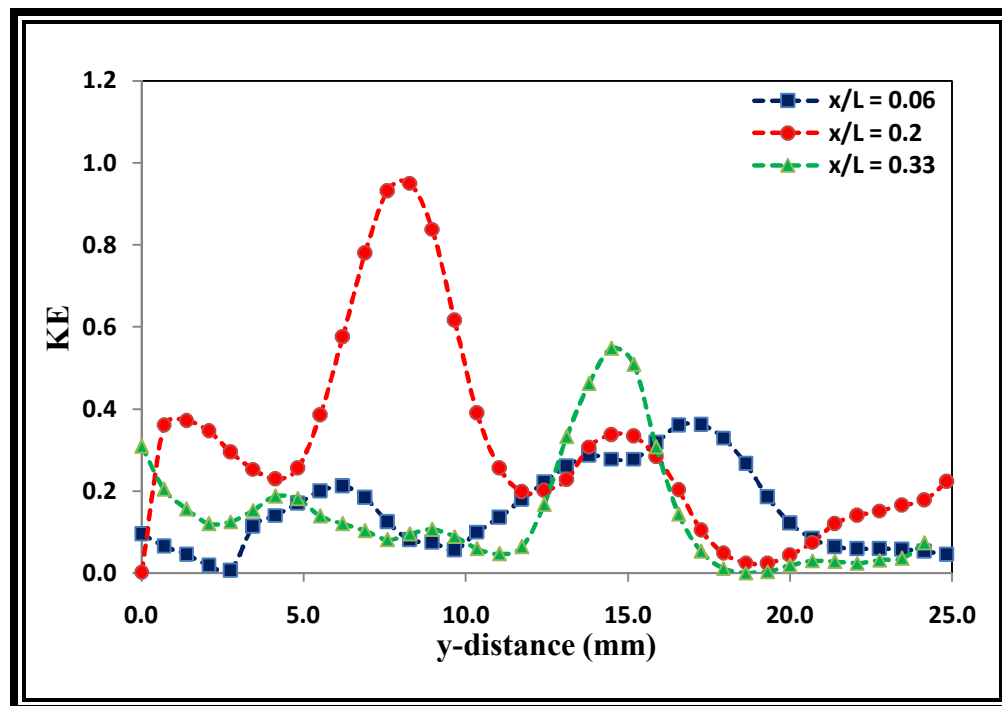


Figure 5. 22: Normalized kinetic energy before the step at $Re = 3500$.

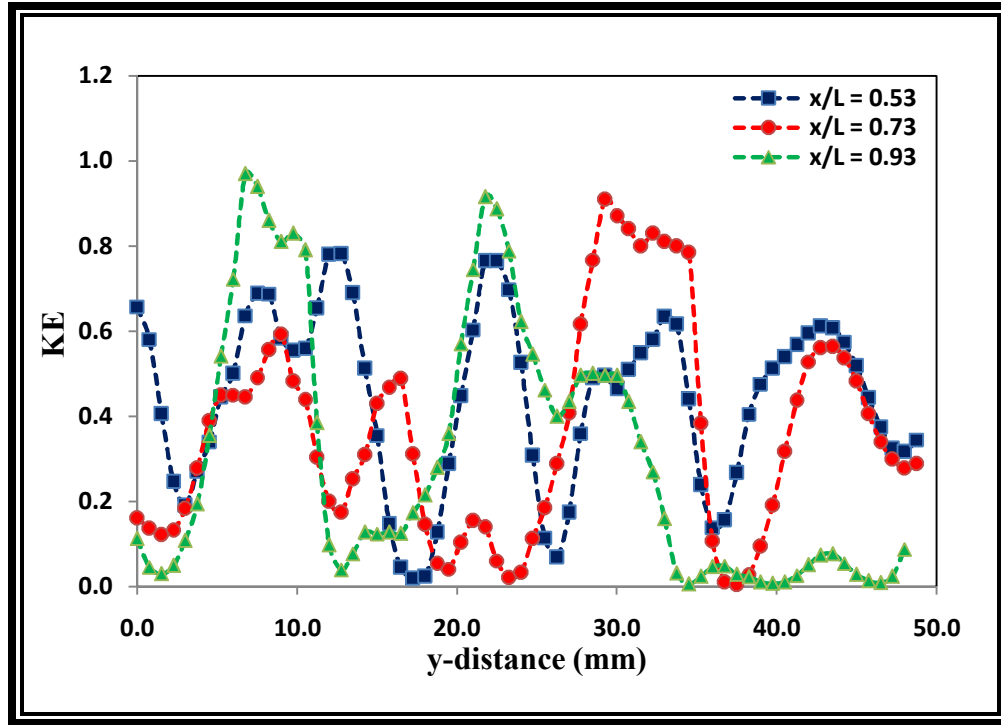


Figure 5. 23: Normalized kinetic energy after the step at $Re = 3500$.

5.1.3 MEASUREMENT OF TURBULENT INTENSITY

The turbulent intensity was measured both qualitatively and quantitatively. The turbulent intensity gives an idea of the velocity fluctuation of the flow field. The turbulent intensity has been calculated by eqn 2.14 described in chapter 2. The PIV images gave the instantaneous velocity components. By calculating the average velocity distribution, it is possible to calculate the fluctuating components from the instantaneous velocity field. This velocity fluctuation also gives the vorticity magnitude for the flow field. Figure 5.24 and 5.25 shows the velocity vector colored by vorticity magnitude at $Re = 815$ and 3500 respectively. Numerous vortex pairs were observed in both cases. The vortex pairs were generated by the grid at the upstream and made the flow field highly turbulent. Quantitative measurements were shown in figure 5.26 which implies the turbulent intensity at three different locations before the step. The figure also implies that the level of turbulent intensity is high close to the grid.

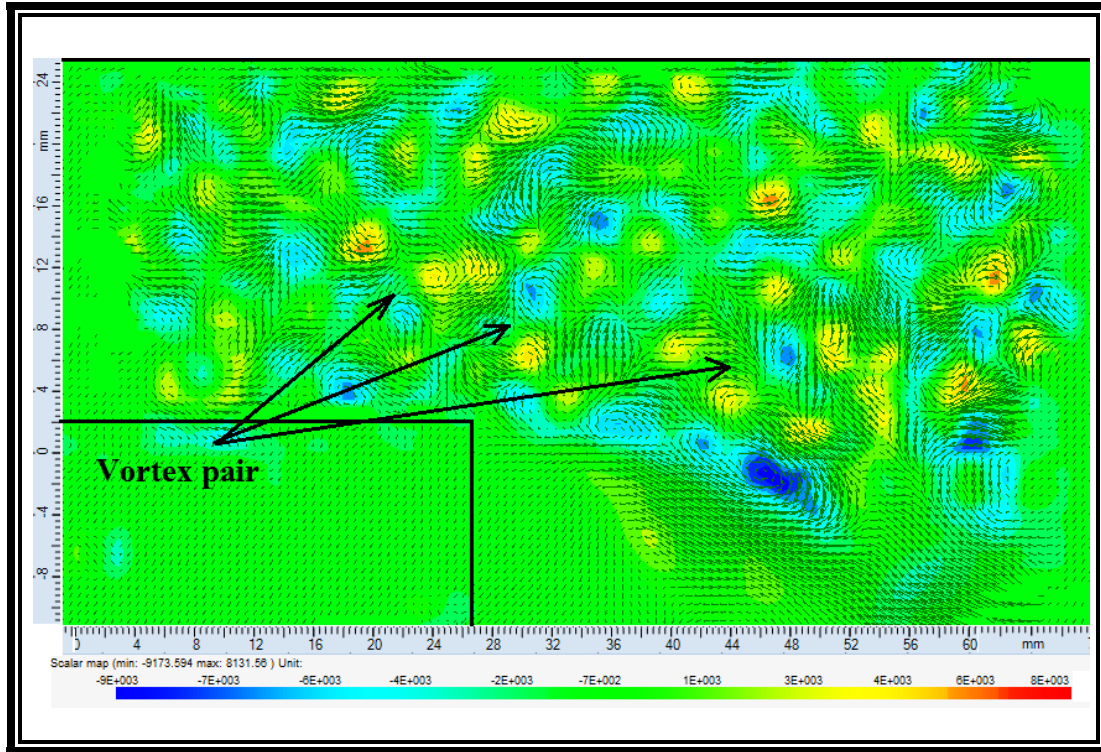


Figure 5. 24: PIV measurements of Vorticity contour at $Re = 815$.

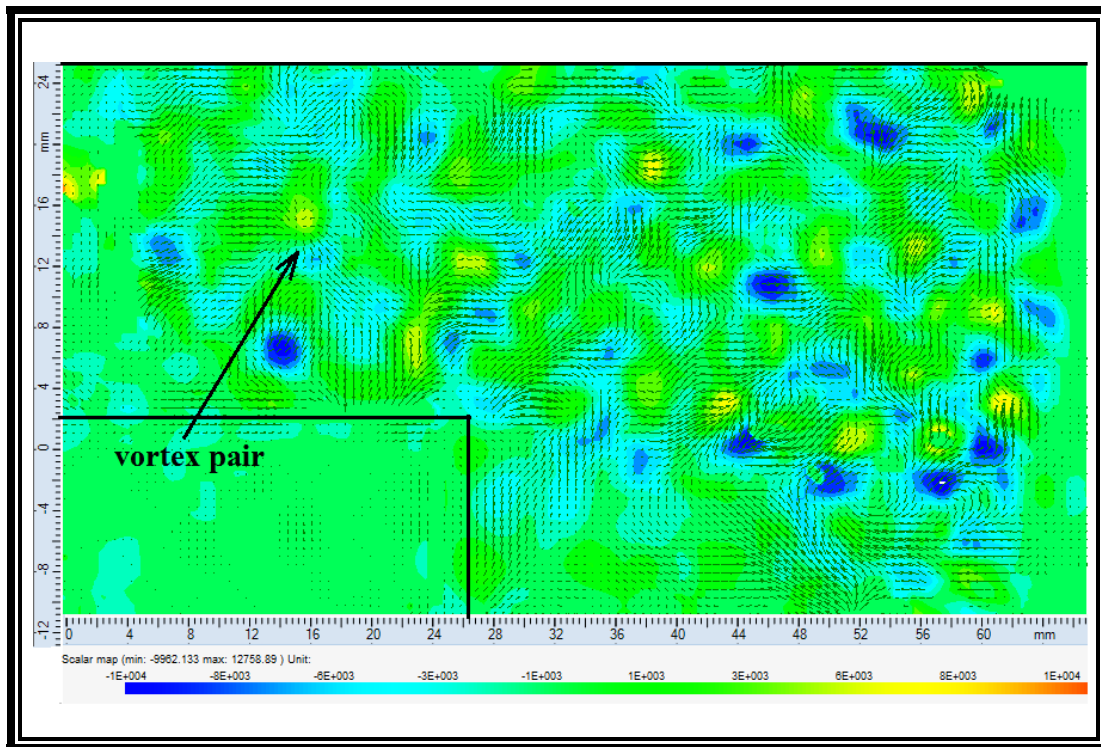


Figure 5. 25: PIV measurements of Vorticity contour at $Re = 3500$.

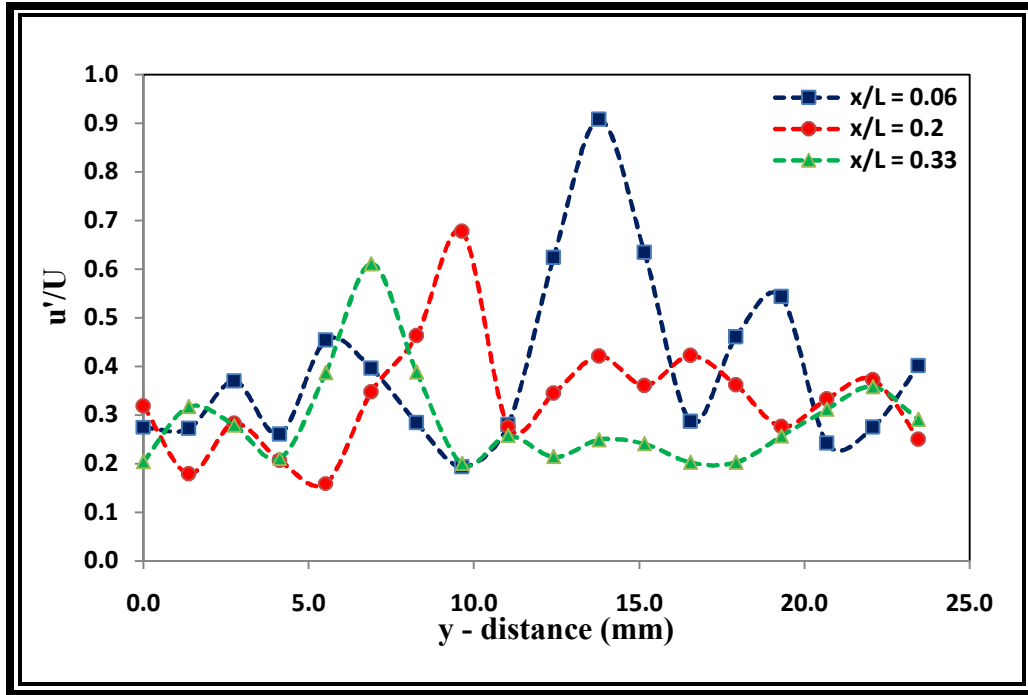


Figure 5. 26: Turbulent intensity before the step at $Re = 815$.

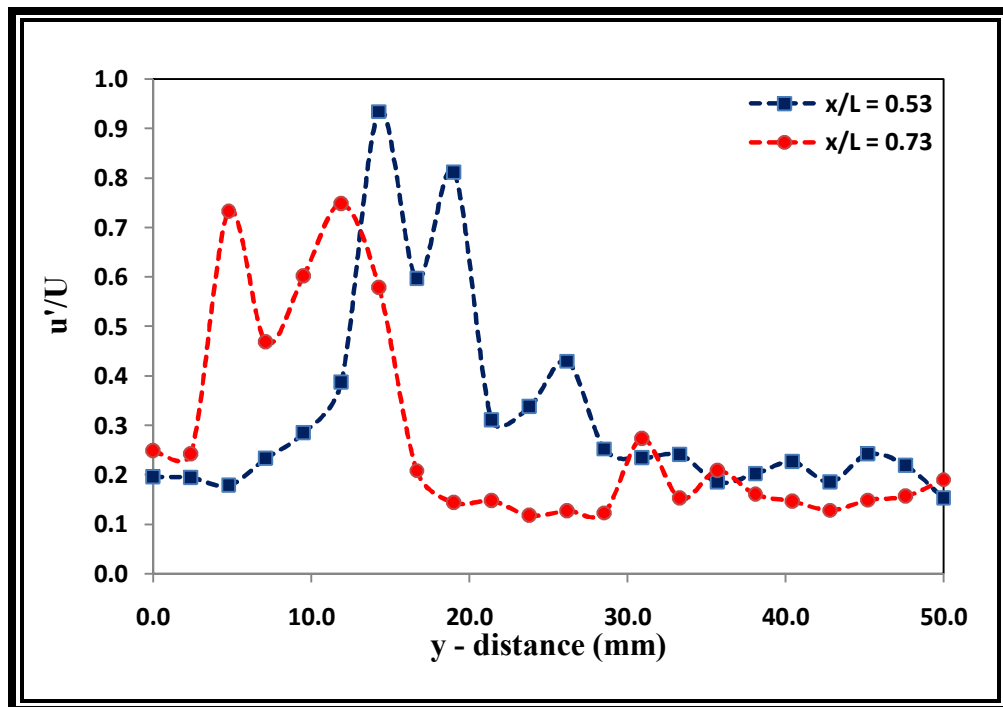


Figure 5. 27: Turbulent intensity after the step at $Re = 815$.

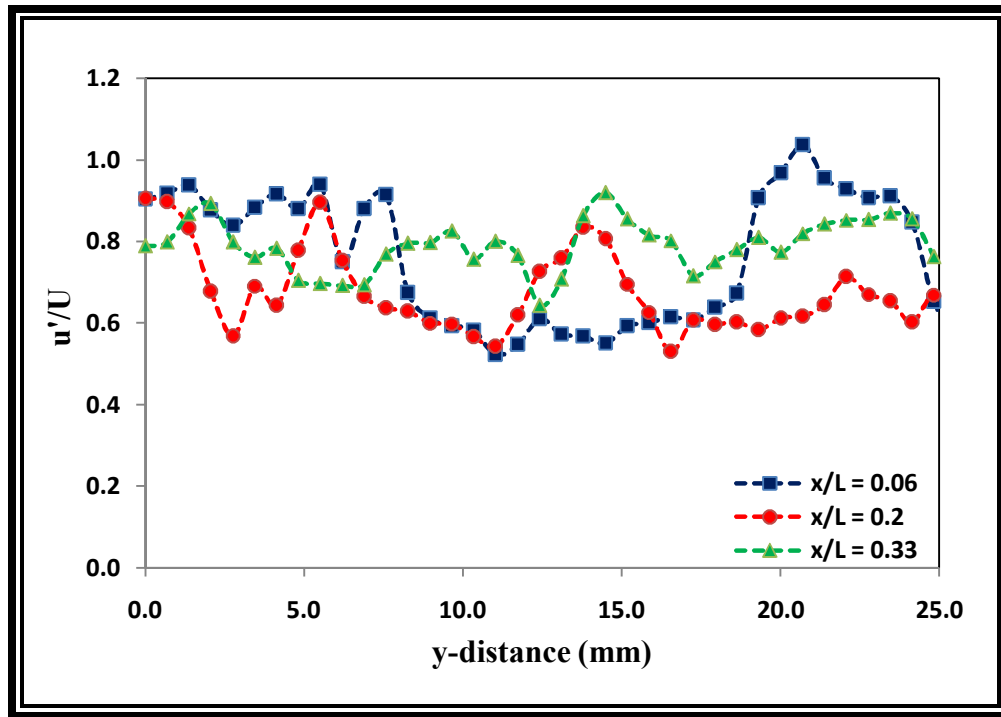


Figure 5. 28: Turbulent Intensity before the step at $Re = 3500$.

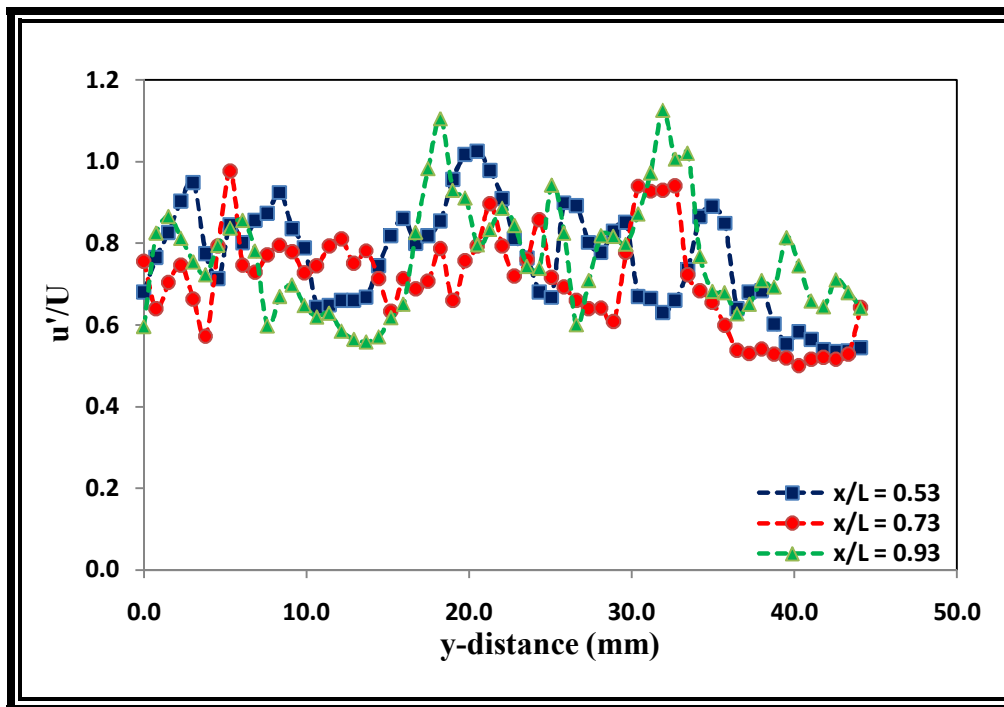


Figure 5. 29: Turbulent Intensity after the step at $Re = 3500$.

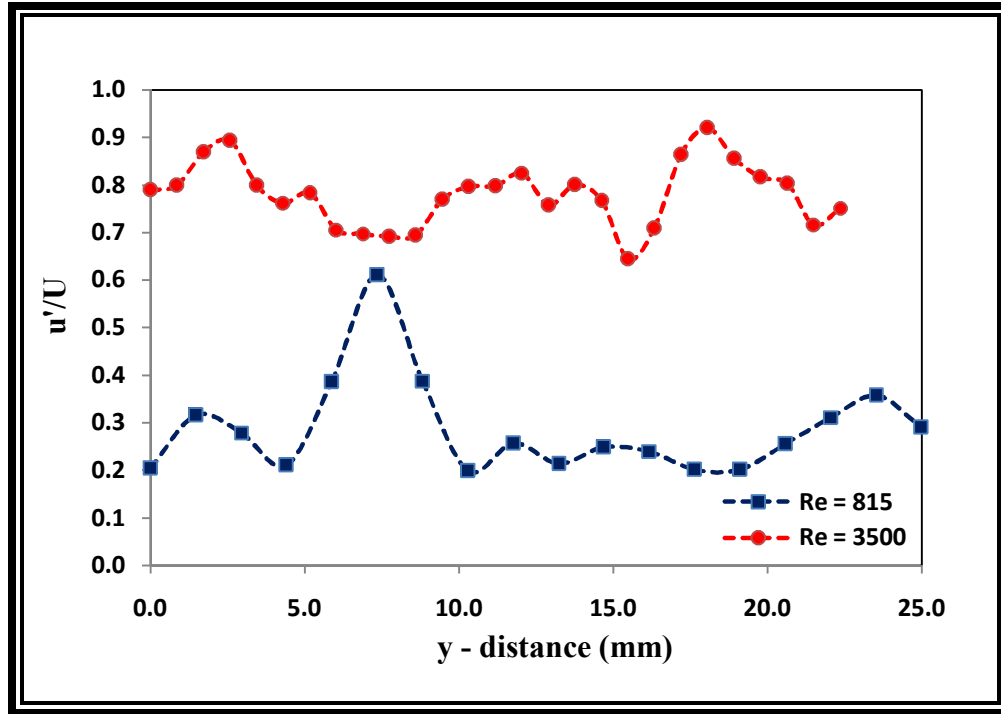


Figure 5. 30: Turbulent Intensity at $x/L = 0.33$ at different Reynolds number.

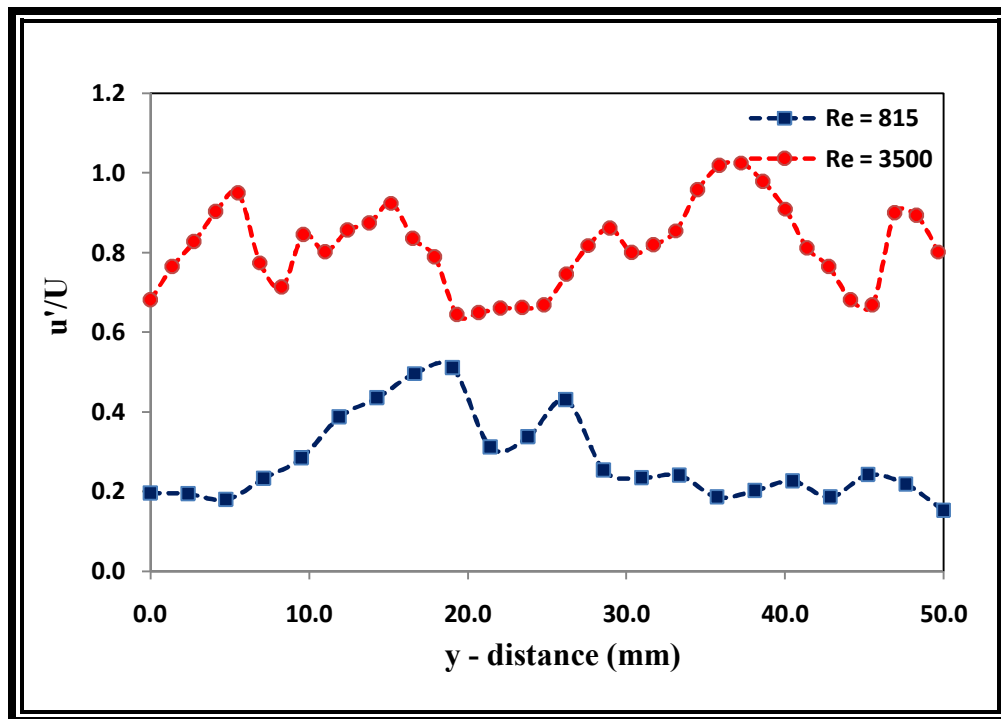


Figure 5. 31: Turbulent Intensity at $x/L = 0.73$ at different Reynolds number.

Figure 5.27 shows the turbulent intensity after the step at $Re = 815$. It is observed that the level of turbulent intensity becomes low after the step due to low velocity recirculation zone. Similar turbulent intensity distributions are shown in figure 5.28 and 5.29 for different locations of the combustor at $Re = 3500$. As the Reynolds number become higher, the turbulent intensity level also become higher. A comparison of turbulent intensity level has been shown in figure 5.30 and 5.31. Figure 5.30 shows the distribution of turbulent intensity at two different Re at $x/L = 0.33$. The figure clearly shows that the turbulence intensity level become higher at high Re value. Similar distributions were observed at $x/L = 0.73$ for the same Re values.

5.2 CFD Modeling

A simplified two dimensional computational modeling has been done for this particulate case. The primary objective of the CFD modeling was to predict the flow field before the design of the combustor had been finalized. The key parameters observed from CFD were the velocity and pressure field and also the vorticity magnitude inside the combustor. As the combustor consists of a backward facing step, some preliminary CFD analysis were done without the grid and compared with the published experimental data.

Flow through a backward facing step is one of the classical internal flow problems in fluid mechanics. Extensive numerical and experimental studies have been done on this topic. Due to the geometric simplicity and flow diagnostic technique, this phenomena has become a practice for numeric validation for computational fluid dynamics (CFD). In this paper fluid flow through a backward facing step has been studied numerically for a 2D channel having an expansion ratio of $(H/h) = 2:1$. Commercial software package *ANSYS Fluent* has been used for the numeric simulation. Different flow characteristics have been calculated at different Reynolds number ($Re = 815$ and 3500) in order to predict the actual flow behavior. Detached Eddy Simulation (DES) has been done for this study. The DES model is often referred as a

combination of RANS & LES model for application such as high-Re flow. The cost of DES computation is significantly low compare to LES modeling as it is based on one equation Spalart-Almaras model, the realizable k- ϵ model and the SST k- ω model. Calculations are done for different flow regimes. Finally the observed data such as horizontal velocity, vorticity, turbulent intensity and turbulent kinetic energy have been compared with PIV data.

5.2.1 COMPUTATIONAL DOMAIN AND MESHING

The Computational domain was developed based on the step size. An expansion ratio of 1:2 is assumed during the development of the geometry. Other parameters are assumed as a function of h . Figure 5.32 shows the schematic of the geometry of a backward facing step. The step size is assumed as 25mm. To predict accurate flow behavior the downstream domain is assumed to be 6 times longer than the step.

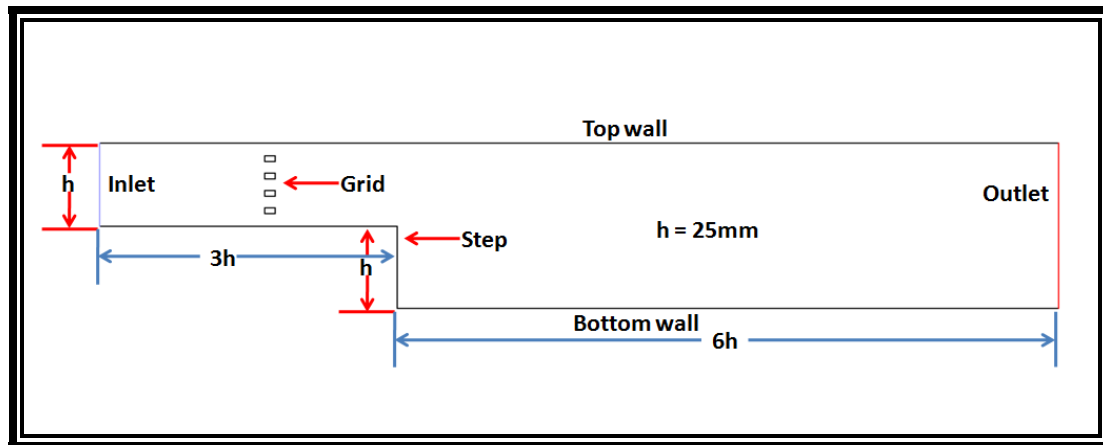


Figure 5. 32: CFD domain of a backward facing step channel.

Around 0.18 million structured quadrilateral mesh were used within the entire domain. The mesh elements were clustered near the wall boundary in order to resolve the boundary layer. Maximum face size of the mesh is assumed as 0.025mm. The orthogonal quality of the mesh remains 0.98 and maximum aspect ratio is 1.43. A mesh independence test was done based on the flow separation length at $Re = 100$. Different mesh sizes were used to check mesh

independence without the grid. Table 5.1 shows the mesh dependency on flow separation length. 5 different cases were checked for this keeping $Re=100$. From the table its clearly shown that the problem become mesh independent at mesh size of 400×450 .

Table 5.1 Mesh independency test.

Iteration	Mesh (<i>width</i> \times <i>Length</i>)	X_r/h
1000	50×100	4.8
1000	100×200	4.5
1000	300×400	3.9
1000	400×450	3.8
1000	500×500	3.8

5.2.2 CASE SETUP AND SOLUTION

A 2D planner pressure based solver was used for the simulation. Air was considered as a working fluid. Inlet boundary condition was determined based on Re . For Re calculation the hydraulic diameter is assumed as $2h$, where h is the step size. Standard least square discretization technique was used. A second order upwind solution method with SIMPLE solver was considered. Re is set as 815 and 3500 as an inlet condition for two different cases. These values were determined from the experiment in the current facility. Pressure outlet was assumed as outflow. DES model with one equation Spalart-Allmaras RANS model was chosen for the simulation. For convergence, the residue for continuity and velocity were set as 0.00001. Each solution was allowed to run 3000 iteration to met the minimum convergence criteria. The time step of each simulation was assumed as $3.33e-6$ sec. To validate the CFD model, flow separation length (X_r/h) at different Re without the grid is compared with experimental data. Figure 5.32 shows the comparison of CFD results which have a good agreement with published experimental data.

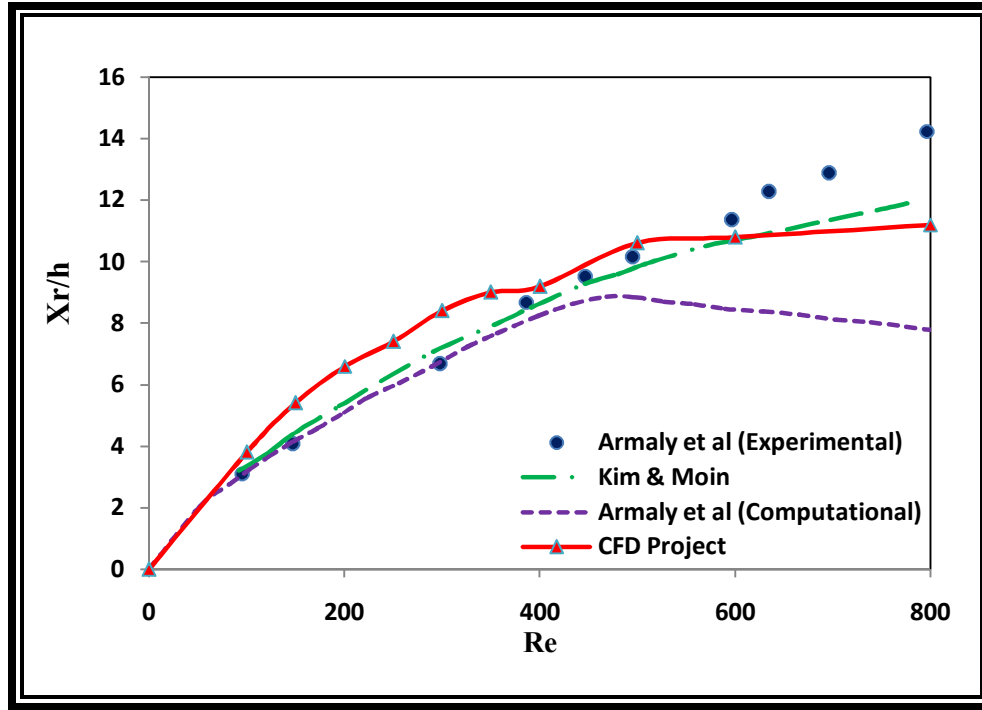


Figure 5. 33: CFD result validation with experimental data. The line 'CFD Project' represents the computational result [35].

5.2.3 CFD MEASUREMENT OF AVERAGE VELOCITY

The instantaneous velocity fields have been determined from the CFD result after the convergence of the solution. Approximately 250 velocity values were taken into consideration. Velocity has been extracted at the same locations as the PIV measurements. Figure 5.33 shows the comparison of average U-velocity distribution for PIV and CFD results. It has been observed that the CFD also predicted the five distinctive velocity peaks. But overall the CFD measurements slightly over predicted the average U-velocity at $x/L = 0.06$ location at $Re = 815$. This happens due to the discrepancy of 2D simulation and 3D experimental measurements. There are out of plane motions in the actual case which cannot be predicted by PIV measurements which acts as a contributing factor for this dissimilarity of the results. Figure 5.34 and 5.35 shows the contour of instantaneous U-velocity and V-velocity at $Re = 815$ respectively. In both case, the low velocity zones were observed after the step.

Figure 5.36 shows the average U-velocity distribution at three different locations before the step. The distributions were similar as the PIV measurements. As the fluid goes far from the grid the velocity peak become less dominants due to dissipation of kinetic energy. Similar distributions have been observed for average V-velocity distributions as well which is shown in figure 5.37. Figure 5.38 shows the instantaneous U-velocity contour at $Re = 3500$. Here the low velocity zone after the step was also observed. At higher Re value the velocity fluctuations were more frequent which was observed in figure 5.38. Similar results have been observed for instantaneous V-velocity contour which is shown in figure 5.39. The distributions of normalized kinetic energy were shown in figure 5.40. The fluctuation of kinetic energy was visible due to the grid. Five distinctive high kinetic energy peaks were observed close to the grid but the dissipation of energy become dominant as fluid goes far from the grid.

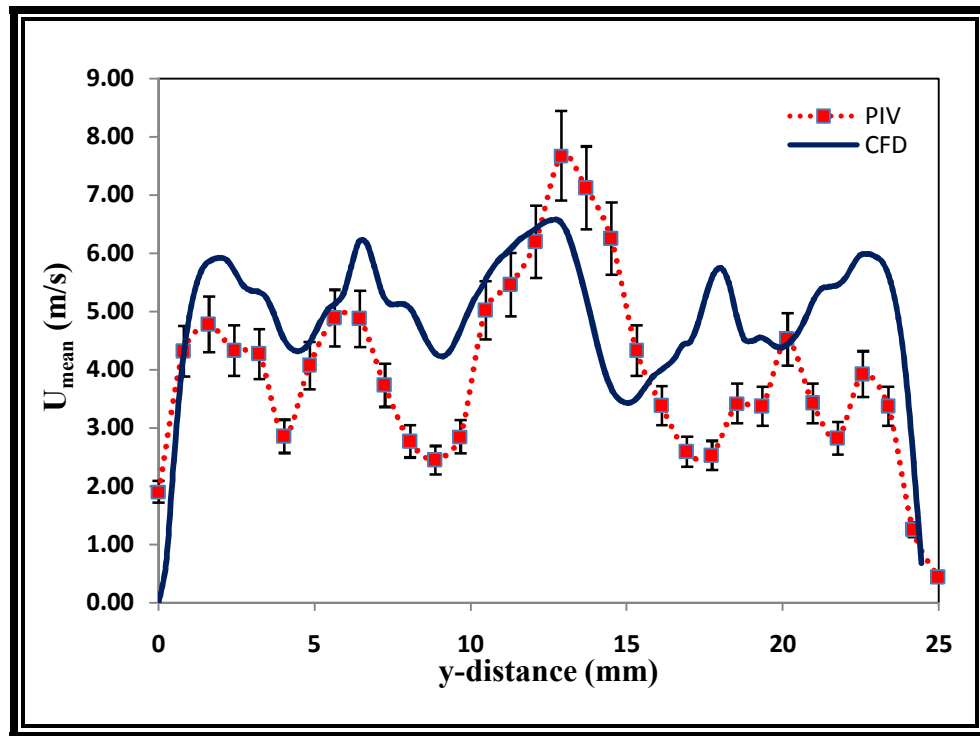


Figure 5. 34: Average U-velocity from PIV and CFD calculation at $Re = 815$ and $x/L = 0.06$.

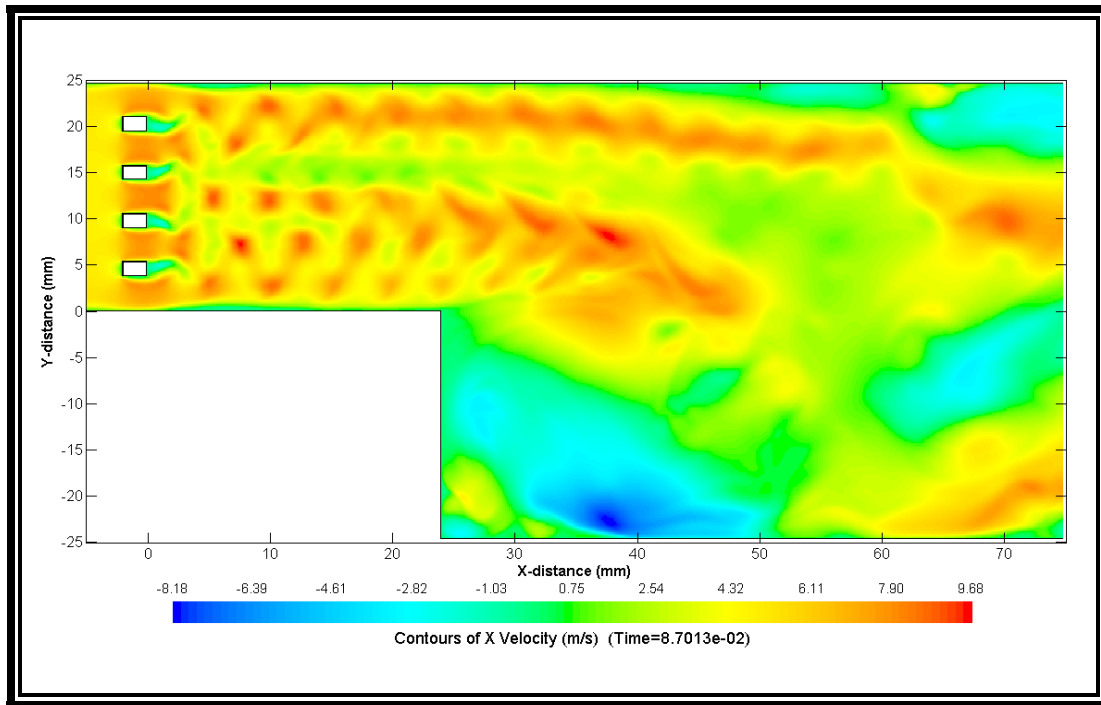


Figure 5. 35: CFD result of instantaneous U-velocity contour at $Re = 815$.

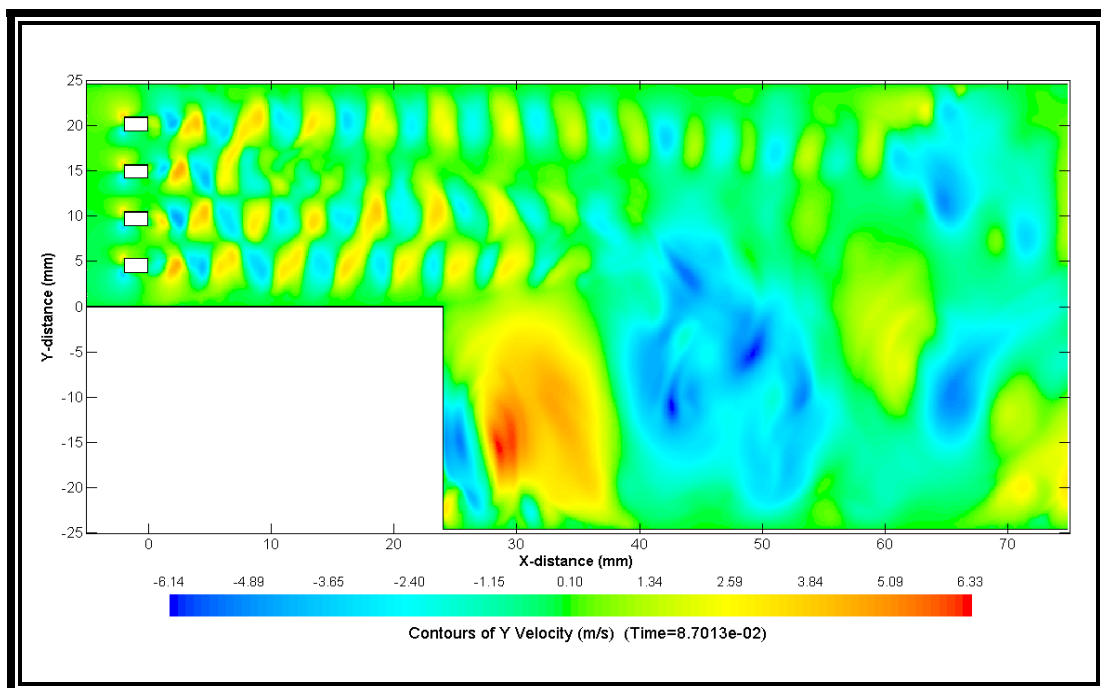


Figure 5. 36: CFD result of instantaneous V-velocity contour at $Re = 815$.

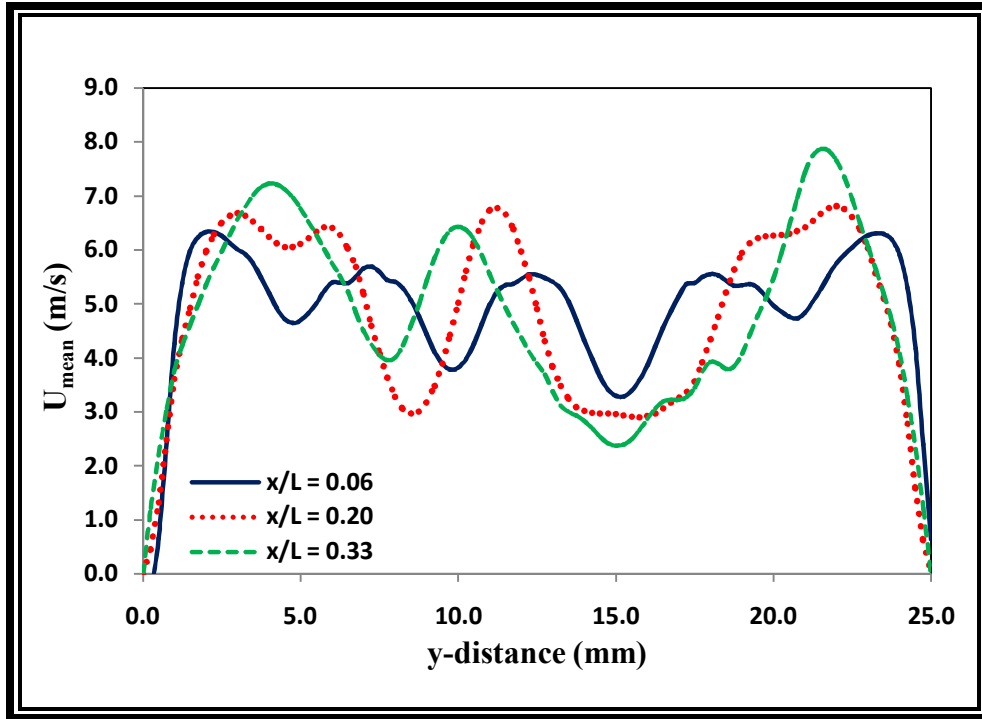


Figure 5. 37: CFD result of average U-velocity distribution before the step at $Re = 815$.

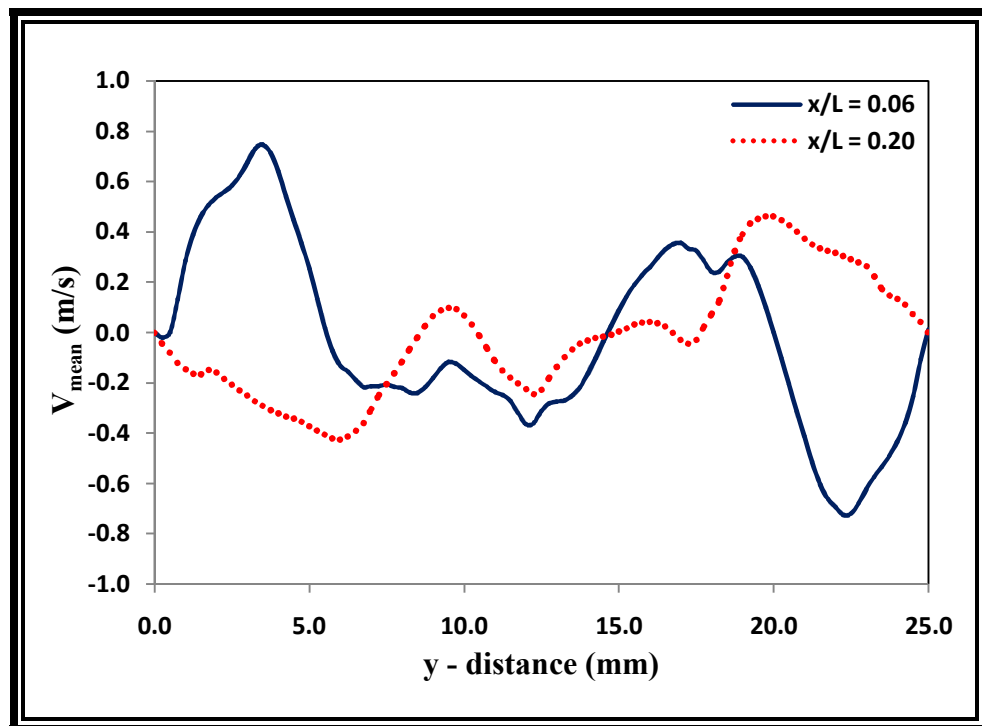


Figure 5. 38: CFD result of average V-velocity distribution before the step at $Re = 815$.

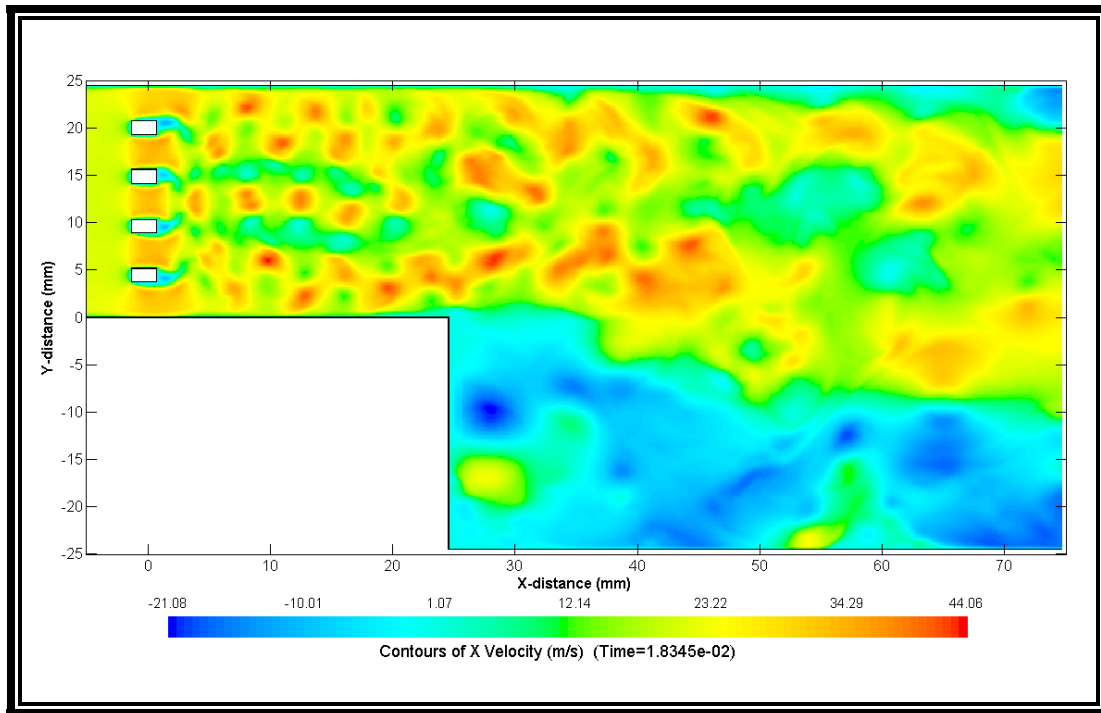


Figure 5. 39: CFD result of instantaneous U-velocity contour at $Re = 3500$.

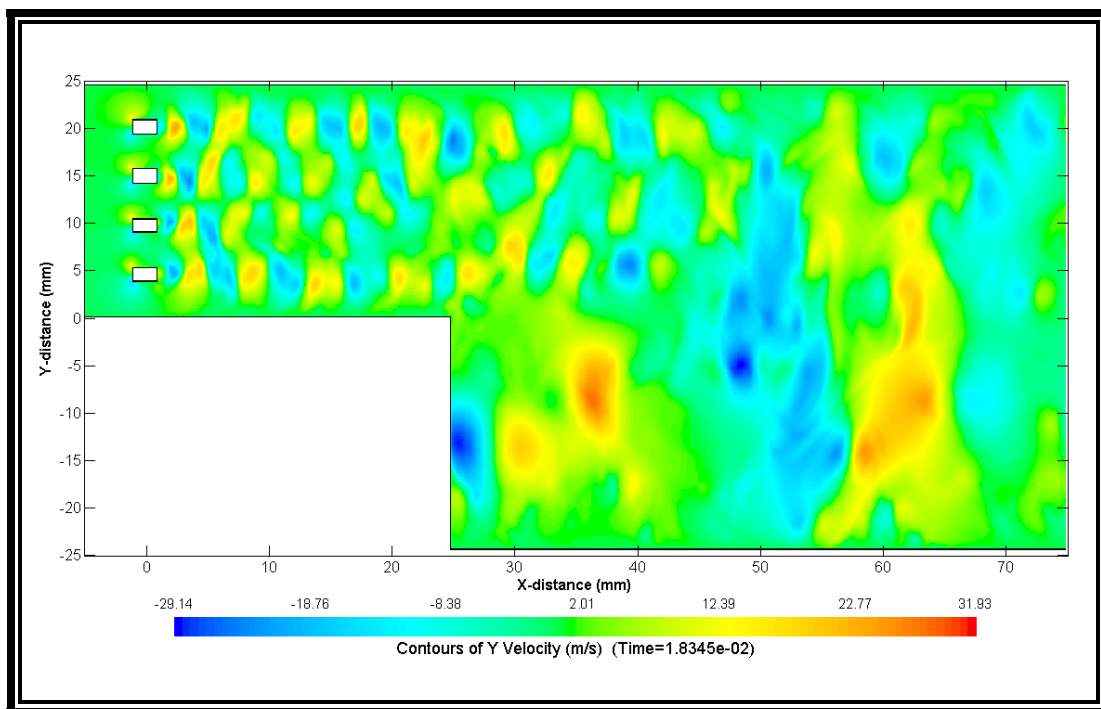


Figure 5. 40: CFD result of instantaneous U-velocity contour at $Re = 3500$.

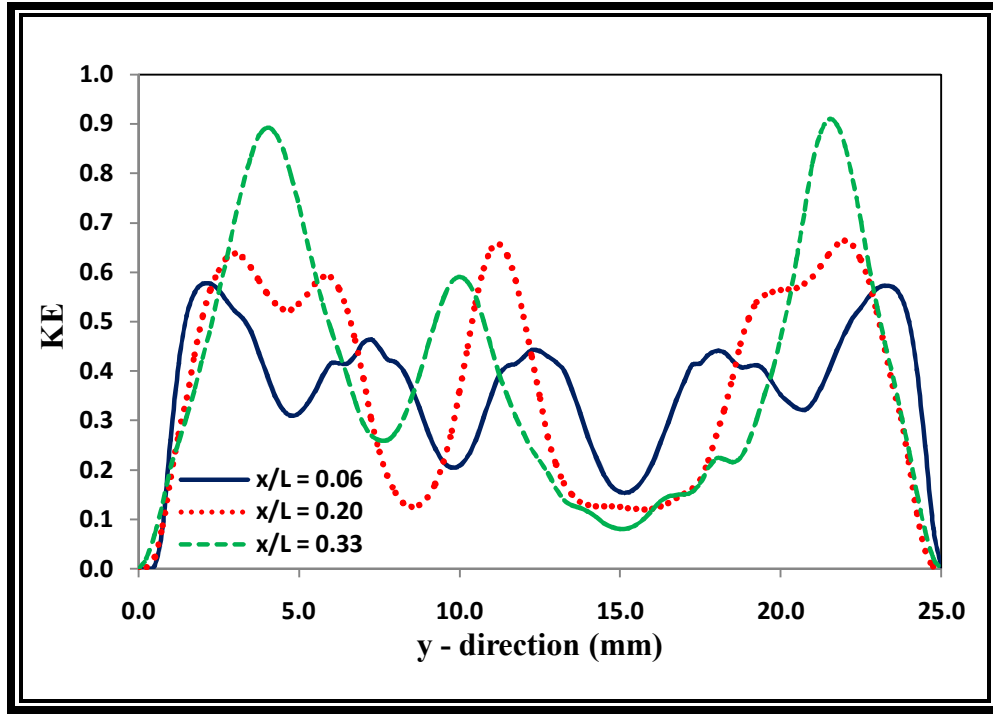


Figure 5. 41: Normalized kinetic energy distribution before the step at Re = 815.

5.2.4 CFD Measurement of Pressure

The pressure measurement shows the different vortex region inside a flow field. In this study, pressure was measured at different locations inside the combustor domain. Figure 5.41 and 5.42 shows the instantaneous static pressure contours at Re = 815 and 3500 respectively. Both figures show the negative pressure zones just after the grid which implies the vortex generation due to the grid. It also implies the vortex breakdown due to the grid turbulence. It is expected that the negative pressure zone after the step will hold the flame by supplying constant fresh air-fuel mixture during the experiment. Figure 5.43 shows the distribution of the static pressure along three different locations before the step at Re = 815. It was observed that the fluctuation of pressure is higher close to the grid and the pressure fluctuations reduce as the x/L increases. Figure 5.44 shows the static pressure distribution after the step and a large pressure drop was observed after the step due to the recirculation zone.

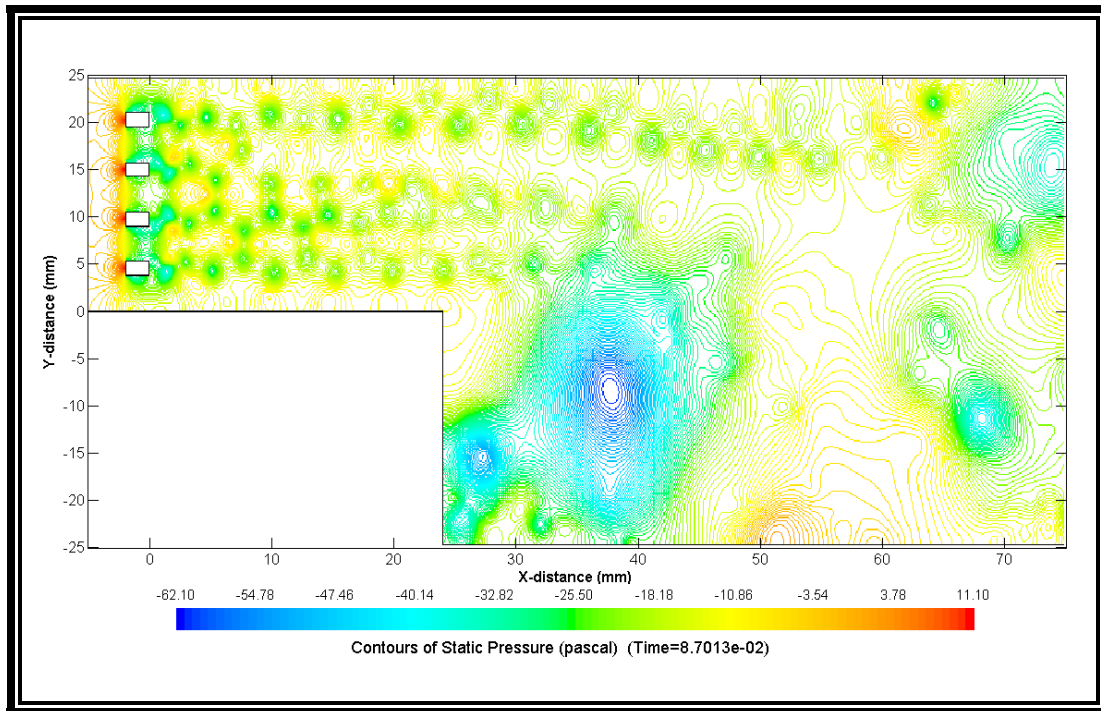


Figure 5. 42: CFD result of instantaneous pressure contour at $Re = 815$.

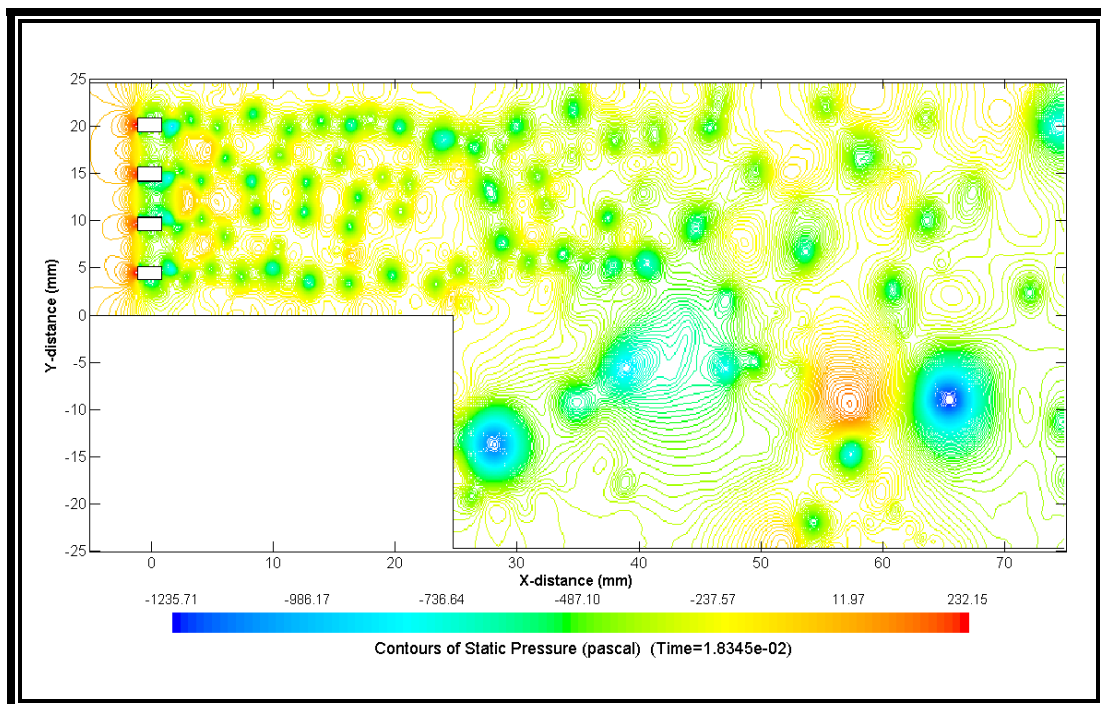


Figure 5. 43: CFD result of instantaneous pressure contour at $Re = 3500$.

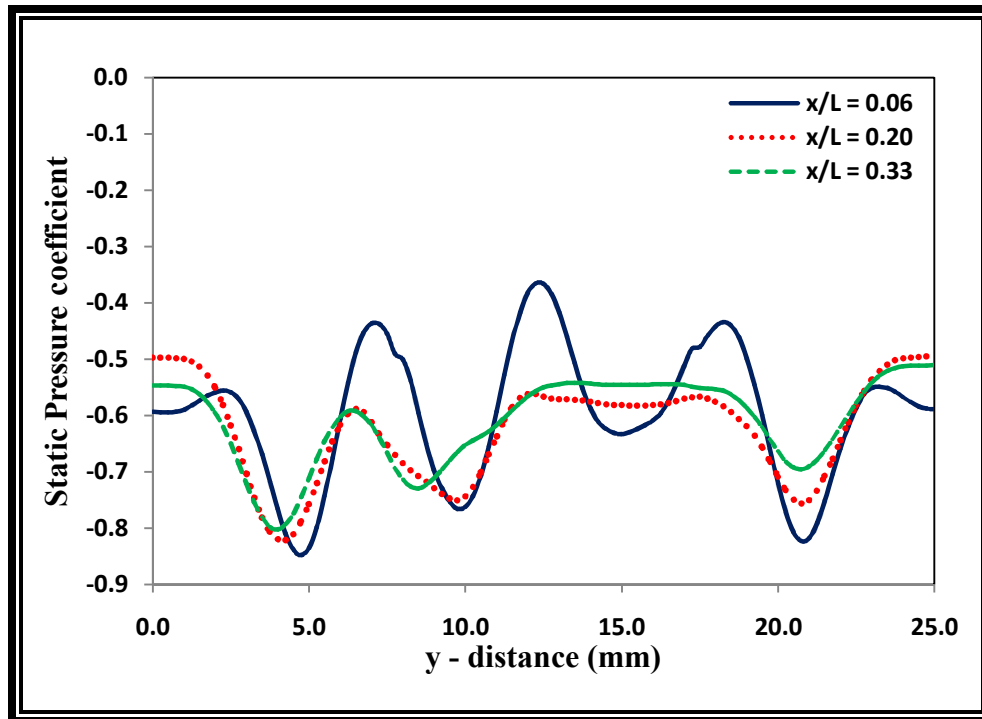


Figure 5. 44: CFD calculation of static pressure coefficient before the step at Re = 815.

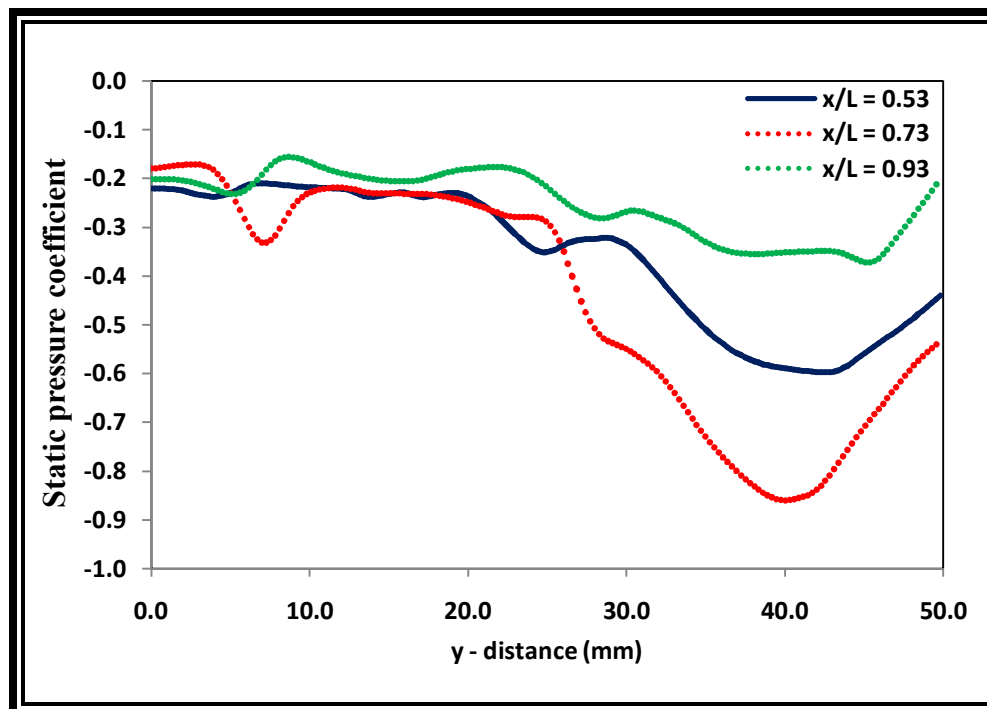


Figure 5. 45: CFD calculation of static pressure coefficient after the step at Re = 815.

5.2.5 CFD MEASUREMENT OF TURBULENT INTENSITY

The turbulent intensity has been calculated by taking 100 instantaneous velocity measurement for a certain period of time. The calculation was done by the similar process used in PIV measurements. The turbulent intensity was also compared with the PIV data which is shown in figure 5.45. It was observed that the CFD over predicted the turbulent intensity then the PIV data. Although the distribution pattern was similar, the CFD predicted higher turbulent intensity due to 2D simulation. Figure 5.46 and 5.47 show the instantaneous vorticity contours at $Re = 815$ and 3500 respectively. The vortex breakdown was clearly observed in both figures. Vortices due to boundary wall were also observed in those figures. The distributions of turbulent intensity before the step are shown in figure 5.48. This distributions were calculated at $Re = 815$. The effects of blockage ratio have been calculated by CFD analysis.

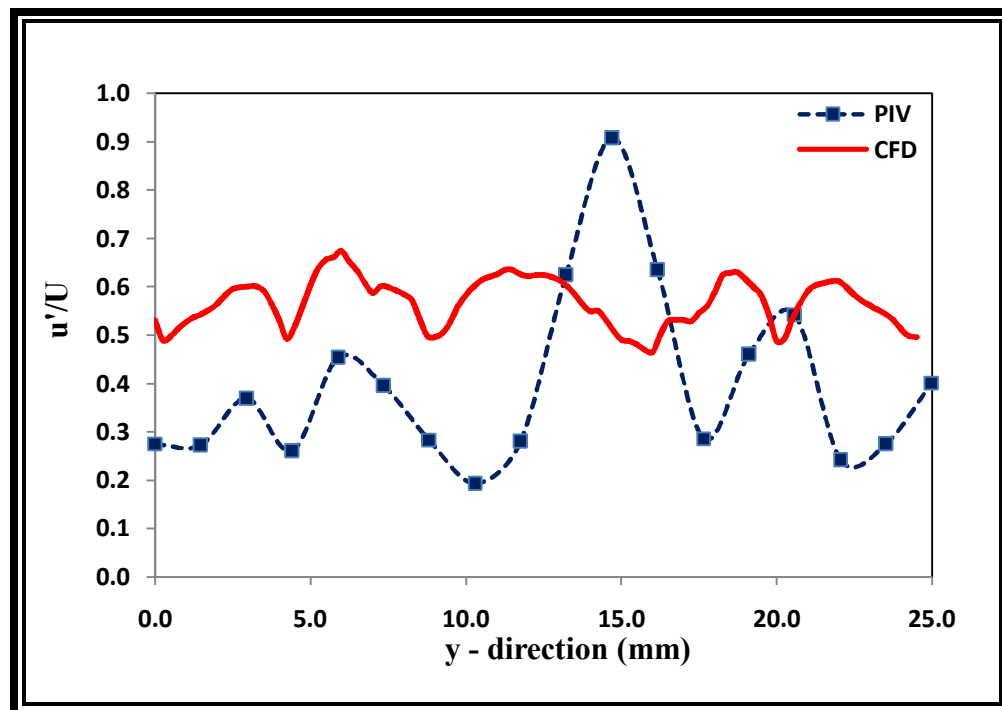


Figure 5. 46: Comparison of Turbulent Intensity at $x/L = 0.06$ for PIV and CFD.

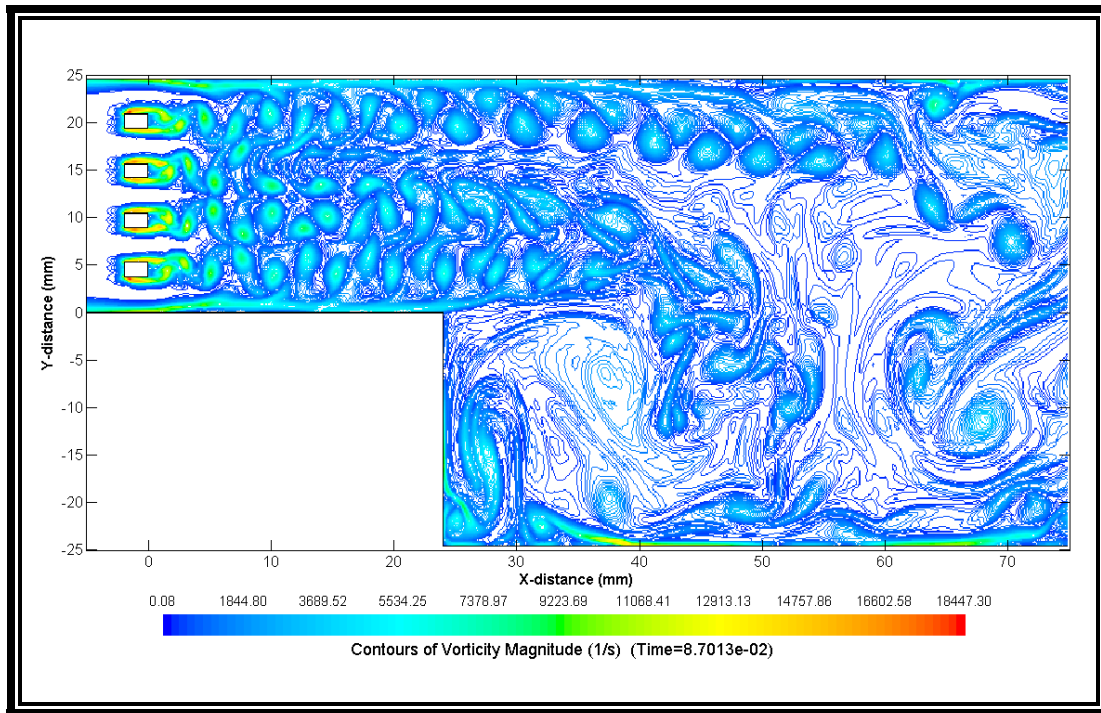


Figure 5. 47: CFD result of instantaneous vorticity contour at $Re = 815$.

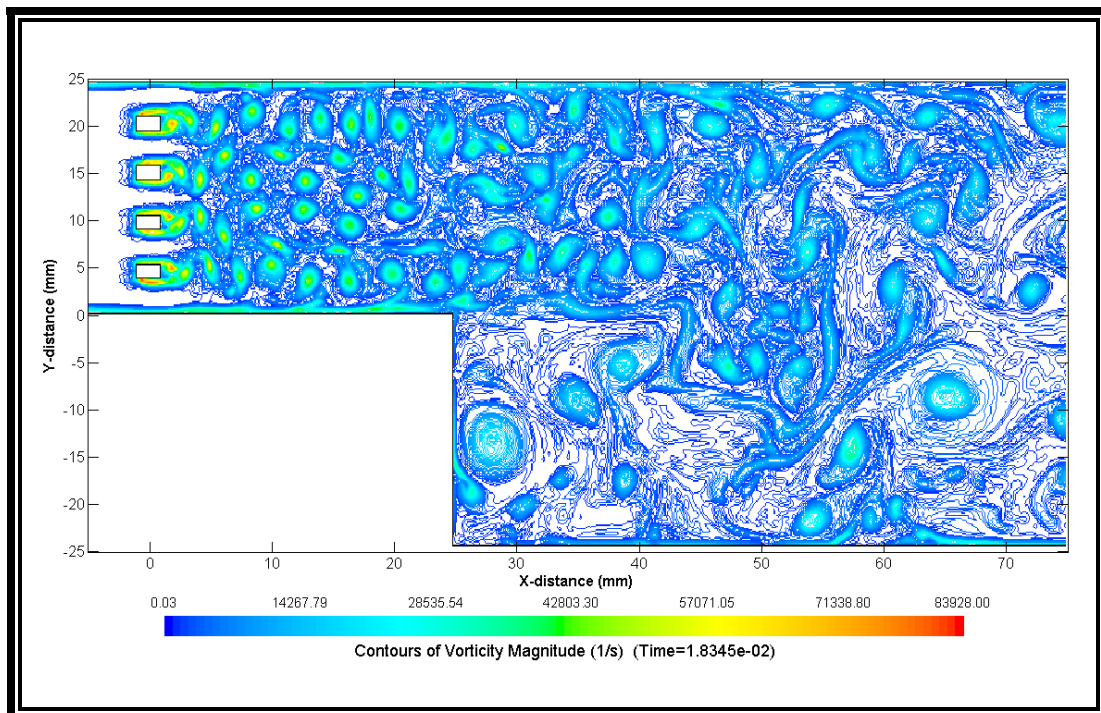


Figure 5. 48: CFD result of instantaneous vorticity contour at $Re = 3500$.

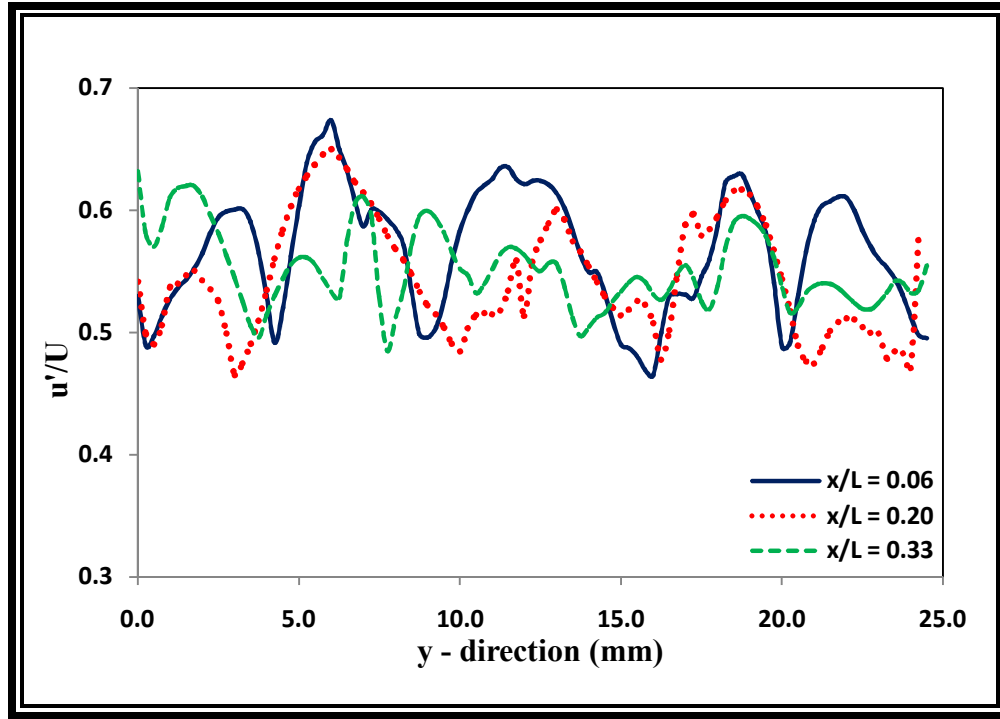


Figure 5. 49: CFD result of turbulent intensity distribution before the step at $Re = 815$.

Three different blockage ratio (BR 54, BR 61 & BR 67) have used during the simulation. The numeric value beside 'BR' represents the percentage blockage in the flow field. Figure 5.49 shows the turbulent intensity distribution for three different blockage ratio at $x/L = 0.33$. It was observed that the turbulent intensity increases as the blockage percentage increases. Moreover, the strain rate has been determined from the CFD result. Figure 5.50 shows the strain rate contour at $Re = 815$. The strain rates are higher in the place where the vorticity magnitude is higher. Figure 5.51 also shows the similar strain rate contour at $Re = 3500$. Finally the pathline has been determined which represents the particle trajectory in the flow field. Figure 5.52 shows the instantaneous pathline at $Re = 815$ which is colored by the stream function.

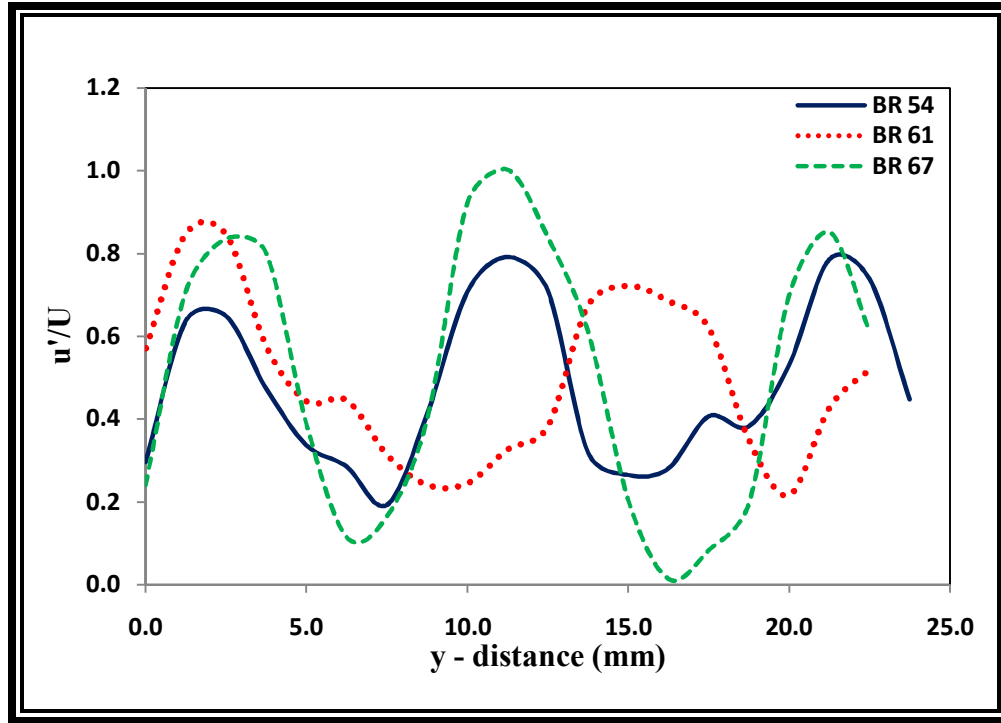


Figure 5. 50: CFD result of Turbulent intensity for different blockage ratio at $x/L=0.33$.

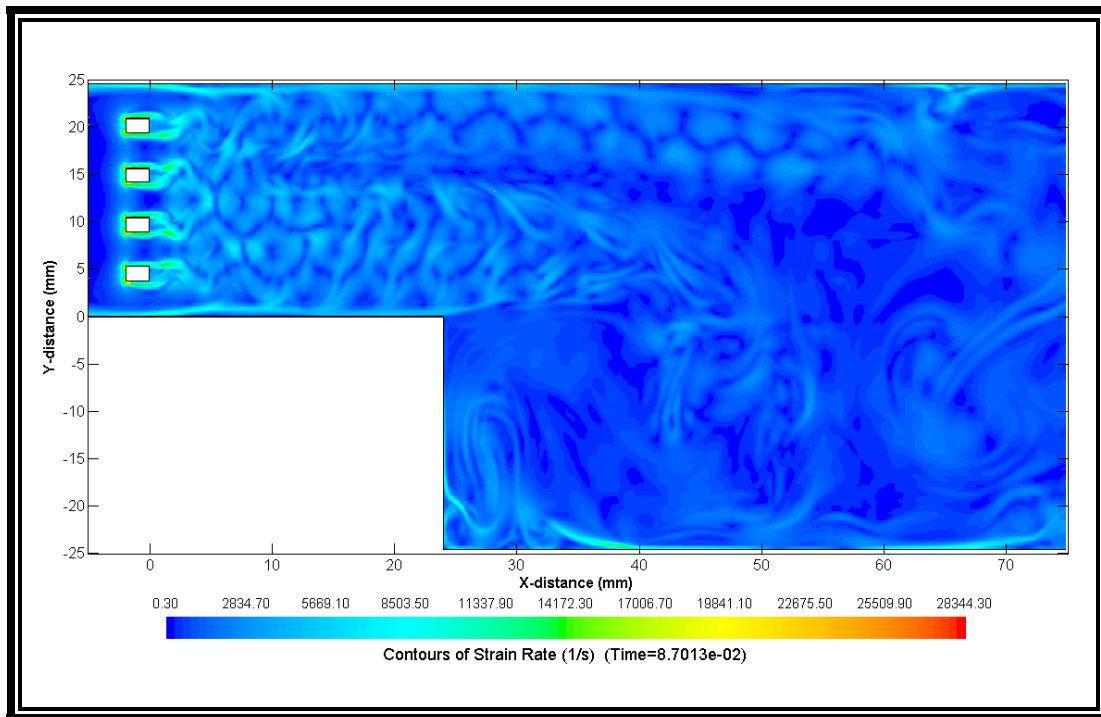


Figure 5. 51: CFD result of strain rate contour at $Re = 815$.

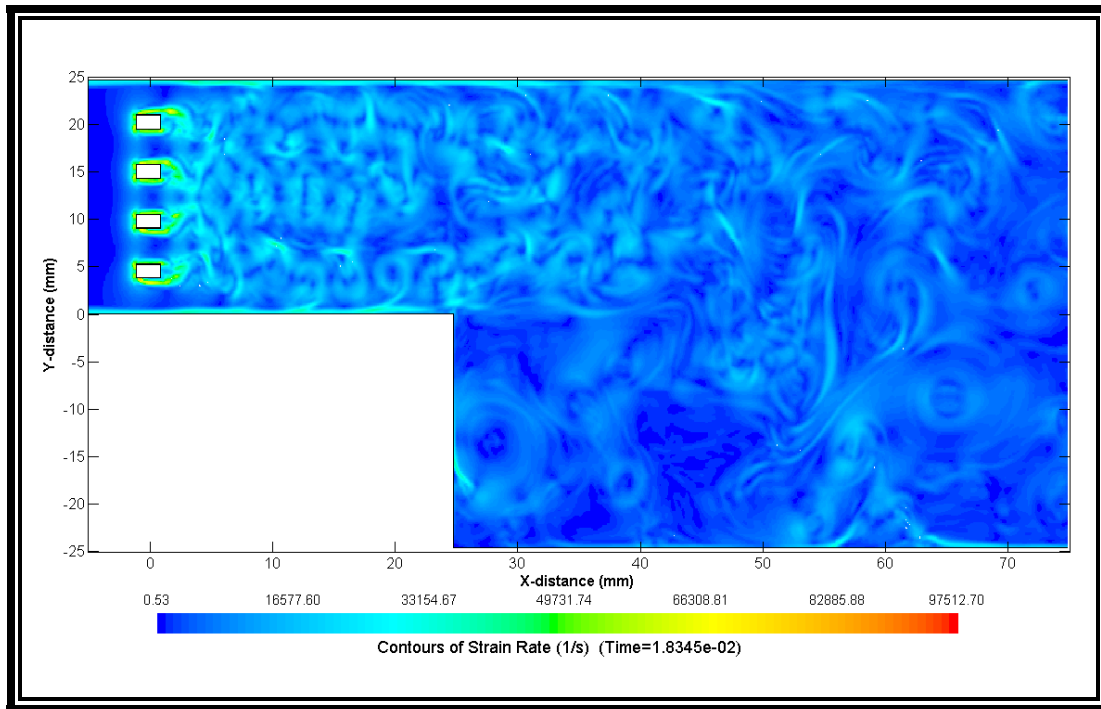


Figure 5. 52: CFD result of strain rate contour at $Re = 3500$.

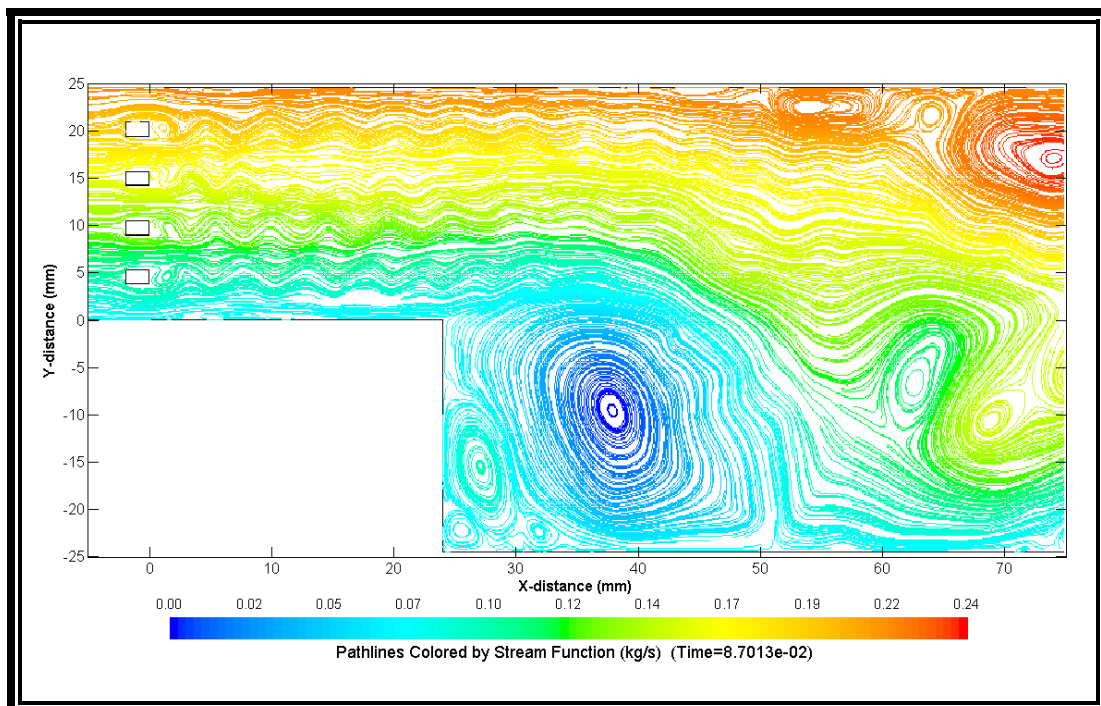


Figure 5. 53: CFD result of path line at $Re = 815$ colored by stream function.

Chapter 6: Conclusion

6.1 Summary

The overall summary of the study can be described as follow-

- An optically accessible combustor has been designed for turbulent combustion study. UNS S316 stainless steel has been selected for the combustor material and fused quartz glass has been selected for the window material. The combustor is designed for a maximum operating pressure of 6 bar. The window is designed according to this pressure and a maximum temperature of 500K.
- In order to create turbulence, a specially designed grid is installed inside the flow path of the combustor. The grid is designed with three different blockage ratio (BR = 54%, 61% & 67%).
- A backward facing step is also installed inside the combustor to achieve a recirculation zone. The sole purpose of this step is to provide fresh air-fuel mixture during experiment in order to achieve stable flame inside the chamber. Separate cooling subsystems have been designed for chamber cooling and exhaust gas cooling.
- A 10 kHz Particle Image Velocimetry (PIV) system and a 3 kHz Planer Laser Induced Fluorescence (PLIF) system have been integrated with the system in order to study the flow and the flame respectively.
- A two dimensional CFD analysis has been done by Detached Eddy Simulation (DES) model in order to resolve the characteristic flow parameters. The Quadratic mesh element is used with a two dimensional pressure based Navier-stock solver. Characteristic flow behavior such as the average U-velocity, static pressure, kinetic energy, turbulent intensity and vorticity contour have been calculated for two different Reynolds number ($Re = 815$ & 3500) and presented. The mean U-velocity is also determined and compared with PIV data.

- Results show significant agreement with experiment. The PIV data also confirms the recirculation zones and vortex breakdown due to the grid.

6.2 Future Work

The overall goal of this project is to investigate the '*Thickened Flame*' regime. In order to achieve that milestone, the following tasks need to be done with a systematic manner-

- Study of the global characteristic of premixed flames at rated condition. A series of measurements need to be done at compressible and high intensity turbulent conditions. The effects of grid and characteristics of recirculation zone will be studied. Moreover, the effect of inlet velocity, temperature, chamber pressure, blockage ratio, and step geometry on velocity fluctuations and integral length scales will be studied.
- Flow field and flame characterization with simultaneous use of TR-PIV & OH/CH PLIF will be performed. In order to capture simultaneous images of flow structures and reaction zone, high resolution imaging will be performed. This high resolution images will capture the time history information of eddies, flame contours, and their interactions.
- Measurement will be performed to understand the effect of high intensity turbulence layer of the flame such as flame wrinkling, corrugation, extinction and broadening of flame fronts due to small eddies with high rotational velocity.

Reference

- [1] Pope S.B. " Turbulent Flow ", Cambridge university press , 2000.
- [2] Reynolds, O. " An experimental investigation of the circumstances which determine whether the motion of water shall be direct or sinuous, and the law of resistance in parallel channels." Philos. R. Soc. London Ser. A 186, 935-982 .
- [3] Reynolds, O. " On the dynamical theory of incompressible viscous flow and the determination of the criterion." Philos. R. Soc. London Ser. A 123-161
- [4] Dahm, W.J.A. and P.E. Dimotakis, " Mixing at large schmidt number in the self-similar far field of turbulent jets", J. Fluid Mech. 217, 299-330
- [5] Batchelor, G.K. ' The theory of homogeneous turbulence" , Cambridge university press.
- [6] Monin, A.S. and A. M. Yaglom, " Statistical Fluid Mechanics: Mechanics of turbulence, Volume 2. Cambridge, MA: MIT Press.
- [7] Panchev, S. " Random functions and turbulence", Oxford: press
- [8] Lesieur, M. "Turbulence in Fluid", 2nd edition. Dordrecht: Kluwer
- [9] McComb, W.D. " The physics of Fluid Turbulence ", Oxford university press
- [10] Kurian T and Fransson J H M 2007 *Fluid Dyn. Res* 41 0217403
- [11] Mordant N, Metz P, Michel O and Pinton, "Measurement of lagrangian velocity in fully developed turbulence", J-F 2001 Phys. Rev. Lett. 87 214501.
- [12] A Arne`odo et al " Universal Intermittent properties of particle trajectory in highly turbulent flow", Phys. Rev. Lett. 100 254504, 2008.
- [13] Tavoularis S 2005 Measurement in fluid mechanics, Cambridge University Press.
- [14] Mckeen B J et al 2007 in Springer handbook of experimental fluid mechanics edited by Tropea C, Yarin A L and Foss J F (Berlin: Springer) pp. 215–471
- [15] Elsinga G E, Scarano F, Wieneke B and van Oudheusden B W 2006 Exp. Fluids 41 933
- [16] P. Saarenrinne, M. Piirto, 'Turbulent kinetic energy dissipation rate estimation rate from PIV velocity vector fields', Experiments in fluids, s300-s307
- [17] Elasnér JW, Elsnér W, 'On the measurement of turbulent energy dissipation', Measurement Sci Technol 7: 1334-1348, 1996
- [18] Saarenrinne P, Piirto M, ' Turbulent kinetic energy dissipation rate estimation from PIV vector fields', Proceedings 3rd International Workshop on PIV'99, Santa Barbara, 1999

- [19] Tsinober A, Kit E, Dracos T , ' Experimental investigation of the field of velocity gradients in turbulent flows', J of Fluid Mech, 242: 169-192 (1992)
- [20] Kolmogorove, A.N. (1941a), 'Dissipation of energy in locally isotropic turbulence.' Dokl. Akad. Nauk SSSR 32, 19-21
- [21] P.A. Davidson, ' Turbulence, An Introduction for scientists and engineers' Oxford University Press 2004
- [22] Comte-Bellot, G. and S. Corrsin (1966), The use of a contraction to improve the isotropy of grid-generated turbulence. Journal of Fluid Mechanics, 25, 657-682
- [23] Armaly, B. F., Durst, F., Peireira, J. C. F., Scho¨nung, B., 1983, Experimental and theoretical investigation of backward-facing step flow, J. Fluid Mech.,127, pp. 473–496.
- [24] Lee, Y. S. and Smith, L. C., 1986, Analysis of power-law viscous materials using complex stream, potential and stress functions, in Encyclopedia of Fluid Mechanics, vol.1, Flow Phenomena and Measurement, ed. N. P. Cheremisinoff, pp. 1105–1154.
- [25] Roache, P. J., 1972, Computational Fluid Dynamics, Hermosa, New Mexico, pp. 139–173.
- [26] Taylor, T. D., and Ndefo, E., 1971, Computation of viscous flow in a channel by the method of splitting, Proc. of the Second Int. Conf. on Num. Methods in Fluid Dynamics, Lecture Notes in Physics, vol. 8, pp. 356–364, Springer Verlag, New York.
- [27] Durst, F., and Peireira, J. C. F., 1988, Time-dependent laminar backward facing step flow in a two-dimensional duct, ASME J. Fluids Eng., 110, pp. 289–296.
- [28] Alleborn, N., Nandakumar, K., Raszillier, H., and Durst, F., 1997, Further contributions on the two-dimensional flow in a sudden expansion, J. Fluid Mech., 330, pp. 169–188.
- [29] Brandt, A., Dendy, J. E., and Ruppel, H., 1980, The multigrid method for semi-implicit hydrodynamic codes, J. Comput. Phys., 34, pp. 348–370.
- [30] Hackbusch, W., 1985, Multigrid Methods for Applications, Springer, Berlin.
- [31] Lange, C. F., Scha¨fer, M., and Durst, F., 2002, Local block refinement with a multigrid flow solver, Int. J. Numer. Methods Fluids 38, pp. 21–41.
- [32] Kim, J., and Moin, P., 1985, Application of a fractional-step method to incompressible Navier-Stokes equations, J. Comput. Phys., 59, pp. 308–323.
- [33] Durst, F., and Peireira, J. C. F., and Tropea, C., 1993, The plane symmetric sudden-expansion flow at low Reynolds numbers, J. Fluid Mech., 248, pp.567–581.
- [34] Kaiktsis, L., Karniadakis, G. E., and Orszag, S. A., 1996, Unsteadiness and convective instabilities in a two-dimensional flow over a backward-facing step, J. Fluid Mech., 321, pp. 157–187.

- [35] M.A Hossain, M. T Rahman, S. Ridwan, ' Numerical Investigation of Flow through a 2D backward facing step channel ', International Journal of Engineering Research and Technology , Vol 2, Issue 10, 2013
- [36] Stephen R. Turns, ' An Introduction to Combustion, concept and application ', McGraw Hill, 3rd ed.
- [37] G. Dixon-Lewis, F.A. Goldsworthy, J.B. Greenberg, Proc. R. Soc. London Ser. A 346 (1976) 261.
- [38] W.C. Gardner Jr. (Ed.), Combustion Chemistry, Springer-Verlag, New York, 1984.
- [39] M. Frenklach, H. Wang, J. Rabinowitz, Prog. Energy Combust. Sci. 18 (1992) 47.
- [40] P. Dagaut, M. Reuillon, J.C. Boetner, M. Cathonnet, Proc. Combust. Inst. 25 (1994) 919.
- [41] N.M. Marinov, W.J. Pitz, C.K. Westbrook, M.J. Castaldi, S.M. Senkan, Combust. Sci. Technol. 116– 117 (1996) 211.
- [42] H.J. Curran, P. Gaffuri, W.J. Pitz, C.K. Westbrook, Combust. Flame 114 (1998) 149.
- [43] E. Ranzi, M. Dente, A. Goldaniga, G. Bozzano, T. Faravelli, Prog. Energy Combust. Sci. 27 (2001) 99.
- [44] J.M. Simmie, Prog. Energy Combust. Sci. 29 (2003) 599.
- [45] M.V Petrova, F.A Williams, ' A small detailed chemical-kinetic mechanism for hydrocarbon combustion ', combustion and flame 144 (2006) 526- 544
- [46] Friedman, R., and Burke, E., 'Measurement of Temperature Distribution in a Low-Pressure Flat Flame,' Journal of Chemical Physics, 22: 824-830 (1954)
- [47] Fristorm, R. M., Flame structure and Process, Oxford University Press, New York, 1995
- [48] Lewis, B., and Von Elbe, G., Combustion, flame and Explosion of gases, 3rd Ed, Academic Press, Orlando , FL, 1987
- [49] Gordon, A.G., The Spectroscopy of Flames, 2d Ed., Halsted Press, New work, 1974
- [50] Gordon, A.G., Wolfhard, H. G., Flames: Their Structure, Radiation and Temperature, 4th Ed., Halsted Press, New York, 1979
- [51] Vagelopoulos, C.N. and Egolfopoulos, F.N., Twenty-seventh Symposium (International) on Combustion, p.513, 1998.
- [52] Vagelopoulos, C.M., Egolfopoulos, F.N., and Law, C.K., *25th Symp. (Int'l.) on Combust.* p. 1341 (1994);
- [53] Van Maaren, A., Thung, D.S. and de Goey, L.P.H. (1994) Measurement of flame temperature and adiabatic burning velocity of methane/air mixtures. Combust. Sci. Technol., 96, 327.

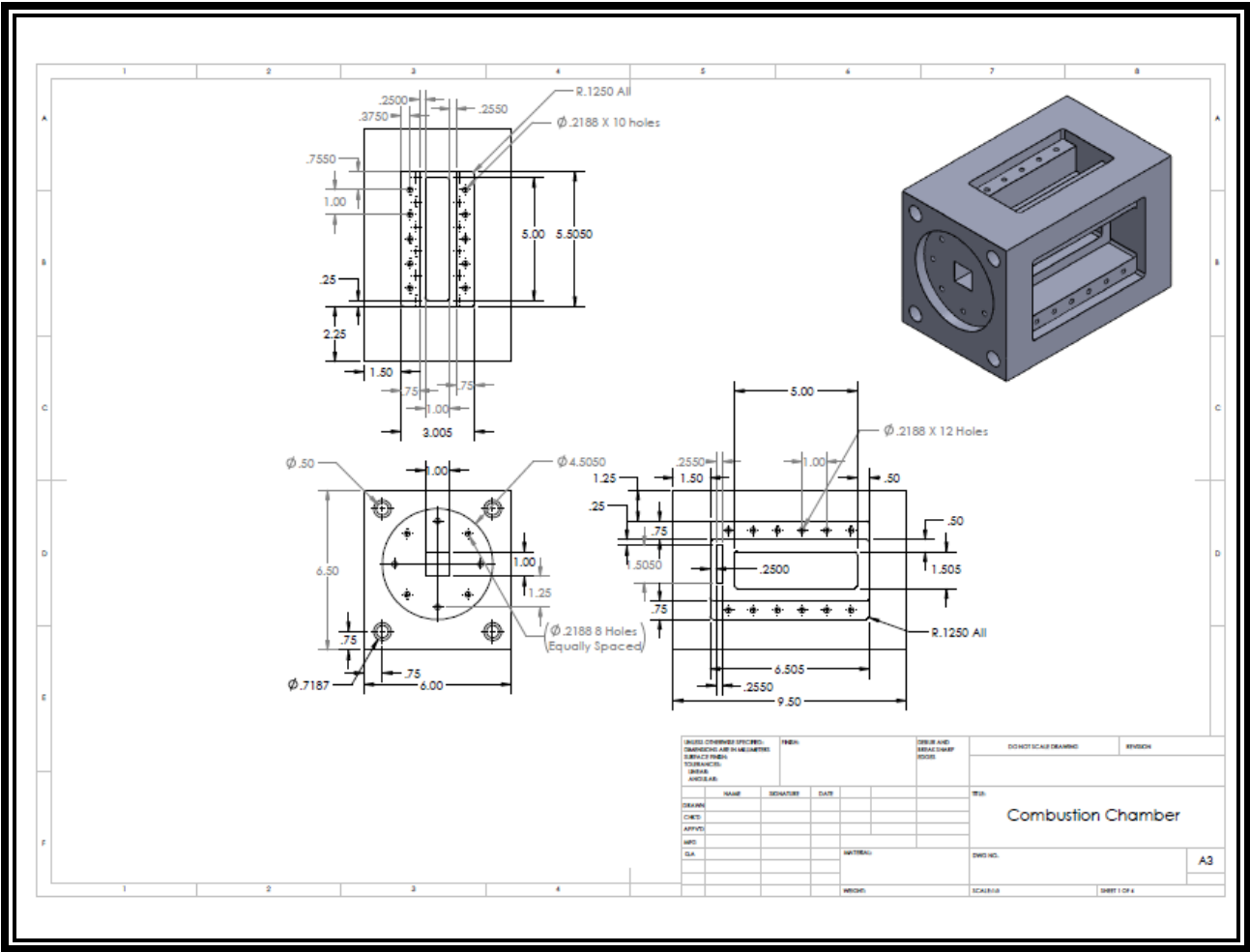
- [54] Yan, B.; Wua, Y.; Liu, C.; Yu, J. F.; Li, B.; Li, Z. S.; Chen, G.; Bai, X. S.; Aldén, M.; Konnov, A. A. *Int. J. Hydrogen Energy* 2003, 36, 3769–3777.
- [55] Takizawa, K.; Takahashi, A.; Tokuhashi, K.; Kondo, S.; Sekiya, A. " Burning velocity measurement of fluorinated compounds by the spherical-vessel method *Combust. Flame* 2005, 141, 298–307.
- [56] Liao, S. Y.; Jiang, D. M.; Cheng, Q. "Determination of burning velocity for natural gas." *Fuel* 2004, 83, 1247–1250.
- [57] Gu, X. J.; Haq, M. Z.; Lawes, M.; Wooley, R., "Laminar burning velocity and Markstein lengths of methane-air mixture", *Combust. Flame* 2000, 121, 41–58.
- [58] Stone, R.; Clarke, A.; Beckwith, P. Correlations for the Laminar-Burning Velocity of Methane/Diluent/Air Mixtures Obtained in Free-Fall Experiments *Combust. Flame* 1998, 114, 546–555.
- [59] Iijima, T.; Takeno, T., " Effect of temperature and pressure on buring velocity", *Combust. Flame* 1986, 65, 35–43.
- [60] Sharma, S. P.; Agrawal, D. D.; Gupta, C. P., " The pressure and temperature dependency on burning velocity in a spherical combustion bomb", *Proc. Combust. Inst.* 1981, 18, 493–501.
- [61] Gregory P. Smith, David M. Golden, Michael Frenklach, Nigel W. Moriarty, Boris Eiteneer, Mikhail Goldenberg, C. Thomas Bowman, Ronald K. Hanson, Soonho Song, William C. Gardiner, Jr., Vitali V. Lissianski, and Zhiwei Qin http://www.me.berkeley.edu/gri_mech/
- [62] Egolfopoulos F.N., Cho, P. and Law, C.K., " Laminar flame speeds of methane-air mixtures under reduced and elevated pressures *Combust. Flame* 76, 375 (1989)
- [63] Garforth, A.M. and Rallis, C.J., " Laminar burning velocity of stoichiometric methane-air: pressure and temperature dependence *Combust. Flame* 31, 53 (1978).
- [64] Babkin, V.S., Kozachenko, L.S., and Kuznetsov, I.L., *Zh. Prikl. Mekhan. Tekn. Fiz.* 145 (1964);
- [65] Babkin, V.S. and Kozachenko, L.S., *Combust. Explosion and Shock Waves* 2(3), 46 (1966);
- [66] Babkin, V.S., V'yun, A.V. and Kozachenko, L.S., *Combust. Explosion and Shock Waves* 2(2), 32 (1966).
- [67] Andrews, G.E. and Bradley, D., *Combust. Flame* 19, 275 (1972). Lijima, T. and Takeno, T., *Combust. Flame* 65, 35 (1986).
- [68] Lijima, T. and Takeno, T., *Combustion and Flame* 65, 35(1986)
- [69] Mohammad Akram, Priyank Saxena and Sudarshan Kumar, ' Laminar Burning Velocity of Methane-Air Mixtures at Elevated Temperature', *Energy and Fuels*, 27, 3460-3466 (2013)
- [70] Cheng RK, Shepherd IG. Intermittency and conditional velocities inpremixed conical turbulent flames. *Combust Sci Technol* 1987;52:353–75.

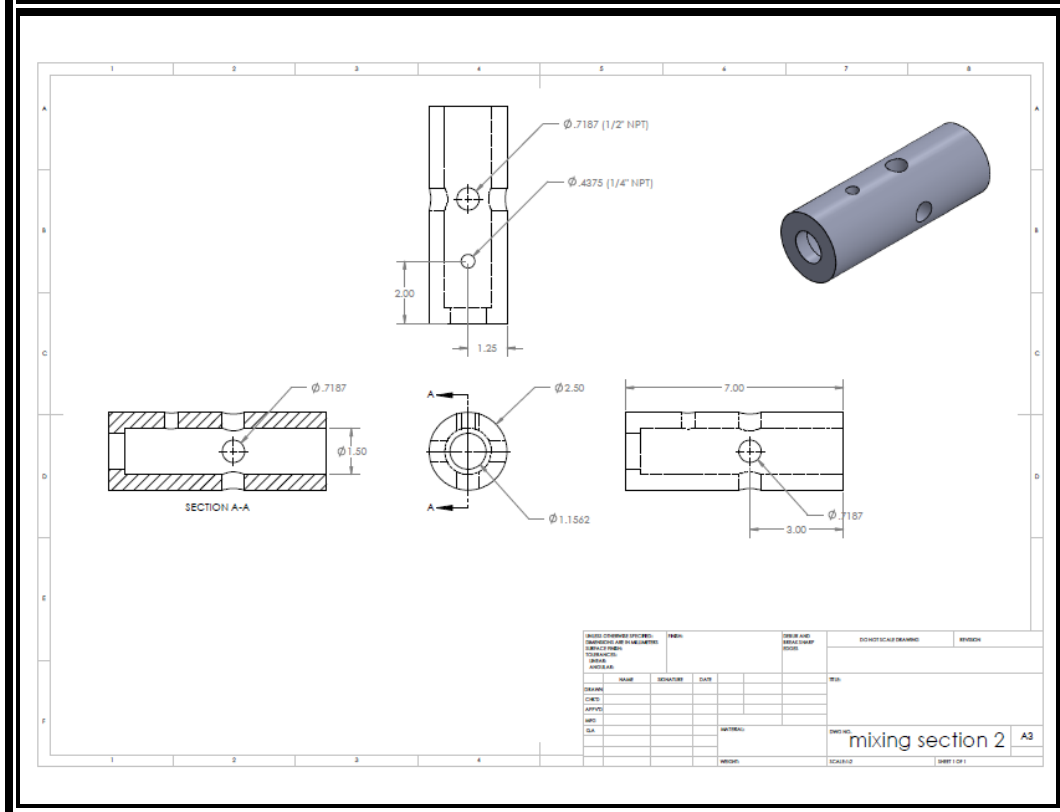
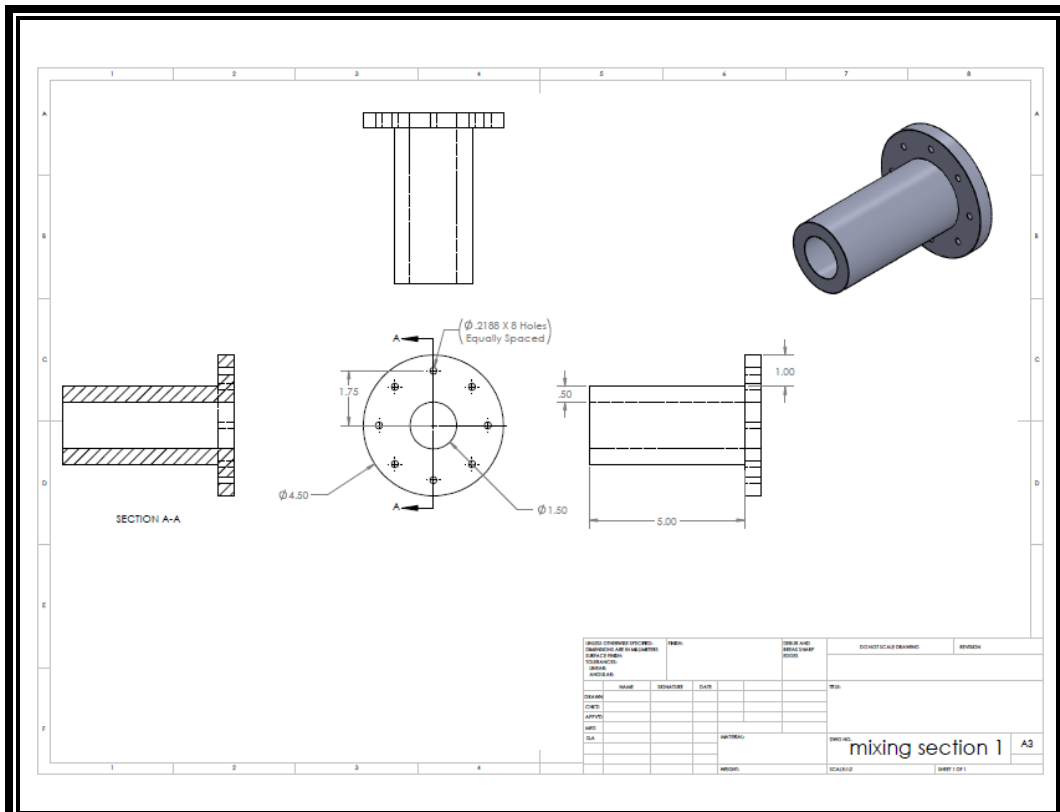
- [71] Chen Y-C, Bilger RW. Experimental investigation of three dimensional flame front structure in premixed turbulent combustion-I: hydrocarbon air Bunsen flames. *Combust Flame* 2002;131:400–35.
- [72] Filatyev SA, Driscoll JF, Carter CD, Donbar JM. Measured properties of turbulent premixed flames for model assessment, including burning velocities, stretch rates and surface densities. *Combust Flame* 2005;141:1–21.
- [73] Cheng RK, Shepherd IG. Intermittency and conditional velocities in premixed conical turbulent flames. *Combust Sci Technol* 1987;52:353–75.
- [74] Shepherd IG, Cheng RK. The burning rate of premixed flames in moderate and intense turbulence. *Combust Flame* 2001;127: 2066–75.
- [75] Driscoll JF, Gulati A. Measurement of various terms in the turbulent kinetic energy balance within a flame and comparison with theory. *Combust Flame* 1988;72:131–52.
- [76] Cheng RK. Velocity and scalar characteristics of premixed turbulent flames stabilized by weak swirl. *Combust Flame* 1995;101:1–14.
- [77] Cho P, Law CK, Hertzberg JR, Cheng RK. Structure and propagation of turbulent premixed flames stabilized in a stagnation flow. *Proc Combust Inst* 1986;21:1493–9.
- [78] Kobayashi H, Kawahata T, Seyama K, Fujimari T, Kim J-S. Relationship between the smallest scale of flame wrinkles and turbulence characteristics of high pressure, high temperature turbulent premixed flames. *Proc Combust Inst* 2002;29:1793–800
- [79] Smith KO, Gouldin FC. Turbulence effects on flame speed and flame structure. *AIAA J* 1979;11,5:1243–50.
- [80] Lawn CJ, Schefer RW. Scaling of premixed turbulent flames in the corrugated regime. *Combust Flame* 2006;146:180–99.
- [81] Kido H, Nakahar M, Nakashima K, Hashimoto J. Influence of local flame displacement velocity on turbulent burning velocity. *Proc Combust Inst* 2002;29:1855–61.
- [82] Borghi, R., *On the structure and Morphology of Turbulent Premixed Flames*. Recent Advances in Aeronautical Science. 1985: Plenum Press, New York.
- [83] Peters, N., *The turbulent burning velocity for small-scale and large-scale turbulence*. *J. Fluid Mech.*, 1999. 384: p. 107-132.
- [84] Buschmann A, Dinkelacker F, Schafer T, Schafer M, Wolfrum J. Measurement of the instantaneous detailed flame structure in turbulent premixed combustion. *Proc Combust Inst* 1996;26:437–45.
- [85] Zimont, V., *Theory of turbulent combustion of homogenous fuel mixture at high Reynolds numbers*. *Fizika Gorenya i Vzryva*, 1979. 15: p. 23-32.

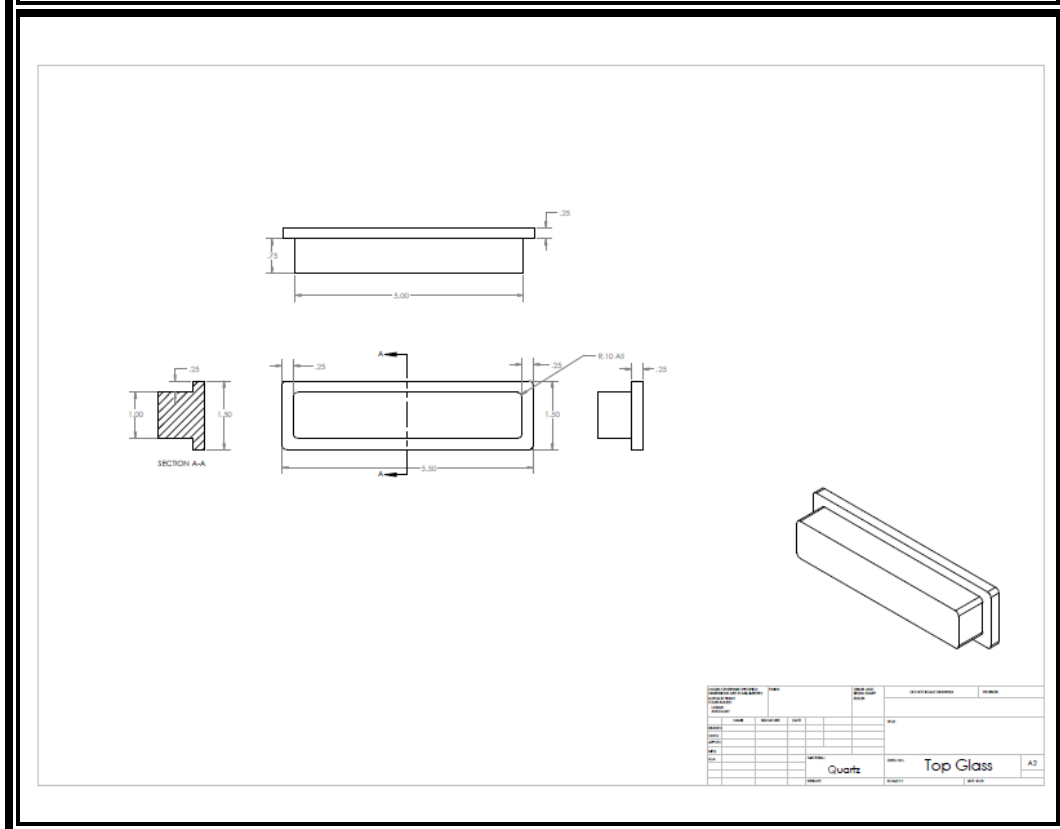
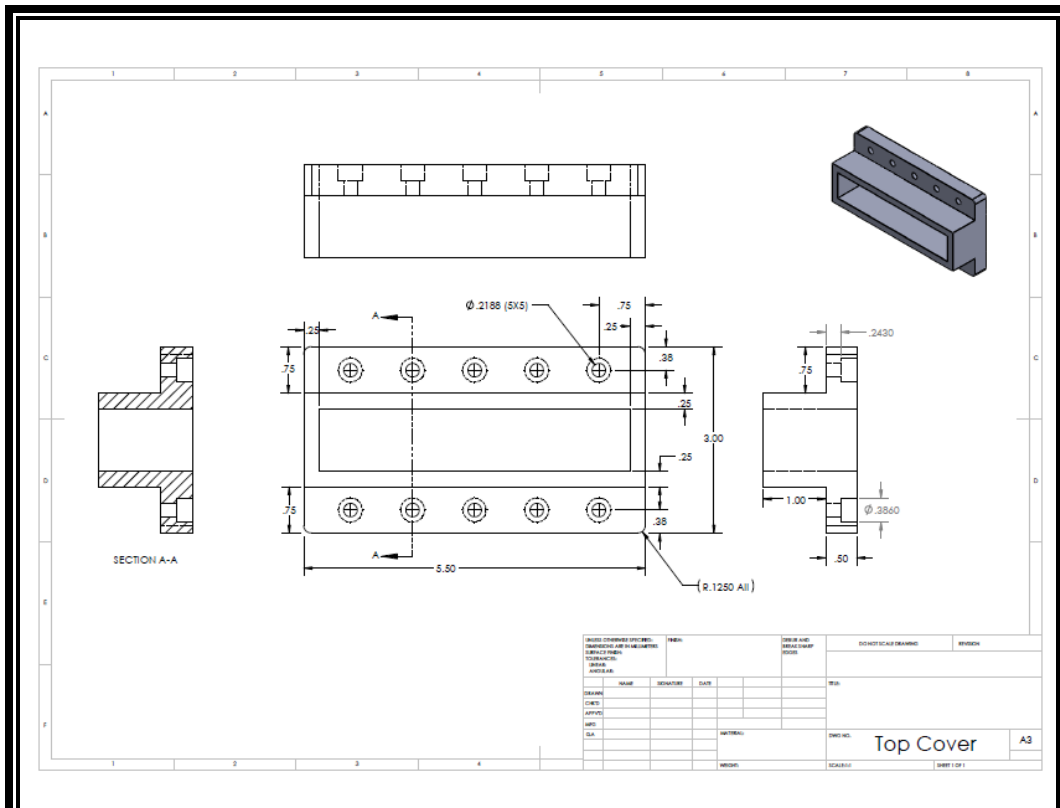
- [86] Cambridge University High Pressure combustion Facility, Department of Engineering, <http://www.g.eng.cam.ac.uk/gtcombustion/facilities/index-facilities.html> (accessed June 2010).
- [87] US Department of Energy. High pressure combustion facility, http://www.netl.doe.gov/onsite_research/Facilities/high-pressure.html (accessed June 2010).
- [88] Frank J, Miller M and Allen M. Imaging of laserinduced fluorescence in a high pressure combustor. In: 37th Aerospace sciences meeting and exhibit, Reno, NV, USA, AIAA, AIAA-99-0773, 1999.
- [89] Tse SD, Zhu D and Law CK. Optically accessible highpressure combustion apparatus. *Rev Scient Instrum* 2004; 75(1): 233–239.
- [90] Tomezak H, Benelli G, Carrai L, et al. Investigation of a gas turbine combustor system fired with mixtures of natural gas and hydrogen. *Int Frame Res Found Combust J* 2002; Article No: 200207.
- [91] Liewen T, Novel D and Zhang Q. Characterization of fuel composition effects in H₂/CO/CH₄ mixtures upon lean blowout. *J Eng Gas Turbines Power* 2007; 129(3): 688–694.
- [92] S Sarker, J Nunez, C Valdez, S Hossain, N Love and A Choudhuri, 'Preliminary design of an optically accessible high-pressure combustor' *Mechanical Engineering Science* 0(0) 1–13, DOI: 10.1177/0954406214536889
- [93] <http://www.azom.com/article.aspx?ArticleID=863>
- [94] Von Mises, R. "Mechanik der Fasten Korper im plastisch deformablen zustand," *Nachr Ges. Wiss. Gottingen*, pp. 582.
- [95] http://www.technicalglass.com/pressure_calculation.html
- [96] Lourenco, L., A. Krothapalli, et al. (1989) *Particle Image Velocimetry. Advances in Fluid Mechanics Measurement*. M. Gad-el-Hak, Springer-Verlag: 128-135
- [97] Adrian, R.J. (1991). Particle-Imaging Techniques for Experimental Fluid Mechanics. *Annual Review of Fluid Mechanics* 23: 261-304
- [98] Grant, I. (1997). Particle image velocimetry: a review. *Proc. Instn, Mech Engrs*. 211(C): 55-76
- [99] Crowe, C.T., Sommerfeld, M., and Tsuji, Y. (1998) *Multiphase flows with droplets and particle*, CRC Press, Boca Raton, Fla
- [100] Merzkrich, W (1987) *Flow visualization*, Academic Press, Orlando
- [101] Raffel, M., Willert, C.E., and Kompenhans, J. (1998) *Particle image velocimetry: a practical guide*, Springer, Berlin; New york
- [102] Santiago, J.G., Wereley, S.T., Meinhart, C.D., Beebe, D.J., and Adrian, R.J (1998) 'Particle Image velocimetry system for microfluidics'. *Experimental in Fluids*. 25(4),316-319

- [103] A.H. Epstein - Quantitative density visualization in a transonic compressor rotor. J. Energ. Power 99 (1977) 460-475
- [104] G. Kychakoff , R.D. Howe, R.K. Hanson - Quantitative flow visualization technique for measurements in combustion gases. Appl. Opt. 23 (1982) 704-712.
- [105] R Miles - Flow-field Diagnostics, Applied Combustion Diagnostics. Edited by Katharina Kohse-Höinghaus & Jay Jeffries, Taylor and Francis Publishers (2002).
- [106] H.B. Najm, P.H. Paul , C.J. Mueller, P.S. Wyckoff - On the adequacy of certain experimental observables as measurements of flame burning rate. Comb. Flame, 113 (1998) 312-332.
- [107] J.M Donbar, J.F Driscoll, C.D. Carter, " Reaction zone structure in turbulent nonpremixed jet flames—from CH-OH PLIF images Combustion and flame 122(1-2) (2000) 1-19
- [108] J.M Donbar, J.F Driscoll, C.D. Carter, "Combustion and flame 125(4) (2001) 1239-1257 Strain rates measured along the wrinkled flame contour within turbulent non-premixed jet flames
- [109] K.A. Watson, K.M Lyons, C.D. Carter, J.M. Donbar, Proc. Combust. Inst 29(2) (2002) 1905-1912
- [110] M. Tanahashi, S. Taka, M. Shimura, T Miyauchi, Exp. Fluids 45 (2008) 323-332
- [111] J. Kiefer a,b , Z.S. Li a,* , J. Zetterberg a , X.S. Bai c , M. Aldén Investigation of local flame structures and statistics in partially premixed turbulent jet flames using simultaneous single-shot CH and OH planar laser-induced fluorescence imaging. Combustion and Flame 154 (2008) 802–818.

Appendix I Detailed drawing for the combustor parts.







Appendix II

Detailed calculation of Entrance and Exhaust section.

The governing equation for the entrance and exhaust transition curvatures is as follows:

$$r = ax^5 + bx^4 + cx^3 + dx^2 + ex + f \quad (1)$$

$$\frac{dr}{dx} = 5ax^4 + 4bx^3 + 3cx^2 + 2dx + e \quad (2)$$

$$\frac{d^2r}{d^2x} = 20ax^3 + 12bx^2 + 6cx + 2d \quad (3)$$

Having the following boundary conditions:

$$@ x = 0 : r = r_i ; \frac{dr}{dx} = 0 ; \frac{d^2r}{d^2x} = 0$$

$$@ x = L : r = r_o ; \frac{dr}{dx} = 0 ; \frac{d^2r}{d^2x} = 0$$

Putting the boundary conditions at eqn 2 and eqn 3, we get the equation of the curve of the entrance section -

$$r = -0.000589x^5 + 0.00736x^4 - 0.02456x^3 + 0.75$$

Similarly the equation of the exhaust section curve:

$$r = 0.0000307x^5 - 0.000786x^4 + 0.005122x^3 + 0.787$$

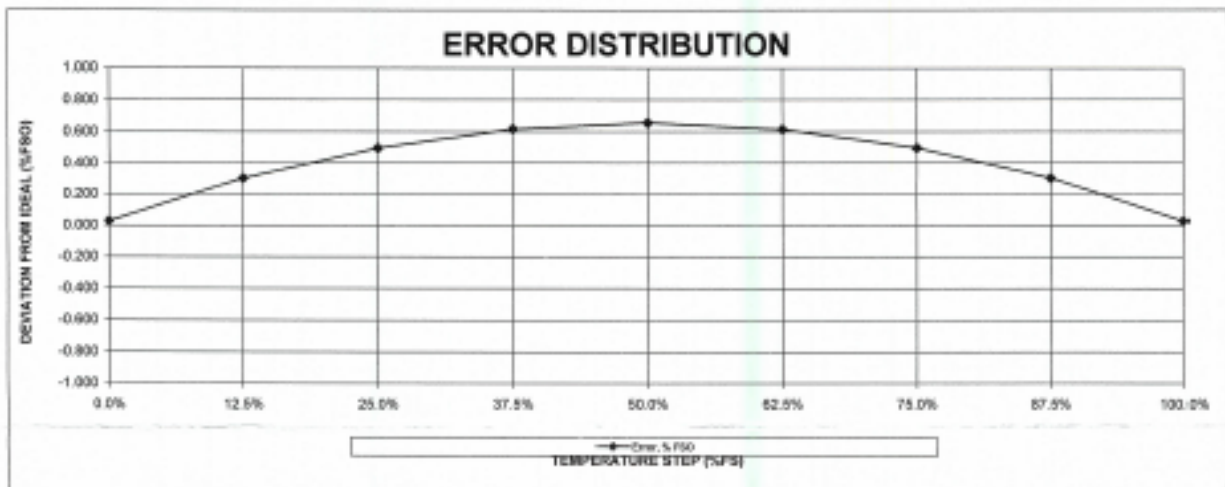
Appendix III Specification of pressure transducer.

LORD STI STELLAR TECHNOLOGY	TC-02	237 Commerce Drive Amherst, New York 14228 USA Tel: 716.250.1900 • Fax: 716.250.1909
------------------------------------	-------	--

TEMPERATURE CALIBRATION RECORD			
CUSTOMER University of Texas @ El Paso	SERIES/PART NUMBER PT1700-150G-171	SERIAL NUMBER 1401446	SALES ORDER 14-0026
CUSTOMER PO 2014047243	CUSTOMER PART NUMBER N/A	MAX/CAL VOLTAGE 18/12 Vdc	
TEMP. RANGE (°F) 0 TO 300	OUTPUT RANGE 0-5 V	CONDITION NEW	

ALL DATA IN °F

STEP	TEMP. (°F)	Output, V	Ideal, V	Error, V	Error, % FSO
0.0%	0.000	0.001	0.000	0.001	0.026
12.5%	37.500	0.640	0.625	0.015	0.301
25.0%	75.000	1.275	1.250	0.025	0.498
37.5%	112.500	1.906	1.875	0.031	0.615
50.0%	150.000	2.533	2.500	0.033	0.654
62.5%	187.500	3.156	3.125	0.031	0.615
75.0%	225.000	3.775	3.750	0.025	0.497
87.5%	262.500	4.390	4.375	0.015	0.301
100.0%	300.000	5.001	5.000	0.001	0.026



SUMMARY			CONNECTIONS		MISC
VALIDATION POINT	149.0°F	2.516	PIN	DESCRIPTION	CONNECTOR
STATIC ACCURACY (% FSO)		0.654	A	EXC+	202031
			D	EXC-	CAL. REC. NO.
			B	PSIG+	41912.42188
			C	PSIG-	QA STAMP
			E	TSIG+	STI 48 QA
			F	TSIG-	9/30/2014

DCN 9028

201905P

CALIBRATION RECORD

CUSTOMER	SERIES/PART NUMBER	SERIAL NUMBER	SALES ORDER
University of Texas @ El Paso	PT1700-150G-171	1401446	14-0026
CUSTOMER PO	CUSTOMER PART NUMBER	PRESSURE RANGE	
2014047243	N/A	0-150 PSIG	
COMP. TEMP. RANGE (°F)	GAGE RESISTANCE	PROOF / BURST PRESSURE	
0 TO 250	5000	225/300 PSI	
OPER. TEMP. RANGE (°F)	MAX/CAL VOLTAGE	CONDITION	
-65 TO 250	18/12 VOLTS	NEW	

ALL DATA IN V

TEST TEMPERATURE: AMBIENT

STEP	INCREASING			DECREASING			HYSTERESIS
	OUTPUT	BEST	DIFFERENCE	OUTPUT	BEST	DIFFERENCE	
0%	0.004	0.007	-0.003	0.008	0.007	0.001	0.004
20%	1.001	1.003	-0.002	1.004	1.003	0.001	0.003
40%	1.998	1.999	-0.001	2.001	1.999	0.002	0.003
60%	2.994	2.994	0.000	2.997	2.994	0.003	0.003
80%	3.990	3.990	0.000	3.991	3.990	0.001	0.001
100%	4.985	4.986	-0.001	4.985	4.986	-0.001	0.000
FSO	4.981					SHUNT	N/A

LOW TEMPERATURE: 0°F

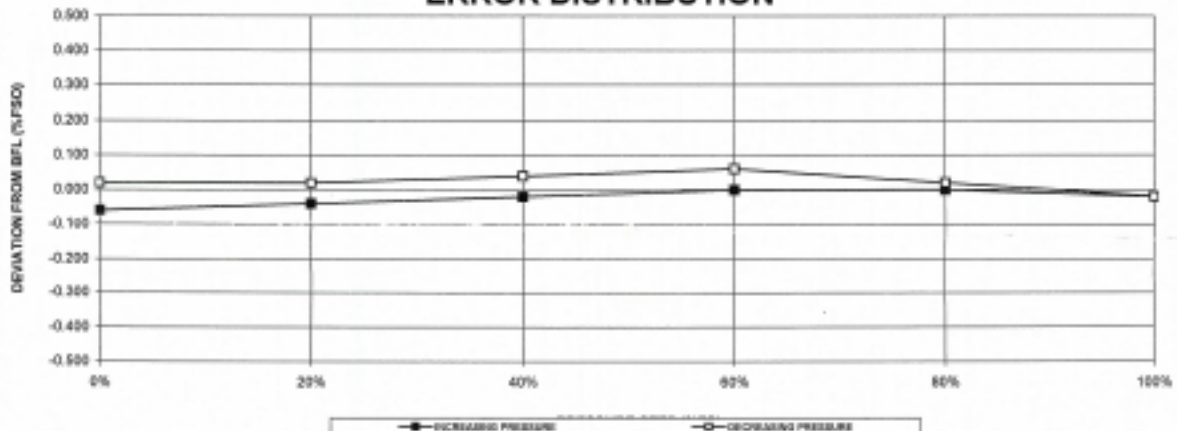
HIGH TEMPERATURE: 250°F

REPEATABILITY @ AMBIENT

STEP	NORMALIZED	STEP	NORMALIZED
0%	0.014	0%	0.002
100%	4.993	100%	4.999
FSO	4.979	FSO	4.997

STEP	OUTPUT 1	OUTPUT 2
0%	-0.003	0.008
100%	4.979	4.982
FSO	4.982	4.982

ERROR DISTRIBUTION



SUMMARY		CONNECTIONS		MISC
ZERO BALANCE	0.004	PIN	DESCRIPTION	CONNECTOR
FULL SCALE OUTPUT	4.981	A	EXC+	202031
STATIC ACCURACY (%FSO)	0.060	D	EXC-	CAL REC. NO.
THERMAL ZERO SHIFT (%FSO / AMB TO HOT PER °F)	0.000	B	PSIG+	41912.42185
THERMAL ZERO SHIFT (%FSO / AMB TO COLD PER °F)	0.002	C	PSIG-	QA STAMP
THERMAL FSO SHIFT (%FSO / AMB TO HOT PER °F)	0.001	E	TSIG+	STI
THERMAL FSO SHIFT (%FSO / AMB TO COLD PER °F)	0.000	F	TSIG-	48
				9/30/2014

CALIBRATION RECORD

CUSTOMER	SERIES/PART NUMBER	SERIAL NUMBER	SALES ORDER
University of Texas @ El Paso	PT1700-150G-171	1401447	14-0026
CUSTOMER PO	CUSTOMER PART NUMBER	PRESSURE RANGE	
2014047243	N/A	0-150 PSIG	
COMP. TEMP. RANGE (°F)	GAGE RESISTANCE	PROOF / BURST PRESSURE	
0 TO 250	5000	225/300	PSI
OPER. TEMP. RANGE (°F)	MAXICAL VOLTAGE	CONDITION	
-65 TO 250	18/12 VOLTS	NEW	

ALL DATA IN V

TEST TEMPERATURE: AMBIENT

STEP	INCREASING			DECREASING			HYSTERESIS
	OUTPUT	BEST	DIFFERENCE	OUTPUT	BEST	DIFFERENCE	
0%	-0.008	-0.006	-0.002	-0.006	-0.006	0.000	0.002
20%	0.989	0.990	-0.001	0.992	0.990	0.002	0.003
40%	1.987	1.987	0.000	1.989	1.987	0.002	0.002
60%	2.984	2.984	0.000	2.985	2.984	0.001	0.001
80%	3.980	3.980	0.000	3.961	3.980	-0.001	0.001
100%	4.976	4.977	-0.001	4.976	4.977	-0.001	0.000
FSO	4.984					SHUNT	N/A

LOW TEMPERATURE: 0°F

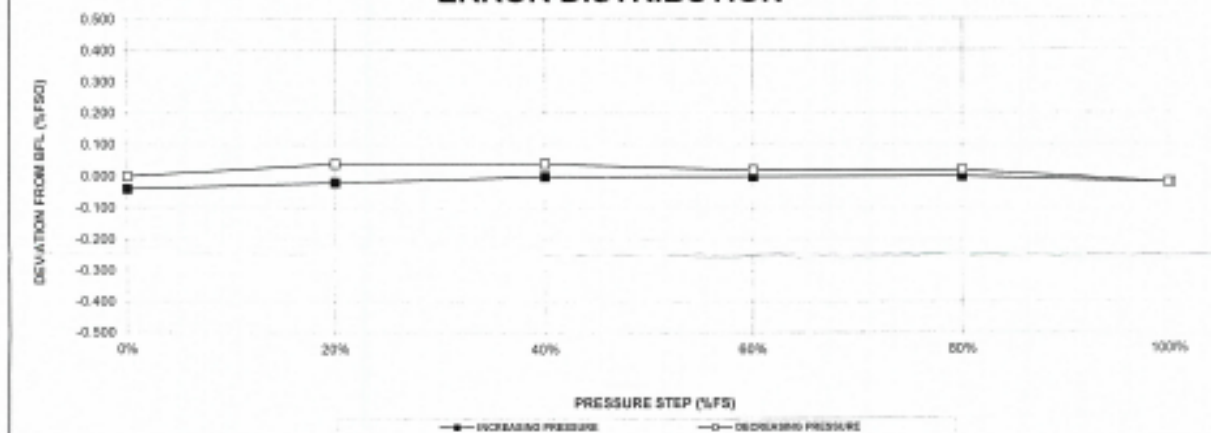
HIGH TEMPERATURE: 250°F


STEP	NORMALIZED	STEP	NORMALIZED
0%	0.036	0%	0.063
100%	4.979	100%	4.992
FSO	4.943	FSO	4.929

REPEATABILITY @ AMBIENT

STEP	OUTPUT 1	OUTPUT 2
0%	-0.010	-0.009
100%	4.974	4.975
FSO	4.984	4.984

ERROR DISTRIBUTION



SUMMARY		CONNECTIONS		MISC
ZERO BALANCE	-0.008	PIN	DESCRIPTION	CONNECTOR
FULL SCALE OUTPUT	4.984	A	EXC+	202031
STATIC ACCURACY (%FSO)	0.040	D	EXC-	CAL REC. NO.
THERMAL ZERO SHIFT (%FSO / AMB TO HOT PER °F)	0.007	B	PSIG+	41912.56585
THERMAL ZERO SHIFT (%FSO / AMB TO COLD PER °F)	0.012	C	PSIG-	QA STAMP
THERMAL FSO SHIFT (%FSO / AMB TO HOT PER °F)	-0.006	E	TSIG+	
THERMAL FSO SHIFT (%FSO / AMB TO COLD PER °F)	-0.011	F	TSIG-	
				9/30/2014

DOX 6628

2112/001

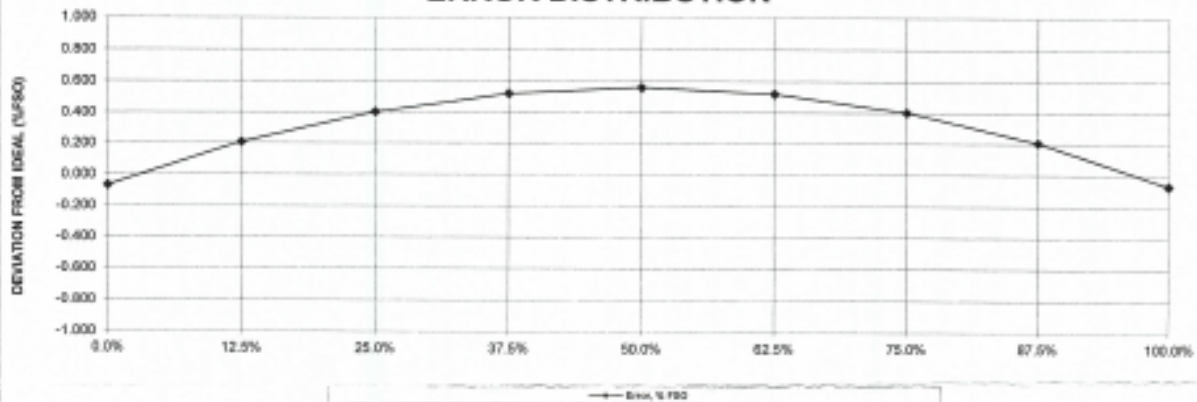
TEMPERATURE CALIBRATION RECORD

CUSTOMER University of Texas @ El Paso	SERIES/PART NUMBER PT1700-150G-171	SERIAL NUMBER 1401447	SALES ORDER 14-0026
CUSTOMER PO 2014047243	CUSTOMER PART NUMBER N/A	MAX/CAL VOLTAGE 18/12 Vdc	
TEMP. RANGE (°F) 0 TO 300	OUTPUT RANGE 0-5 V	CONDITION NEW	

ALL DATA IN °F

STEP	TEMP.(°F)	Output, V	Ideal, V	Error, V	Error, % FSO
0.0%	0.000	-0.003	0.000	-0.003	-0.068
12.5%	37.500	0.635	0.625	0.010	0.207
25.0%	75.000	1.270	1.250	0.020	0.403
37.5%	112.500	1.901	1.875	0.026	0.521
50.0%	150.000	2.528	2.500	0.028	0.560
62.5%	187.500	3.151	3.125	0.026	0.521
75.0%	225.000	3.770	3.750	0.020	0.403
87.5%	262.500	4.385	4.375	0.010	0.207
100.0%	300.000	4.997	5.000	-0.003	-0.068

ERROR DISTRIBUTION

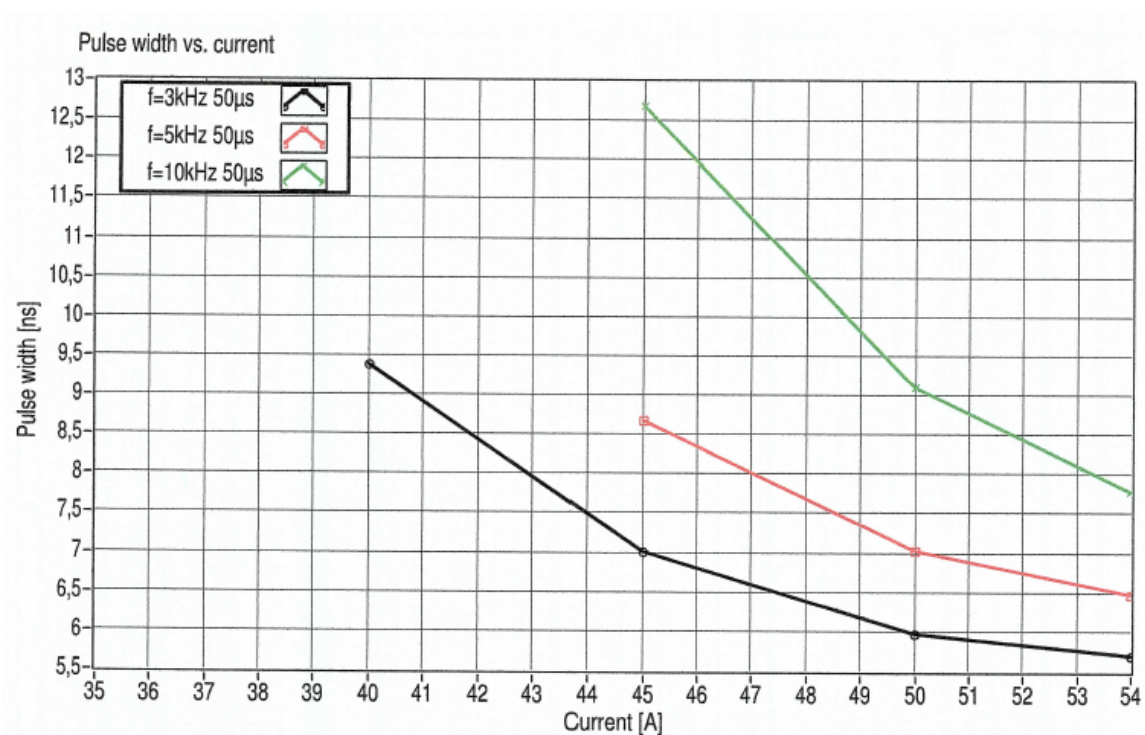
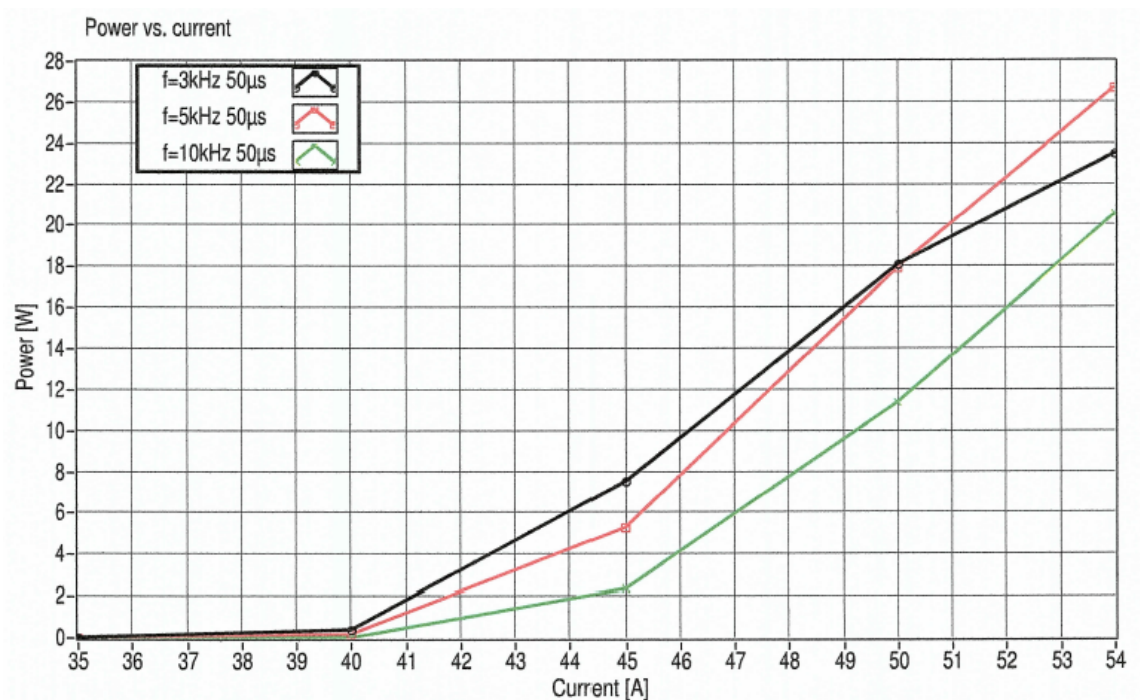


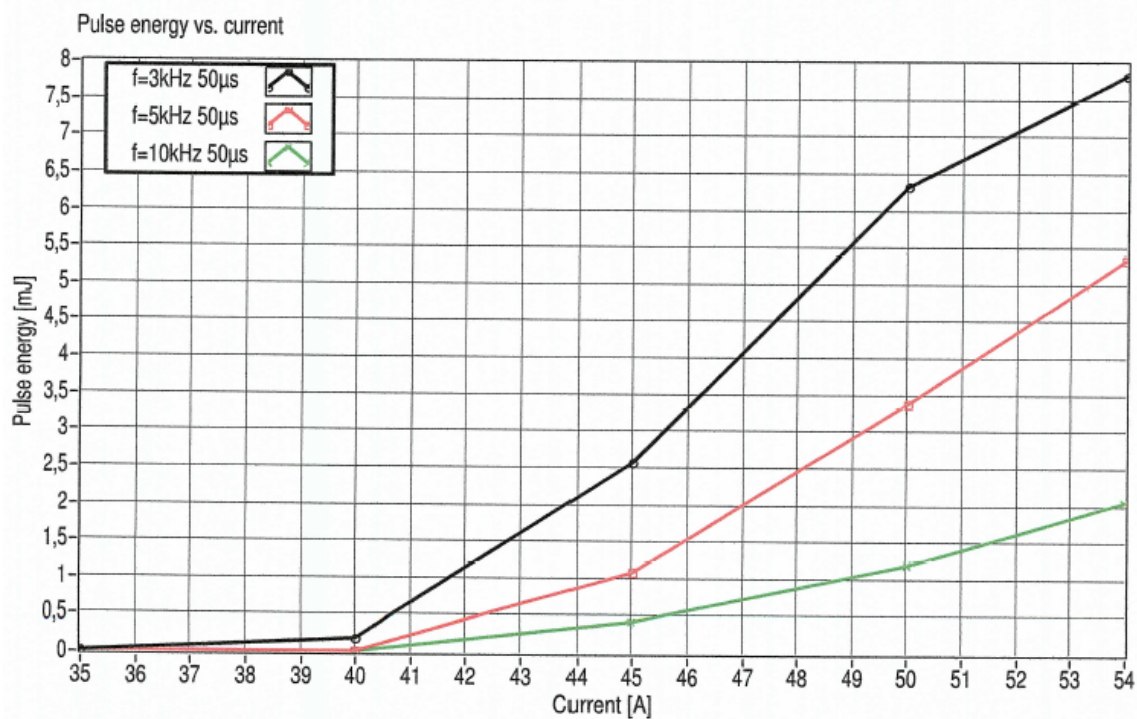
SUMMARY			CONNECTIONS		MISC
VALIDATION POINT	150.0°F	2.528	PIN	DESCRIPTION	CONNECTOR
STATIC ACCURACY (% FSO)		0.560	A	EXC+	202031
			D	EXC-	CAL REC. NO.
			B	PSIG+	41912.56689
			C	PSIG-	QA STAMP
			E	TSIG+	
			F	TSIG-	

Appendix IV

Specification of PLIF laser and Image Intensifire.

Laser power sheet





Frequency	35 A	40 A	45 A	50 A	54 A
$f=3\text{kHz } 50\mu\text{s}$	0,00 W	0,37 W	7,53 W	18,10 W	23,47 W
$f=5\text{kHz } 50\mu\text{s}$	0,00 W	0,18 W	5,30 W	17,95 W	26,68 W
$f=10\text{kHz } 50\mu\text{s}$	0,00 W	0,00 W	2,35 W	11,38 W	20,52 W

Frequency	35 A	40 A	45 A	50 A	54 A
$f=3\text{kHz } 50\mu\text{s}$		9,4 ns	7,0 ns	6,0 ns	5,7 ns
$f=5\text{kHz } 50\mu\text{s}$			8,7 ns	7,0 ns	6,5 ns
$f=10\text{kHz } 50\mu\text{s}$			12,7 ns	9,1 ns	7,8 ns

Frequency	35 A	40 A	45 A	50 A	54 A
$f=3\text{kHz } 50\mu\text{s}$	0,01 mJ	0,18 mJ	2,56 mJ	6,32 mJ	7,82 mJ
$f=5\text{kHz } 50\mu\text{s}$	0,01 mJ	0,01 mJ	1,08 mJ	3,38 mJ	5,34 mJ
$f=10\text{kHz } 50\mu\text{s}$	0,01 mJ	0,01 mJ	0,42 mJ	1,19 mJ	2,05 mJ

●Image intensifier

Parameter		C10880-01C	C10880-03F	Unit
Luminous sensitivity (Typ.)		230		$\mu\text{A/lm}$
Radiant sensitivity (Typ.) ¹⁾		53		mA/W
Quantum efficiency (Typ.) ¹⁾		15		%
Photocathode window material		Synthetic quartz		-
Photocathode material		Multialkali		-
Spectral response range		185 to 900		nm
Wavelength of maximum response		430		nm
Photocathode diameter		25 ⁴⁾		mm
Input lens mount		C-mount	F-mount	
Phosphor screen window material		Glass		-
Phosphor screen material		P-46		-
Luminous gain (Typ.)		1×10^5		$(\text{lm/m}^2)/\text{lx}$
Radiant emittance gain (Typ.) ¹⁾		4.2×10^3		$(\text{W/m}^2)/(\text{W/m}^2)$
EBI (lumen) (Typ.) ²⁾		2×10^{-9}		lm/cm^2
EBI (radiant) (Typ.) ^{1) 2)}		2×10^{-14}		W/cm^2
Limiting resolution (Typ.)		38		Lp/mm
Image magnification		0.67		-
Maximum input light intensity (Typ.)	³⁾	5.0×10^{-3}		lx
	^{1) 3)}	8.0×10^{-10}		W/cm^2

Glossary

(In order of appearance)

Symbol	Description	Unit
M	Mach number	
T_0	Inlet air temperature	K
BR	Blockage ratio	
Re	Reynolds number	
U	Free stream velocity	m/s
L	Integral length scale	m
u	Instantaneous velocity	m/s
u'	Fluctuation of velocity	m/s
KE	Turbulent kinetic energy	J
ε	Turbulent dissipation rate	m ² /s ³
τ_{ij}	Viscous stress	
δ_{ij}	Dirac delta function	
I	Turbulent intensity	
ν	Fluid viscosity	Kg/m.s
η	Kolmogorove length scale	m
t_η	Kolmogorove time scale	s
S_L	Laminar flame speed	cm/s
T_u	Unburned mixture temperature	K
δ_T	Brush thickness	
I_0	Stretch factor	
Re_T	Turbulent Reynolds number	
Da	Damkohler number	
Ka	Karlovitz number	
σ_{hyd}	Hydrostatic stress	MPa
σ_{VM}	Von Mises stress	MPa
σ_y	Yield stress	Mpa
σ_t	Tnagential stress	MPa
τ_s	Particle relaxation time	s
d_p	Particle diameter	m
k	Boltzman constant	

Vita

Mohammad Arif Hossain completed his Bachelor of Science Degree in Mechanical Engineering from the Bangladesh University of Engineering and Technology (BUET) in March, 2012. After finishing his Bachelor degree he joined as a lecturer at the department of Mechanical and Production Engineering (MPE) at Ahsanullah University of Science and Technology (AUST), Dhaka, Bangladesh. Then he enrolled in the Master's program at the University of Texas at El Paso in summer 2013. He joined as a Graduate Research Assistant at the NASA Center for Space Exploration Technology Research (cSETR) and started experimental work on turbulent combustion. Within this period he published five ASME conference proceedings and one journal paper. One of his papers has been awarded for the ASME Young Engineers Paper (YEP) award at the ASME IMECE 2014 conference. In his personal life, he is a self-motivated and positive person who loves to make new friends and likes to work in groups. He is going to start his PhD at the Department of Mechanical and Aerospace Engineering at the Ohio State University from fall 2015.

Permanent address: 'Chaya Neer', 55 PN Road
Old Satkhira, Satkhira-9400.
Bangladesh

This thesis was typed by Mohammad Arif Hossain.